MODELLING AND EXPERIMENTAL INVESTIGATIONS OF A BI-MODAL UNMANNED UNDERWATER/AIR SYSTEM

A thesis submitted in fulfilment of the requirements for the degree of Master of Engineering

Dian GUO

Bachelor of Engineering, Shenyang Aerospace University

School of Engineering

College of Science, Engineering and Health

RMIT University

April 2019

Declaration

I certify that except where due acknowledgement has been made, the work is that of the author alone; the work has not been submitted previously, in whole or in part, to qualify for any other academic award; the content of the thesis is the result of work, which has been carried out since the official commencement date of the approved research program; any editorial work, paid or unpaid, carried out by a third party is acknowledged; and ethics procedures and guidelines have been followed.

Signature: Dian Guo

Date: 29 March 2019

Acknowledgements

I would like to express my great appreciation to Prof. Pier Marzocca for his valuable and constructive guidance during this research work throughout two years. He is my best role model for his enthusiasm and hard work towards research work.

I must express my gratitude to Prof. Cees Bil for his continued support and precious advice. I am very grateful to his knowledge and many insightful discussion and suggestions on this project. His approach, vision and guidance in research enabled me to learn a lot.

I am extremely lucky to have Prof. Pier Marzocca and Prof. Cees Bil as my supervisor who care so much on my work and respond my questions and queries so promptly. It is very enjoyable to be the student of those two professors, and it is a fantastic research journey.

Thanks for the RMIT University for the Translational Research Seed Grant to provide financial support for this project.

I would also appreciate the help from RMIT workshop and all the staffs. This vehicle cannot be there without the help from them. Thanks for the nicest guy Paul Muscat of the composite lab helping me in every situation. It is a pleasure to work with him. Thanks to the technician Michael Delaney and Michael Scherf for the mechanical section, Eli for the computer numerical control (CNC) machine. Also, a lot of thanks given to Gil Atkin and Greg Osward for the suggestion and help for the wind tunnel test and experiment arrangement and thanks to James for the propulsion system test. In addition, I will never forget our Santa Claus Patrick. Especially thanks to the Dr. Matthew Marino and the UAS team for providing the resources and help for the propulsion system test. Also, thanks to Junrong Ye and Mark Simpson for the contribution on this project.

I also thank my friends for providing support and friendship that I need. Thanks to my research mate Antonio, I can't forget the time that we work together and create great achievement. A lot of thanks to Federico, my gym coach, sansei, and desk mate. The guy who worked with me till late and share so many good memories. Also, thanks to my best roommate Loyld, my little spoon Tito, Afanti Reza, my buddy Eli, Buddha Arpen, Organiser Anne, Second Fede, Nichacorn, my sunshine Enrico, Joyce, Alessia, who limited my homeless and gave me all best memories in the last two years. Thanks to my senior Chen Dongyang, Li yufei and Prof. Han for the guidance on the research. Special thanks to my mate Liu Da in China.

Thanks for your technical and emotional support. I am the groomsman always ready for you. Also, thanks to my friends Hou Liguo, Hong Tu for the long time international calls and meditation from far away. Thanks to Jennifer, Frida, Amber, and all the friends from city, who opened my world to art and it is always good time spent with you guys. I would like to express my special thanks to my best friend, beloved Julia. There is a love can't be conveyed by words. Thank you for the unconditional support during my research, life and every beautiful time shared with the beautiful you. At last, but not least, I would like to convey a lot of thanks to my family, and my parents, the best parents in this world, thanks for the courage to support me study overseas and always stand by my side no matter when I hold the trophies or went through the tough time.

The life is a book where you write your tales on. My colourful book is because every one of you.

Table of Contents

List of Figures

List of Tables

List of Abbreviations

ABS	Acrylonitrile butadiene styrene
AUV	Autonomous underwater vehicle
BUUAS	Bi-modal unmanned underwater/air system
CAD	Computer aided design
CFD	Computational fluid dynamics
CG	Centre of gravity
CNC	Computer numerical control
CONOPS	Concept of operations
DC	Direct current
ESC	Electronic speed control
FDM	Fused deposition modelling
FEM	Finite element method
LiPo	Lithium polymer battery
NACA	National Advisory Committee for Aeronautics
NASA	National Aeronautics and Space Administration
MAC	Mean aerodynamic chord
PWM	Pulse width modulation
PVC	Polyvinyl chloride
RPM	Revolutions per minute
SST	Shear stress transport
UAS	Unmanned aircraft system
UAV	Unmanned aerial vehicle
VOF	Volume of fluids

List of Symbols

Conceptual Design and Performance Analysis

A_{front}	Front area (m^2)
A_{plan}	Total area of wing and tail (m^2)
AR	Aspect ratio
b	Wingspan (m)
b_w	Wingspan (m)
c	Wing chord (m)
$\bar{c}$	Wing mean aerodynamic chord (m)
c_r	Root chord (m)
c_t	Tip chord (m)
C_D	Drag coefficient
$C_{D_{water}}$	Underwater drag coefficient
C_{D_0}	Zero-lift drag coefficient
C_{f_e}	Equivalent skin friction coefficient
$C_{F_{flat}}$	Skin friction coefficient
$C_{F_{form}}$	Total drag coefficient
$Cl_{max,3d}$	Maximum lift coefficient in three dimensions
$Cl_{max,2d}$	Maximum lift coefficient in two dimensions
C_L	Lift coefficient
C_{L_α}	Lift curve slope
$C_{L_{max}}$	Maximum lift coefficient
C_P	From drag coefficient
D	Drag (N)
D_{hull}	Hull diameter (m)
D_{water}	Underwater drag (N)
D_0	Zero-lift drag (N)
e	Oswald efficiency
g	Acceleration due to gravity (m. s^{-2})
I_{prop}	Propulsion system current (A)
k	Induced-drag parameter factor
K_P	Form drag coefficient factor
L	Lift (N)
L/D	Lift to drag ratio
L/D_{max}	The maximum lift to drag ratio

L_f	Length of fuselage (m)
L_h	The mean aerodynamic chord for the swept wing (m)
L_{hull}	Hull length (m)
L_H	Horizontal tail moment arm (m)
L_V	Vertical tail moment arm (m)
L_0	Characteristic length dimension (m)
$m_{component}$	Mass of the components (kg)
m_{total}	Mass of the whole vehicle (kg)
m_{wing}	Mass of the wing (kg)
n	Load factor
N_{batt}	Number of batteries
P_{air}	Flight power (W)
P_{water}	Underwater cruise power (W)
q	Dynamic pressure ($kg.m.s^{-2}$)
Q_{batt}	Total battery capacity (mAh)
$Q_{batt_{air}}$	Battery capacity for flight (mAh)
$Q_{batt_{water}}$	Battery capacity for underwater cruise (mAh)
R_e	Reynolds number
$R_{e_{water}}$	Reynolds number in water
$R_{F_{flat}}$	Frictional resistance (N)
$R_{F_{form}}$	Form drag (N)
$R_{surface}$	Wing and tails skin friction (N)
S	Wing area (m^2)
S_{cr}	Wing area in cruise condition (m^2)
S_{hull}	Wetted area of hull (m^2)
S_H	Horizontal tail area (m^2)
S_{ref}	Wing reference area (m^2)
S_{stall}	Wing area in stall condition (m^2)
S_V	Vertical tail area (m^2)
S_{wet}	Wing wetted area (m^2)
S_w	Wing area (m^2)
$S_{Y_{onefin}}$	One fin area of the inverted Y tail (m^2)
S_{Y_V}	Vertical tail of the inverted Y tail area (m^2)
$S_{Y_{V_{oneside}}}$	One side area of V tail of the inverted Y tail (m^2)
$S_{Y_{VT_V}}$	V tail of the inverted Y tail area (m^2)
t_{flight}	Flight time ($hour$)
T/W	Thrust to weight ratio

U_{batt}	Overall efficiency of the propulsion system
V	Airspeed vector of airplane mass center ($m.s^{-1}$)
V_{batt}	Battery voltage (V)
V_{cr}	Cruise velocity ($m.s^{-1}$)
V_H	Horizontal tail volume ratio (m^3)
V_{stall}	Stall velocity ($m.s^{-1}$)
$V_{R/C}$	Rate of climb velocity ($m.s^{-1}$)
V_{turn}	Turn velocity ($m.s^{-1}$)
V_V	Vertical tail volume ratio
V_{water}	Underwater cruise velocity ($m.s^{-1}$)
W	Weight (N)
W/S	Wing loading ($kg.m^{-2}$)
W_t	Total weight (N)
W_0	Initial estimated weight (N)
x_{cg}	Location of CG from nose (m)
$x_{compnent}$	Location of component from nose (m)
x_{wing}	Location of the wing (m)
y^+	Dimensionless distance to the wall
α	Angle of attack (º)
κ	Angle of the force line between the line perpendicular to moment arm (º)
λ	Wing taper ratio
λ_Y	Taper ratio of inverted Y tail
ν	Kinematic viscosity of the fluid ($m^2.s^{-1}$)
ξ_{hull}	Hull form factor
ρ	Fluid density ($kg.m^{-3}$)
ρ_{water}	Water density ($kg.m^{-3}$)
τ_{de}	Wing deploying torque (Nm)
Γ	Wing dihedral angle (º)
Γ_H	Anhedral angle of Horizontal tail (º)
Γ_Y	Y tail anhedral angle (º)
Λ	Wing sweep angle (º)
ν	Kinematic viscosity of air ($m^2.s^{-1}$)

Manufacturing and Structure Analysis

A	Cross section area (m^2)
b_s	Width of mount cross section (m)
E	Young's modulus (Pa)

h_{cspar}	Height of the spar (m)
h_r	C spar root height (mm)
h_s	Height of the sleeve beam (m)
h_s	Height of mount cross section (m)
h_t	C spar tip height (mm)
I_{min}	Minimum area moment of inertia (m^4)
$I_{x,b}$	Second inertial of area of the web (m^4)
$I_{x,f}$	Second inertial of area of the flanges (m^4)
$I_{x,s}$	Second inertial of area of the sleeve beam (m^4)
$I_{x,total}$	Second inertial of area of the spar (m^4)
l	Length of the spar (m)
l_s	Length of the moment arm of the sleeve beam (m)
L_s	Load on the sleeve beam (N)
L_w	Vertical load on wing tip (N)
M	Moments on the spar (Nm)
$M(z)$	Moments distribution along the spar (Nm)
M_s	Moments on the sleeve beam (Nm)
n_c	Safe factor of C-spar
n_w	Wing load factor
t_b	Thickness of the spar web (m)
t_f	Thickness of the spar flange(m)
t_s	Thickness of the sleeve beam (m)
w	Width of the spar (m)
w_r	C spar root width (m)
w_s	Width of the sleeve beam (m)
w_t	C spar tip width (m)
W	Vehicle weight (N)
y	Vertical distance normal to wall direction (m)
y_c	Distance to neutral surface (mm)
z	Distance along the spar (m)
σ	Stress (MPa)
σ_c	Compressive stress of carbon fiber (MPa)
σ_s	Stress on the sleeve beam (MPa)

Wind Tunnel Experimental Testing and Stability Analysis

AR	Aspect ratio
b	Wingspan (m)
$\bar{c}$	Wing mean aerodynamic chord (m)

C_D	Drag coefficient
C_l	Rolling moment coefficient
$C_{l_\beta}, C_{l_p}, C_{l_r}$	Rolling moment coefficient derivatives $\frac{\partial C_l}{\partial \beta}, \frac{\partial C_l}{\partial p}, \frac{\partial C_l}{\partial r}$
C_L	Lift coefficient
C_{L_α}	Lift curve slope
$C_{L_{\alpha_t}}$	Tail lift-curve slope
C_{L_u}	Lift force coefficient derivative $\frac{\partial C_L}{\partial u}$
C_{L_0}	Lift coefficient for zero-angle of attack
C_m	Moment coefficient
C_{m_α}	Pitching moment slope
$C_{m_{\dot{\alpha}}}$	Pitch moment coefficient with a change of angle of attack
C_{m_p}	Moment coefficient measured on the sting
C_{m_q}	Pitch moment coefficient with pitch rate
C_{m_0}	Airplane pitching moment coefficient at zero α
C_M	Moment coefficient
$C_{n_\beta}, C_{n_p}, C_{n_r}$	Yawing moment coefficient derivatives $\frac{\partial C_n}{\partial \beta}, \frac{\partial C_n}{\partial p}, \frac{\partial C_n}{\partial r}$
C_{n_p}	Yawing moment coefficient measured on the sting
C_N	Yawing moment coefficient
C_P	Form drag coefficient
C_R	Rolling moment coefficient
C_T	Thrust force coefficient
C_{T_u}	Thrust force coefficient derivative $\frac{\partial C_T}{\partial u}$
C_{w_0}	Weight coefficient
C_{x_u}	Axial force coefficient derivative $\frac{\partial C_x}{\partial u}$
C_y	Side force coefficient
$C_{y_\beta}, C_{y_p}, C_{y_r}$	Side force coefficient derivatives $\frac{\partial C_y}{\partial \beta}, \frac{\partial C_y}{\partial p}, \frac{\partial C_y}{\partial r}$
C_Y	Side force derivative
C_{z_α}	Normal force coefficient derivative $\frac{\partial C_z}{\partial \alpha}$
C_{z_u}	Normal force coefficient derivative $\frac{\partial C_z}{\partial u}$
D	Drag (N)
D_0	Zero-lift drag (N)
e	Equilibrium condition
h	Location of the CG
h_0	Position of the aerodynamic centre of the wing on the standard mean chord

h_H	Vertical distance between tail mac to wing mac in x-y plane (m)
h_n	Position of neutral point as a decimal fraction of the wing standard mean chord
I_x, I_y, I_z	Moment of inertia
$\hat{I}_y$	Non-dimensional moment of inertia about the Y axis
I_{zx}	Moment of inertia
K_N	Static margin
l_H	Horizontal distance between tail mac to wing mac in x-y plane (m)
l_t	Distance between CG and tail mean aerodynamic center (m)
l_v	The distance between CG and vertical tail aerodynamic center (m)
L	Lift (N)
L_v, L_p, L_r	Rolling moment derivatives $\frac{\partial L}{\partial v}, \frac{\partial L}{\partial p}, \frac{\partial L}{\partial r}$
(L, M, N)	Scalar components of $\boldsymbol{G}$ in F_B (Nm)
m	Mass (kg)
$\boldsymbol{M}$	Mach number
N_v, N_p, N_r	Yawing moment derivatives $\frac{\partial N}{\partial v}, \frac{\partial N}{\partial p}, \frac{\partial N}{\partial r}$
p_d	Dynamic pressure ($kg.m.s^{-2}$)
(p, q, r)	Scalar components of $\boldsymbol{\omega}$ in F_B ($rad.s^{-1}$)
S	Wing area (m^2)
t^*	The characteristic length divides the velocity (s)
u	Velocity of the fluid with respect to the object ($m.s^{-1}$)
u_0	Reference flight speed ($m.s^{-1}$)
(u, v, w)	Scalar components of V in F_B ($m.s^{-1}$)
V	Airspeed of wind tunnel ($m.s^{-1}$)
V_H	Horizontal tail volume ratio (m^3)
x_{ac_t}	Location of tail aerodynamic center from nose (m)
x_{cg}	Location of CG from nose (m)
x_p	Location of the center of wind tunnel sting (m)
X_u	Axial force derivative $\frac{\partial X}{\partial u}$
(X, Y, Z)	Components of resultant aerodynamic force acting on the air plane, in F_B (N)
Y_v, Y_p, Y_r	Side force derivatives $\frac{\partial Y}{\partial v}, \frac{\partial Y}{\partial p}, \frac{\partial Y}{\partial r}$
z_v	The distance the vertical tail aerodynamic center is above the vehicle center of mass (m)
Z_u	Normal force derivative $\frac{\partial Z}{\partial u}$
α	Angle of attack (^{o})

β	Sideslip angle (º)
ζ	Damping ratio
η_H	Efficiency factor of the horizontal tail
η_s	Stabilizer efficiency
λ	Wing taper ratio
λ	Eigenvalue
ϵ	Downwash angle (º)
θ	Angle of attack (º)
μ	Relative density of the aircraft
ρ	Fluid density ($kg.m^{-3}$)
(ψ, θ, ϕ)	Euler angles (rad)
$\boldsymbol{\omega}$	Angular velocity vector of the airplane ($rad.s^{-1}$)
ω_n	Undamped circular frequency ($rad.s^{-1}$)
Λ	Wing sweep angle (º)
$\Lambda_{c/4}$	Sweepback angle of the wing 1/4 chord line (º)

Transition Propulsion System

A	Water chamber exit area (m^2)
B	Buoyancy (N)
C_D	Drag coefficient
C_{D_w}	Underwater drag coefficient
C_L	Lift coefficient
D	Drag (N)
g	Acceleration due to gravity (m. s^{-2})
G	Small vehicle weight (N)
$h_{require}$	Required launch height (m)
H	Water/air interface height (m)
l	Reminded underwater fuselage length of small vehicle (m)
l_f	Fuselage length of small vehicle (m)
L	Lift (N)
$L_{chamber}$	Water chamber length (m)
m	Mass (kg)
$\dot{m}$	Mass flow rate ($kg.s^{-1}$)
$\boldsymbol{M}$	Mach number
P	Pressure (MPa)
P_{atm}	Atmospheric pressure (MPa)
R	CO_2 gas constant
S	Small vehicle reference area (m^2)

t	Time (s)
T	Thrust (N)
$\boldsymbol{T}$	Temperature (K)
$T_{experiment}$	Thrust from experiment (N)
v	Water jet velocity ($m.s^{-1}$)
V	Small vehicle velocity ($m.s^{-1}$)
V_b	Volume of water chamber (m^3)
V_{CO_2}	CO_2 cartridge volume (m^3)
V_f	Optimized volume of water chamber (m^3)
V_w	Water volume inside water chamber (m^3)
V_0	Initial volume of water chamber (m^3)
V_1	Small vehicle velocity component ($m.s^{-1}$)
V_2	Small vehicle velocity component ($m.s^{-1}$)
z	Axial distance from the bottom or outlet of the water chamber (m)
γ	Heat capacity ratio
ε	Actual pressure drop coefficient
ε_0	Initial pressure drop coefficient
η	Actual wall friction and general losses coefficient
η_0	Initial wall friction and general losses coefficient
ρ	Air density ($kg.m^{-3}$)
ρ_w	Water density ($kg.m^{-3}$)

Hybrid Propulsion System Design

C	Gear center distance (m)
d	Gear pitch diameter (m)
$\boldsymbol{m}$	Gear module
$\boldsymbol{G}$	Resultant external moment vector, about the mass center (Nm)

Abstract

The ability to perform underwater and coastal area monitoring missions without surfacing would increase submarine's safety and its combat ability. An innovative bi-modal unmanned/underwater air system (BUUAS) and its concept of operations (CONOPS) are proposed to reduce the risk of submarine's exposure. The BUUAS is firstly released from a submerged submarine and travels underwater to keep a distance from the submarine. Then it will exit the water using an innovative propulsion system that would allow a transition from water to air with the purpose of carrying out a planned air mission. When the airborne mission is finished, the BUUAS will dive back into the water and cruise to the submarine to be collected.

This study aims to design and develop this system that can achieve the proposed CONOPS. The project addresses three critical aspects, namely, i) the study of an optimised configuration considering both aerodynamic and hydrodynamic performance aspects, ii) the exploration for an effective transition between water/air media and iii) the design of the water/air hybrid propulsion system. A variable-sweep wing configuration with a novel wing-deployment mechanism is considered for an efficient operation in water and air. Numerical simulation, water and wind tunnel experimental tests were conducted to assess the performance characteristics of the propulsion unit in water and the aerodynamic characteristics in air. The assessment data supports the feasibility of the bi-modal vehicle configuration and the stability analysis demonstrates the vehicle has static and dynamic stable behaviour during its flight. The water jet transition propulsion system is powered by pressurized CO_2 and was developed to enable a fast take-off transition from water to air. The preliminary design covers the system sizing using an analytical model calibrated by the high-fidelity numerical simulation approach and the design of a specialized gas release mechanism adopted in the propulsion unit. The thrust and launch experiments were performed to verify the transition propulsion system design results and applicability. The air and water experimental results of the customized compact hybrid propulsion system confirm its provision of sufficient power for flight and underwater cruise.

Chapter 1: Introduction

1.1 MOTIVATION

With the continuous development of modern underwater tracking technology, submarines risk of being easily exposed even during submerged operations. An innovative bi-modal unmanned/underwater air system (BUUAS) and its concept of operations (CONOPS) are proposed to reduce the risk of exposure of the submarine. As shown in the mission profile in Figure 1-1, a submarine is equipped with a BUUAS. When a surveillance, reconnaissance or targeting mission is to be carried out, the BUUAS is released from a submerged submarine to cruise underwater for a sufficient distance without giving away the submarine's position. Then it will ascend just below the water surface, take-off from the water using a water jet propulsion system and reconfigure for the flight to carry out its mission in a similar way that other unmanned aerial vehicles (UAV) would do. At the end of the flight, the vehicle reconfigures for underwater operation, dives and travels underwater as to be collected by the submarine. If the transition water-to-air and air-to-water occur far away from the submarine, the BUUAS will not expose the location of the submarine keeping its stealth performance. Moreover, the vehicle can reduce the risk of itself being detected by having a prolonged underwater stealth to increase the mission effectiveness. In other words, the BUUAS processes the rapid manoeuvrability of a small UAV and excellent stealth performance of the AUV (Autonomous Underwater Vehicle) [1].

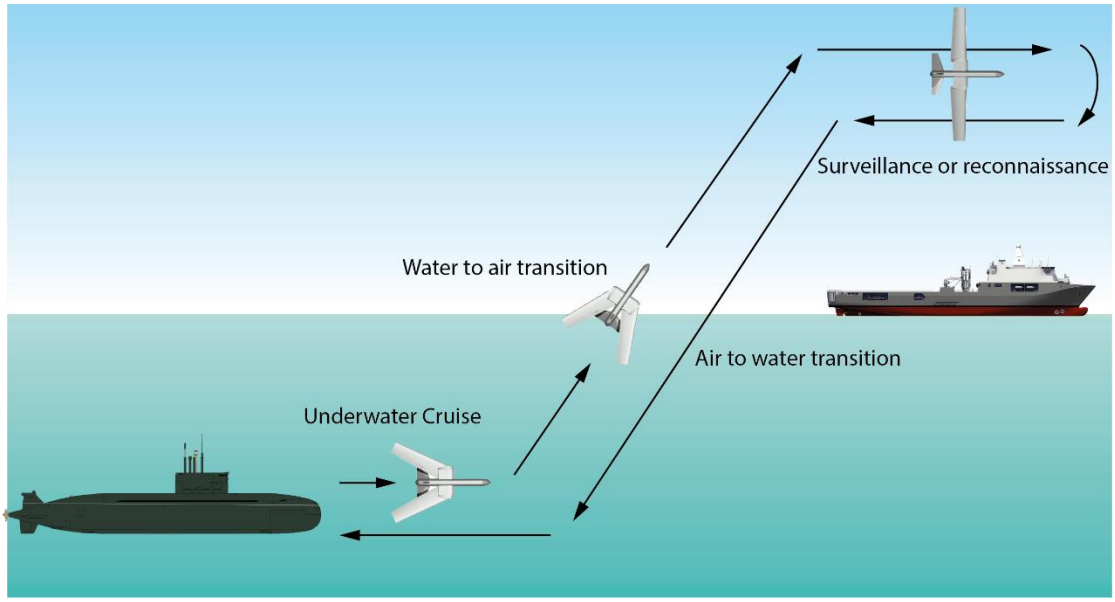

Figure 1-1: Mission profile

Given its ability to perform aerial monitoring and underwater data collection, the BUUAS has also significant potentials in the civil market. These features of the BUUAS increase its application value in areas such as search and rescue, and surveying for natural resources. One example is that such vehicle can map the toxic spill when there is an oil leakage on the ocean. Since the vehicle can quickly travel in the air and collect samples from water, this capability makes search and rescue more efficient and effective. Moreover, this tool can also be used in oceanography research for sample collection and observation [1].

To the best of the author's knowledge, no vehicle is currently capable of these operations in a single mission. It is worth mentioning that to date there are other BUUAS concepts being proposed in the US and Europe, but they are mostly at the design stage and/or initial sub-system technology development [2].

The novelty of the BUUAS is that it integrates the features from aerial and marine vehicles such as configuration and propulsion system to achieve the high efficiency function in both air and water. Based on the previous studies and experience in the field, an original concept is proposed in this research. The development and testing of the BUUAS will fill in the knowledge gap required to solve critical design aspects and address the scientific research questions presented later in this chapter. The data and experience throughout this research have the potential to assist the future development toward a higher technology readiness level of the presented concept.

1.2 TECHNOLOGY DEMONSTRATOR

To achieve the technology and explore the behaviour of the bimodal vehicle, this research begins with building a technology demonstrator. The reason is that building a fully functional product for the whole mission profile is time consuming and needs sophisticated engineering experience, which is unrealistic, since this research is started from zero, and few relevant designs are presented. The technology demonstrator does not need to finish the operation of the whole mission profile. It is a basic platform which should have the ability to realize the major functions in the mission profile, such as the operation in the air and water and transition from water to air. The research toward those functions can provide the knowledge and experience for the development of a fully functional vehicle. Therefore, the design concept above derives the three main design aspects, which are the configuration development, the transition propulsion system, and the hybrid propulsion system. The research and experimentation are concerned on

those design aspects. As a result, the BUUAS is used for containing the system above to demonstrate the bi-model vehicle technology.

The airborne surveillance mission is the design priority and the underwater mode is only for the stealth movement. Consequently, the vehicle design is focused on the flight mode with compromises for the underwater mode. With this background, the underwater characteristics such as added mass, propulsor cavitation, the underwater displacement of the vehicle, its centre of buoyancy and underwater stability will not be investigated but can be considered in the future development based on the presented work in this thesis. Further, the design of the prototype will emphasize the convenience of the research and testing, so payloads such as camera and sensors are not considered at this moment. In addition, it is the priority to realize the design aspects. On the other hand, it should also consider the properties of the vehicle for completing the actual mission profile during the design, as this research is laying the foundation for the final fully functional product.

1.3 OBJECTIVES

The primary goal of this research is accomplishing the BUUAS that can realize functions in the mission profile. In order to achieve this, the project starts with developing elemental aspects of the BUUAS. The configuration and propulsion system are two basic elements that the BUUAS must have to realize successfully operation. Besides, the necessary transition process between water and air must be investigated and carried by a conceived system. Those demands establish the main project objectives which are:

- Development of BUUAS, a system capable of both air and water operations.
- Development of a transition propulsion system that can achieve an effective water-to-air transition.
- Development of a hybrid propulsion system, which can efficiently operate in both water and air.

1.4 PROJECT STRUCTURE

In order to achieve three objectives, this project consists of three main sections correspondingly, which are in the green area of the flow chart in Figure 1-2. The sequence of the project is to design the configuration and fabricate the vehicle based on the established mission profile and requirement. Then, the transition and hybrid propulsion systems can be developed according to the proposed first-generation vehicle configuration. The proposed

configuration sets the requirement, which defines the function and specification, for developing propulsion systems. This design sequence reduces the risk of the propulsion systems failure and increases their usability. Finally, propulsion systems can be integrated into the fabricated vehicle, which is also the whole vehicle assembly.

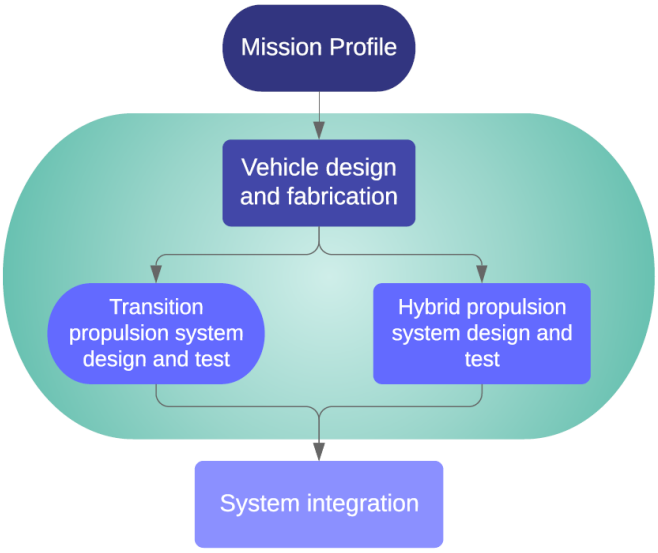

Figure 1-2: Project structure overview

1.4.1 Configuration of BUUAS

The configuration development of the BUUAS is determined by its bi-modal capability of operating in air and underwater. However, the physical properties of air and water are different. The aerodynamic configuration of the normal airplane may not be suitable for the underwater operation. For instance, according to the mission profile, the surveillance mission needs the long-duration flight, which leads to a high aspect ratio wing and large wing area designs. Nevertheless, the characteristics above would affect the underwater maneuverer capability of the BUUAS. To achieve the combined capability of operation in water and air, a configuration change between water and air and vice versa is necessary. Therefore, this research will investigate a variable-sweep wing configuration concept. It is optimized for both air and water operation to increase the flight duration, reduce the underwater drag and protect the BUUAS from any damage especially during the diving phase.

The buoyancy related the volume of the vehicle should be properly considered, since excessively low or high buoyancy will increase the working load of the buoyancy control system. For an efficient underwater travel, the neutral buoyancy design is preferable, which is the vehicle neither sink down nor float up in water but travels at a specific depth. The neutral buoyancy design can allow the vehicle to travel underwater without the buoyancy control

system; such control would increase the weight penalty and to float up and sink down are time-consuming operations. Finally, to assess the performance of the configuration, the numerical simulation will be conducted from both aerodynamic and hydrodynamic point of view. Further, the vehicle will also be fabricated and tested in the wind tunnel to verify the design and numerical simulations results.

1.4.2 Transition propulsion system

One of the innovative features of the BUUAS is the capability of water-to-air transition, which is different from the normal take-off and landing. Comparing to the take-off from runway, there are large resistance and adhesion forces in water acting on the vehicle before take-off, and waves in a rough sea state can also disturb the vehicle. To avoid these problems, the BUUAS will adopt a transition propulsion system, water-jet propulsion powered by pressurized CO_2, which produces sufficient thrust to rapidly propel the vehicle from water-to-air. Malhotra [3] assessed experimentally the thrust generated by high-speed CO_2 gas discharged from a pressurized CO_2 cartridge. As a result, high-pressure gas can be used to expel water from a chamber to generate high impulse thrust capable of propelling the vehicle out of the water. Based on the previous experiments and tests, this research would focus on four design aspects for the transition propulsion system: i) the design of the gas release mechanism to discharge the pressurized CO_2, ii) the study of a scaled propulsion system using analytical model calibrated by high-fidelity numerical simulations, and iii) the development of a trajectory prediction model for the vehicle accounting for the vehicle water-to-air transition. Finally, as a verification of the design, the analytical model and the numerical simulations, iv) underwater thrust generation and water-to-air launch experiments will be conducted.

1.4.3 Hybrid propulsion system

A novel propulsion system must be developed to efficiently propel the vehicle in air and water, since propellers used in aircraft and submarines are different. There are two potential solutions: i) to equip the BUUAS with two distinct water and air propellers; ii) to develop a new type of propeller and propulsion system, which is suitable for both air and water. The first solution will require either two propellers and two motors or two propellers and one motor with a transmission system. However, this solution comes with significant weight penalties. On the other hand, the second solution can save weight and simplify the power system. If the number of components is minimised, one motor only is used to drive the novel propellers. The air propeller commonly runs at 6,000 revolutions per minute (RPM), while for underwater operation the propeller usually runs at few hundreds RPM. In this case, a transmission system

is to be used to provide steady RPM output in both water and air. Further, the whole system should be waterproofed and integrated with the transition propulsion system. Experiments have been carried out to verify the propulsion unit performance in both water and air.

1.5 LITERATURE REVIEW

In recent years, the BUUAS concept is in rapid development, since this multi-functional vehicle can be used in the area of military, environmental monitoring, disaster management and military surveillance [4]. The first aquatic-aerial vehicle concept called the flying submarine was proposed in 1934 [5]. It was a combination of the seaplane and the submarine. The function of this vehicle was to fly in the air and travel underwater. There were also several similar prototypes such as LPL prototype [6], and RFS-1 prototype [7] shown in Figure 1-3. They had the potential of operation in air and underwater. However, none of them accomplished the full function of operating in both air and water. Since the design principle of the aircraft and submarine are totally different, it is obvious that it is difficult to build such a vehicle.

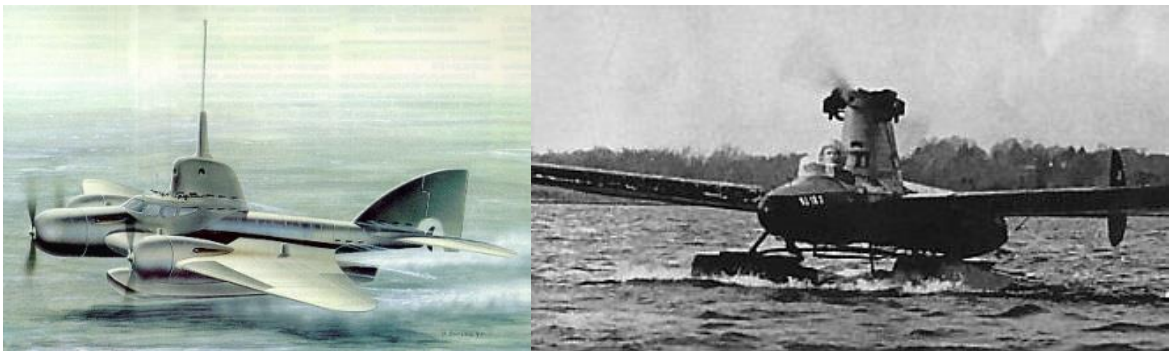

Figure 1-3: LPL prototype (left) [6], PFS-1 prototype (right) [7]

On the other hand, the UAV system has made impressive technological progress. They include the same systems in manned aircraft, with the exception of some airborne element, such as the equipment and facilities for aircrew [8]. In addition, the launch, landing, recovery, and communication can be redesigned for the UAV system to be suitable for mission requirements. Besides, the AUVs have seen significant development in the area of ocean data collection, underwater surveillance and reconnaissance over the past decades [9]. The sophisticated underwater operation technique of the AUV can be utilized for building a bi-modal vehicle. As a result, the application of unmanned vehicle technology makes the full functional aerial and aquatic prototype vehicle realizable.

Due to the combined advantages of UAV and AUV, and wide applications, research toward the development of a fully functional vehicle is steadily increasing. However, only a few concepts are currently under development and at an advanced stage. From literature survey,

the research gap can be identified and consists of the three critical aspects: i) Aerodynamic and hydrodynamic configuration, ii) Transition between water and air including take-off from and dive into the water, iii) The water/air hybrid propulsion.

1.5.1 Aerodynamic and hydrodynamic configuration

Hydrodynamic configuration

The underwater vehicles, such as submarines and AUVs have a sophisticated hydrodynamic configuration. The geometry of the submarine is straightforward, and mostly the hull is an axisymmetric body [10]. Similar to a submarine, the most common AUVs has the streamlined configuration [11] and the control surfaces are at the back of the vehicle shown in Figure 1-4.

For achieving the goals of underwater long endurance operation and low energy cost, the underwater glider, which is a special type AUV, is invented. The underwater gliders have a similar configuration to the fixed-wing aerial vehicle, but the wing size is smaller than the normal aircraft at the same weight level [12]. The locomotion of the underwater glider is similar to the air glider. By changing their buoyancy, they can gain vertical velocity in the water. In the meantime, the lift created by their wing push them to move forward [12]. The underwater gliders use exceedingly little power during cruise, but the cruise speed is very slow. Nonetheless, the utilization of the wing for the underwater movement is a feasible scheme for the BUUAS in the future design. The underwater gliders also provide the idea of trimming the vehicle underwater by using the wing and other control surfaces.

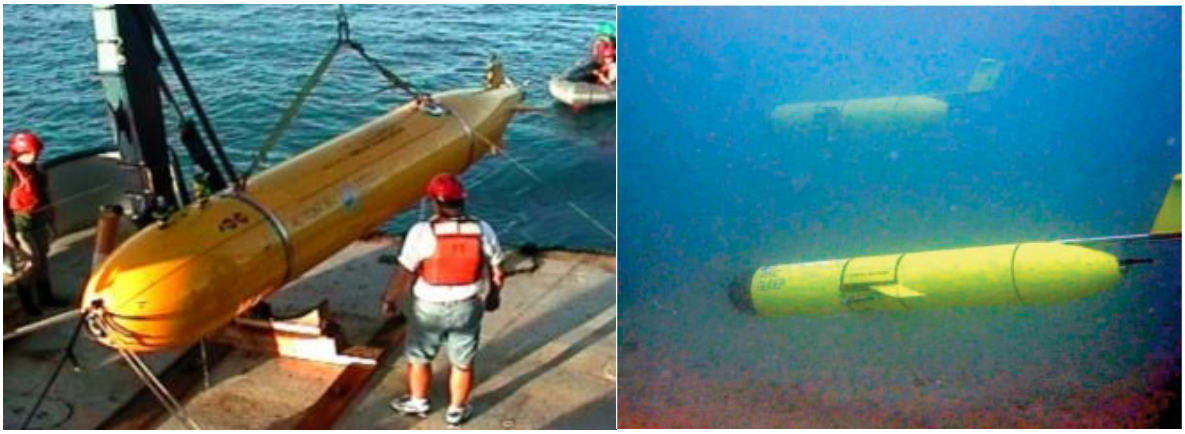

Figure 1-4: AUTOSUB Southhampton Oceanography Centre [13] (left), Slocum Glider [14] (right)

Comparison between flexible and rigid wing

In the mission profile, the requirement for the air operation section is the long endurance flight for the detection mission, which leads to a high aspect ratio design. For the water

operation section, the requirement is an underwater sneak with relatively low velocity similar to the submarine. One design term for the submarine geometry is the perfectly symmetrical shape around its longitudinal axis [10]. However, this term is contradicting to the high aspect ratio design. A long wing for air operation has a substantial detrimental effect on the hydrodynamic performance of the vehicle. It can affect the manoeuvring ability and create huge form drag. It is necessary to change the configuration of the vehicle to adopt two different media.

Table 1-1: Comparison of different configuration

Category		Advantages	Disadvantages
Flexible deployable wing - NASA I2000 project [15]		Occupy small volume Low weight	Difficult to build No control surface
Rigid deployable wing - MIT vehicle [16]		Control surface Easy to develop	High volume High weight

There are several strategies from the literature to eliminate or reduce the wing effect for underwater manoeuvre. The first one is using a flexible deployable wing; the second one is adopting rigid deployable wing. Most of the flexible deployable wing use flexible material. A typical example is the project of NASA I2000 [15] in Table 1.1. It has an inflatable wing. The pressurized gas is inflated into the wing to support the shape of the wing for flight. By simply discharging the gas, the wing can be folded. This discharging design dramatically decreases the negative effect of the wing by eliminating the volume of the wing. Another similar example is the robotic flying fish developed by Gao and Techet [17]. The wing of robotic flying fish is constructed by the polyurethane coated nylon, which makes it flexible. The wing texture is like cloth, so it can be easily folded with the help of the mechanism. However, this technology needs the background of material, and it takes tremendous time to develop only the wing section. Moreover, the flexible wing cannot take the load as much as conventional structure aircraft. So, it is not suitable for the BUUAS development.

The rigid deployable wing is the best choice, due to its fast development and short time manufacturing advantages. The similar concept from the MIT [16] is displayed in Table 1-1. It has the conventional aircraft wing structure, but the wing can be folded back for compromising the underwater locomotion. The volume of the rigid wing is also a parameter that has an influence on the underwater movement. However, the control surface such as the aileron and flap can be equipped on the rigid wing structure, which can enable the vehicle to achieve more manoeuvres in the air and water.

Aerodynamic configuration

There are several vehicles with a rigid deployable wing configuration that can achieve parts of the BUUAS mission. They adopt the swept wing to mitigate the hydrodynamic loads and impact force. In 2016, Siddall, Ancel and Kovac from imperial college developed a morphing wing aircraft, which can dive into the water [18] as shown in Figure 1-5. The wing consists of three parts. Two parts on both sides can rotate around the pivot from 0º to 90º driven by the gear and servo. The wing adopts small chamber about 5%, because the thick watertight wing can create enormous buoyancy, which will affect the underwater movement as mentioned, and the water-permeable wing has the problem that the water will remain inside. The small camber can also reduce the drag after it is folded, since it creates a relatively small front area. This vehicle has a promising test result on both aerodynamic and hydrodynamic aspects. Because the lift and drag are reduced when the wing is sweeping, the vehicle can passively dive from flight smoothly.

The same wing configuration was also used in the hybrid aerial underwater vehicle designed by MIT Lincoln Lab to reduce the impact force when the vehicle is diving as presented in Figure 1-5. The wing can be folded completely in 0.25s, and the folding wing mechanism is only 8% of total weight. However, this folding wing mechanism is driven by a spring, so it is not reusable in one mission. Based on the study of previous models, the change of configuration is inevitable for BUUAS if high performance is desired in both fluids. In addition, trade-offs are needed toward operation in water and air during the configuration design.

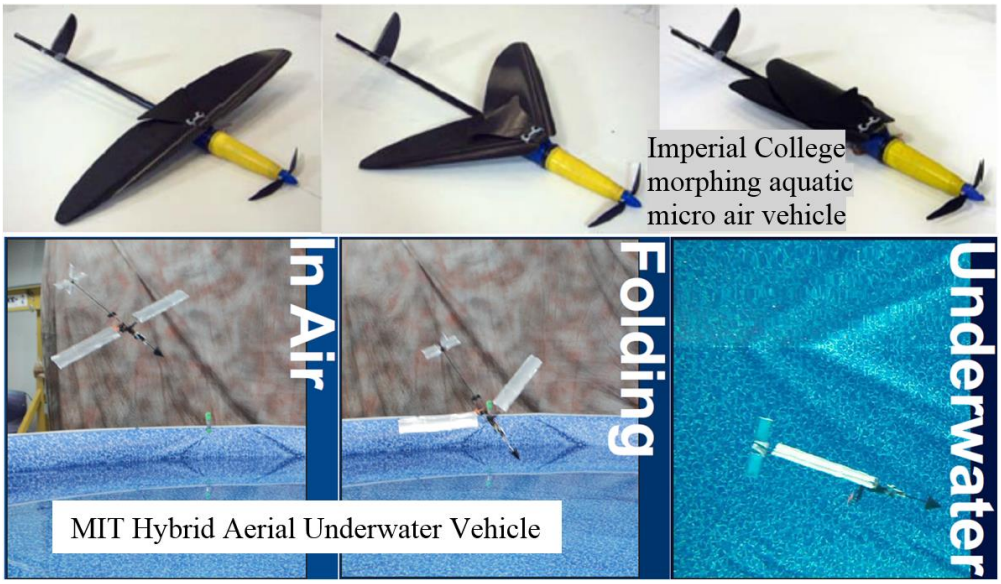

Figure 1-5: Folding wing strategy from the Imperial College [19] and MIT [16]

1.5.2 Transition process

According to the published research works, the technical issues with the transition process are broadly classified into two categories, namely the instant transition strategy [20-22] and the buoyancy control transition strategy [23, 24].

Instant transition strategy

In 2005, Lockheed Martin Corporation developed the *Cormorant* UAV [20], which is launched from a submarine missile launch tube using rocket boosting to exit the water as illustrated in Figure 1-6. The *Cormorant* is an immersible unmanned aircraft and it adopts a morphing wing structure. After the mission is completed, the *Cormorant* will return to its landing site, and a parachute will be deployed. Then the vehicle will splash down on the water surface. Finally, the submarine will use a remote device to retrieve the *Cormorant*. However, the underwater travel ability of the *Cormorant* is only confined to the take-off phase. Further, the retrieve process can expose the position of the submarine.

The Hybrid Aerial Underwater Vehicle developed by the MIT Lincoln Laboratory team has a novel transition strategy for water recovery [16]. The vehicle imitates the gannet birds, which will plunge dive into water to prey fish as shown in Figure 1-6. The wing of the vehicle can be folded, and the vehicle processes a special nosecone design to protect the vehicle with impact on water. The further research is conducted to make the taking off from water come true and the versatility is being added to the vehicle. Although the vehicle has an incomplete function regarding the operation in both air and water, the plunge-diving strategy is identified as an optional design direction for other explorers in this area.

The aquatic micro air vehicle from the Imperial College demonstrates a fast aquatic escape technology by using acetylene explosions to expel the water to produce thrust like the water jet [25], which is shown in Figure 1-6. The generated thrust can be over 20N, which is enough to propel the vehicle out of water. The water can be collected from the operational environment of the vehicle conventionally. It inspires that the most accessible water can be the propellant. However, the chemical reaction is relatively hard to control. It can be easily replaced by other pressurized gas resources that can make the propulsion more applicable.

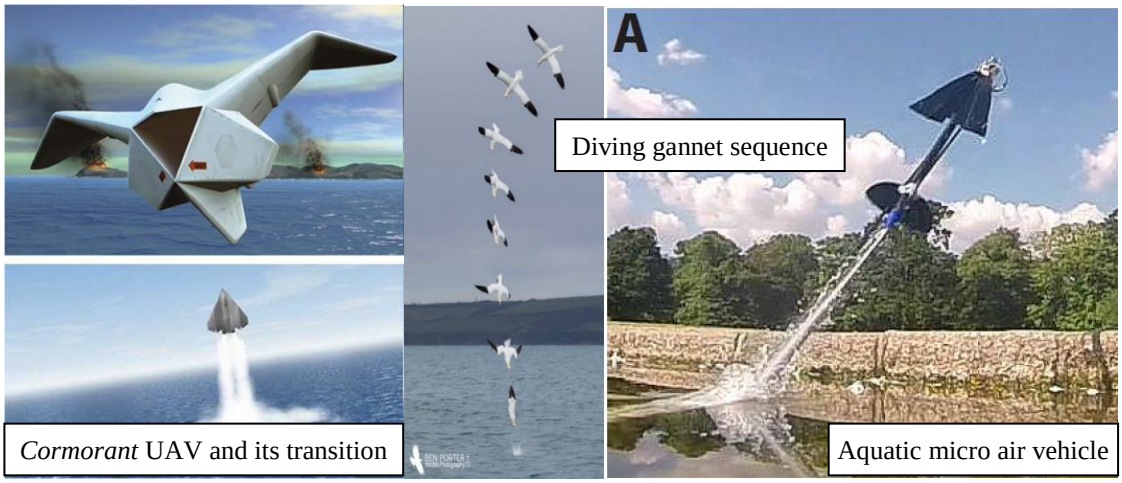

Figure 1-6: Exiting [22] [25]and diving[21] transition strategy

Buoyancy control transition strategy

Comparing to instant transition strategy, the buoyancy control transition is gentler and more time consuming. It is more used in the air-to-water transition phase. In 2014, Beihang University built a submersible unmanned flying boat [24] shown in Figure 1-7. It has the same way of landing on and taking off from the water surface as a normal seaplane. The vehicle realizes the submerging and floating through a buoyancy control system called water volume regulation system to supply and drainage the water in the fuselage. In addition, the wing, empennage and the mechanical cabin are water permeable for increasing the vehicle density during the submerging. Unfortunately, the transition between air and water uses 15 to 20 mins, which is inefficient, and the underwater propulsion ability is limited. This is harmful to the concealment of the mission. And the whole system undoubtedly increases the weight of the vehicle, which is unfavourable. In the contrast, the Hybrid Aerial Underwater Vehicle made by MIT Lincoln Lab was designed to be as close to the neutral buoyancy as possible, so there is no process for adjusting buoyancy when it is diving into the water [16]. In addition, the neutral buoyancy is more achievable for small unmanned vehicle system comparing to a large vehicle. The neutral buoyancy vehicle has the advantages of less complexity and lightweight, since no

additional weight balancing device is needed. In the maritime, dynamic submarines use the identical strategy. Being different from the static submarine, which uses the compressed gas to add the water in ballast blank and push the water out to control buoyancy, dynamic submarines do not have the buoyancy control system. Actually, most of them have certain buoyancy to float up. So they usually use thrust generated by the propeller and motor or other similar devices to control dive or float [23]. The torpedo is another neutral buoyancy design example. The torpedo keeps its depth by using the lift generated from its configuration during it is running, whenever it is in positive or negative buoyancy [26]. It should note that the torpedo operates in high speed normally. A small unmanned vehicle may be not as fast as a torpedo, whereas it can be compensated by another method, such as increasing the lift by improving the configuration. In conclusion, it is beneficial that the vehicle is built in neutral buoyancy for the air-to-water transition and using instant transition strategy to exit the water to reduce the transition time and possible obstruction from the wave.

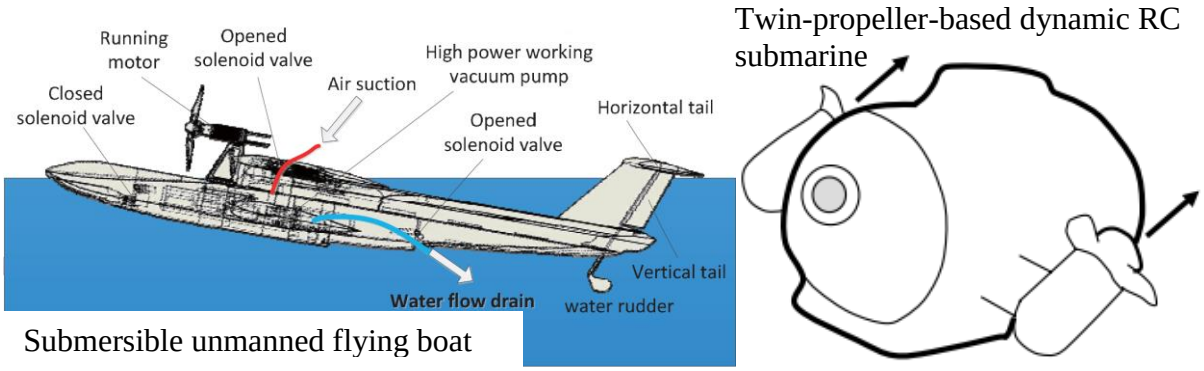

Figure 1-7: Buoyancy control strategy from Beihang University [24] and dynamic RC submarine [23]

1.5.3 Hybrid propulsion

The underwater travelling is necessary for BUUAS, but the full functional vehicles are extremely rare. The technical difficulty on the propulsion development for both air and water has hampered the development of submersible UAV. In this section, several underwater locomotion methods and propulsion systems used in a partly featured submersible aerial vehicle are presented, which offers valuable information for the further exploration for the BUUAS.

In 2011, a biomimetic robotic flying fish was proposed by A. Gao and A.H. Techet shown in Figure 1-8, and the concept of this aerial-aquatic robotic is that it can swim underwater by flapping the wing and glide in the air, which is like the real flying fish in nature [17]. Through their design exercise, they found the actuation technology is crucial to driving the fin ray to push robotic forward. However, the conventional electromagnetic actuators cannot satisfy the great specific power requirement. The authors rose two ways to reduce the required power

density, scaling the vehicle up and reducing the wanted underwater velocity. Even though the unsolved issues exist, this concept has advanced perspective for the slow velocity underwater travel.

In 2012, R.J. Lock, R. Vaidyanathan and S.C. Burgess designed and tested a flapping wing as the propulsion to carry the aquatic movement by flapping motion to enable the aerial and aquatic locomotion of the robotic [27]. Inspired by the morphing wing of guillemot, which can retract for aquatic operation and expend for aerial, the researchers classified the wing into extended and retracted to conduct the experiment. The result indicates that the retracted wing has the capability to drive a feasibly sized vehicle. Even though the research verified the underwater performance of flapping wing, the prototype that has this wing structure has not been built yet. The wing flap motion for the underwater movement reveals acceptable potential. Nevertheless, at the current state of the art, this technology is not mature enough and no accomplished bi-modal prototype with this propulsion system has been proposed.

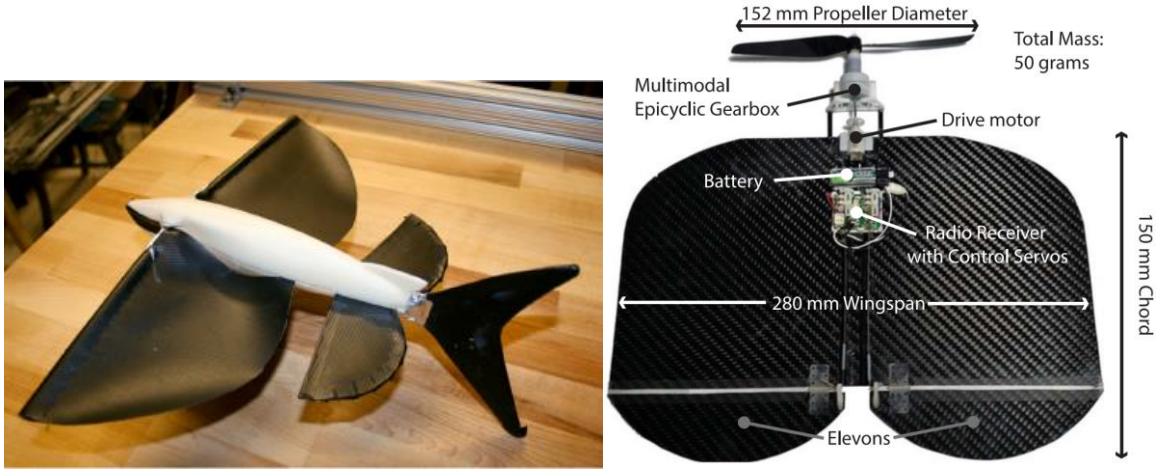

Figure 1-8: Robotic flying fish [17] (left), the vehicle with a single propulsion system [28] (right)

In July 2017, a single propulsion system, which can operate in both air and water, was developed by Y.H. Tan, R. Siddall, and M. Kovac [28] presented in Figure 1-8. The novel system uses a gearbox, which can realize the velocity reduction and torque increased by changing the rotation direction of the motor. This system is compact and only one propeller optimized for operating in both water and air is equipped in the system. The experiment result of this system is very promising. The prototype with the propulsion system works well in the suitable speed in both fluids. In addition, S.A. Watson in his paper points out that propellers were the best option for Micro-Autonomous Underwater Vehicles [29]. In the current state of the art, the propeller propulsion is more feasible. The favourable feature of the adoptable

propulsion system should be multifunctional, which means that one system can be used in both air and water.

1.6 RESEARCH QUESTIONS

The objective for this project is realizing the design aspects of a bi-modal unmanned underwater/air system (BUUAS) that can achieve the operation in both air and water and to have an effective transition between those two fluids. The project will tackle three important design aspects associated with the research questions, the aerodynamic and hydrodynamic configuration, the transition strategy development, the hybrid propulsion system.

Based on the study of literature, the three research questions of this research were as follows:

- What are the critical design challenges for a bi-modal underwater/air vehicle and what novel solutions are available to overcome them?
- What propulsion system is best suited for a rapid transition of a bi-modal vehicle from underwater to air in high sea states?
- What propulsion system is best suited for sustained underwater and air travel of a bi-modal vehicle?

Chapter 2: Conceptual Design and Performance Analysis

2.1 DESIGN PROCESS AND REQUIREMENTS

Table 2-1: Requirements for BUUAS

Category	Value
Flight ceiling	400 m
Air cruise speed	20 m/s
Underwater cruise speed	1 m/s
Stall speed	15 m/s
Turn speed	20 m/s
Weight	3-4 kg
Underwater cruise duration	20 minutes
Airborne duration	10 minutes

The design requirements presented in Table 2-1 have been established for the vehicle based on the purpose of demonstrating the technology. Firstly, the flight test will be remotely controlled by the human pilot same as the aero models. So, the flight ceiling is set at the visual range around 400 m. The duration is distributed into sections of the airborne and underwater cruise to serve the performance demonstration in the experiment. Due to the slow underwater cruise velocity, the vehicle will consume plenty of time to travel underwater to keep away from the submarine. Hence, 20 minutes is allowed for the underwater cruise. On the other hand, the flight velocity is relatively high, and more power will be required. Accordingly, the flight demonstration time is assigned to 10 minutes so that the vehicle can show the performance and stability. Evidently, there are more requirements assigned for the flight such as the stall speed and flight ceiling, because the airborne surveillance mission is the design priority and the underwater mode is only for the stealth movement. Consequently, the design flow chart for the BUUAS is depicted in Figure 2-1:

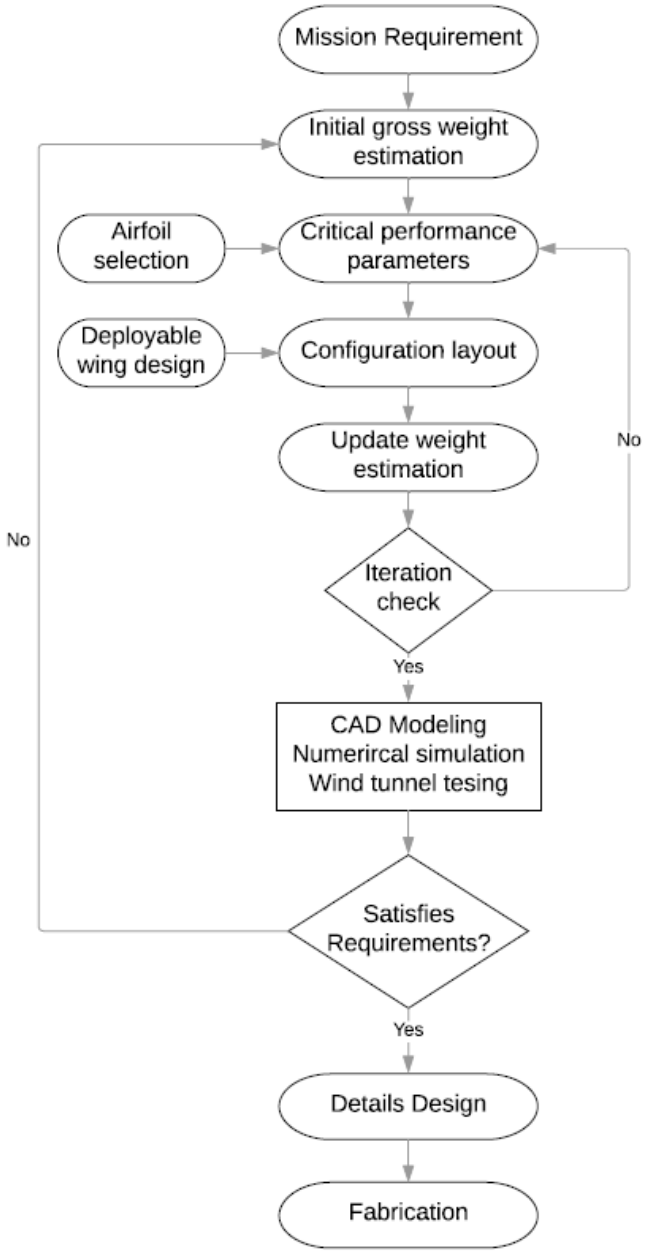

Figure 2-1: Design flow chart

The configuration design is focused on the flight mode with compromises for the underwater mode. For the BUUAS, the wing is mainly used in the airborne mission. In the contrast, the vehicle can operate without a wing in water, and the ballast tanks and trim tanks can control buoyancy to suspend the underwater vehicle. Further, the wing geometry sizing is an important part in this conceptual design phase, so the flight mode is more emphasized compared with the underwater mode during the design.

2.2 CRITICAL PERFORMANCE PARAMETERS

2.2.1 Initial weight estimation

In the beginning, the total vehicle weight was estimated at 3.5 kg. It is close to the weight of most model aircraft and the small unmanned vehicles that can reach the requirement [30-33], and the commercial components for those vehicles are easy to acquire. Besides, the vehicle can also be handled easily for research and experimentation at this weight. According to the data by Roskam [34] and the review by Mangesh. M and Pradip [35], the payload fraction is typically from 10% to 20% of the gross weight of the unmanned aerial vehicle. Regarding this technology demonstrator, the payload is the transition propulsion system for demonstrating the technology, so the fraction of the transition propulsion system is assigned within the above range. Moreover, the aquatic micro air vehicle from the imperial college uses a similar water escape strategy [18]. Its water jet weight is 18% of the total weight, but it only has an aerial propulsion system, which shares less weight distribution. Considering the more weight distribution for the hybrid propulsion system of the BUUAS compared with the aquatic micro air vehicle, the weight distribution of the transition propulsion system is decreased slightly while other components remain the same. In addition, a lightweight transition propulsion system is preferred, which can leave more development space for other components. As a result, a 15% weight distribution is set for the transition propulsion system in the initial estimation.

Due to the changeable configuration design for operation in both air and water, the estimation for the wing weight distribution should include the wing-deployment mechanism. Comparing with the flexible wing in the literature review, the design is settled on the rigid deployable wing due to its benefits of fast development, short time manufacturing. In addition, the rigid wing has the structure advantage, which can place the aileron and flap unlike the flexible wing. Based on the research of Jacob and Smith on the deployable wing configuration for small and low altitude UAVs [36], the deployable rigid wing has large span allowance, but the large geometry such as span and taper ratio will increase the deployment mechanism weight fraction regarding the whole vehicle. They classified the deployment wing weight fraction from 0.1 to 0.5 with the increasing wingspan. The long endurance flight is necessary for surveillance of the BUUAS, but long wingspan is not beneficial for a fast wing deployment, which can quickly acquire enough lift during the transition. Furthermore, the large wing weight fraction will affect the development of other components. Therefore, the 30% weight distribution is given for the wing. For other components, the weight distribution is made by studying other

similar size aerial vehicles [30-33]. The pie chart described in Figure 2-2 represents the initial estimated weight distribution:

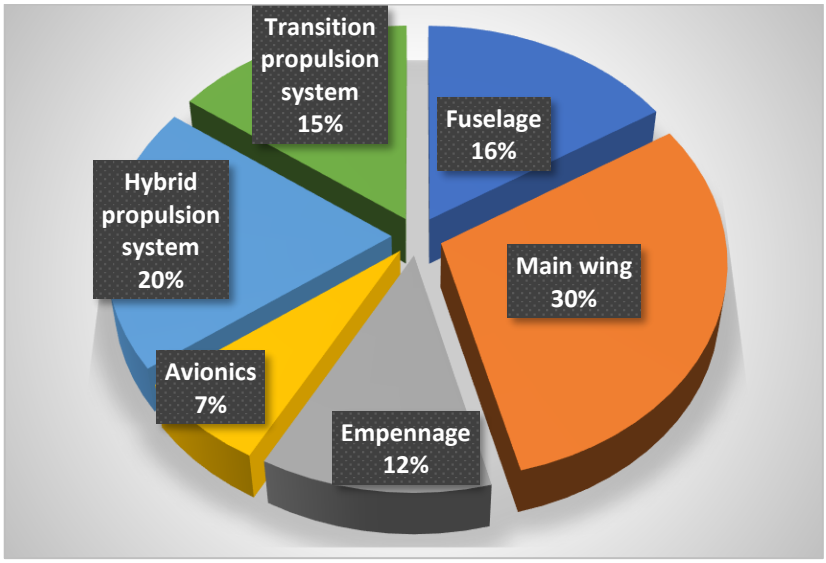

Figure 2-2: Relative weight distribution

2.2.2 Airfoil selection

To start with, the airfoil is selected for the rigid deployable wing. Due to the water/air operation environment, there are some limitations in the airfoil selection for the BUUAS, which compose requirements below.

Requirements

High $C_{L_{max}}$ and lift- to- drag ratio

From an aerodynamic point of view, the airfoil with high lift coefficient is favourable. This benefits the long endurance flight and helps the water to air transition. Especially, at the end of the transition, the vehicle may face the danger of stall when the transition propulsion system stops working and the hybrid propulsion system may not generate enough thrust. The wing with high C_L airfoil can provide more lift to overcome this dangerous scenario.

Thin profile

The thin profile requirement is set by considering the hydrodynamic configuration design. The volume of the wing can produce unwanted buoyancy in water. This increases the difficulty to stabilize the vehicle. Besides, an amount of form drag is generated by the wing with the large front area when the vehicle is cruising underwater. The thin profile airfoil can reduce the unfavourable volume and form drag. Furthermore, considering the configuration of the wing will be changed for air and water, the wing with low thickness profile is easy to be stowed or folded.

Reynolds number calculation

The operation Reynolds number is estimated before the selection of airfoil by Eq. (1). The vehicle is assumed to operate in a 15ºC environment. Therefore, the kinematic viscosity v is 1.461×10^{-5} m^2/s. The value of L_0 is chosen as the mean aerodynamic chord. By studying similar size UAVs [37-40] with weight from 2 kg to 5 kg, it is assumed that the mean aerodynamic chord is 0.15 m initially. Under 20 m/s cruise velocity, the Reynolds number is,

$$R_e = \frac{VL_0}{v} \tag{1}$$

Eq. (1) yields the Reynolds number 281,447.

Airfoils

By following the requirements, aerofoils are selected based on the data from the website *www.airfoiltool.com*, and they are compared in Table 2-2. At $R_e = 300{,}000$, the properties of airfoils were evaluated with the commercial software Profile® and shown in Figure 2-3.

Table 2-2: Comparison of wing airfoils

Name	Max thickness	Max camber	Profile
S7075	9%	2.8%	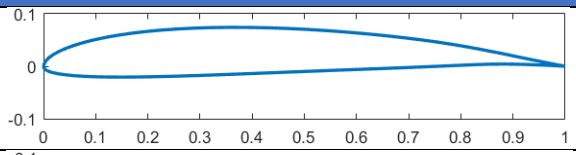
PSU 94-097	9.7%	4%	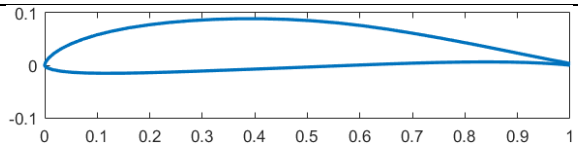
OAF 117	11.5%	2%	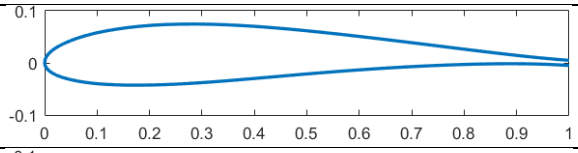
TsAGI R-3a	12.1%	3.1%	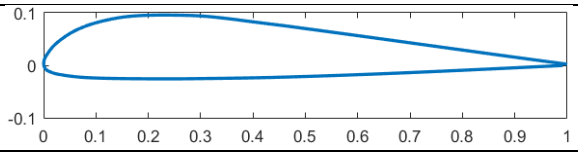

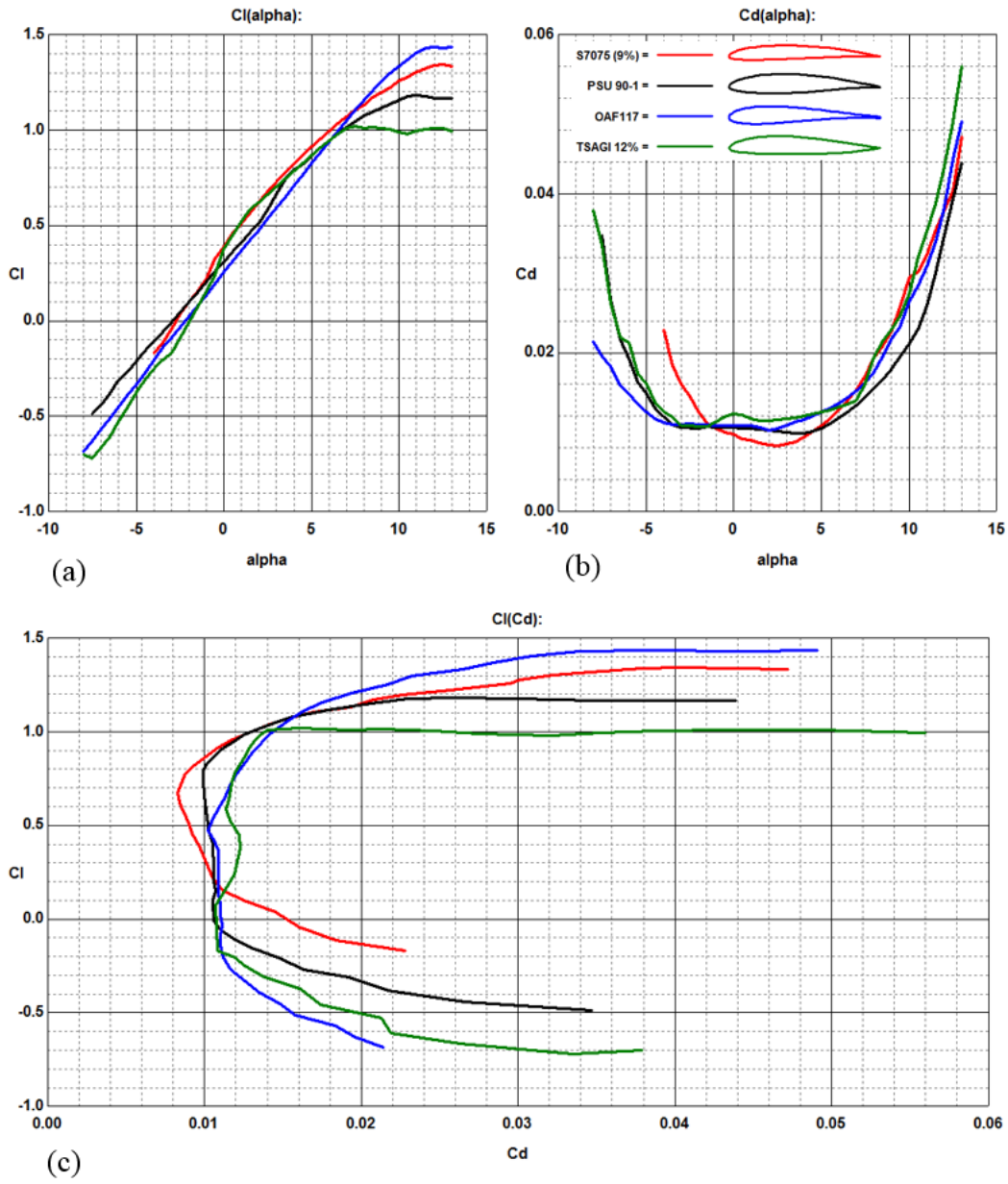

Figure 2-3: Graphs of aerodynamic coefficients of airfoils: (a) Angle of attack versus lift coefficient, (b) Angle of attack versus drag coefficient, (c) Drag polar curve

Results

Figure 2-3 presents that the S7075 profile has a high $C_{L_{max}}$, lift-to-drag ratio and thin profile with the max thickness of 9%, which is the smallest among others. Consequently, the S7075 was selected as the airfoil for the wing. Even though the OAF has the highest value of $C_{L_{max}}$, the relatively large thickness holds it back. A similar method is used in the airfoil selection for the tail and the wing fairing. The wing fairing is placed in the wing root area connected to the fuselage. It is used to cover the wing-deployment mechanism, reduce drag and improve appearance. For this reason, the NACA 0015 airfoil is selected, since a large thickness

profile is needed to contain the mechanism. All the airfoils applied to the vehicle are depicted in Table 2-3.

Table 2-3: Airfoils in different sections

Name	Max thickness	Max camber	Location	Profile
S7075	9%	2.8%	Wing	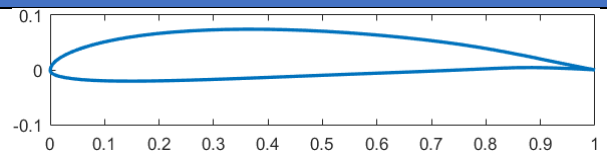
S9026	9.5%	0%	Tail	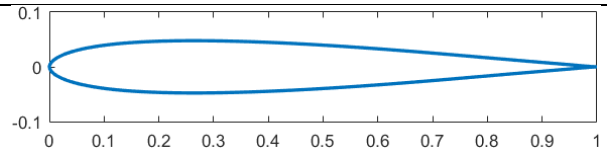
NACA 0015	15%	0%	Wing Fairing	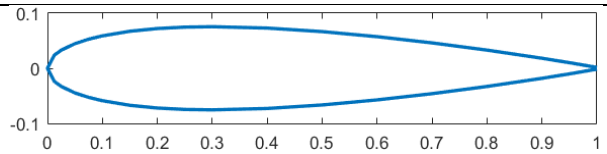

For further development, the following parameters are gained from the Profile® and evaluated. The maximum lift coefficient is estimated according to the Eq. (2),

$$Cl_{max,3d} = 0.9 \times Cl_{max,2d} \tag{2}$$

where the $Cl_{max,2d} = 1.396$. The Eq. (2) yields the $Cl_{max,3d} = 1.256$.

2.2.3 Wing Loading

Driven by the requirements, wing loading and thrust to weight ratio, which are two important parameters, are calculated. Firstly, the wing load is evaluated at critical performance conditions, which are the cruise and stall.

1. Maximum wing loading for the stall speed,

$$\frac{W}{S}_{stall} = \frac{1}{2} \times \frac{\rho \times {V_{stall}}^2 \times C_{L_{max}}}{g} \tag{3}$$

where the ρ is the air density $\rho = 1.225\ kg/m^3$ at 15ºC.

$$\frac{W}{S}_{stall} = 15.391\ kg/m^2$$

2. Wing loading according to the cruise speed,

$$\frac{W}{S}_{cr} = \frac{1}{2} \times \frac{\rho \times {V_{cr}}^2}{g} \times \sqrt{C_{D_0} \times \pi \times AR \times e} \tag{4}$$

$$C_{D_0} = C_{f_e} \frac{S_{wet}}{S_{ref}} \tag{5}$$

where the AR is the aspect ratio, which is estimated as 9 initially for a long endurance flight. This estimation is based on the investigation of the similar size surveillance UAVs. The aspect ratio range for those UAVs [41-46] can be from 7 to 14, such as the civil surveillance UAV from [41] has the 13.5 aspect ratio for achieving long endurance. However, an extremely high aspect ratio will make wing deployment difficult and increases the possibility of interference with other components such as tails during folding or deploying. Therefore, the aspect ratio is set as 9 at the beginning stage. e is the Oswald efficiency, and is estimated at 0.85, which is very common for the initial estimation. The equivalent skin friction coefficient $C_{f_e} = 0.0045$ is estimated from Table 12.3 in [47]. Likewise, the ratio of wetted area to reference area is 4 estimated based on Figure 3.5 from [50]. Thus, $C_{D_0} = 0.018$,

$$\frac{W}{S}_{cr} = 16.443\ kg/m^2$$

2.2.4 Reference area

The reference area is calculated based on the wing loading during the stall velocity. The reason for this is that the small value of the wing loading can yield the biggest wing area that can be used in all the case. Therefore,

$$S_{ref} = \frac{W_0}{\frac{W}{S}_{stall}} \tag{6}$$

$$S_{ref} = 0.227\ m^2$$

2.2.5 Thrust to weight ratio

Thrust to weight ratio for cruise flight

The thrust to weight ratio should fulfil the basic cruise requirement. The equations below are used to evaluate the required thrust to weight ratio,

$$\frac{T}{W} = \frac{qC_{D_0}}{W/S_{ref}} + \frac{W}{S_{ref}}\left(\frac{n^2}{q\pi ARe}\right) \tag{7}$$

$$q = \frac{1}{2}\rho {V_{cr}}^2 \tag{8}$$

where n is the load factor. In the cruise, n is appointed as 1. Eq. (7) yields $\frac{T}{W}_{cruise} = 0.289$ under the cruise condition.

Thrust to weight ratio for turning flight

$$\frac{T}{W} = \frac{qC_{D_0}}{W/S_{ref}} + \frac{W}{S_{ref}}\left(\frac{n^2}{q\pi ARe}\right) \tag{9}$$

$$q = \frac{1}{2}\rho {V_{turn}}^2 \tag{10}$$

Since the vehicle is not required to have high manoeuvrability, the n is appointed as 2.5 during turning. Eq. (9) gives to the thrust to weight ratio $\frac{T}{W_{turn}} = 0.110$. The power should reach the highest power requirement, so the final thrust to weight ratio is $\frac{T}{W} = 0.289$.

2.2.6 Fuselage sizing

Unlike the conventional fuselage with the undercarriage for take-off and landing, the fuselage for the BUUAS is designed practically to contain the necessary components, such as transition propulsion system, hybrid propulsion system and avionics without landing gears.

$$L_f = aW_0^C \tag{11}$$

The fuselage length can be estimated according to Eq. (11) from Table 6.3 in [50]. The coefficient a and C are decided by the type of the vehicle. The aircraft type of the BUUAS is similar to the powered sailplane, which has $a = 0.71$, $C = 0.48$, due to its long endurance surveillance mission. This yields the fuselage length $L_f = 1.295\ m$. According to [50], in the design of the fuselage cross section, the payloads, which are the propulsion systems, must take priority. Thus, by studying propulsion system size of other close size UAVs [30-33], a small diameter of 80 mm with large fineness ratio fuselage cross section is determined. Considering the submarine long cylindrical mid-body shape, a 79.7 mm outside diameter glass fibre tube is used to build the main part of the fuselage. However, this result needs to be compromised with the hydrodynamic aspect. According to the research of Gertler [48], the decrease of the length to diameter ratio will decrease the friction resistance, but the form resistance will increase. Moreover, Moonesunn [49] proposed that for the cylindrical middle body submarine, the optimum range of fineness ratio $\frac{L_{hull}}{D_{hull}}$, which is the value of the hull length over maximum diameter, is $7\sim10$. However, this will shrink the 38% length of the fuselage, which will influence the moment arm length of the tail in the next step design. Besides, the hybrid propulsion system and transition propulsion system will occupy the space inside the fuselage. Under the compromise between airborne and marine, the final fuselage length is designed as $L_f = 860\ mm$ with 10.79 fineness ratio, which is close to the optimum range. The nose of the

fuselage is designed as a cone shape to reduce drag and the risk of damage when the vehicle dives into the water.

2.2.7 Drag for underwater cruise

The drag of the submarine is mainly composed by the skin friction and the form drag. Because of the configuration of the vehicle is unknown, the underwater drag is estimated by the method of the book [10], and some coefficients are picked based on the parameters from the similar size AUVs [50]. Unlike to evaluate the drag of the whole configuration, the drag is calculated from separated components mainly the hull, wing and tail, which is easy and accurate for the unknown configuration.

Hull skin friction

The skin friction coefficient can be estimated based on the underwater Reynolds number. Under the 1 m/s travelling velocity $R_{e_{water}} = 678{,}769$, so the skin friction coefficient is,

$$C_{F_{flat}} = \frac{0.067}{(\log_{10} R_{e_{water}} - 2)^2} \tag{12}$$

The frictional resistance can be obtained from the Eq. (13),

$$R_{F_{flat}} = \frac{1}{2}\rho_{water} S_{hull} {V_{water}}^2 C_{F_{flat}} \tag{13}$$

$$S_{hull} \approx 2.25 L_{hull} D_{hull} \tag{14}$$

The shape of the fuselage is not finalised, so the fuselage wetted area is estimated by the Eq. (14). Accordingly, the Eq. (13) yields the frictional resistance is $R_{F_{flat}} = 0.351\ N$.

Hull form drag

The form drag is another component of the total drag produced by the hull due to the front area A_{front}. It can be obtained by the equations below:

$$C_{F_{form}} = \frac{0.075}{(log_{10} R_{e_{water}} - 2)^2} \tag{15}$$

$$C_P = K_P C_{F_{form}} \tag{16}$$

$$K_P = \xi_{hull} (\frac{L_{hull}}{D_{hull}})^{-1.7} \tag{17}$$

$$R_{F_{form}} = \frac{1}{2}\rho_{water} {V_{water}}^2 A_{front} C_P \tag{18}$$

where, in Eq. (16) the form drag coefficient is acquired from the function of the total drag coefficient $C_{F_{form}}$ and factor K_P. The K_P is related to the fineness ratio and hull form factor

ξ_{hull}, which is from 3 to 6 depending on the type of the hull. Since the fuselage shape of the BUUAS is close to the modern submarine shape, ξ_{hull} is selected at 5. Finally, the form drag is obtained as a function of the front area and form drag coefficient in Eq. (18). The result is the $R_{F_{form}} = 0.0140\ N$

Wing and tail skin friction

Another part of the drag is contributed by the wing and tails. The deployable wing configuration has already determined, so the front area of the wing can be reduced to a small value for travelling underwater. In addition, the wing and tail have relatively thin profiles comparing to the fuselage. Therefore, it is assumed that all the drag from wing and tail is contributed by the skin friction, and it can be calculated by the Eq. (19),

$$R_{surface} = \frac{1}{2}\rho_{water}{V_{water}}^2 A_{plan} C_{D_{water}} \tag{19}$$

As mentioned in [10], the value of 0.01 to 0.02 can be used for $C_{D_{water}}$ as a first estimation. Thus, a conservative value of 0.02 is selected to make sure the vehicle can complete the required endurance. The A_{plan} is the wing area plus the tail area. Since the tail area is unknown, it is estimated as half of the wing area. This value is estimated by studying the similar size UAVs [30-33], their tail area is from 20% to 40% of the wing area. So, in this initial estimation, a conservative value 50% is selected. Consequently, the obtained drag is $R_{surface} = 3.3948\ N$. By summing all the drag together in Eq. (20), the total drag $D_{water} = 3.760\ N$.

$$D_{water} = R_{F_{flat}} + R_{F_{form}} + R_{surface} \tag{20}$$

2.2.8 Battery capacity estimation

The internal combustion reciprocating engine does not work underwater, so the electronic motor is used for the hybrid propulsion system. The battery capacity of the electronic motor is estimated based on the required duration of the vehicle. For estimating the battery usage during flight, the method of Traub [51] for estimating the range and endurance of battery-powered aircraft is used.

The battery capacity Q_{batt} is the function of the flight time, battery voltage and current, which is related to the required power and voltage during the flight. For the BUUAS, the commercial battery with the standard 14.8 V voltage is used, since it is widely used for UAVs similar size to the BUUAS, and can match plenty of supplementary electric motors. The U_{batt} is the overall efficiency of the propulsion system. Generally, electric motors have the efficiency from 50% to 100% under the load, but 75% is commonly the maximum efficiency for most

motors [52]. Besides, most of efficient UAVs use propellers can have an efficiency of 65% [53], and the small marine propeller such as the AUV propeller can achieve 75% efficiency [54]. Therefore, the propulsion system efficiency starts at the place of 48.75% for air travel and 56.25% for water travel. The avionics include the micro actuators, ESC, receiver and actuators for the transition propulsion system. Particularly, the actuators for the transition are designed to work instantaneously to achieve a short time transition. Therefore, those avionics will not consume much of battery capacity, and 10% is estimated at the beginning to assure that the calculated capacity is enough for the requirement.

$$Q_{batt_{air}} = \frac{I_{prop} t_{flight}}{N_{batt} U_{batt}} \tag{21}$$

$$I_{prop} = \frac{P_{air}}{V_{batt}} \tag{22}$$

$$P_{air} = \frac{1}{2}\rho {V_{cr}}^3 S_{ref} C_{D_0} + \frac{2W^2 k}{\rho V_{cr} S_{ref}} \tag{23}$$

$$k = \frac{1}{\pi e AR} \tag{24}$$

The required power for flight can be obtained by the Eq. (23), which is based on the flight velocity and vehicle characteristics. In Eq. (23), the drag coefficient is applied by using the formula: $C_D = C_{D_0} + k{C_L}^2$. This relation implies that minimum drag occurs at zero lift, which is the case of uncambered airfoil. For the selected S7075 small camber airfoil which only has maximum 2.8% camber, the relation above can be used with an acceptable approximation at the beginning stage, especially when the $C_{D_{min}}$ and $C_{L_{min}}$ is unknown. To solve Eq. (23), the induced drag parameter factor k is introduced by Eq. (24), which is a function of the Oswald's efficiency factor e and aspect ratio AR. By calculating from the equations above, the required power for flight is $P_{air} = 37.626\ W$ and the capacity is $Q_{batt_{air}} = 869.151\ mAh$.

$$P_{water} = D_{water} V_{water} \tag{25}$$

Since the underwater drag has been calculated in the previous section, the underwater power can be simply acquired by multiplying the underwater cruise velocity with the drag in Eq. (25). Under the 1 m/s velocity, the power is $P_{water} = 3.760\ W$. This result is put into the Eq. (21) and Eq. (22) same as the airborne mode. The obtained capacity for the underwater cruise is $Q_{batt_{water}} = 150.534\ mAh$. Therefore, counting on the battery capacity for avionics, the total battery capacity is $Q_{batt} = 1121.654\ mAh$. Then, a $14.8\ V$ Dualsky® Li-Po battery with $1{,}300\ mAh$ capacity is selected as the power source.

2.3 CONFIGURATION LAYOUT SELECTION

2.3.1 Pusher layout

As mentioned in the introduction, a hybrid propulsion system with a hybrid propeller is built for this vehicle. The design is facing the choice of the tractor or pusher configuration. Each has its own merits. Considering marine vehicles, most of the submarines and AUVs have the propulsion system located at the rear. The aft propulsion system is beneficial for keeping the efficient long cylindrical mid-body with the elliptical bow and stern shape to minimize drag. Conversely, aircraft usually have the tractor configuration. However, it is not difficult to find lots of UAVs adopt the pusher configuration. The reason is that most surveillance UAVs need to carry the camera in the front to have a clear view. For all the reasons above, the final decision is settled on the pusher configuration. The only problem is the nozzle of the transition propulsion system may interfere with the hybrid propulsion system, but it can be solved by rearranging the location of the nozzle or offset the location of the motor.

The components inside fuselage are arranged after the determination of the drive configuration, which is displayed in Figure 2-4. The transition and hybrid propulsion systems are arranged in the rear. Since the amount of water will be introduced as the propellant, the transient propulsion system is longer. Moreover, the battery and the avionics are placed in the front. In this arrangement, the nose works as the hatch for maintaining the avionics and propulsion systems inside.

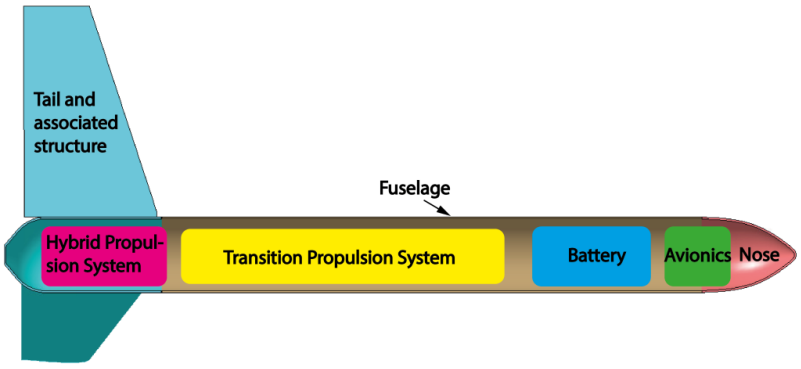

Figure 2-4: BUUAS weight distribution

2.3.2 Deployable wing layout

Several configuration change strategies were conceived for the rigid deployable wing. The layout of the wing should be compatible with both aircraft and submarines. In this background, the decision matrix shown in Table 2-4 is built to select the best concept from five different configurations.

The criteria in the decision matrix for selecting the best configuration include the surface friction, form drag, manoeuvrability, and the predicted deployment duration. For this vehicle, the air configurations are generally same, which is similar to normal fixed-wing UAVs, but significantly different for underwater. Consequently, the criteria such as the surface friction, form drag, and manoeuvrability are the underwater parameters. The mechanical complexity is the extent of design, fabrication and operation difficulty of the wing-deployment mechanism. Another critical parameter is the deployment duration. The vehicle uses a fast escape strategy to exit the water with a short duration, so a fast wing deployment method is necessary. In the matrix, the numbers 1 to 5 represent the performance of each item, and a large number means it has the advantage on this item. Moreover, in the configuration figures, the green wing is the flight configuration, and the red wing is the underwater configuration when the wing is folded. Additionally, the yellow circles represent the wing rotation pivots.

The result indicates the folded back strategy number 3 is the optimal choice. It has low form drag and medium friction drag with the wing folded back. Its mechanism design for the folded back wing is much easier than the upward folding wing number 2 and the telescopic wing number 4, since the former needs to build the mechanism in a thin profile, which is difficult. Also, the latter should change the structure of the main wing to contain the retracted outside wing. Consequently, this changes the normal structure of the wing, and it is hard to build structure between the skin of the main wing to the spar. So, the force acting on the skin cannot be carried by the spar, and the structure is easy to be damaged.

The surface friction is ranked based on the wetted area. Among those five strategies, number 1, 3 and 5 expose all their wing surface to the water, while number 2 and 4 reduce the wetted area by folding its wing upward and shrinking the wing inside. Regarding to the form drag, which is ranked by the front area and vehicle shape, the number 3 and 4 has relatively small front area by folding the wing back and shrinking the wing inside. However, by folding the wing upward, the number 2 strategy acquires relatively large front area which increases its form drag. Finally, the manoeuvrability is decided by the configuration effect in both longitudinal, lateral and roll direction movement. It is obvious that a long wing span can make the control at roll direction sluggish, and a long fuselage will have the same problem in the longitudinal direction. Therefore, number 3 is the optimal choice for manoeuvrability.

Table 2-4: Decision matrix: Deployable wing strategies

Configurations	Surface Friction	Form Drag	Manoeuvrability	Mechanism Complexity	Predicted Deployment Duration	Total
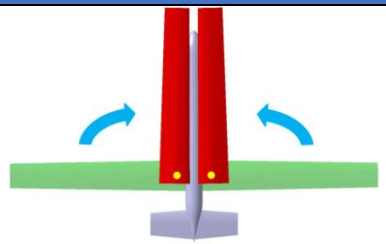 ①	3	3	4	3	4	17
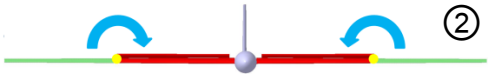 ②	4	2	3	2	2	13
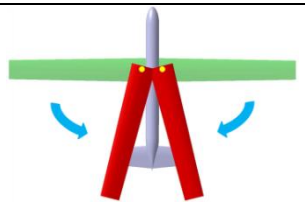 ③	3	4	4	4	4	19
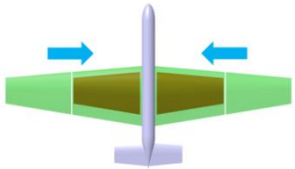 ④	4	4	4	2	4	18
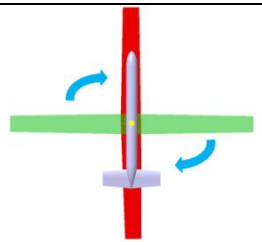 ⑤	3	3	3	3	4	16

The predicted deployment duration is the duration for deploying a wing. It counts the deploying method and the locomotion of the wing during the deployment. For the scheme number 1, 3, 5, the wing is doing the rotation locomotion, and the rotation angle is around 90 degrees or less. If the same actuator is used for all of them, the deployment time should be similar. The scheme 2 needs to rotate the outside part of the wing 180° during the short transition time, which definitely increases the deployment duration.

2.3.3 Tail layout

In the tail design process, the aircraft design and the submarine design are both considered for a compatible design in two fluids. The conventional, T, V, H, Y tails are ubiquitous for the aircraft [47]. For the submarine tail, there are cruciform configuration, X-form configuration, inverted Y configuration, and pentaform configuration. Among the tails, the structure of the convention tail is similar to the cruciform tail of the submarine. And the Y tail and inverted Y tail are used in both the aircraft and the submarine. X-form tail configuration is similar to the V tail on the aircraft. The similar configurations for the submarine and aircraft are paired in Table 2-5 and the decision matrix is composed.

Table 2-5: Decision matrix: Tail selection

Aircraft	Submarine	Integration with wing	Control	Structure complexity	Acoustic noise	Total
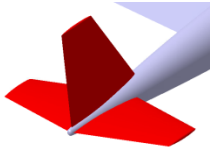	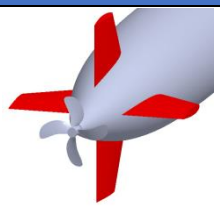	1	3	3	1	8
	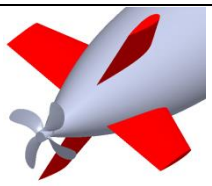	3	1	2	1	7
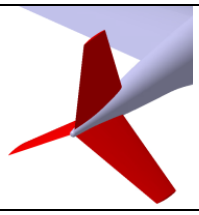	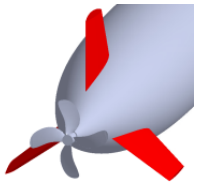	3	2	3	3	11

The selection criteria include the control, structure complexity, integration, and acoustic noise. It is worth to mention that the design of 4 blades hybrid propeller was proposed during the design. Therefore, the tail with 4 fins may create acoustic noise with 4 blades propeller. Also, the interference between the folded back wing and the tail should be avoided. In the design

matrix, the tails are scored from 1 to 3. The high score represents the tail configuration has advantage on the category.

As a result, the inverted Y tail is the best choice among all the designs. The special mission profile without landing and taxing process benefits the design of inverted Y tail. Because, there is no concern about the elevator of inverted Y tail will touch the ground during the landing and taxing, and the anhedral of the horizontal tail can be designed just following the aerodynamic and hydrodynamic need. In addition, the transition from water to air needs the vehicle to take a high angle of attack. In this process, the horizontal tail plays a vital role. The inverted Y tail can avoid elevators under the wake from the wing, and increases the vehicle stability in this critical process.

Particularly, among those three configurations, the V tail and inverted V tail of aircraft are similar to the X tail. However, the X tail needs 4 fins, which will generate acoustic noise with the same number of blades. In addition, since the fold back wing configuration is determined, the configuration of tail should be compatible with the folded back wing. The item of integration with wing ranks the capability of compatible with folded back wing. In this item, the horizontal tail of conventional tail configuration has the highest potential to interfere the folded back wing in the future design. Regarding to the item of control, the conventional tail is the most appropriate in both controllability and redundancy in air and water modes, since for the V tail and inverted Y tail, the pitch and yaw surface deflections are coupled. Furthermore, the control of the X tail is different from a normal airplane, which also increases the design complexity. On the other hand, the X tail has more complicated structure than others.

2.4 VEHICLE SIZING

2.4.1 Wing geometry

For the deployed configuration, the wingspan is calculated from the aspect ratio and the reference wing area by the Eq. (26),

$$b = \sqrt{AR \times S_{ref}} \tag{26}$$

$$b = 1.43\ m$$

The wing without dihedral will keep its small front area after folding back, which is favourable for minimizing the drag, so the dihedral angle is set as $\Gamma = 0$. The 0.73 was estimated as the taper ratio to increase the aerodynamic efficiency, and the sweep angle Λ is also zero. The finalized wing geometry is depicted in Figure 2-5.

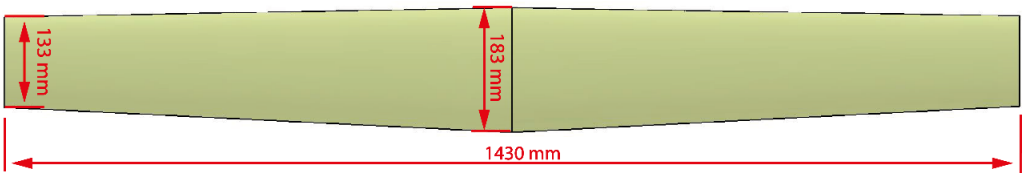

Figure 2-5: Initial wing geometry

2.4.2 Initial centre of gravity estimation

The initial position of the centre of gravity is estimated. It can obtain the moment arm, which is the distance between the tail average quarter-chord location to the centre of gravity of the vehicle, for the next tail design. The weights of components are estimated based on the weight distribution chart, and the distances, which are the distances of the centre of gravity of the components to the nose, are estimated based on the components arrangement. The details are presented in Table 2-6.

Table 2-6: Initial weight estimation

Components	Weight(g)	Distance to Nose(mm)
Hybrid propulsion system	500	800
Transition propulsion system	525	350
Avionics (receiver, ESC)	245	90
Battery	200	140
Tails with the structure and servos	420	735
Fuselage tube	560	382.388
Wing	1,050	450

Thus, the centre of gravity is calculated based on the equation below,

$$x_{cg} = \frac{\sum(m_{component} x_{compnent})}{\sum m_{component}} \tag{27}$$

where $m_{component}$ is the weight of different components, $x_{component}$ is the distance between the nose and the centres of gravity of components. Eq. (27) yields,

$$x_{cg} = 465.468\, mm$$

2.4.3 Tail sizing

The tail sizing follows the design process of a conventional tail to develop the vertical and horizontal tails then convert them into the inverted Y tail based on the calculation of projected areas on the vertical and horizontal plane.

All moving tail design

The tails are designed as the all moving tail. Comparing with the conventional tail with the same tail area, it is more effective in producing moment. In addition, the proposed hybrid propulsion and transition propulsion systems are arranged in the rear of the vehicle, which moved the centre of gravity (CG) afterwards. This normally requires the location of the wing moves backwards to balance the vehicle. Nevertheless, it shortens the tail moment arm. For this reason, a big tail area is inevitable for a conventional tail to counter the moments produced by the main wing. The all moving tail design demands less volume coefficient so that a small tail area can be obtained. It reduces the tail volume and weight penalty. From the structure point of view, the all moving tail has a simple structure and places the actuators inside the fuselage, which benefits the waterproof design.

Vertical tail

The sizing of the inverted Y tail is similar to the design of the V tail. In here, the method from Raymer [47] is followed, and the inverted Y is sized into the same area as the conventional tail. The area of vertical tail is calculated firstly,

$$S_V = \frac{(1 - 15\%)V_V b_W S_W}{L_V} \tag{28}$$

From a similar size UAV [55], it can be known the vertical tail volume coefficient can be from 0.02 to 0.07. Therefore, the 0.03 is estimated as the initial volume coefficient for the vertical tail. And a 15% volume coefficient is reduced because of the all moving tails design. According to the book [47], the moment arm of 0.387 m is estimated as 45% of the length of the fuselage. However, the tails will interfere with the propeller if their location is set according to this length. So, the moment arm is estimated at 0.3 m initially. Consequently, the size of the vertical tail is,

$$S_V = 0.0276\, m^2$$

Horizontal tail

Horizontal tail volume coefficient for small UAVs is usually from 0.3 to 0.66 [55]. The 0.35 was estimated at the beginning. The procedure for sizing the horizontal tail area is the same as the vertical tail,

$$S_H = \frac{(1 - 15\%)V_H \bar{c} S_W}{L_H} \tag{29}$$

where the $\bar{c}$ is the mean aerodynamic chord of the wing, $\bar{c} = 0.158\,m$, $L_H = 0.3\,m$ same as the arm of the vertical tail.

Thus,

$$S_H = 0.0356\,m^2$$

Conventional tail converts to inverted Y tail

The inverted Y tail is composed by the inverted V tail and the vertical tail on the top of the fuselage as described in Figure 2-6.

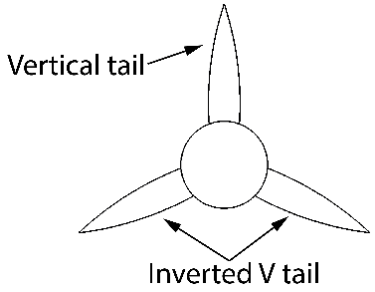

Figure 2-6: Inverted Y tail diagram

Due to the inverted Y tail design, the horizontal tail with anhedral can provide part of the effective vertical area. So, the projected total vertical area is the sum of the vertical tail area S_{Y_V} and the vertical projected area of the inverted V tail $S_{Y_{VT_V}}$,

$$S_V = S_{Y_V} + S_{Y_{VT_V}} \tag{30}$$

The projected total vertical area should be equivalent to the area of the conventional vertical tail. Considering the axisymmetric body design, the large horizontal tail area is not preferred. Hence, it is estimated that one-third of the total vertical tail area S_V is provided by the vertical projected area of the inverted V tail $S_{Y_{VT_V}}$. This yields $S_{Y_{VT_V}} = 0.008\,m^2$, and $S_{Y_V} = 0.0196\,m^2$.

The equation for the V tail anhedral angle is used to evaluate the inverted V tail anhedral angle,

$$\Gamma_Y = \arctan\sqrt{\frac{S_{Y_{VT_V}}}{S_H}} \tag{31}$$

Eq. (31) yields $\Gamma_Y = 25\ degrees$. Considering the interference between the folded wing and the inverted V tail, the anhedral angle is feasible.

Thus, the converted V tail area in one side is

$$S_{Y_{V_{oneside}}} = \frac{1}{2}\frac{S_H}{\cos(\Gamma_Y)^2} \tag{32}$$

$$S_{Y_{V_{oneside}}} = 0.0218\ m^2$$

From the result, it can be seen those three fins (the vertical tail and 2 fins of inverted V tail) have a similar area. Finally, the size of 3 fins was designed into the same value without reducing the effectiveness of tails. Same size tails can make the manufacturing easy, since only one mould needs be made to build 3 composite fins. In addition, it follows the axis-symmetry design of the submarine. Thus, the size of the tail is estimated as:

$$S_{Y_{onefin}} = 0.022\ m^2$$

The trailing edge of the tail is designed to be perpendicular to the fuselage and 20 mm away from the propeller rotation plane. This moves the tail mean aerodynamic chord (MAC) afterwards and extends the moment arm. Thus, the effectiveness of the tail can be increased. Figure 2-7 presents the geometry of the tail. The tail taper ratio λ_Y is set as 0.5. The sweep angle at a quarter of the chord is 13.8º, and the aspect ratio is 1.96.

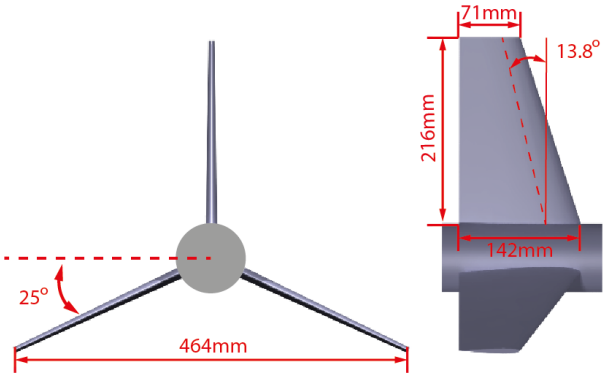

Figure 2-7: Designed Inverted Y tail

2.5 IMPROVED WEIGHT ESTIMATION

Improved weight estimation is conducted to update the initial weight estimation based on the available geometry and update the position of the centre gravity. The weight of the aircraft frame, the wing and the tails are evaluated based on the available literature [56] and the experience from manufacturing. Specifically, the tail and wing are made from carbon fibre reinforcement skin with a foam core, and the density of a similar structure is 80 kg/m^3 [56]. The dimensions of the parts are estimated from the 3D model in CATIA®. The avionics, such as the receiver and electronic speed control (ESC), are available components, so their weights can be measured. Because the location of the wing has not been decided, the weight estimation below is without the wing. The details are displayed in Table 2-7.

Table 2-7: Improved weight estimation

Components	Weight(g)	Distance to Nose(mm)
Hybrid propulsion system	460	800
Transition propulsion system	520	350
Avionics (receiver, ESC)	280	90
Battery	200	140
Tails with the structure and servos	445	735
Fuselage tube	500	382.388
Nose	64	69.919

Thus, the centre of gravity without the wing is estimated by Eq. (27) which yield,

$$x_{cg} = 456.032\ mm$$

2.6 WING LOCATION

Because the location of the wing and wing-deployment mechanism are different, their weights and locations estimations are separated. The weight of the wing-deployment mechanism is estimated as 380 g based on the structure and predicted devices. From [50], the 25% of the mean aerodynamic chord of the wing is arranged at the position of the CG for a stable subsonic aircraft. By following this method, the centre of gravity of the wing is at $x_{wing} = 467\ mm$. After putting locations and weights of the wing and the wing-deployment mechanism in the Eq. (27), the CG moves backward slightly where is $x_{cg} = 463.639\ mm$ in the rear of a quarter of the mean aerodynamic chord, which is adverse for the longitudinal stability. In order to keep the wing in the right location, the iterations were conducted towards the location of centre of gravity and the wing with the mechanism.

In the Z-axis direction, the wing is located at the centre of the fuselage. It meets axisymmetric configuration design of the submarine. Besides, the axisymmetric weight distribution can benefit the dynamic of the transition. Since the thrust of the transition propulsion system will be along the axis of the fuselage, the axisymmetric weight distribution will not produce pitch up or down moments. Finally, the positions of the centre of gravity and the wing are determined. The refined location of wing components is presented in Table 2-8.

Table 2-8: Refined weight and location of wing components

Components	Weight(g)	CG Distance to Nose(mm)
Wing	640	493.463

Wing-deployment mechanism	380	495.312

Finally, the total estimated weight of the vehicle is $m_{total} = 3.489\,kg$, and the CG location is $x_{cg} = 467.978\,mm$. The final geometry is depicted in Figure 2-8.

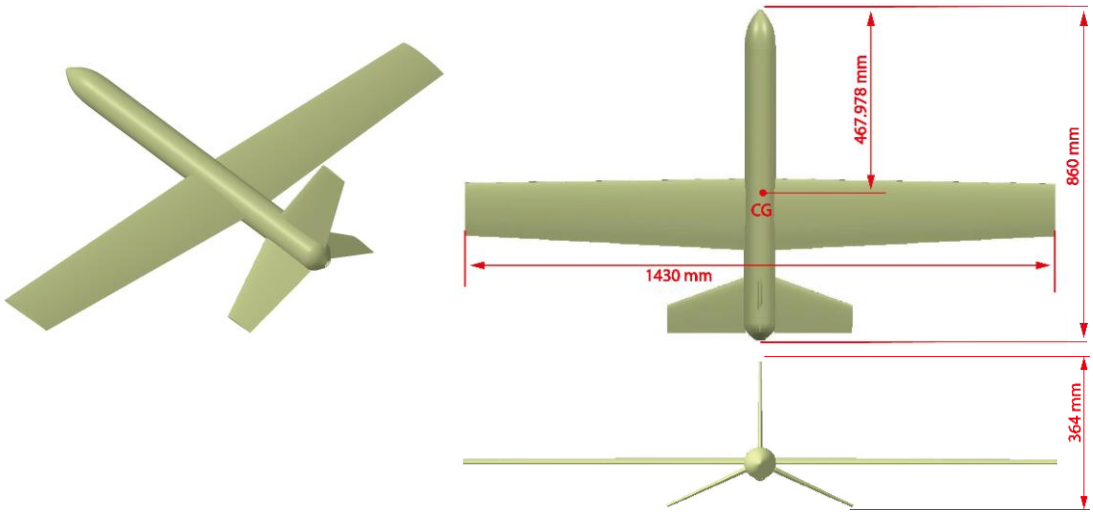

Figure 2-8: 3D model of the aircraft initial configuration

2.7 VARIABLE-SWEEP WING DESIGN

2.7.1 Design requirements

The requirements are established according to the mission profile and existed literature.

Deploy and fold the wing

In the mission profile, the vehicle needs to deploy the wing during the water to air transition. It also needs to fold the wing back during the diving process to reduce the impact and drag for an underwater cruise.

Short time deployment

The water to air transition is a short time procedure. This requires the mechanism to deploy the folded wing into a long span, high aspect ratio wing quickly to obtain enough lift as soon as possible.

Self-locked in a certain location

The deployment mechanism opens the wing, but the drag acting on the wing also drives the wing to fold back during the flight, and then the moments acting on the mechanism may damage the actuator. Hence, a locking mechanism is needed to lock the wing during the flight and transfer the moment to the structure to protect the actuator.

Lightweight and Low complexity

Lightweight is necessary for the aerial vehicle. Moreover, a mechanism with low complexity can decrease the failure possibility and fabrication time.

2.7.2 Location of the pivot and rotation angle

The position of the pivot

The location of the pivot determines the modification level and the rotation angle of the wing. If the pivot is excessively close to the fuselage, the shape of the wing root area will be modified due to the interference with the fuselage. In the contrast, if the pivot is excessively far from the fuselage, a long structure to carry the pivot is needed. This long structure is covered by the fairing, but the fairing cannot provide the lift as much as the main wing, which will increase the lift losses. For these reasons, the position of the pivot should be investigated.

As illustrated in Figure 2-9, the pivot is allocated just under the quarter of the wing chord in the X-axis direction where the wing main spar normally is allocated at. The shaft on the pivot carries the load from the main spar. For this reason, it is beneficial to allocate them closely for enough structure strength. In the Y-axis direction, the distance between the pivot and fuselage centre line is set at 110 mm. The decision was made to minimise the shape modification on the wing with the shortest structure carrying the pivot. It can be seen from Figure 2-9 that a small part of the wing root trailing edge overlaps with the fuselage. This small modification on the wing results in a larger fold back angle which is worthwhile.

Fold back angle

The fold back angle is limited by the interference between the folded wing with the propeller and the fuselage. Accordingly, the 65 degrees rotation angle is the maximum without any collision between the wing and other components.

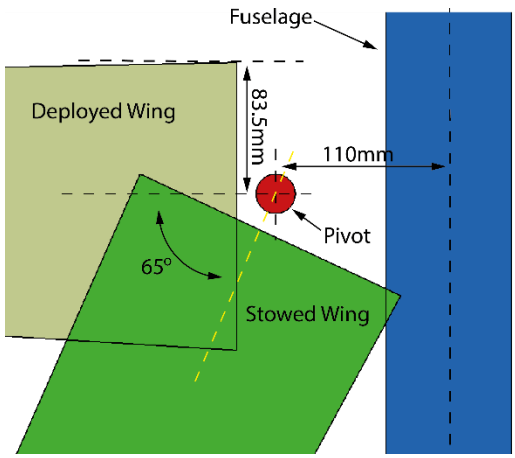

Figure 2-9: Wing rotation angle and pivot dimension

Deployment torque estimation

The required torque is evaluated in the extreme condition that the vehicle takes the vertically take off from the water to air to guarantee that the mechanism can work in every possible situation. In this process, the gravity of the wing produces most of the torque. Compared with the gravity, the drag is very small, so it is neglected in this situation. The position of the centre of gravity and the inertia of the wing are estimated from the 3D model in CATIA®. In this initial estimation, the friction in the mechanism is neglected. Accordingly, the torque needed for the deployment changed with the sweep angle is estimated by the Eq. (33),

$$\tau_{de} = \frac{1}{2} m_{wing} g \frac{b}{2} \cos \Lambda \tag{33}$$

The result is shown in Figure 2-10. The maximum torque is $0.930\ Nm$ at the initial deployment, then the torque decreases to $0.412\ Nm$ at the end. This value gives the requirement for designing the deployment mechanism. On the other hand, the deployment time is not evaluated here, since it mainly relies on the actuator, which is decided by mechanism and actuator specification. For this reason, one of the parameters used to select the actuator is its operation speed, which should be fast enough with sufficient power.

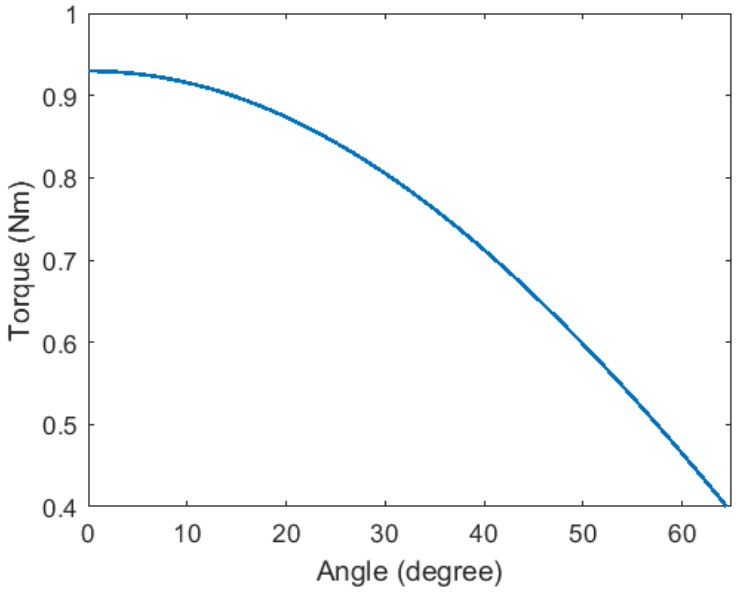

Figure 2-10: Required torque versus deploying angle

2.7.3 Rotary mechanism

Two schemes are designed following requirements. They are the rotary mechanism driving the wing through the gears and the linear actuator using the linear force to rotate the wing. The detail of the rotary mechanism is illustrated in Figure 2-11. It is driven by the rotary movement of the servo. The most significant advantage of the rotary mechanism is the high

efficiency, as the torque generated by the servo can be transferred by the gears or directly rotate the wing. In addition, the wing rotation speed can be adjusted by the power of the servo and the gears transmission ratio. The actuator is a servo with high rotation speed and lightweight, but relatively small torque. Its specification is displayed in Table 2-9. The transmission ratio of the whole system is 3.88:1.

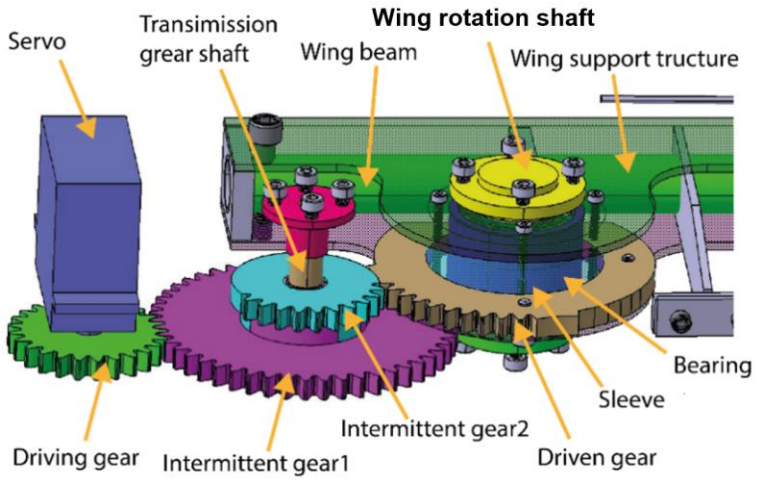

Figure 2-11: Rotary mechanism 3D model

Table 2-9: Specifications of the rotary mechanism

Category	Value
Output	2 Nm
Weight	69 g
Dimension	40 × 20 × 41 mm
Rotation speed	0.13 sec / 60 degrees
Rotation angle	360 degrees

The working principle is that the servo rotates the gears, which transmit the torque to rotate the wing around the wing rotation shaft. Especially, the intermittent gear 2 and driven gear not only transfer torque but also have a self-lock function. This avoids the torque generated by the drag on the wing to act on the servo. The intermittent gear 1 and the intermittent gear 2 are engaged by spline joints.

The wing spar is fixed to the wing support structure, which consists of two carbon fibre plates. Two bearings for wing rotation are fixed into the sleeve, which is screwed on the support structure. All the bending moment on the wing can be transferred to the wing rotation shaft through the bearings. As a result, the wing rotation shaft is the main load bearing part. It is fixed to the beam box, which is connected to the fuselage.

Self-lock mechanism

The intermittent gear 2 and the driven gear are designed as incomplete gears, so two stop arcs arranged at the driven gear to lock the mechanism in wing deployed and folded configurations. The range of the tooth on the driven gear corresponds to the wing rotation angle. After teeth engagement is finished, the intermittent gear 2 continues to rotate until its non-tooth area engages with the stop arc on the driven gear. When the non-tooth area fully attaches on the stop arc, the mechanism is locked. The torque acting on the wing will not be transferred to the servo through the tooth. It will be taken by the transmission gear shaft, which is mounted on the box beam, through the attachment between stop arc and non-tooth area. The details of the transmission and the transmission ratios between the gears are indicated in Figure 2-12.

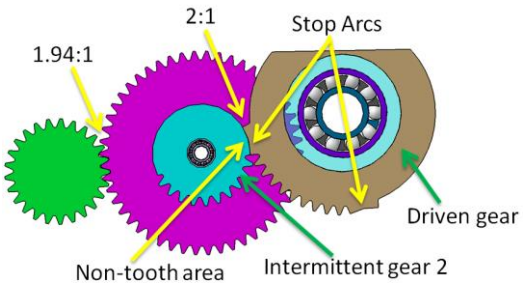

Figure 2-12: Gear transmission ratio distribution

The mechanism is located at the wing root area, which is presented in Figure 2-13. It is fixed by the structure of the beam box connected to the fuselage. The mechanism is covered by a fairing to keep the streamline shape to reduce the drag.

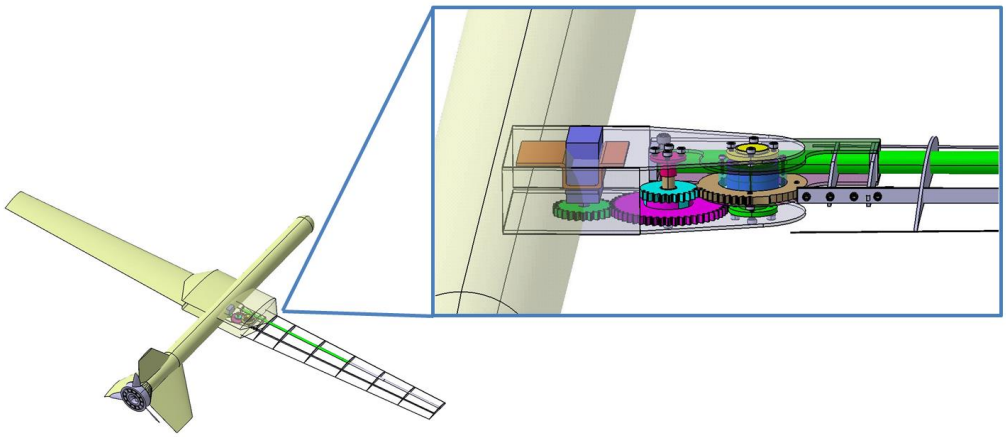

Figure 2-13: Location and structure of the rotary mechanism

2.7.4 Linear mechanism

The linear mechanism has advantages such as a simple structure, easy for manufacturing and maintaining. Figure 2-14 demonstrates the prototype of the linear mechanism. In particular, the wing rotation shaft remains the same design as the rotary mechanism. Two carbon fibre

plates are introduced to mount with two extended wing spars to build a box structure, which connects the wing with wing-deployment mechanism. In the linear mechanism strategy, a sleeve beam is introduced. The linear actuator is mounted on the pivot 1 and the pivot 2, which are the hinges on the sleeve beam and carbon fibre plates. For saving the weight, aluminium is applied to build the wing-deployment mechanism.

With the linear actuator extending from the start point to the end point, the wing is deployed with 65 degrees rotation to the deployed configuration. Vice versa, the wing folds back into the folded configuration with the linear actuator retracting from the end point to the start point. The designed stroke is 28 mm, which is the distance between the start point and the end point.

The torque generated by the linear actuator is the linear force times the distance L_a and times the $\cos\kappa$. Notably, the distance L_a is from the axis of the wing rotation shaft to the pivot 2, L_a= 26 mm. κ is the angle between the force line of the linear actuator and the tangent of the pivot 2 track. κ is changed from -32.5º to 32.5º, which corresponds to 65º wing rotation angle.

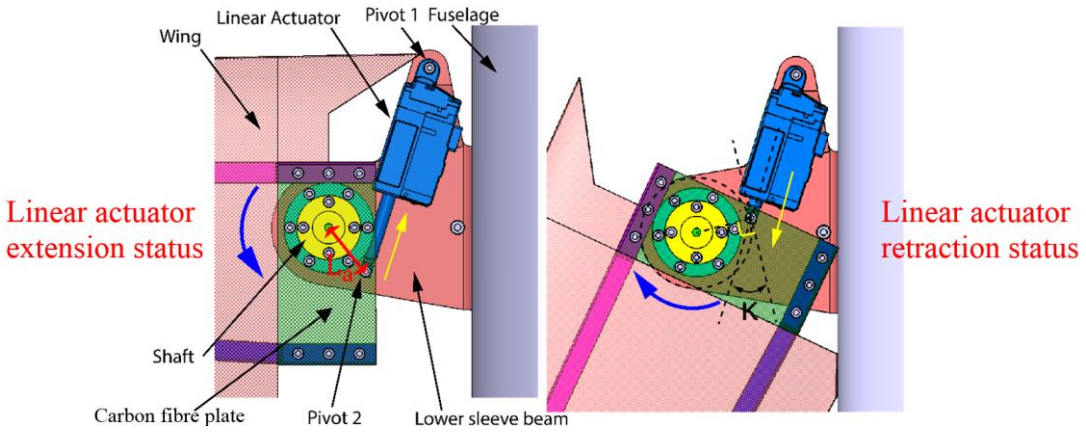

Figure 2-14: Linear mechanism movement direction

Linear actuator

The linear mechanism is driven by the Mighty ZAP® mini linear actuator. The selection of the linear actuator is based on the required torque and lightweight property. Especially, the stroke of the actuator is 30 mm, which is satisfied with the required stroke. Furthermore, this linear actuator has its own self-lock mechanism. Due to this unique mechanism design, the linear actuator can keep its position with up to 80 N force acting on it. As a result, the external self-lock mechanism can be removed, which saves an amount of weight. Since the linear actuator is exposed in the outside, a waterproof case can be built to cover it. Figure 2-15 presents the geometry of the linear actuator, and Table 2-10 displays its specifications.

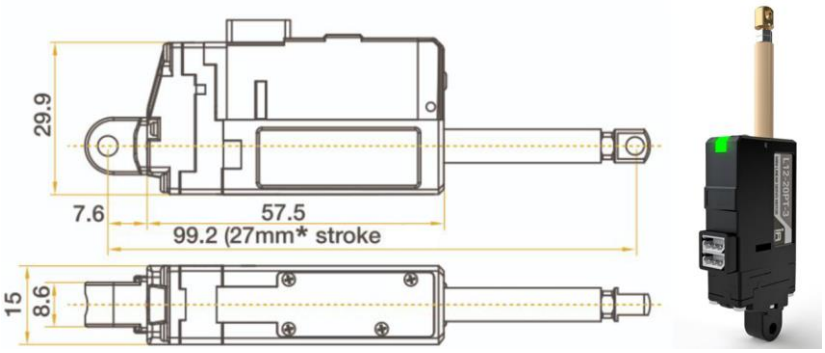

Figure 2-15: Dimension of the linear actuator and 3D model [57]

Table 2-10: Specifications of the linear actuator

Category	Value
Model	L12-40PT-3
Rated Force	40 N
Max Speed (No Load)	28.0 mm/s
Input Voltage	7.4 V
Stroke	30 mm
Weight	65 g
Dimension	57.5 (L) × 29.9 (W) × 15(H) mm

The torque produced by the linear actuator changing with the angle κ is calculated based on the dimension of the mechanism and the specification of the actuator. The result is shown in Figure 2-16. At the start point, the torque generated by the linear actuator is 0.945 Nm, which fulfils the required torque.

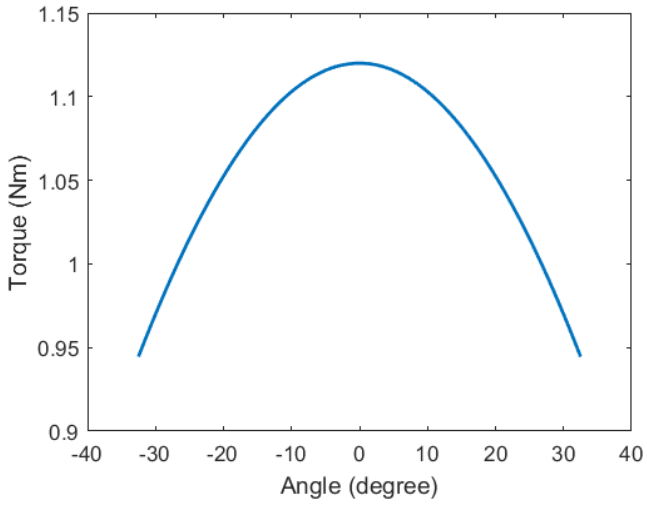

Figure 2-16: The torque generated by linear actuator changing with the rotation angle

Eventually, the linear mechanism is chosen for the vehicle. Between those two schemes, the power of actuators is similar, but the linear mechanism has a simpler structure without the external locking mechanism. It reduces the possibility of mechanical failure. Besides, lots of

fabrication time can be saved for the same reason. The removable and easy assembly design can also benefit the experimental test and modification.

2.7.5 Final CG

After determining the wing-deployment mechanism and structure, the weight estimation on the wing and wing-deployment mechanism is refined. The location of the CG is updated after the refinement, and the results are shown in Table 2-11. The total weight of the vehicle is 3,512 g, which is considerably close to the initial estimation. Moreover, the final CG location is 467.361 mm.

Table 2-11: Final components weight estimation and location

Components	Weight(g)	Distance to Nose(mm)
Hybrid propulsion system	460	800
Transition propulsion system	520	350
Avionics (receiver, ESC)	280	90
Battery	200	140
Tails with the structure and servos	445	735
Fuselage tube	500	382.388
Nose	64	69.919
Wing	640	493.463
Wing-deployment mechanism	252	494.312
Sleeve beam	150	496.981
Total	3,512	----
Location of the CG	----	467.361

2.8 FINAL VEHICLE CONFIGURATION

After introducing the wing-deployment mechanism and refining the location of the CG, the configuration of the vehicle is finalized. The aspect ratio increases to 9.27, due to the modification of the wing for the deployment mechanism. This produces a longer wing, which may have some lateral destabilizing issues, but it can compensate the lift losses from the fairing. The details of the final configuration are presented in Table 2-12.

Table 2-12: Specifications of the final configuration

Components	Value
Wing area	$0.238\ m^2$
Tail area	$0.023\ m^2$
Fuselage length	$0.831\ m$

Wing dihedral	0 $degree$
Tail Anhedral	25 $degree$
Aspect Ratio	9.27
Wingspan	1.485 m
Root chord	0.183 m
Tip Chord	0.133 m
Mean aerodynamic chord	0.158 m
Tail Root chord	0.142 m
Tail Tip chord	0.071 m
Tail mean aerodynamic chord	0.110 m

Figure 2-17 and Figure 2-18 illustrate the final deployed and folded configuration. The whole vehicle is an axisymmetric design, which is recommended for the underwater travelling and transition. The airfoil shape fairing (yellow part) can create some extent of lift, but the bluff shape at the rear will produce an amount of the pressure drag during the flight. After folding the wing back, the front area is effectively reduced. It can be known from the 3D model that the tail can be deflected in the clearance between the folded wing and tail, which provides the manoeuvrability for the underwater cruise. The only problem is the folded wing provides huge stabilize surface in the rear of the vehicle, which may make the underwater longitudinal control sluggish. Nevertheless, the aileron can also work as the control surface to increase the control force.

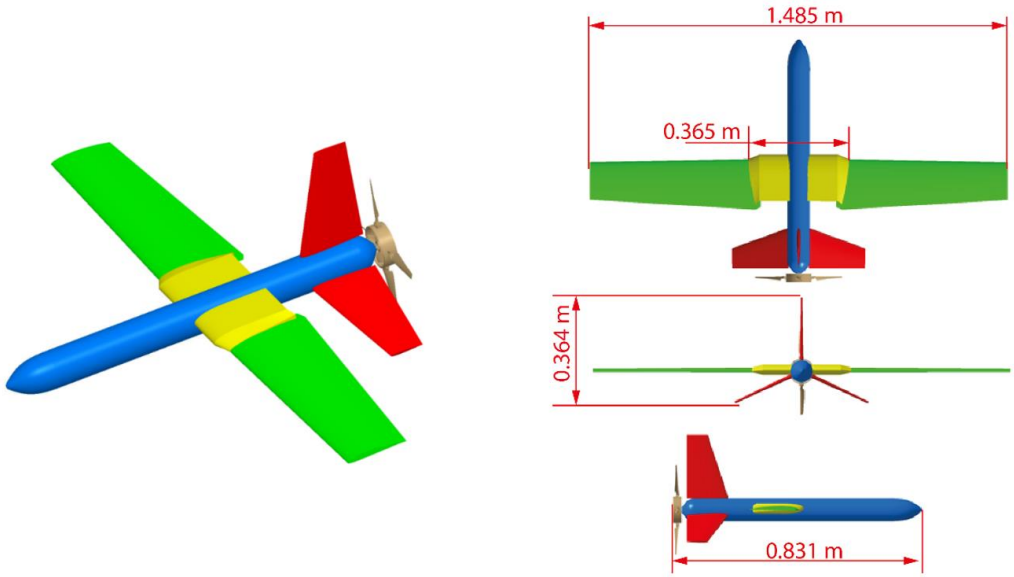

Figure 2-17: BUUAS 3D model and three views of the deployed configuration

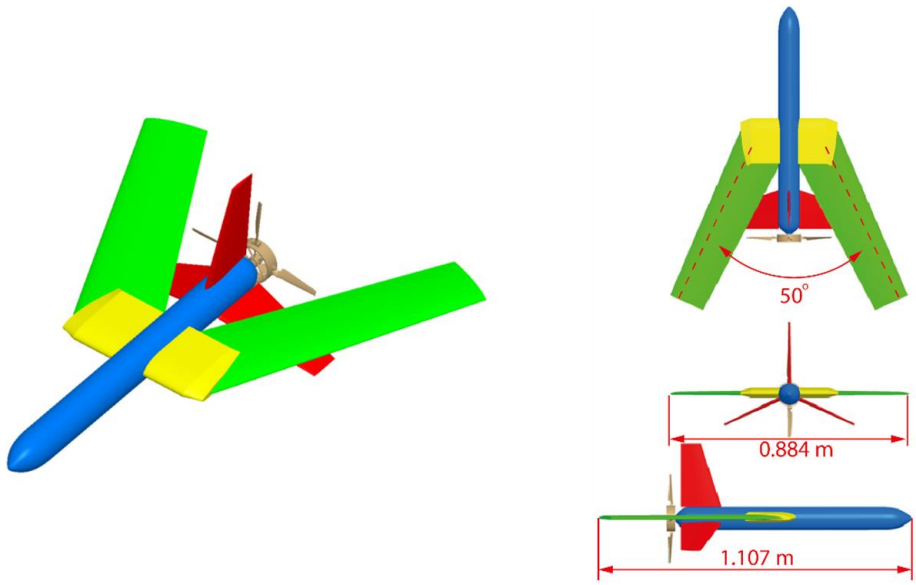

Figure 2-18: BUUAS 3D model and three views of the folded configuration

2.9 PERFORMANCE VERIFICATION

After the configuration is finalized, the verification was conducted to check if the vehicle meets the initial requirement. Then the next numerical simulation and wind tunnel test can be started.

2.9.1 Wing loading

The wing loading is obtained from the function of updated reference area and total weight W_t by Eq. (34),

$$W/S = \frac{W_t}{S_{ref}} \tag{34}$$

Eq. (34) yields $\frac{W}{S} = 14.756\ kg/m^2$. Therefore, the updated stall velocity can be gained,

$$V_{stall} = \sqrt{\frac{W/S \cdot g}{\frac{1}{2}\rho C_{L_{max}}}} \tag{35}$$

The velocity of the stall is $V_{stall} = 13.708\ m/s$, which is smaller than the design value. This gives more operational velocity range of the vehicle.

2.9.2 Thrust to weight ratio

The updated wing loading is used to calculate the thrust to weight ratio during the cruise condition,

$$T/W = \frac{qC_{D_0}}{W/S} + \frac{W}{S}\left(\frac{n^2}{q\pi ARe}\right) \tag{36}$$

The Eq. (36) yields $T/W = 0.301$, which is slightly big than the original calculation.

2.9.3 The best rate of climb velocity

Eq. (37) can obtain the best rate of climb velocity,

$$V_{R/C} = \sqrt{\frac{2}{\rho}\sqrt{\frac{k}{3C_{D_0}}}\frac{W}{S}g} \tag{37}$$

This equation yields the best rate of climb rate $V_{R/C} = 18.807\ m/s$. This value can give an indication for the design of the transition propulsion system, which should launch the vehicle that is close to the $V_{R/C}$.

2.9.4 Endurance

The refined endurance is 10.089 minutes for the flight and 19.162 minutes for the underwater cruise, which fulfils the initial requirements.

2.10 NUMERICAL SIMULATION

The numerical simulation is conducted for the deployed and folded configurations. Its purpose is to validate the design by using an economical method before the wind tunnel experimental test and fabrication. A couple of angles of attack are simulated for the aerodynamic configuration when the wing is fully deployed. Besides, one set of simulate is performed for the hydrodynamic configuration at the zero angle of attack when the wing is full folded, since the underwater manoeuvre is not critical as the flight performance in the configuration development based on the requirement.

2.10.1 Aerodynamic configuration mesh building

Geometry preparation

In the commercial software Fluent®, which carries the numerical simulation, a half of the mirror symmetrical physical geometry can be simulated by using the symmetry boundary condition to reduce the computation load. Therefore, only half of the geometry is prepared, and then mesh cells are created according to the prepared geometry. There are some details on the geometry, which have a limited contribution to the overall aerodynamic and hydrodynamic performance, need plenty of mesh cells to make the mesh smooth and continuous. This will

increase the meshing difficulty and computational effort. Further, it will make the whole simulation more complicated and increase the unnecessary simulation time. In addition, the mesh can only be made from the geometry that has a complete closed surface without any leakages, holes, gaps, or self-intersecting surfaces. Therefore, the 3D model geometry in the CATIA® was cleaned to remove the complicated details before the meshing,

The significant refinement was made in wing-deployment mechanism area. The fairing is open to contain the folded back wing in the actual geometry. However, the fairing should be closed in order to build the complete surface for constructing the mesh. Since the outflow is examined, the internal mechanism with many details is eliminated. Besides, there are also gaps between wing and fairing, fairing and sleeve beam. Those gaps are filled with surfaces, and details around them are simplified. In addition, the sleeve beam is removed in the geometry, because of the thin sleeve beam on fuselage has a small effect on the aerodynamics and hydrodynamics, and it can lead to a lot of meshing works. The refined geometry is shown in Figure 2-19. The similar approach is also used in other areas, such as empennage and wing.

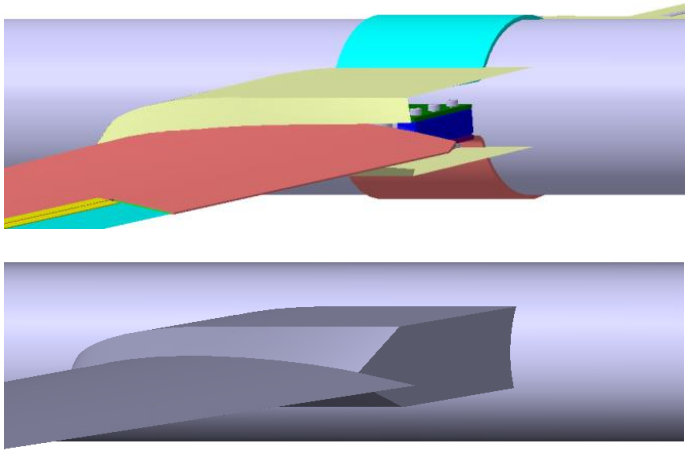

Figure 2-19: Original geometry (top), simplified geometry (bottom)

Finally, the half geometry is simplified and sealed with the symmetry plane. This improved geometry displayed in Figure 2-20 has a complete close surface without any self-intersecting.

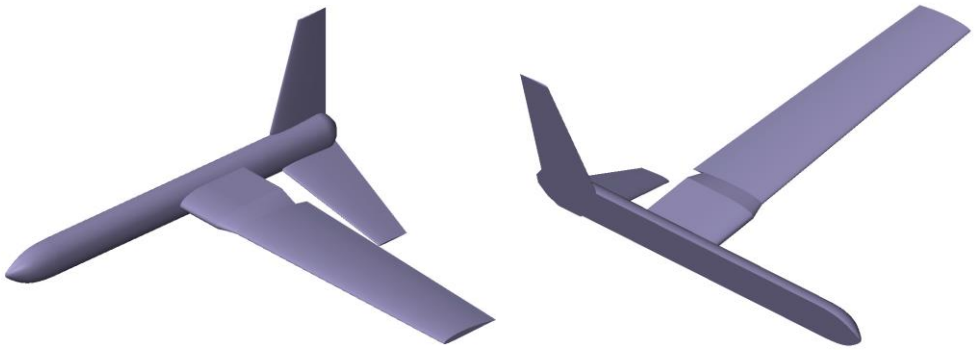

Figure 2-20: Improved geometry

Structured Mesh Building

The mesh building software ICEM® is selected to establish the structured hexahedron mesh. The structured mesh is generally high space efficiency. It has fewer cells number comparing to the unstructured mesh, which means that it can reduce the simulation workload. This is beneficial for the flight configuration simulation, since tremendous time can be saved for the whole simulation on a couple of angles of attack. It also has a better convergence and resolution over the unstructured mesh.

The simulation domain, which is also the flow field, is established. The domain size is 17 m (L) × 15 m (W) × 6 m (H) shown in Figure 2-21. It is twenty times bigger than the half vehicle size to reduce any influence from the boundary. In the domain, surfaces with different colours are the different parts. They will be given different boundary conditions in the solver.

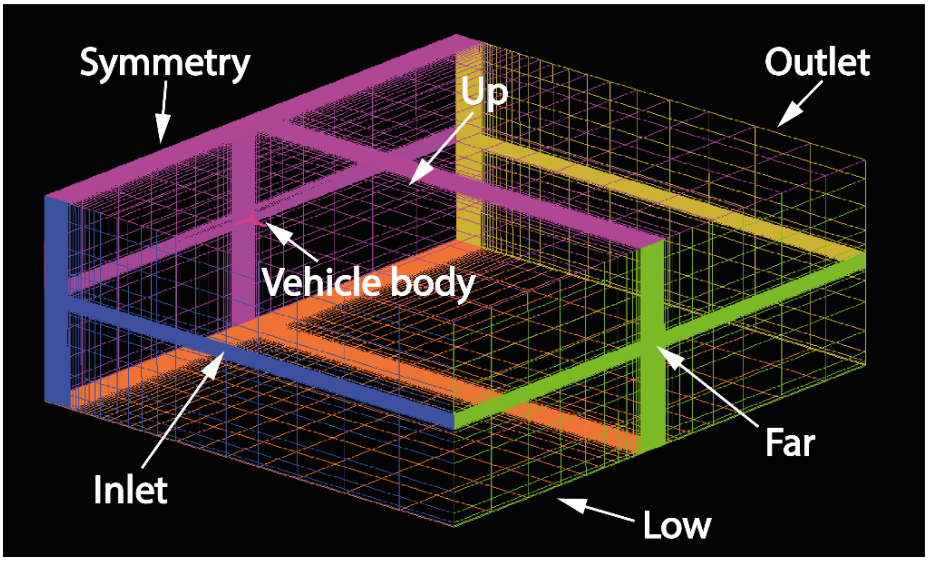

Figure 2-21: Computational domain

It is important that the mesh near the vehicle geometry is properly sized in order to make sure an accurate simulation on the flow field. The size of the boundary layer mesh, which is

indicated in Figure 2-22, is evaluated by using the online tool from Pointwise®. It provides an estimated grid space of the first layer with the input of the velocity, density, dynamic viscosity, reference length, which is the MAC, and desired y^+. All the values can be obtained from the requirements and the vehicle characteristics except the value of y^+. The first layer is in the viscous sublayer region, then the $y^+ < 5$ [58]. In this case, the y^+ is appointed as 1 to gain a fine boundary layer [31]. The first layer grid space value is evaluated as 0.015 mm. The size of the rest boundary layers is increased with the ratio of 1.2 from the first layer in the boundary layer zone.

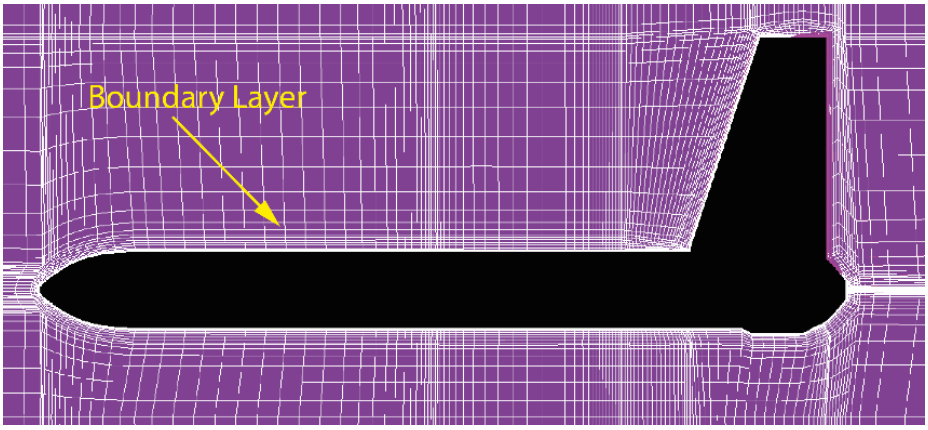

Figure 2-22: Deployed configuration cross-section mesh

The basic principle of the meshing in ICEM® is to define the large blocks and then divide them into smaller hexa elements. To begin with, the first block is initialized. Then, the block is divided into smaller blocks by separating the complicated geometry into several simple small geometries where the mesh can be built easily. The boundary edges and vertices on the blocks are associated with the geometry lines and points on the model to help the software to recognize surfaces on the geometry and build the mesh on it. Each edge is also divided by arranging the nodes on it, so that blocks are divided into small cells. The boundary layer is generated by O-grid function with the dimension calculated above.

In the critical flow fields such as the vehicle surface, the high computational mesh resolution is needed to increase the simulation accuracy. In other flow zones, the medium computational mesh resolution is enough for the simulation with the minimized simulation workload. An amount of fine mesh elements is precisely defined around the wing geometry since the wing has the most influence on aerodynamic characteristics. The mesh elements at the critical leading and trailing edge are dense, and smoothly transited to the sparse mesh on the main surface. This is beneficial for the simulation efficiency, accuracy and convergence. After the overall mesh establishment, the mesh quality such as aspect ratio and angle are checked to

fulfil the solver requirements before exporting. Finally, the structured block mesh is converted into unstructured hexa mesh and exported for simulation. The total number of mesh elements is 1,135,611. The finished mesh is depicted in Figure 2-23.

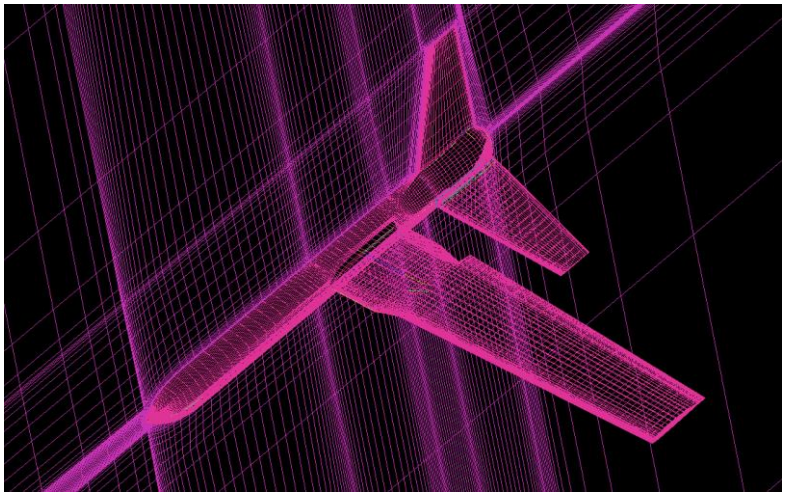

Figure 2-23: Mesh on the vehicle body of the deployed configuration

2.10.2 Aerodynamic simulation

Numerical model

The finalized mesh was imported into the Fluent® to conduct the numerical simulation based on computational fluid dynamics (CFD). The cruise velocity, which is the velocity magnitude, is 20 m/s and the Mach number is 0.06. The flight ceiling is 400 m. Thus, the flow can be regarded as the incompressible flow. Besides, the Reynolds number is 2×10^5, which is highly possible to be turbulence comparing to the Reynolds number of 2,000. However, in this case, the description of the transition flow field is also crucial for both lift and drag coefficient [31, 59, 60]. To obtain the optimum result, the shear stress transport (SST) k-omega (2 eqn) model with Low-R_e Corrections carries the airflow resolve. The solver is pressure-based and steady in time, and the pressure-velocity coupling scheme is coupled. In addition, the pressure, momentum, specific dissipation rate, and turbulent kinetic energy are second-order upwind to achieve high accuracy.

The purpose of this simulation is to compute lift, drag and predict stall of this vehicle which is an important flow separation, and the SST model is one of the most accurate models for the separation prediction. In addition, regarding to the whole vehicle simulation, the transition flow will mostly happen on the wing and tail, but the cylinder fuselage will generate lots of turbulent flow with the increase of angle of attack. Therefore, the K-omega model is suitable in this case by considering the overall flow zone, since this model comes out to be widely used for the turbulent and transition flow field.

Boundary condition

As mentioned, the flow field is cuboid. The six surfaces are considered as the boundaries. The cases were run for an angle of attack from -6 to 16 degrees with 2 degrees increment. This increment will be divided into smaller value around the stall angle of attack. To simulate different angles of attack, the direction of the velocity is changed in the solver. Hence, the inlet, low, and up surface are defined as the velocity inlet. In these boundaries, the velocities in X and Z-direction are specified with the simulated angle of attack. This can be achieved by multiplying the velocity magnitude with X and Z components. In the cartesian coordinate system, the X-Components of the flow is $\cos\alpha$ and the Z-Component is $\sin\alpha$. As a result, the flow with direction is determined. The side wind is not considered in the simulation, so the velocity in Y-direction is always zero.

Subsequently, other boundaries conditions are defined as follow: the far surface is defined as the stationary wall with shear stress of zero; the symmetry surface on the mesh is set as the symmetry; the outlet is considered as the pressure outlet where the gauge pressure is zero; the vehicle surface is determined as the stationary wall with the no-slip shear condition; the interior boundary condition is applied to the flow field inside; the reference length is the length of the mean aerodynamic chord, which is 0.158 m, and the reference area is the half of reference wing area of 0.119 m^2.

Results

It is essential to examine the flow around the vehicle. The visualization of the streamlines over the vehicle at $\alpha = 0°$ are shown in the Figures 2-24 to 2-26. In the velocity visualization in Figure 2-24 and 2-25, the velocity after the fairing is slowed down, because the fairing sheds most of the wake. Specifically, since the shape of the fairing is bluff, the separation starts after the boundary layer flow over the surface of the fairing. The separated flow is produced by an adverse pressure gradient behind the fairing. This separation creates a wake where eddies are formed. Eddies further contribute to pressure losses. Therefore, a pressure drag is generated. This is the dominant source of drag for a bluff body. The pathlines of turbulence in Figure 2-26 also confirmed the theoretical conclusion. As a result, the fairing produces a large part of drag at $\alpha = 0°$. At this angle, the pressure gradients on the top and bottom surface of the wing are not strong, so the boundary layer is attached along the entire chord length. Accordingly, the wake after the trailing edge is tiny.

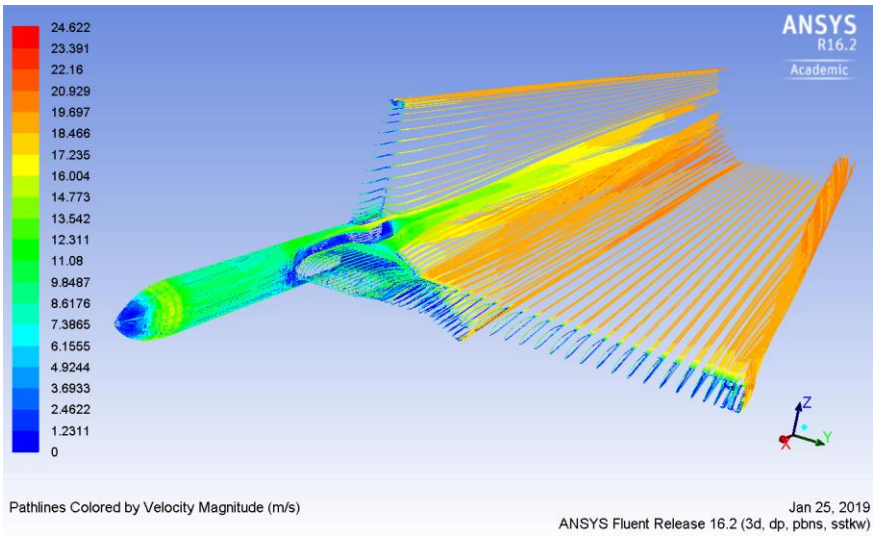

Figure 2-24: Pathlines colored by velocity magnitude front view

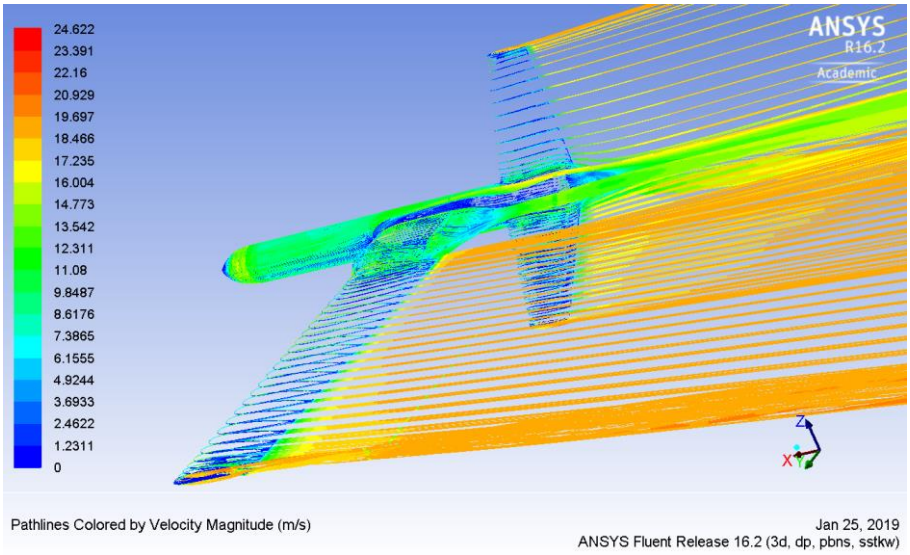

Figure 2-25: Pathlines colored by velocity magnitude back view

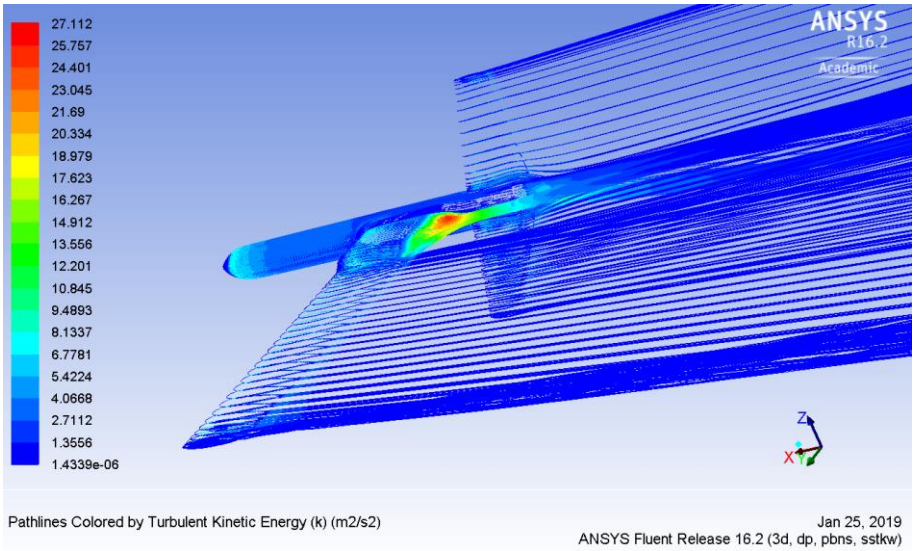

Figure 2-26: Pathlines colored by turbulent kinetic energy

Figure 2-27 demonstrates the variation of the lift coefficient with different angles of attack. Below 10 degrees, the lift coefficient increases linearly with increasing angle of attack. At angles of attack from 11 to 15 degrees, a large fraction of the flow over the top surface of the wing is separated. Consequently, the vehicle is stalled, and the lift coefficient starts to decrease. At this moment, the pressure drag is much greater than the viscous drag. As indicated in Figure 2-27, the stall angle is at 11 degrees. The maximum lift coefficient is 1.085 with 0.126 of drag coefficient. At the stall angle, the vehicle can produce 63.243 N lift with 7.143 N drags. This substantiates the vehicle can easily fly with the required propulsion system.

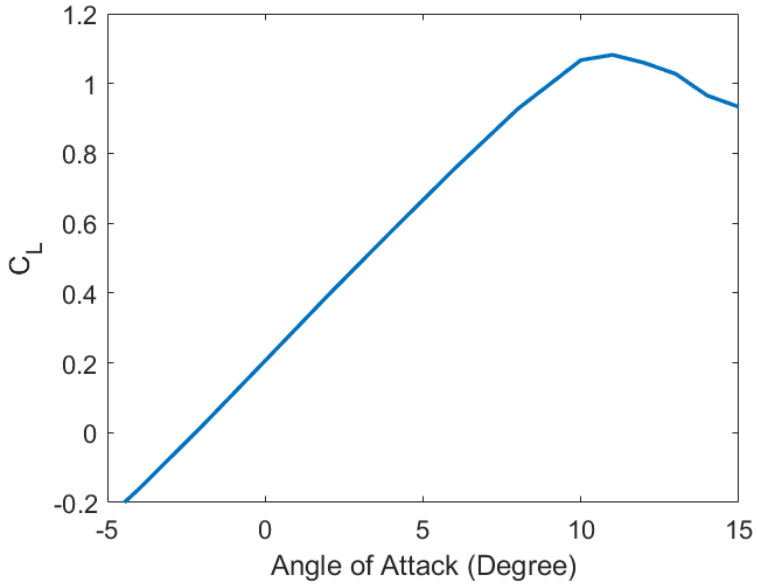

Figure 2-27: Angle of attack versus lift coefficient

Figure 2-28 depicts the curve of the drag coefficient varying with the angle of attack. Evidently, the variation of the drag coefficient is relatively slow at a low angle of attack from -5 to 10 degrees when the airflow is attaching on the wing surface. However, the airflow starts to separate from the vehicle surface at 11 degrees. Therefore, the drag begins to increase rapidly, and the vehicle is in the stall condition.

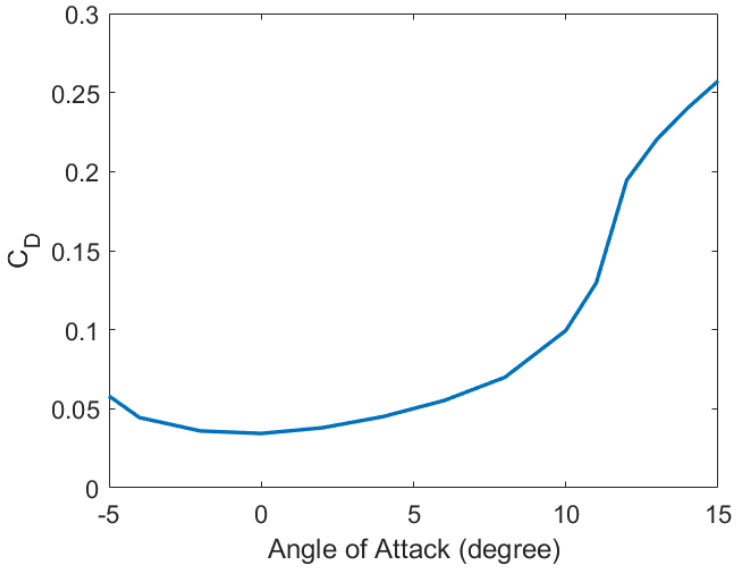

Figure 2-28: Angle of attack versus drag coefficient

The L/D versus angle of attack is presented in Figure 2-29. From the -5 to 6 degrees angle of attack the lift-to-drag ratio is increasing from the minimum value of -4.584 to the L/D_{max} of 13.704 then starts to decrease. This gives the optimum flight condition for the vehicle.

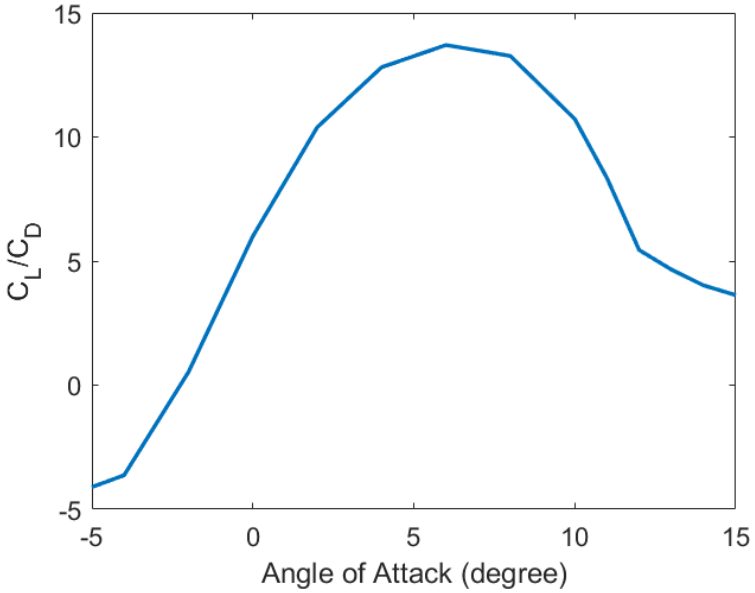

Figure 2-29: L/D versus angle of attack

2.10.3 Hydrodynamic configuration mesh building

Geometry preparation

The geometry preparation process for the folded configuration is similar to the deployed configuration. The fairing is still the primary modified area, which is closed same as the deployed configuration as illustrated in Figure 2-30. In the original geometry, the root of wing

marked in the blue circle is modified to adapt with the fuselage. In the circle, there is a designed gap between wing and fuselage to avoid collision after folding. In the improved geometry, the surface of the wing and fuselage are connected as one surface to reduce the meshing complexity. The closed half geometry is created and displayed in Figure 2-31. Then, the finished geometry is imported into the ICEM® to be meshed.

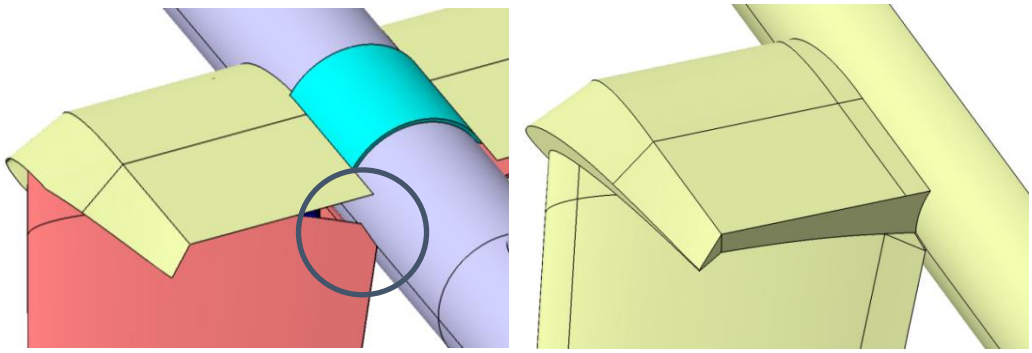

Figure 2-30: Fairing geometry improvement

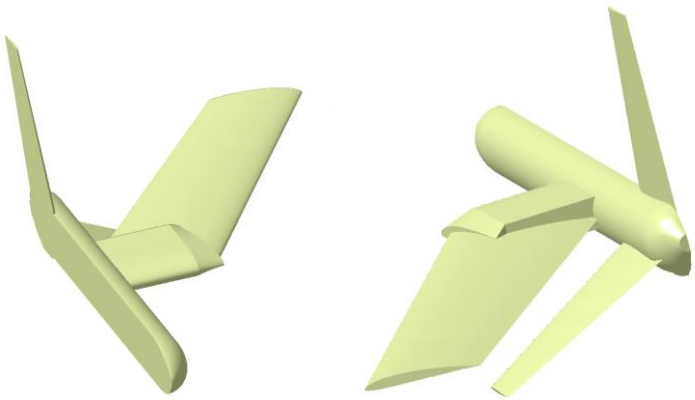

Figure 2-31: Finished geometry: fairing details, front view, back view (left to right)

Unstructured Mesh Building

An unstructured mesh is constructed for the folded configuration. Different from the deployed configuration, the mesh of the folded wing and the tail are coupled together on the folded configuration. It raises the difficulty to build a structured mesh, because the block dividing is complicated at the coupled wing and tail area. In addition, unlike the aerodynamic simulation, only the $\alpha = 0°$ cruise condition is examined due to the limited underwater manoeuvre. Since the hydrodynamic simulation load is limited, the advantage of the structured mesh is not obvious. Instead, the meshing working time on the folded configuration can be reduced by the unstructured mesh. Therefore, the unstructured mesh is selected for the hydrodynamic simulation.

As mentioned, the computational mesh resolution has a significant influence on the evaluation of aerodynamic and hydrodynamic coefficients. In the critical computational area, the adequate mesh resolution is necessary to obtain the result independent with the small mesh variation [61]. Therefore, the unstructured tetrahedral mesh with prism boundary-layer cells is constructed around vehicle configuration as presented in Figure 2-32. This hybrid mesh can yield a favourable combination of accuracy, efficient calculation time and less meshing effort. Specifically, the boundary layer prism cell is in the form of inflation layers as illustrated in Figure 2-32. The mesh in the inflation layers is orthogonal to the vehicle surface and the boundary layer flow direction. It can capture the boundary layer effects effectively and efficiently. The first layer thickness is 0.02 mm calculated by y plus approach. For this calculation, the y^+ number must be close to 1 for this kind of hydrodynamic simulation [62, 63]. The number of layers is set to 5, and the increase ratio is 1.2 as default. Since the wing is folded, the mean aerodynamic chord for the swept wing is changed to $L_h = 0.380\ m$.

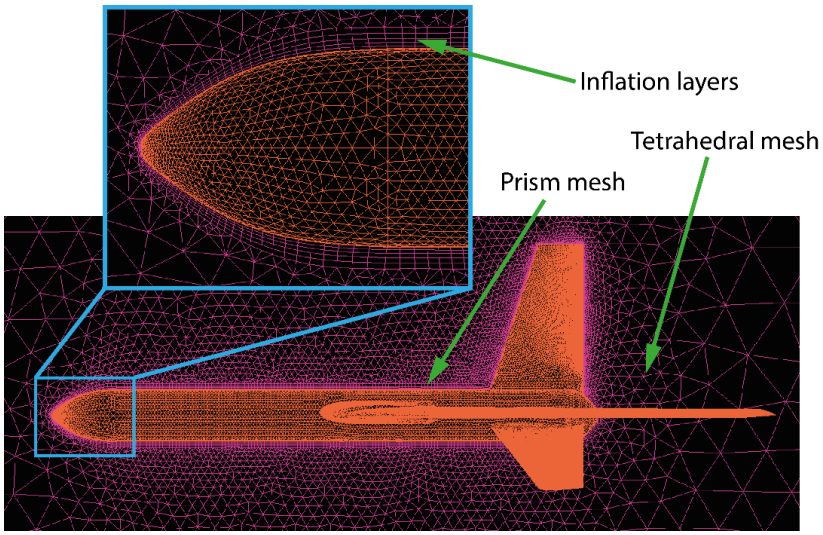

Figure 2-32: Mesh distribution

The size of the hydrodynamic simulation domain is 20 m (L) × 9 m (W) × 6 m (H) twenty times bigger than the dimension of the folded configuration, which is depicted in Figure 2-33. In the domain, the tetrahedral and prism mesh are created in the global mesh function. This function can control the maximum element size, which is 500 for the tetrahedral mesh. After the overall set-up, the unstructured tetrahedral mesh can be computed and generated. The initial mesh is course, then it is refined by the smooth hexahedral mesh function. Further, the mesh density at the nose, leading edge and trailing edge of the wing and tail are adjusted, and then the mesh and its grid lines are refined in global before exportation. The final total number of elements is 1,563,260. Figure 2-34 displays the finalized mesh on the body.

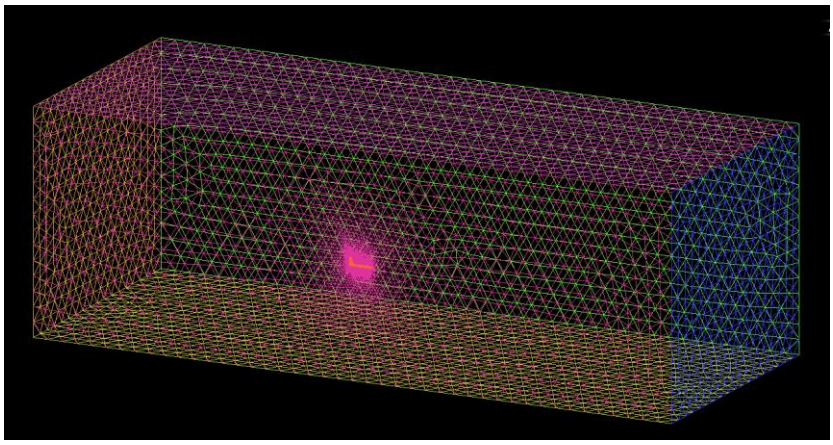

Figure 2-33: Computational flow domain

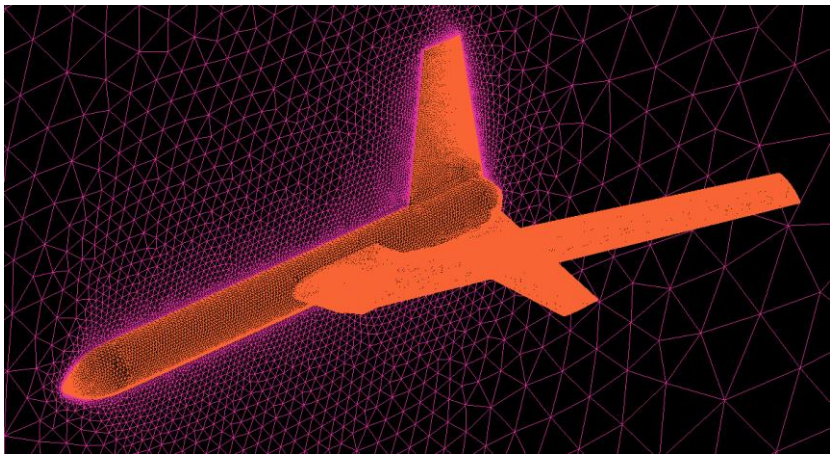

Figure 2-34: Mesh on the vehicle body of the folded configuration

2.10.4 Hydrodynamic simulation

Numerical model

The Reynolds number for the hydrodynamic simulation is $R_{e_w} = 425{,}685$, which is based on the mean aerodynamic chord of the swept wing. The $k - \omega$ SST turbulent model is used to carry the simulation, since it presents accurate prediction capabilities for this size vehicle with low Reynolds number [64].

Boundary condition

The set-up of the boundary condition is similar with the aerodynamic simulation, but the cruise velocity is 1 m/s with zero angle of attack. And, the fluid material is set as water. Additionally, the reference length is updated to the MAC of the swept wing.

Results

The visualizations of the velocity and turbulence streamlines over the vehicle are in Figure 2-35 and 2-36. The wake at the rear of the fairing is reduced, since the folded back wing relieved separation phenomenon caused by the bluff shape of the fairing. This decreases the

pressure drag and is promising for the underwater cruise. Furthermore, the wake from the fairing and the wing trailing edge do not have much effect on the inverted Y tail. This indicates that the control ability of the tail is not affected a lot by the folded wing. The lift and drag coefficient are presented in Table 2-13, which also indicates the future propulsion system design. It is worth to mention that the drag coefficient of 0.348 is close to the initial estimation which is 0.317. The slightly bigger drag may increase the needed underwater travelling power and decrease the duration. But considering the function of the vehicle, the duration is still enough to demonstrate the technology.

Table 2-13: Underwater simulation results

Underwater Result	Value
Drag coefficient	0.0348
Lift coefficient	0.0375

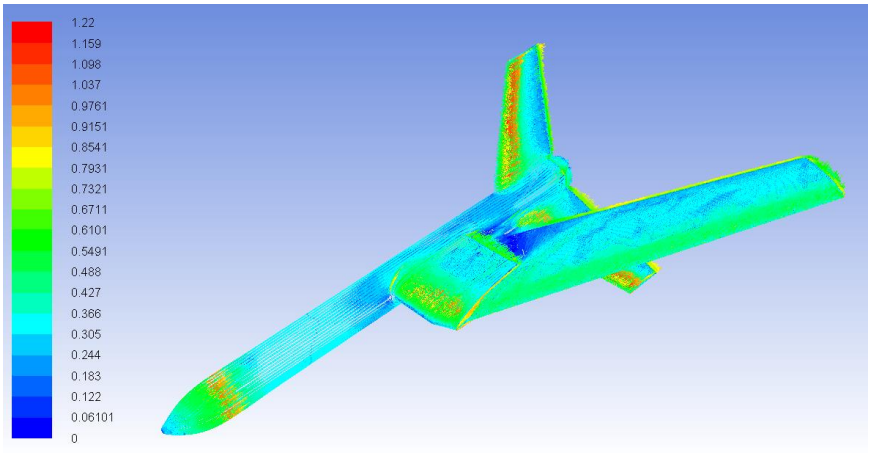

Figure 2-35: Pathlines colored by velocity magnitude front view

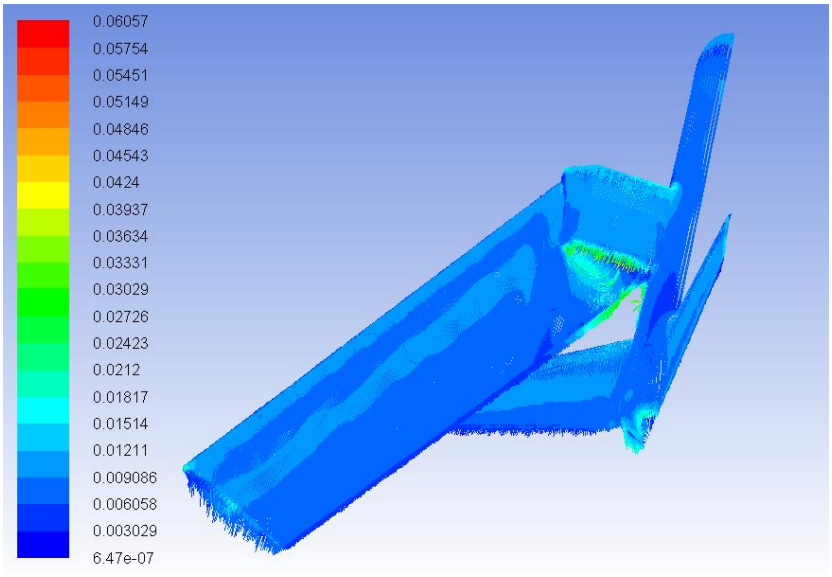

Figure 2-36: Pathlines colored by turbulent kinetic energy

2.11 WIND TUNNEL TESTING

Based on the numerical simulation, the wind tunnel experimental test for scaled down models of both deployed and folded configurations were conducted to verify the conceptual design, flight performance and predict the folded configuration performance after the vehicle exits from the water during the water to air transition.

2.11.1 3D printed scaled model

The scaled models were used for the wind tunnel test, and the scale ratio was 0.28. The models were built by using 3D printing technology. The 3D printing technology has a rapid fabrication advantage and can provide sufficient strength under small scale. Limited by the printing space of the 3D printer, the models were printed in several components. Then they were assembled by the mortise-and-tenon joint with glue. Since the wing has a thin shape, this made the warping happened at the wing tip area during the 3D printing. This slight distortion on the wing might create some turbulence and make the result less accurate.

2.11.2 Wind tunnel experimental test set-up

The industry wind tunnel in RMIT University was used. Its size is 2 meters in height and 3 meters in wide. The maximum wind velocity that it could provide is 120 km/h. Figure 2-37 shows the control panel and the structure of the whole wind tunnel. The JR3 400 N load cell was used. It can measure forces and moments in six directions. Particularly, the load cell had its own data acquisition system, which was installed on the computer. It took 10 seconds to acquire the raw data and take an average.

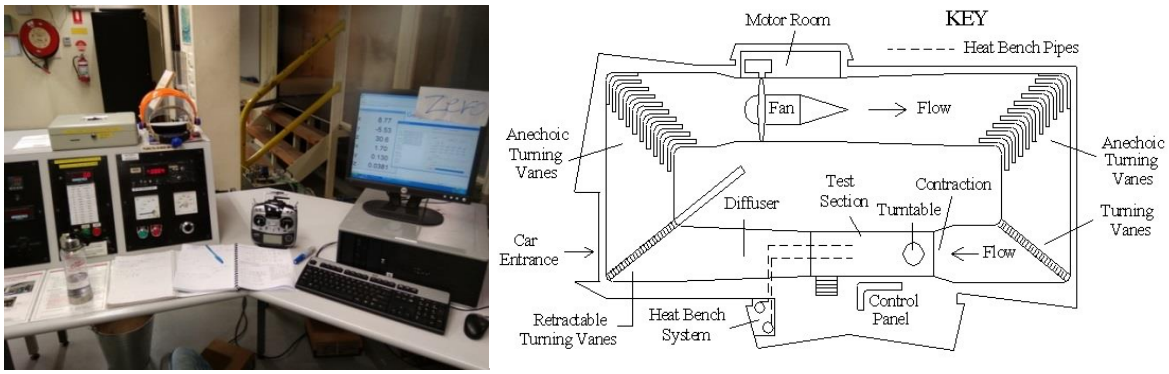

Figure 2-37: Wind tunnel control panel and the plan view of the RMIT Industrial Wind Tunnel

Figure 2-38 shows two configurations on the sting in the wind tunnel. A sting was built to hold the model inside the tunnel. Specifically, the model was bolt on the top of the sting by the nut through the hole on the model. The bottom of the sting was fixed on the load cell by screws rigidly. Then, the load cell with the sting went through the hole on the floor of the wind

tunnel and was fixed on a platform under the wind tunnel floor by clamps. The pitch angle was adjusted through the pivot and triangle structure on the sting inside the wind tunnel. Besides, the yaw angle was set on the platform under the wind tunnel floor by aligning the sting with the test angle on the protractor and tightening the clamps.

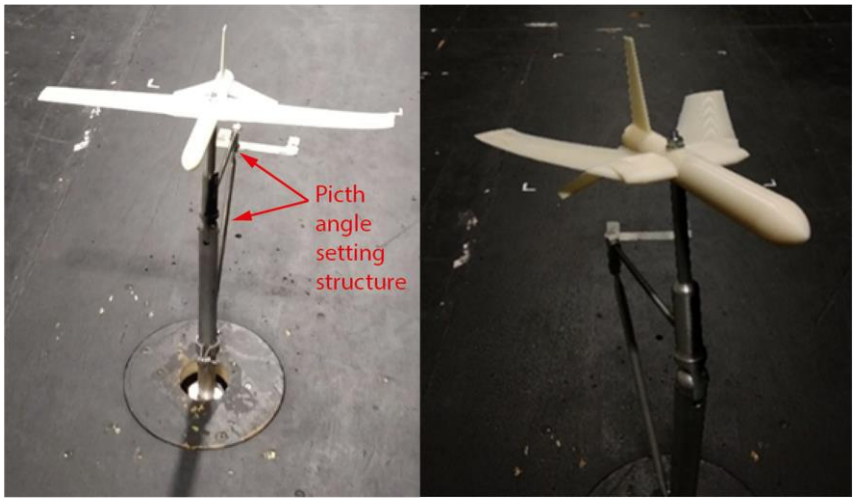

Figure 2-38: 3D printed models on the test rig in wind tunnel

2.11.3 Testing and data correction

The wind tunnel was running at the 75 km/h wind velocity. This velocity was limited by the structure strength. The Reynolds number under this circumstance is 0.6×10^5. Therefore, the velocity under the equivalent Reynolds number for the full-scale vehicle is 6.5 m/s. The data correction work was done by collaboration with the Imperial College [65] [66].

2.11.4 Results

The test results for the folded and deployed configurations are shown in Figure 2-39. Evidently, the gradient of the lift curve slope is reduced with the increase of the sweep angle, and the deployed configuration has a higher C_L, which proves its long endurance flight benefit. Moreover, the folded configuration has a relative higher critical angle of attack compared with the deployed configuration. However, limited by the pitch setting range of test rig, the $C_{L_{max}}$ for the folded configuration is not achieved. The phenomenon above can be explained by the Polhamus theory [67]. To be more specific, the folded configuration has similar behaviour to the delta wing, which has a low aspect ratio and can produce a high lift at a high angle of attack. At the high angle of attack, the separation flow over the leading edge produces the vortex. Those vortex merges with the tip vortex, thus the fast-moving flow over the wing is created. The fast-moving flow generates the pressure gradient between low pressure upper surface and high pressure lower surface. As a result, the leading edge suction force is created, which brings an

extra lift called 'vortex lift'. The extra lift keeps the $C_{L_{max}}$ in high angles of attack. This produces a lot of benefit for the water to air transition process when the vehicle may face a high angle of attack during the transition. It can help the vehicle reduce the risk of stall.

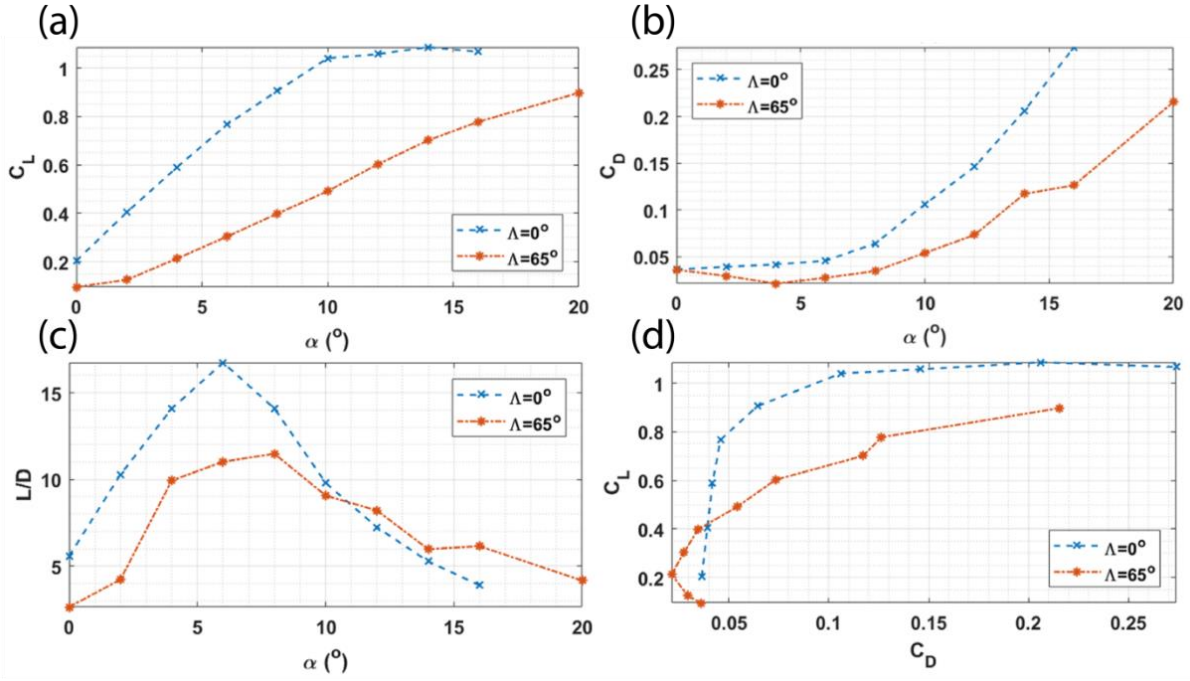

Figure 2-39: Angle of attack versus lift coefficient (a), Angle of attack versus drag coefficient (b), L/D versus angle of attack (c), Drag polar curve (d)

The lift-to-drag ratio is a critical measurement for the performance of the vehicle. The *L/D* of the deployed configuration is much higher than the folded configuration before the critical angle of attack. The high aspect ratio configuration presents the advantage of large $(L/D)_{max}$. On the other hand, the folded configuration with the delta wing shape has the benefit of the linear growth of *L/D* curve in more angles of attack.

Figure 2-40 and Table 2-14 present the comparisons between the simulation and experiment results for the deployed configuration. The results reveal a satisfactory consistent between the wind tunnel experimental test and numerical simulation. There is only a 2.37% difference in the linear section of curves. However, at the $C_{L_{max}}$, the angle of attack 14° of the experiment and 11° of the simulation are inconsistent with 3° offset. The simulation gives a reasonable prediction, but the experiment presents the unexpected change of the lift coefficient around the critical angle of attack. The reason for this is that results of the corrected wind tunnel experimental tests are still different from the results from the numerical simulation for the full scaled vehicle at a higher Reynolds number. On the other hand, the large difference between the simulation and experiment appears after the flow separation in both lift and drag curves. This illustrates that the inaccurate results of the simulation or experiment happen in a high

turbulent flow separation environment. In the next wind tunnel test on the full scaled model, the accuracy of the simulation will be investigated. In spite of the inconsistent at the critical angle of attack, the consistency on the linear section, especially the lift-to-drag ratio, still validate that the study on deployed and folded configurations is correct before the flow separation.

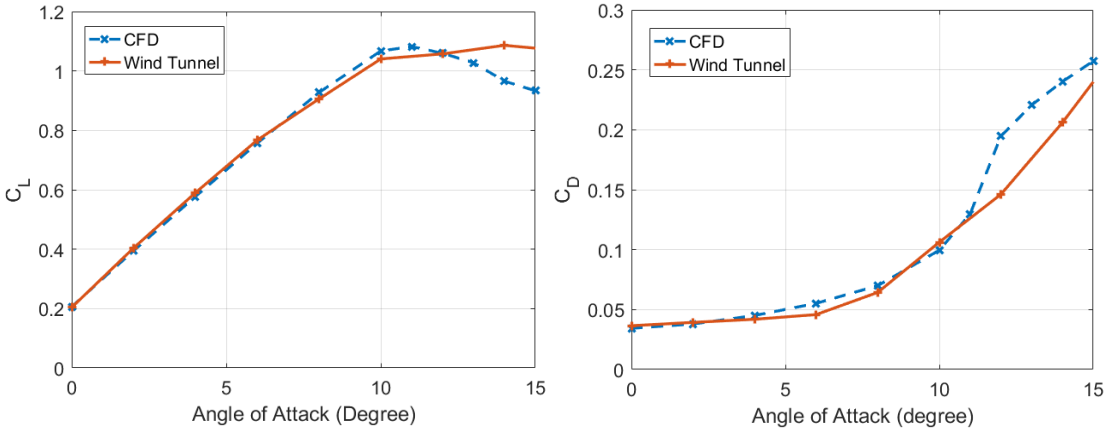

Figure 2-40: Comparison of aerodynamic coefficients between wind tunnel experiment test and simulation - Angle of attack versus lift coefficient (left), Angle of attack versus drag coefficient (right)

Table 2-14: Aerodynamic performance characteristics for the experiment of two configurations

	C_{L_α}	$C_{L_{max}}$ & α	α for C_{Lmax}	$(L/D)_{max}$	α for $(L/D)_{max}$	C_{D_0}
Deployed ($\Lambda = 0°$)	5.06 rad^{-1}	1.09	14.1°	16.7	6.0°	0.033
Folded ($\Lambda = 65°$)	2.49 rad^{-1}	–	–	11.6	7.8°	0.022

Table 2-14 presents the zero-lift drag coefficients of the deployed and folded configurations. They are obtained by acquiring the zero-lift angle of attack from the one-dimensional equation of the linear section of the lift curve, and then bringing zero-lift angle of attack into the polynomial expressing the drag curve. The result shows that 33% of the zero-lift drag is reduced from the deployed configuration to the folded configuration due to the decreasing of the frontal area. This favourable characteristic fulfils the design purpose that the vehicle can achieve a high efficient underwater cruise and have a relatively low impact load when the vehicle is diving into the water. In addition, the small drag of the folded configuration can also reduce the transition propulsion system load at the beginning stage of the water to air transition.

Chapter 3: Manufacturing and Wind Tunnel Experimental Testing

3.1 COMPOSITE MATERIAL SELECTION

A composite material is a combination of two or more materials. It has a wide range of applications in the aerospace industry. In this project, the Carbon Fibre Reinforced Polymer (CFRP), Glass Fibre Reinforced Polymer (GFRP), Kevlar Fibre Reinforced Polymer (KFRP), and foam core with carbon fibre sandwich structure are used. Figure 3-1 illustrates the material distribution on the whole vehicle.

The lightweight structure is critical for the BUUAS, since it needs to be launched from water, and its range and flight duration must be maximised. Indeed, the used of composites can reduce the overall UAV weight by 15-45% [68] and dramatically improve the flight performance. In addition, composites have properties such as excellent corrosion resistance, high strength, and high resistance to fatigue. Specifically, on corrosion resistance, this is a critical quality given that the BUUAS has frequent changes from water to air environments and vice-versa. Besides, the high resistance minimises the potential damage when the vehicle re-enters water. From the manufacturing point of view, composites can reduce the machining work, and complex shapes can be manufactured without fastening and without mechanical assembly processes [68].

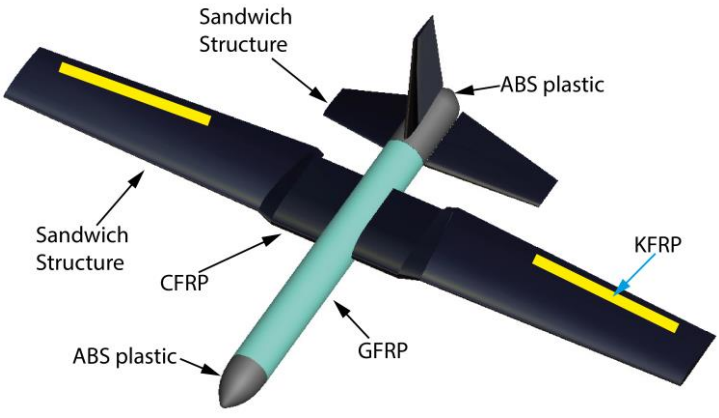

Figure 3-1: BUUAS materials distribution

The carbon fibre reinforced polymer (CFRP) is the primary material used in the construction of the airframes. Additionally, the sandwich structure is also made from the carbon fibre reinforced polymers. The CFRP has significant benefits including high stiffness, high

tensile strength, low weight, and high chemical resistance, which make the vehicle light and strong with improved structural performance. CFRP also has directional strength properties, which can be specified by arranging the layout method and proportion of the carbon fibre. Technically, the composite consists of two parts: a matrix and a reinforcement [69]. In general, CFRP composites use epoxy resin as the matrix to bond with carbon fibre reinforcement. The epoxy resin cures with the carbon fibre, which works as the primary structural component to provide the strength after heating or in room temperature.

A sandwich-structured composite is made by attaching two thin but stiff skins to a lightweight thick core. The core material is normally low strength material, but its higher thickness provides high bending stiffness for the sandwich composite with the overall low density. Inside the wing, the foam core with carbon fibre sandwich structure uses the CFRP as the stiff skin to attach the thick foam core. The foam core is made by the Styrofoam, which is extruded polystyrene foam with the light blue colour. Its density is only 50 kg/m^3, and the closed-cell structure produces its lightweight and waterproof property, which is a perfect filler for the wing structure. Regarding the fuselage, a GFRP tube typically used in rocket models is used as the main structure. The tube has 79.7 mm diameter with 1.65 mm thickness.

Kevlar® is used for the aileron's hinges and bonded with the epoxy resin to compose the rigid aileron sandwich structure. Kevlar® 49, generally used in aerospace applications, has a density of 1,440 kg/m^3, elastic modulus of 131 GPa, and strength of 3,800 MPa. The high tensile strength, high elastic modulus, high fracture toughness and low weight enable the Kevlar® 49 fibre to be the best candidate of aileron hinge. Furthermore, the KFRP possess the property similar to the CFRP. It can be the stiff skins for the aileron sandwich structure. The mechanical properties of the composites (fibre with the epoxy resin cured under 120°C) are shown in Table 3-1 [70]. Those values in the table will be used in the strength analysis on the structure and the weight estimation.

Table 3-1: Mechanical properties of CFRP and KFRP

	CFRP	KFRP
Young's Modulus (GPa)	70	30
Major Poisson's Ratio	0.10	0.20
Ult.Tensile Strength (MPa)	600	480
Ult.Compress Strength (MPa)	570	190
Ult.In-plane Shear Strength (MPa)	90	50
Density (kg/m^3)	1,600	1,400

3.2 STRUCTURE LAYOUT

3.2.1 Wing structure

The wing design for the BUUAS is fairly simple as it does not include components, such as oil or fuel tanks. The inside of the wing can fill with foams instead of the ribs to make the wing water resistant, since the common rib and spar structure will be filled with water if there is any leakage when the vehicle is submerged in water. Further, the water can increase the vehicle weight and damage the structure and electronic devices. Consequently, the wing adopts the sandwich structure as illustrated in Figure 3-2. It consists of two spars with foam cores covered by the carbon fibre skin. The main spar and the aft spar are designed as the C shape, which are the front and aft C spar respectively indicated in Figure 3-2. Comparing to other shapes, the C shape spar with foam cores provides a much simpler structure whereby the foam core is restrained inside the wing, front spar and aft spar. Moreover, the C spar has a wider flange, which is sufficient for a strong bonding area between the spar and the wing-deployment mechanism. The foam core is separated into five parts as described in Figure 3-2, the green and blue parts are the foam cores inside the wing and the aileron. The foam cores are cut by CNC router to the shapes that can fit the inside of the wing and the C spars.

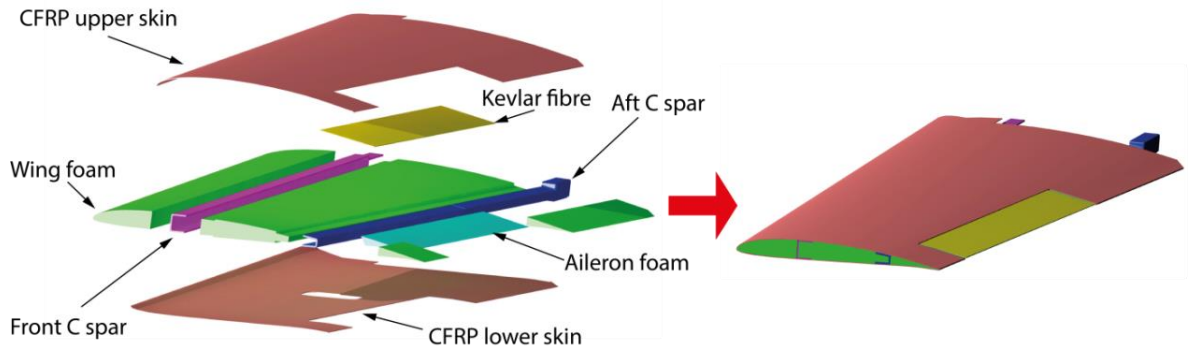

Figure 3-2: Structure arrangement inside the wing

3.2.2 Wing-deployment mechanism structure

The wing-deployment mechanism is mounted on the sleeve beam, which is a carry-through spar. The sleeve beam includes upper and lower parts as shown in Figure 3-3. Same as the beam box, the sleeve beam carries the load from the wing by the wing rotation shaft and transfers it to the fuselage. The sleeve beam design is similar to that of the I beam. The upper and lower sleeve beams resist most of the bending moment and twist with the lightweight and high efficiency composites. They are fixed together by the wing rotation shaft structure and six M4 bolts positioned near the fuselage. At both ends, the sleeve beam is fastened on the pads of the wing rotation shaft and shaft seat flange by M2 screws, and the rotating shaft and shaft seat

flange are assembled by a M4 screw. The upper and lower sleeve beams clamp the cylinder fuselage tightly through tightening M4 bolts near the fuselage. Accordingly, the disassembly can be done efficiently by releasing these bolts. This is convenient for the modification, assembly, and experimental test. The sleeve beam also provides the hinge, which is pivot 1, for mounting the linear actuator.

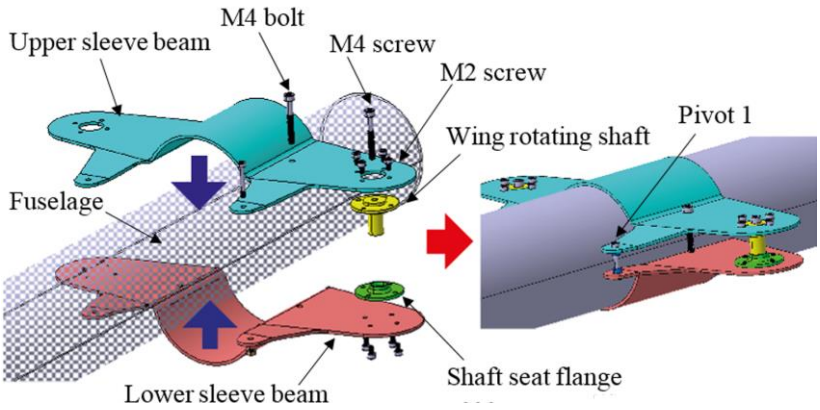

Figure 3-3: Sleeve beam assembly with the fuselage

The structure from the pivot 1 to the main part of sleeve beam is a trapezoid configuration (yellow dash lines) to resist the load from the linear actuator and compromise the shape of the fairing as illustrated in Figure 3-4. The angle of the side of the trapezoid with the horizontal line is 7.8 degrees. Additionally, the linear actuator is slightly rotated according to the pivot 1 while working. A fairing is introduced to reduce the drag and protect the wing-deployment mechanism shown in Figure 3-4. It is designed into the shape that can fit with the wing and fuselage under any sweep angle. The fairing is fixed on the sleeve beam by an M4 screw.

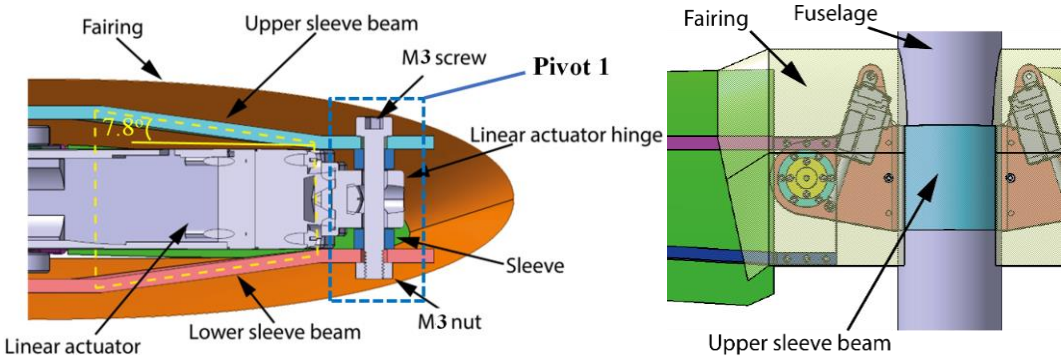

Figure 3-4: Cross-section of the linear actuator mounting on sleeve beam

The details of the structure around the mechanism, especially the wing rotation shaft and pivot area are shown in Figure 3-5. A flange sleeve, which is used for containing the interference fitted 6700 bearing for rotation, is fastened between two carbon fibre plates by screws. The 6700 bearing is lightweight and can provide sufficient strength for the wing

rotation. In addition, the plates also clamp the outer ring of bearings to fix them in the axis direction.

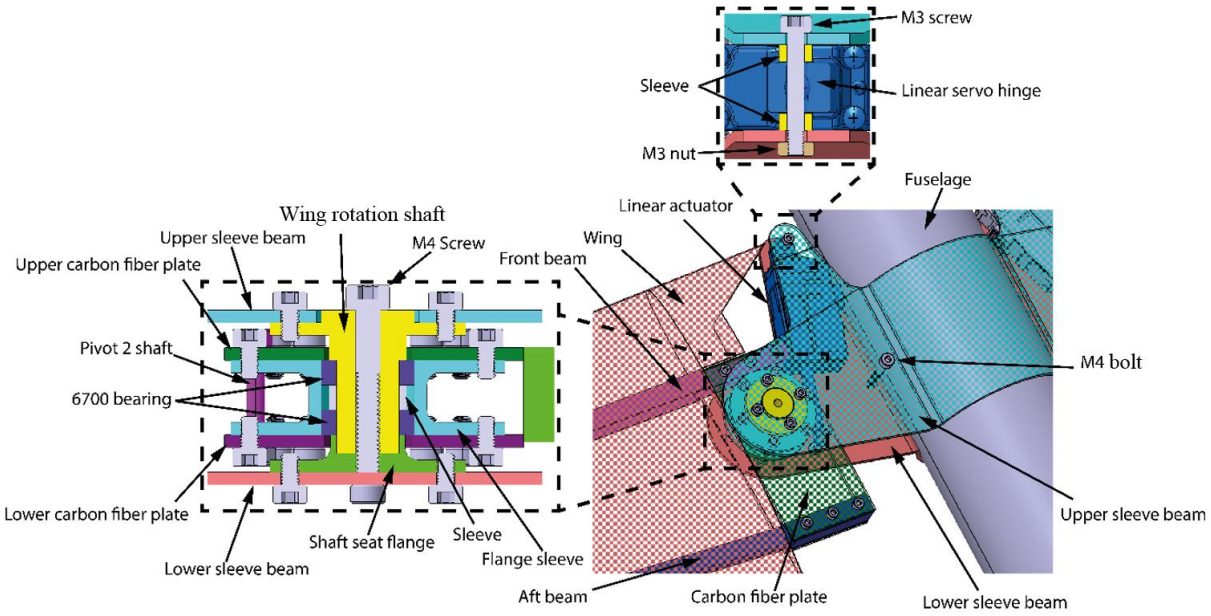

Figure 3-5: Linear mechanism structure 3D model

3.2.3 Aileron structure

A Kevlar® fibre strip is used as the hinge connecting to the aileron and wing, since the thickness of the aileron leading edge is only around 5 mm which provides limited space for the installation of a traditional hinge. As demonstrated in Figure 3-6, the placement of the Kevlar® fibre strip is divided into the two KFRP sections and the one hinge section in the middle. The hinge section is the 2 mm pure Kevlar® fibre without epoxy resin to maintain its flexibility to operate like the rotating shaft hinge for the aileron movement. On the aileron, the Kevlar® fibre bonds with the epoxy resin to compose the KFRP providing the reinforcement for the aileron structure. On the wing attachment section, the KFRP is clamped tightly in the middle by wing skin and aft C spar through resin epoxy as illustrated in Figure 3-6.

The 3D printed aileron arm is mounted on the aileron, so that the servo can drive the aileron to rotate around Kevlar® fibre hinge through the linkage, which connects the servo arm and aileron arm. Due to the thin profile of the airfoil, a low-profile servo is used. Because, the servo needs to be covered in the wing to keep the aerodynamic shape. The details of the servo are presented in Table 3-2.

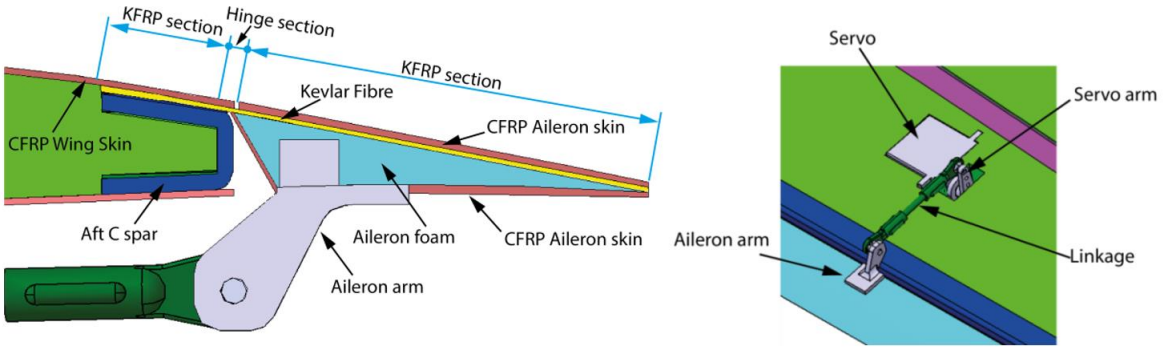

Figure 3-6: Kevlar® placement and Structure of aileron control

3.2.4 Aft fuselage structure

The aft fuselage structure is built based on the function of tail control and propulsion system mounting. The structure of the tail control is illustrated in Figure 3-7. Specifically, the structure of the tail is the sandwich structure made from the foam core covered by the carbon fibre. An 8 mm diameter carbon fibre tube is used as the tail spar. It is fixed with the rotation horn by M2 bolts. Then, the sleeve of the rotation horn is fitted into the 6700 bearing, which is mounted on the fuselage. A servo is mounted on the fuselage inner wall to deflect the tail through the linkage. This structure keeps all the electronic components inside. The only leakage may happen in the hole for the tail spar on the fuselage. To solve this, the waterproof bearing is chosen. In addition, the rotation horn, tail spar and bearing are assembled with an interference fit. In the front view of the fuselage structure, the red circle is the reserved space for the transition propulsion system. To avoid any interference, the whole tail control structure is designed in a low profile, and the servo with low profile is selected. The specification of the tail control servo is presented in Table 3-2.

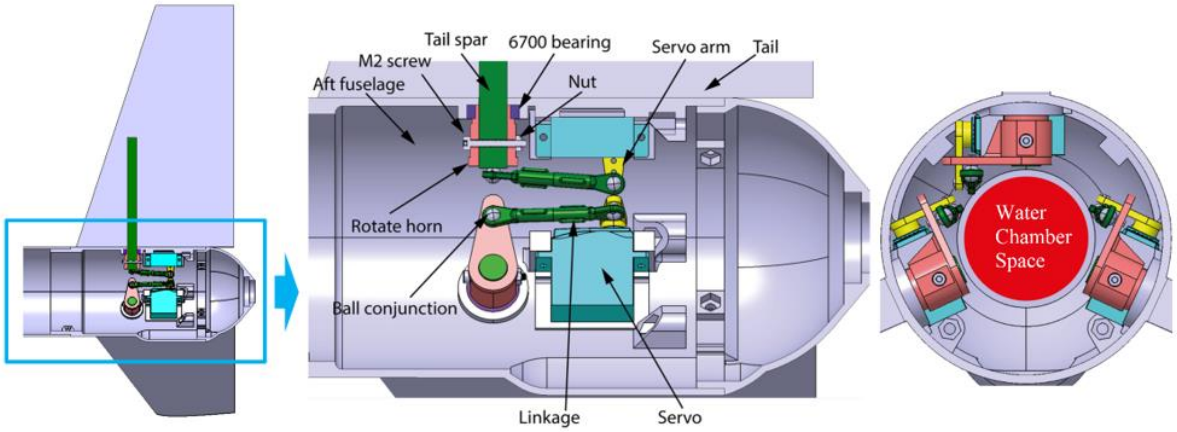

Figure 3-7: Structure of tail control

Table 3-2: Specifications of servos

Specification	Aileron servo	Tail servo
--		
Model	Corona 919MG	Spektrum A3030
Dimension	22.5×11.5×24.6 mm	23.6×11.5×25.5 mm
Torque	1.5 kg·cm	1.66 kg·cm
Weight	12.5 g	8.6 g
Operating Speed	0.07 sec / 60º	0.12 sec / 60º

3.3 MAIN LOAD BEARING STRUCTURE

3.3.1 Front C spar strength analysis

Since the first vehicle prototype will be used in the laboratory and wind tunnel experimental tests, it is designed to be fairly stiff. Before the estimation of the spar thickness, the assumption is made that the total load acting on the vehicle is carried by the front C spar, which is the main spar. For the C spar, the flanges of the spar resist most of the bending moment while the web is to resist the main shear force, and connect the flanges. Moreover, the spar is regarded as a cantilever beam, and the load L is applied on the free end of the beam.

The width and height of the spar are tapered from the root to the tip along the taper of the wing, since the outside surface of the spar is bonded to the skin inner surface, and the required strength is varied along the wing span. To evaluate the strength, the cross section of the spar is depicted in Figure 3-8. The height and width of the root are $h_r = 12\ mm$, $w_r = 10\ mm$, and the height and width of the tip are $h_t = 11.75\ mm$, $w_t = 10\ mm$. The spar is made by CFRP, which can be built into the desired shape with the moulds. This stress analysis for the spar also gives the indication the layup of the carbon fibre.

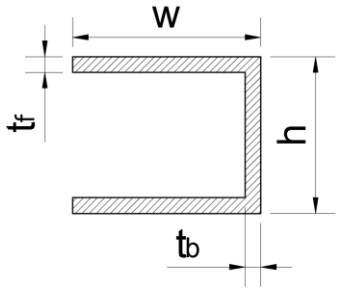

Figure 3-8: Cross-section of the C-spar

The total load acting on the vehicle can be obtained by Eq. (38),

$$L_w = \frac{1}{2} n_w W \tag{38}$$

Thus, the moment along the spar is:

$$M(z) = -L_w(l - z) \tag{39}$$

where l is the length of the spar inside the wing, which is from the wing tip to the wing root $l = 607\ mm$. Then, the second moment of area is calculated for the flanges and the web.

The second inertial of the area of the flanges is:

$$I_{x,f} = 2\left(\frac{w t_f^3}{12} + \left(\frac{h_{cspar} - t_f}{2}\right)^2 w t_f\right) \tag{40}$$

The second inertial of the area of the web is given by:

$$I_{x,b} = 2\frac{t_b {h_{cspar}}^3}{12} \tag{41}$$

$$I_{x,total} = I_{x,b} + I_{x,f} \tag{42}$$

The equation of the stress is given by,

$$\sigma = \frac{M}{I_{x,total}} y_c \tag{43}$$

where y_c is measured from the neutral surface. The maximum stress will be at where the y_c is the maximum. In this case, the maximum y_c is the half height of the section.

The whole spar is also tapered in the thickness to provide sufficient strength in a minimum weight. This is achieved by reducing the layers of carbon fibre. Each layer of the carbon fibre mixing with the epoxy resin has an average thickness of $0.250\ mm$. The reduction of the thickness of the spar is in six sections as explained in Figure 3-9, and then the stress is verified in a different section. The results are presented in Table 3-3.

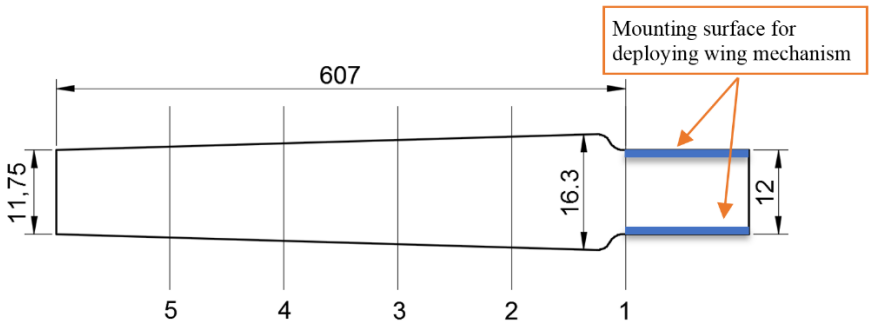

Figure 3-9: Plane view of the sections distribution

Table 3-3: Stress changing with sections

Cross Section	Height (mm)	Flange Thickness t_f (mm)	Web Thickness t_b(mm)	σ (MPa)
1	12	1.5	1	164.48
2	15.39	1.25	0.75	111.29
3	14.48	1	0.5	112.16
4	13.57	0.75	0.5	100.74
5	12.66	0.5	0.5	74.58

The result demonstrates that the spar with tapered thickness can provide sufficient strength under less structure weight. The maximum stress 164.48 MPa is at the root of the spar near the mounting surface. This area can be specially reinforced by the additional carbon fibre. For the sake of safety, the tip area of the spar keeps 2 layers of carbon fibre. The safety factor of the main C spar is obtained by Eq. (44),

$$n_c = \frac{\sigma_c}{\sigma} \tag{44}$$

where σ_c is the compress strength of the carbon fibre, $\sigma_c = 570\ Mpa$. The safety factor is,

$$n_c = 3.48$$

3.3.2 Sleeve beam strength analysis

The sleeve beam is attached on the fuselage and transfers the twist and bending moment. A long sleeve along the fuselage direction is preferred, since it is more stable. In addition, the long sleeve can have a thin thickness with an equivalent strength, which can reduce the form drag. On the other hand, an excessively long sleeve will increase the difficulty to integrity with the fuselage and wing. Accordingly, the final length of the sleeve beam is settled on 80 mm.

The sleeve beam carries the total load from the wing. Its root area, which is close to the fuselage, has the maximum bending moments and more failure risk. Then, the strength analysis is mainly focused on the root area. The cross section of the root area is depicted in Figure 3-10.

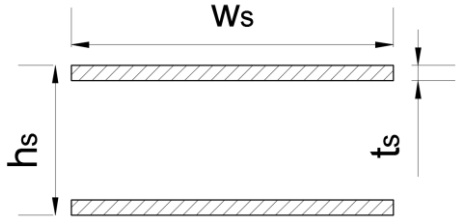

Figure 3-10: Cross-section of the sleeve beam

The second inertial of the area of the beam is given by:

$$I_{x,s} = 2\left(\frac{w_s t_s^3}{12} + \left(\frac{h_s - t_s}{2}\right)^2 w_s t_s\right) \tag{45}$$

where t_s is the sleeve beam thickness. Since the sleeve beam is made out of 4 carbon fibre layers, the total thickness is 1 mm. The width is $W_s = 80\,mm$, and the height of the sleeve beam is $h_s = 28\,mm$

The moment is the value of the moment arm times the lift, and the lift is the same value at the spar strength analysis $L_s = L_w$,

$$M_s = -L_s l_s \tag{46}$$

where $l_s = 703\,mm$ is the length from the wing tip to the sleeve beam root.

The max stress on the beam is,

$$\sigma_s = \frac{M_s}{I_{x,s}} y \tag{47}$$

$$\sigma_s = 17.36\,Mpa$$

The max stress is far below the compress strength of the carbon fibre. However, the thickness of the sleeve beam is kept as 1 mm to avoid the squashing caused by the tightened screws on the attachment of sleeve beam. In addition, continuing to reduce the ply number of the carbon fibre will reduce a large fraction of strength due to the small ply number.

3.3.3 Finite element analysis

Finite element analysis (FEA) is conducted in the commercial software Abaqus® to verify the design of the sleeve beam with the screw connections, which is complex to analyse in the analytical model. In order to reduce the simulation time and complexity, the analysis is established on the half of the symmetrical sleeve beam. The structure for supporting the linear

actuator is removed in this section, since it has limited effect on the main spar strength. The main loading for the sleeve beam is the bending moments and the lift from the wing.

The simplified 3D model for analysis is established in CATIA®. The rigid wing rotation shaft and three connection bolts are simplified into cylinders. In the FEA model, six parts are established. They are three bolts, lower sleeve beam, upper sleeve beam and shaft. There are two kinds of materials used in this analysis. One is the aluminium for the shaft and screws; another is the CFRP for the upper and lower sleeve beam. The properties of materials are presented in Table 3-4. Especially, the type of elastic and plastic is isotropic for both materials.

Table 3-4: Materials property of the sleeve beam structure

Material	Density	Young's Modulus	Poisson's Ratio	Yield Stress
Aluminium	2,700 kg/m^3	70 GPa	0.35	310 MPa
CFRP	1,600 kg/m^3	70 GPa	0.1	570 MPa

In the model, the parts are assembled together by constraining with thin pads, which are used for locating and providing constraint between parts. Thin pads only have 0.01 mm thickness to minimize their effect on the simulation as indicated in red circles in Figure 3-11.

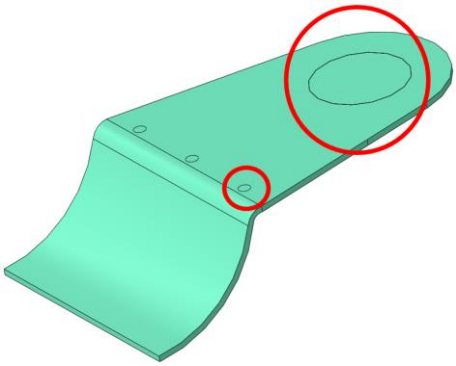

Figure 3-11: Simplified sleeve beam 3D model with thin pads

Boundary conditions

The fuselage contact surface and symmetrical plane are set as a type of encastre as shown in Figure 3-12, since the inner surface of the beam is strongly clamped on the fuselage under the bolt connection, and there is no movement at the contact surface between the fuselage and sleeve beam. Two types of load are assigned to the model as presented in Figure 3-13. One is the pressure, which is the lift; another is the bending moments. Since the load is transferred to the sleeve beam through the wing rotation shaft, the pressure is assigned to the bottom of the shaft cylinder and the bending moments is assigned to the middle of the cylinder.

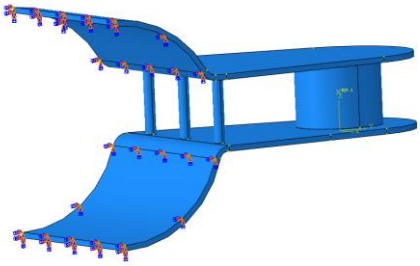

Figure 3-12: Sleeve beam boundary conditions

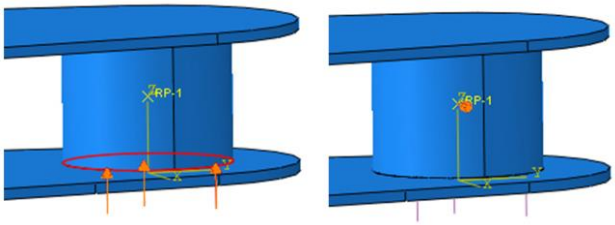

Figure 3-13: Boundary conditions on the wing rotation shaft pressure (left) and moments (right)

Results

The stress on the sleeve beam and the deformation with a scale-up factor of 314.491 are displayed in Figure 3-14 and 3-15. The maximum stress 57.19 MPa occurs at the corner between the sleeve area and plane plate area on the sleeve beam. This value is smaller than the yield stress, which confirms the sufficient strength. Furthermore, the assembly of the three bolts has no detrimental effect on the strength of the sleeve beam. Nevertheless, there is stress concentration at the inner contact area between the wing rotation shaft and the sleeve beam. In the manufacturing process, this area will be reinforced by laying the additional carbon fibre material. In conclusion, the finite element analysis substantiates the strengths of the sleeve beam and conjunction area are sufficient for the vehicle.

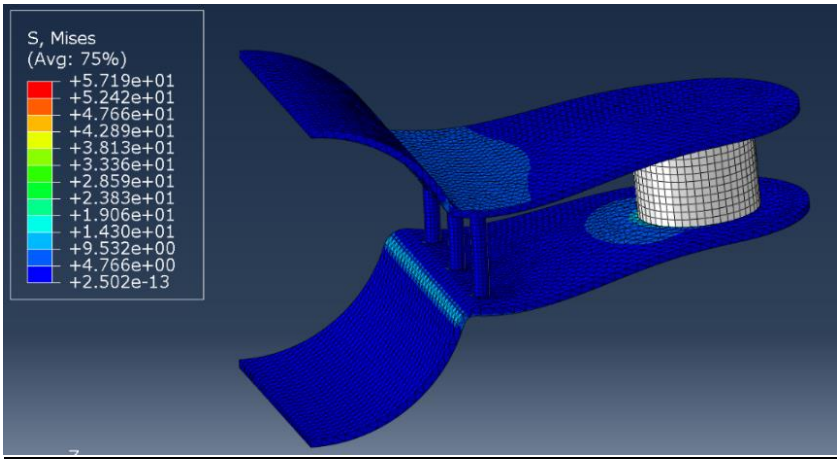

Figure 3-14: Stress distribution and deformation of the sleeve beam (top view)

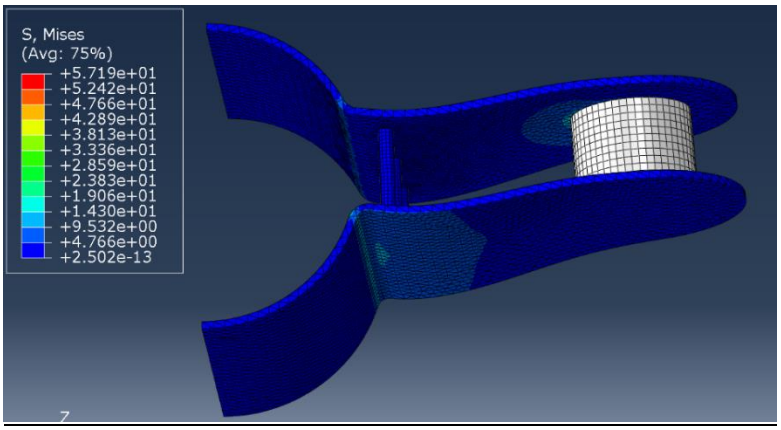

Figure 3-15: Stress distribution and deformation of the sleeve beam (bottom view)

3.4 MOULDS BUILDING

The manufacturing process is carried out to transform the raw material into the final vehicle after the completion of the design and material specification. The vehicle is adopted different manufacturing technics in different areas. For the most aerodynamic surface, the composite material is used. It has the lightweight and high strength. And for the structures and mechanisms, the 3D printing technology is used. It has a rapid manufacturing advantage and is not limited by the part shape. Some load-carrying parts such as shafts are made of aluminium by the machining process. To start with, moulds are made to form the composite parts.

3.4.1 Moulds design

In order to acquire the designed shape and fine aerodynamic surface, moulds were built for manufacturing the wing, faring and tail which are made of the plain weave carbon fibre. The mould design principle is to acquire fine surface quality and release the finished parts easily. The selected mould material is the high-density blue foam. It is beneficial for prototype manufacturing, since it is more economical and has less pores compared with other foams. After the design in CATIA®, all the moulds were cut by the CNC router machine. Table 3-5 displays all twelve moulds for the right side of the vehicle.

The female moulds, which can produce the high outside surface quality, are built for the front and aft C spars, since the outside surfaces of the front and aft C spars need to attach with the wing inner surface. Further, the front C spar mould is divided into two parts as displayed in Table 3-5. Because the front C spar has the trapezoid section shape, it cannot be taken out after curing in a single female mould. These two parts of the front C spar mould are assembled by the pins and bolts to ensure the accuracy. After the curing, the front C spar can be released by separating the mould. Moreover, the upper and lower wing skins are fabricated separately. Then, they are assembled by the epoxy resin with components inside. The assembly illustration

has been explained in Figure 3-2 in section 3.2.1. The same technique is also used for the fabrication of fairings and ailerons.

Table 3-5: Moulds building

Front spar mould right	Front spar mould left
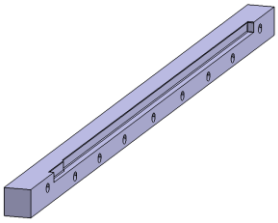	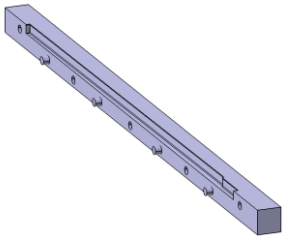
Lower wing mould	**Upper wing mould**
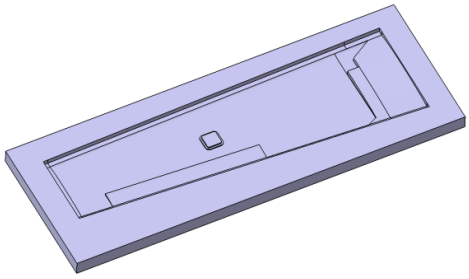	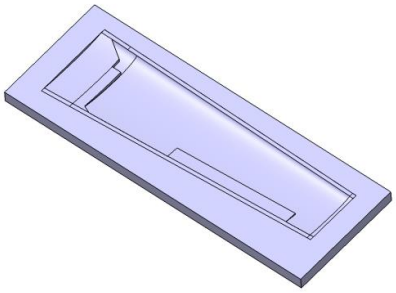
Lower fairing mould	**Upper fairing mould**
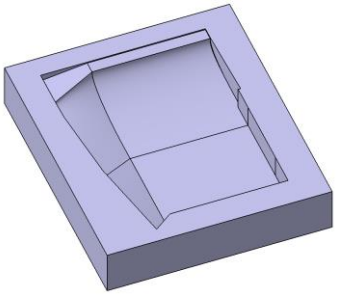	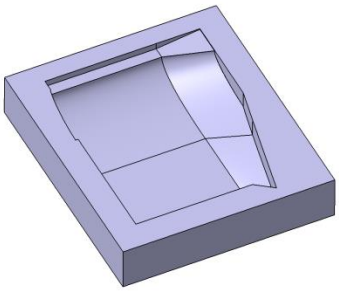
Sleeve beam upper	**Sleeve beam lower**
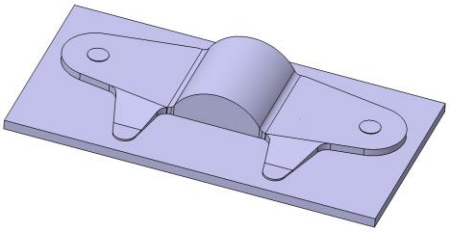	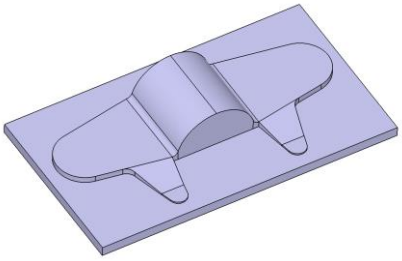
Aileron upper mould	**Aileron lower mould**
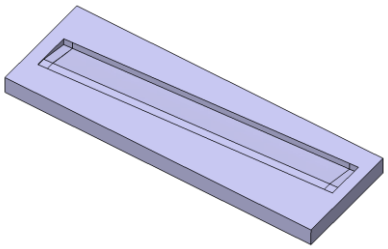	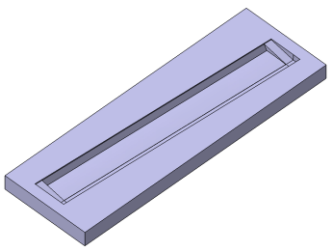
Servo hatch mould	**Aft spar mould**

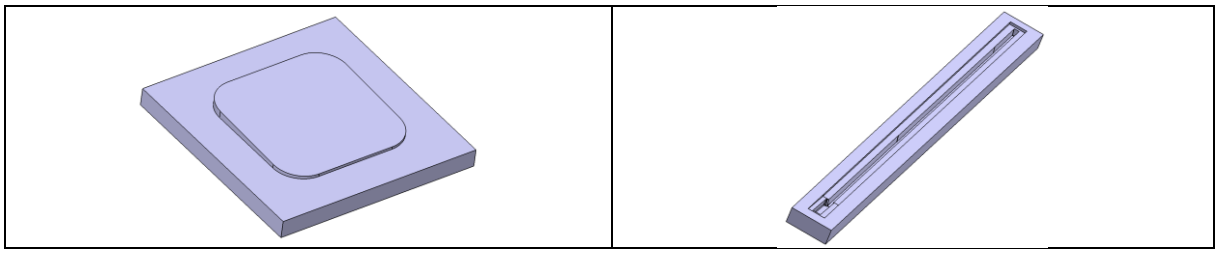

3.4.2 Moulds polish and refine

After being cut by the CNC router machine, the mould is finished with a rough surface, which is not favourable for the layup. The composite materials can stick on the rough surface during curing and will be hard to release. In order to solve this problem, the moulds were polished by sandpaper. Defects on the mould were filled by the lightweight filler mixed with epoxy resin, and then sanded until smooth. Afterwards, the liquid polyvinyl chloride (PVC) was applied on the surface to fill the reminded tiny pits. The PVC is a coating, and it will leave a layer of thin film after the liquid PVC dries. The PVC film has a smooth surface, which avoids the plies sticking to the mould. Subsequently, the mould with PVC film would continue to be polished to remove the small bubbles on the film and coarse area, and then a new layer of the PVC film would be applied. This process was repeated several times until a desired smooth and exact surface was achieved. The moulds before and after processing are presented in Figure 3-16.

Figure 3-16: Wing moulds before (left) and after (right) applying PVC material

For spar moulds, the above process is difficult to operate in their narrow inner space. However, the inside of spar moulds is the flat surface mostly. Therefore, the release film, which can also avoid laminate sticking, was attached on the inner surface by its adhesive side. The release film was cut into the shape that could fit corners so that the laminate could grab the shape details. Outside of the mould layup area was covered by the blue release tape to prevent sticking. The processed spar moulds are presented in Figure 3-17.

Figure 3-17: The spar mound after applying release tape

3.5 LAYUP AND VACUUM BAGGING

The main materials used for layup were the plain weave carbon fibre plies and epoxy resin. In particular, the WEST SYSTEM® 105 Resin was used. This epoxy resin is specifically designed to bond with reinforcing fabrics. It was used with the WEST SYSTEM® 206 slow hardeners. The mix ratio was one part of hardener to five parts resins by volume and weight. Table 3-6 presents the uncured properties and cure characteristics of the epoxy resin.

Table 3-6: The uncured properties and cure characteristics

Epoxy resin with 206 slow hardener	
Physical State	Clear pale yellow liquid
Pot life -100g @ 25ºC (in air)	20 minutes
Thin laminate cure time @ 25ºC	17 hours

Before the layup, the carbon fibre plies were prepared. Firstly, the carbon fibre cloth was placed in the plastic bag. The plastic bag had the sketch and ply number. The sketch was used as a guide for cutting the cloth to the required shape, and the ply number was used to identify the sequence during the layup. Then, the mixed epoxy resin was poured on the cloth. After that, a spatula was used to smear the epoxy resin evenly on the cloth and squeeze the redundant epoxy resin out of the bag. By doing this, the carbon fibre inside the plastic bag is the same as the prepreg carbon fibre. It has the proper amount of the epoxy resin. Then, the carbon fibre cloth with epoxy resin was cut by following the sketch. Finally, the prepared carbon fibre was taken out of cover and placed on the mould according to the sequence of the number.

The vacuum was conducted, after the layup of the laminate and vacuum bagging materials. The layup process of vacuum bagging materials was adopted the well-known technique, and technical details are presented in Appendix C. The vacuum provided the pressure that pressed the part on the mould to grab the shape and squeeze out the excess resin. Each vacuum and cure took 17 hours in room temperature. Figures 3-18 shows part of the components being vacuumed.

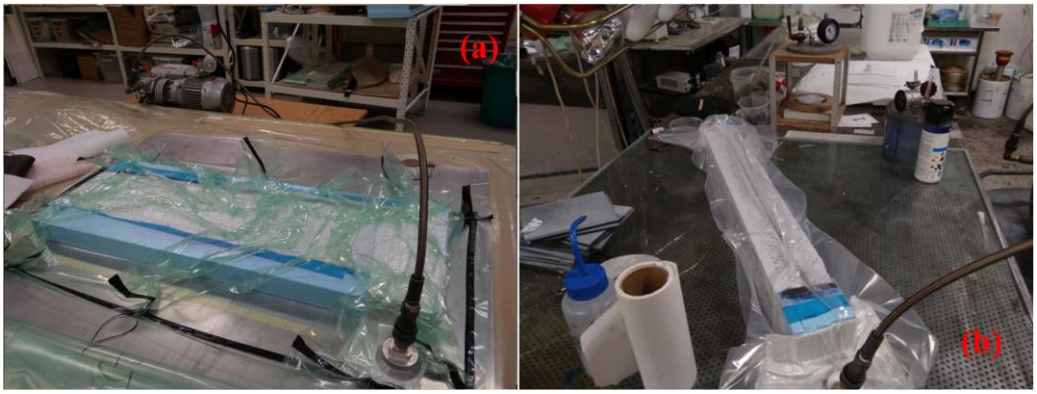

Figure 3-18: Upper wing skin (a) and C-spar (b) in vacuum

3.6 PROCESS AND ASSEMBLY

The parts were taken out from the moulds and cleaned by the angle grinder after the vacuum was completed. Figure 3-19 shows a couple of finished parts. The outcome shows that the smooth outside surface with details was acquired, and the general quality was satisfactory. However, there were also some defects such as the uneven surface and small bubbles. This was caused by the excessively sharp corners on the mould. Those defects were fixed by patching up with carbon fibre and filling the filler.

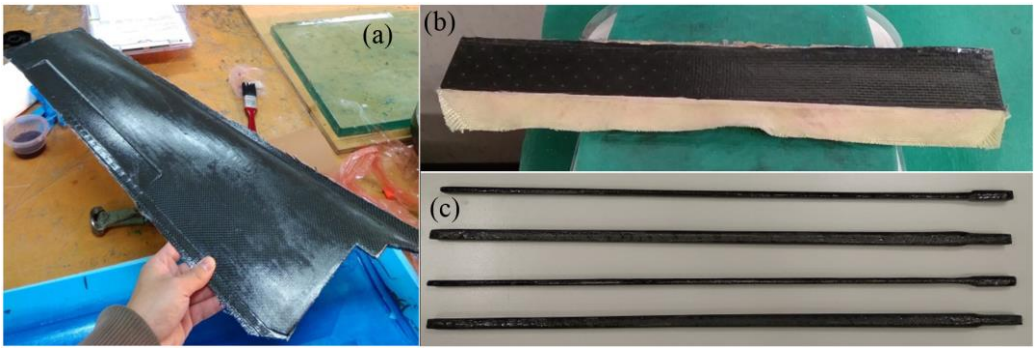

Figure 3-19: Upper wing skin (a), Aileron (b), and C-spars (c) after vacuum

The completed parts were processed for assembly. Especially, the aileron with Kevlar® hinge displayed in Figure 3-19 (b) was assembled before the wing assembly. Additionally, after the lower skin was polished, a hatch was installed on it for accessing the servo. The hatch consists of a door made from carbon fibre and a groove on the lower skin. Specifically, the door with a piece of rubber adhered on its inside surface is fastened on the groove by screws. Therefore, the rubber tightly attaches on the groove to seal the hatch effectively. The nuts for the screws were fixed on the lower skin around the groove before assembly. In addition, a tunnel on the foam core for the cable and servo was cut out and it was covered by a strip of release tape to prevent the epoxy resin immersing inside during assembly.

After the process above, the wing components as shown in Figure 3-20 were assembled. A positioning mould (green part in Figure 3-20) was used to locate the two spars. During the assembly, the epoxy resin was brushed on the contact surface between components. Then, the upper wing skin and lower wing skin were closed together. The overall assembly was put into the vacuum bag to be vacuumed in order to remove the excess resin and provide the pressure to tight the upper and lower wing skins together.

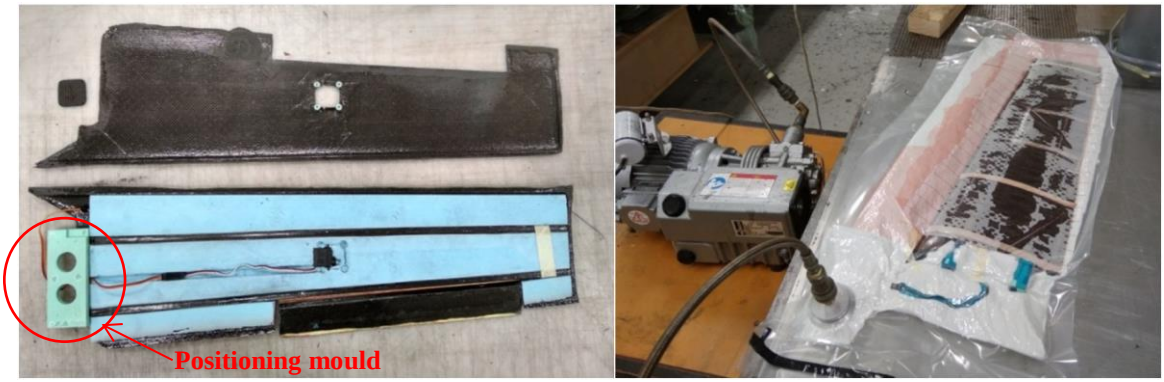

Figure 3-20: Wing components before assembly (left), Wing final vacuum (right)

The wing was sanded and polished after curing to remove burrs and smooth the surface. The finished two side wings with the wing rotation structure are displayed in Figure 3-21. As a result, the surface finish is very smooth. Besides, the aileron works very good with the Kevlar® hinge. The weight of the left semi-wing is 330.2 g, and the right semi-wing is 337.2 g. The after fabricated weight increased by 4.28% compared to the predicted weight of 640 g. The reason of the increased weight is that the applied epoxy resin filled the cavities inside the assembled wing during the vacuum bag curing. In conclusion, the overall wing assembly with a tiny weight increase and good surface and structure quality is satisfactory to general design requirement.

Figure 3-21: Wings after polishing

3.7 TAIL AND FAIRING

The manufacturing of the tail and fairing is easier than the wing due to their simple structure. The foam core of the tail was cut by the CNC router machine. It was then covered by prepared carbon fibre and vacuum bag cured. After curing, it was polished to achieve a smooth surface as shown in Figure 3-22. A hole for installing the tail spar was drilled on the finalized tail, and then the tail spar was inserted into the hole and fixed with the epoxy resin. Finally, the after fabricated weight of one single tail is only 42.4 g.

The technic for building the fairing is similar as wing skin. The faring was also separated into upper and lower two parts to construct, and then they were assembled together. The difference is the upper and lower parts of the fairing were conjunct in the leading edge by covering the carbon fibre cloth with epoxy resin. A positioning mould (the green part in Figure 3-22) was built to locate the distance between the upper and lower parts.

Figure 3-22: Fairing (left) and tail (right) after vacuum and polishing

3.8 3D PRINTING TECHNOLOGY

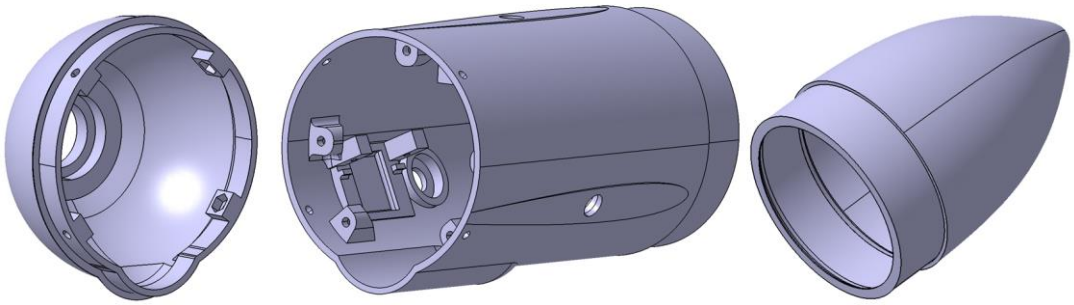

Figure 3-23: Tail cone, Aft structure, Nose (from left to right)

The 3D printing technology, which is additive manufacturing, is mainly used in fabricating parts of the structure and the mechanism. Figure 3-23 shows the 3D printed components of the fuselage structure. From the left to the right, they are the tail cone, aft fuselage, and nose. The inner structure of the aft fuselage is complicated. Because it has plenty of mounts for installing components such as servos and bearings, and it also has the support

structure used for integrating with the main fuselage and tail cone. This complex geometry is difficult to be achieved by the composite material or machining techniques. However, the 3D printing technology, which is not limited by the part geometry, can easily build this type of structure. Additionally, the additive manufacturing has the advantage of short operation time in producing complicated parts compared to traditional manufacturing methods, which is beneficial for the prototype building. Further, it can be used as rapid verification for the fit and tolerance between mechanisms and structures.

In this project, the fused deposition modelling (FDM) technology is used for 3D printing. The printing material is the ABS plastic filament. Its density is 1.05 g/cm^3 and it has the properties of high strength, impact resistance, toughness, moisture resistant, and high strength to weight ratio [71]. It is a favourable material for the complicated structures on the vehicle.

3.9 VEHICLE ASSEMBLY

The airframe of the vehicle was assembled after the manufacturing. Figure 3-24 shows the assembled vehicle in both deployed and folded configurations. The whole surface is covered by the lightweight vinyl. It smooths the surface, and the grey colour makes the vehicle easy to be observed in the black wind tunnel. Without the propulsion and avionics system, the total weight of the airframe is 2141.4 g. There is a minor increase in weight of 89.4 g compared to the initial design estimated weight. The weight increase is mainly attributed to the manufacturing process.

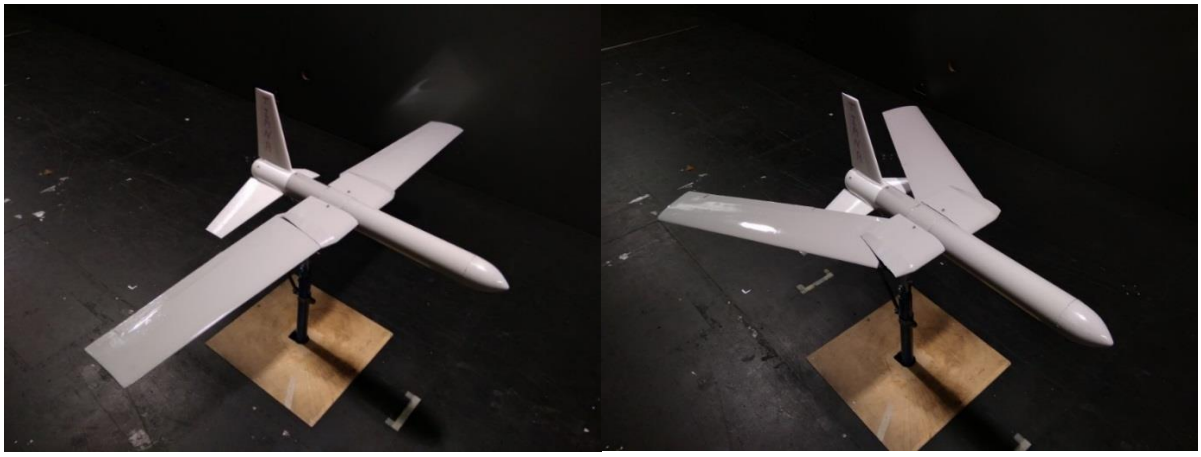

Figure 3-24: The experimental prototype deployed configuration (left), folded configuration (right)

3.10 WIND TUNNEL EXPERIMENTAL TEST SET-UP

The wind tunnel experimental test was performed on the full-scaled vehicle after the manufacturing. It was used to verify the pervious numerical simulation, and validate the flap

function, vehicle structure strength and wing-deployment mechanism. This wind tunnel experimental test also acquired the measurement from different sweep angles. Further, the coefficient and derivatives obtained from the experimental test were employed in the stability analysis and transition model building.

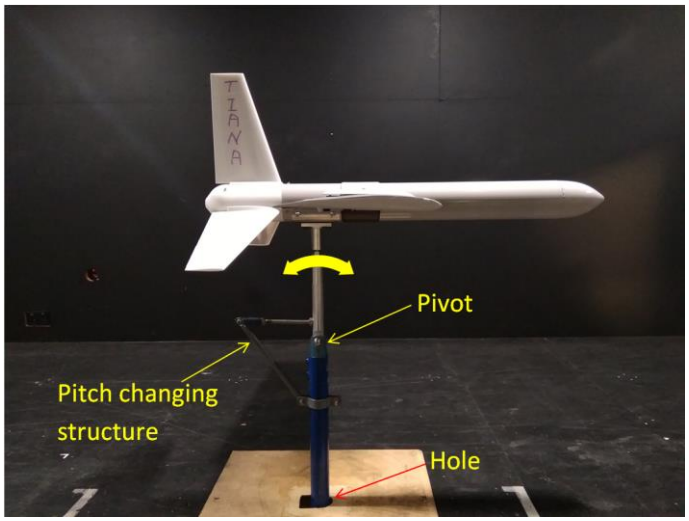

Figure 3-25: Wind tunnel experiment test set-up

Same as the previous test, the RMIT industrial wind tunnel and JR3 400N load cell were used for testing. The set-up is presented in Figure 3-25. The sting was modified to hold the full-scaled vehicle inside the tunnel. Specifically, the vehicle was fixed on the top of the sting while the bottom of the sting was fixed on the load cell under the wind tunnel floor. As illustrated in Figure 3-26, the load cell was mounted on a steel plate, which was placed on the basement and fixed rigidly by the clamps. The pitch angle could be adjusted through a hinge and a triangular rod supporting structure on the sting above the wind tunnel floor. Besides, the yaw angle was set on the basement under the floor by aligning the sting with the protractor.

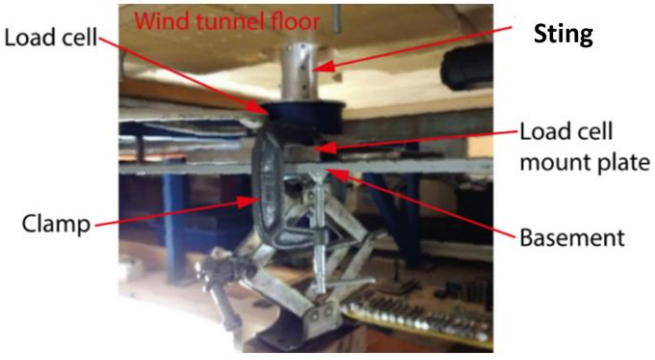

Figure 3-26: The load cell installed under the floor of the wind tunnel

Figure 3-27 reveals the details of the connection between the sting and vehicle. An aluminium cylinder was slid into the fuselage, and then the fuselage was clamped in the middle tightly by the cylinder, curved plate and flange mount, which were fastened by the screws. The

above structure was supported by a 12 mm diameter steel spar, which was slid into the flange mount and fastened by three M4 thrust screws. In this way, the vehicle was rigidly connected with the sting without any inaccuracy caused by the movement between connections.

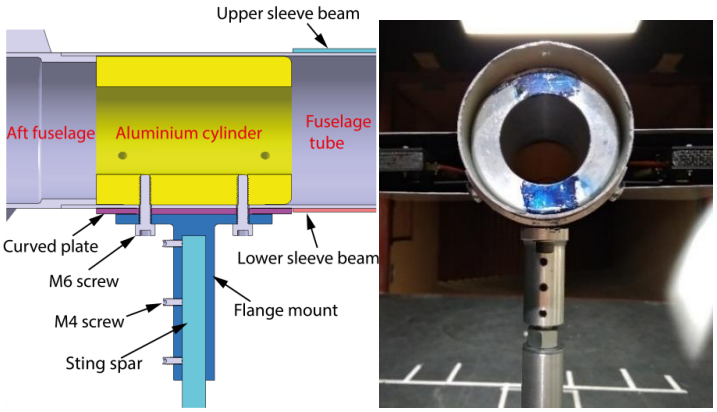

Figure 3-27: Structure of the sting and vehicle connection

Eight different sweep angles as shown in Figure 3-28 were tested. The tested pitch angle for each configuration is 0° to 12° with 2° increments, and the yaw angle is from 0° to 15° with 3° increments. The test wind velocities are 10 m/s, 15 m/s, 20 m/s, and 25 m/s. Particularly, the function of the flap, which works as aileron during the flight, is investigated to evaluate its contribution in the water to air transition. In this case, the flap deflect angle is 15°.

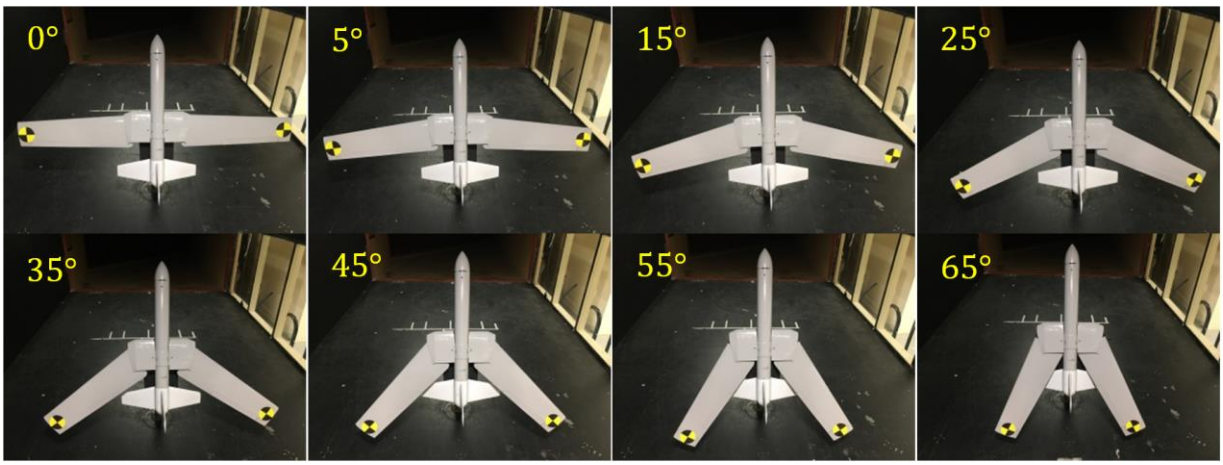

Figure 3-28: Configurations with different deployed angles

3.11 WIND TUNNEL EXPERIMENTAL TEST RESULT

Below 20 m/s, the aerodynamic performance results are displayed in Figure 3-29 to 3-31. The lift and drag coefficients for various angles of attack were extracted from the numerical simulation and compared with the wind tunnel experimental test measurements. The result shows that the consistent in stall angle of 11° between the numerical simulation and the wind tunnel experimental test. Besides, the lift and drag coefficients obtained from those two

methods indicate similar trends, but there is a systematic error of about 0.1 in the $C_L - \alpha$ curve. The discrepancy of the curves can be caused by the wind tunnel walls interference effects and the mismatch between the CFD turbulent model for predicting the flow separation and high turbulence in the industrial wind tunnel. In addition, inaccuracies in manually setting of the angle of attack in the wind tunnel can also produce the discrepancy.

The variations of the L/D versus angle of attack from the numerical simulation and wind tunnel experimental test are presented in Figure 3-31. The optimum flight conditions of two methods are consistent at 6 degrees angle of attack, but there is 6.411% offset of L/D between wind tunnel test and numerical simulation. In the more realistic wind tunnel test, the L/D is smaller. The reason for this is same as the offset between the lift coefficient curves, but the consistent trend of two curves in Figure 3-29 to 3-31 confirms the valuable prediction from the numerical simulation.

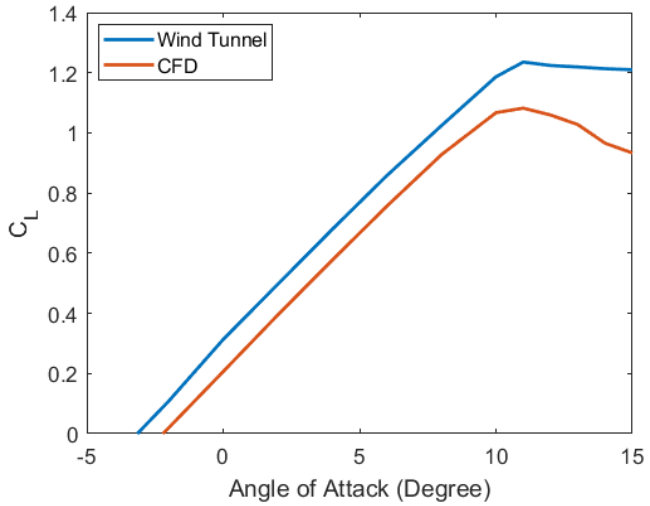

Figure 3-29: Lift coefficients – wind tunnel test and numerical simulations comparisons

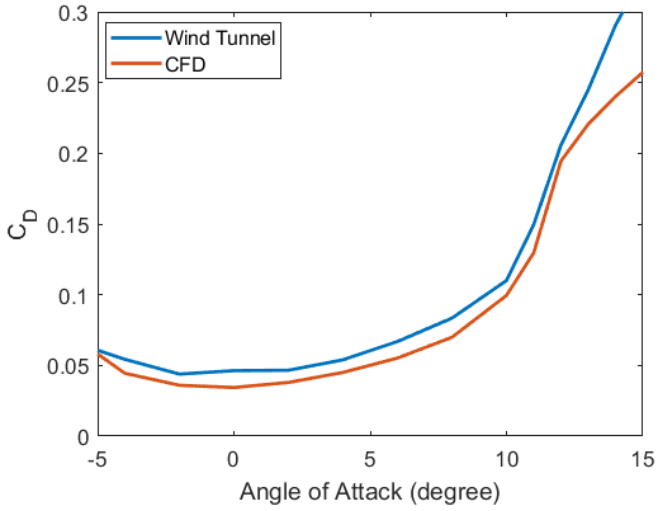

Figure 3-30: Drag coefficients – wind tunnel test and numerical simulations comparisons

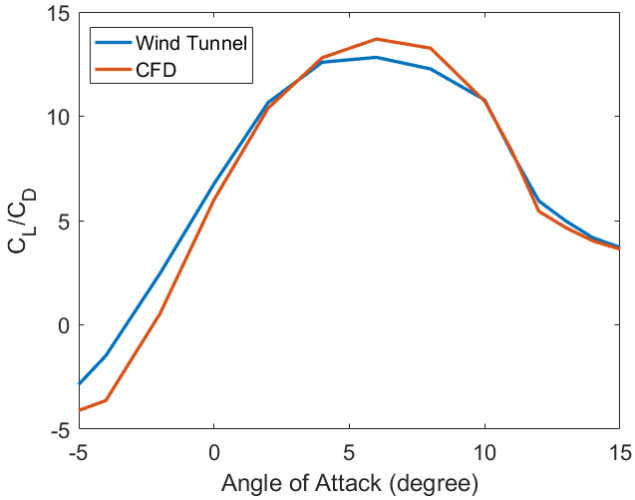

Figure 3-31: L/D versus angle of attack – wind tunnel test and numerical simulations comparisons

Figure 3-32 to 3-33 describe the lift and drag coefficient for different sweep angles in with and without the function of flaps two status. Obviously, the deployment of the wing increases the lift and drag coefficient. In particular, the fully deployed configuration increases the maximum of 51.88% lift compared to the fully folded configuration, which proves the benefit of the deployed configuration for the long endurance flight. Besides, the fully folded configuration reduced around 10.43% drag at around 10 degrees angle of attack compared to the deployed configuration. The result indicates that at the beginning stage of the transition when the wing is not fully deployed, the folded configuration can reduce the resistance and relief the load of the transition propulsion system. In addition, from 55° to 65° wing sweep the effect of the flap is limited, while under 55° wing sweep the flap increases lift by 8.5%. This proves the flap is more effective when the wing is deployed. On the other hand, the flaps provide approximated a 40% increase in drag. This shows that the flap is useful to provide extra lift during the water to the air transition at low velocity.

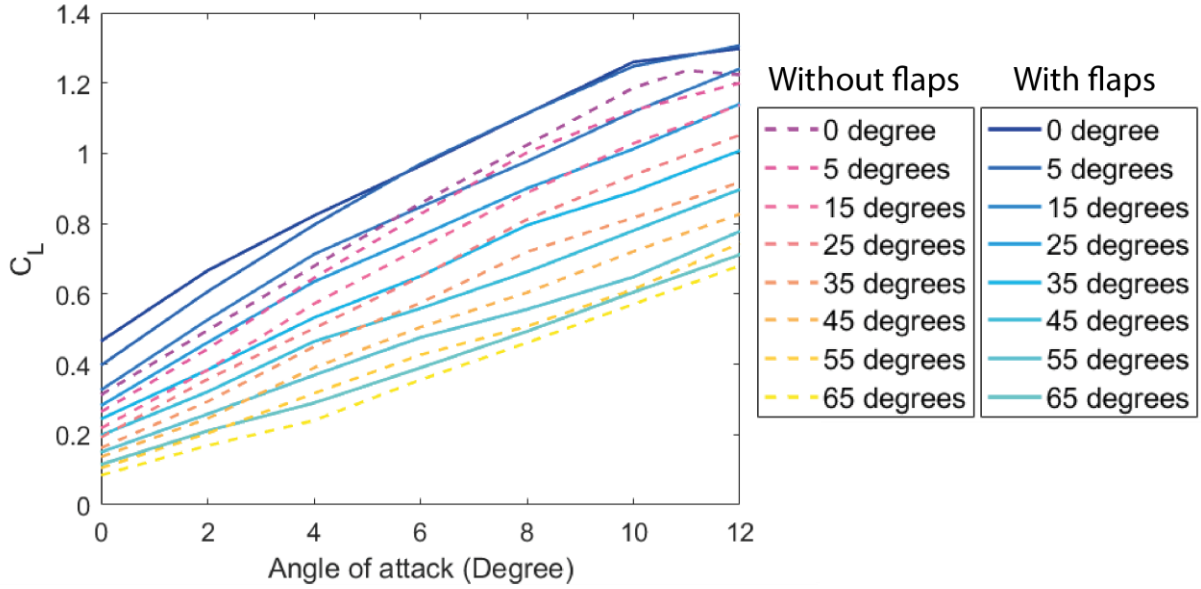

Figure 3-32: Lift coefficient for different sweep angle with flaps and without flaps

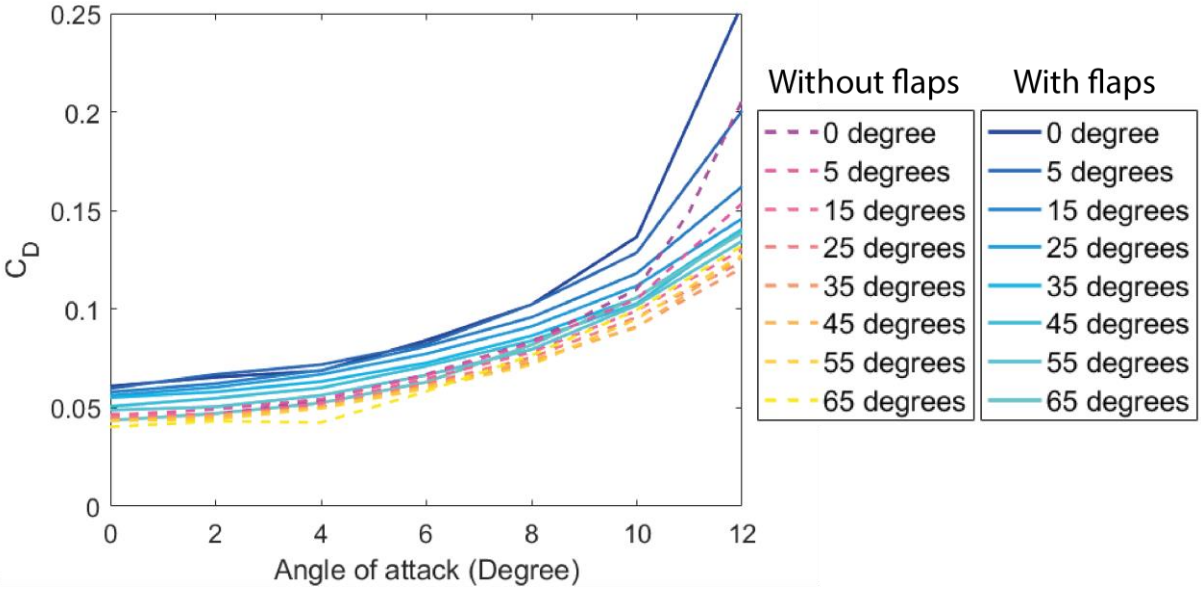

Figure 3-33: Drag coefficient for different sweep angle without flaps and with flaps

3.12 WING-DEPLOYMENT MECHANISM VERIFICATION

The design of the wing-deployment mechanism is also verified in the wind tunnel on the sting. The vehicle was placed on the extreme condition to simulate the water to air transition with a high angle of attack. Limited by the structure of sting, the maximum pitch angle that it could provide is 74° as shown in Figure 3-34. This is relatively a high pitch angle for taking off.

Figure 3-34: Placement of the vehicle for verifying the wing-deployment mechanism

The motion of wing was recorded by the camera in front of the vehicle. Afterwards, the videos were imported into the post-process software Kinovea®. Two crash dummy symbols on the tip of the wing were tracked in the Kinovea® to analyse the deploying and folding duration, further the trajectories and rotation speed of the wing. The centre of the crash dummy symbol is 0.6 m far from the pivot of the wing. As presented in Figure 3-35, the red lines are the trajectories of the crash dummy symbols tracked by Kinovea®.

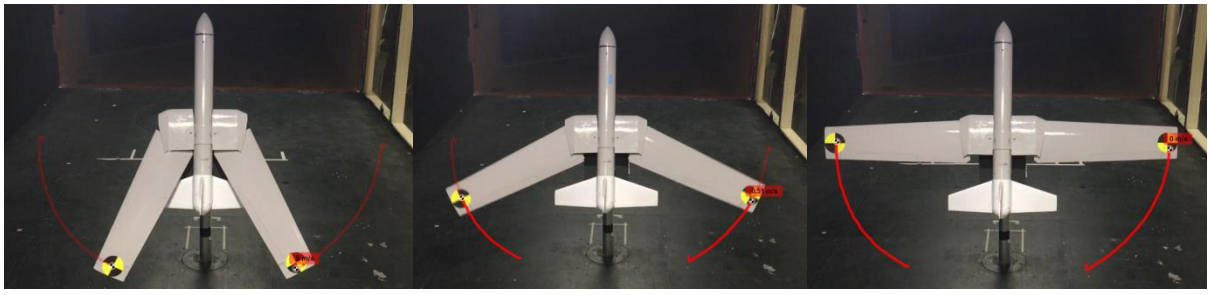

Figure 3-35: Track path in Kinovea® and the position of crash dummy symbols

In the deploying status, the variation of the rotation speed with time is presented in Figure 3-36. The rotation speed is quickly growing to maximum and decreases slowly until the deployment is finished, and the average rotation speed is around 0.9 rad/s. Theoretically, the linear actuator with 28 mm/s velocity will use 1s to complete the 28 mm stroke in the mechanism design. However, during the test, it took 1170 ms to deploy the wing. There is a little delay due to the load on the actuator, but the loss is only 170 ms. This test proves that under the large load the linear actuator can still work properly, and the mechanism performance is very stable.

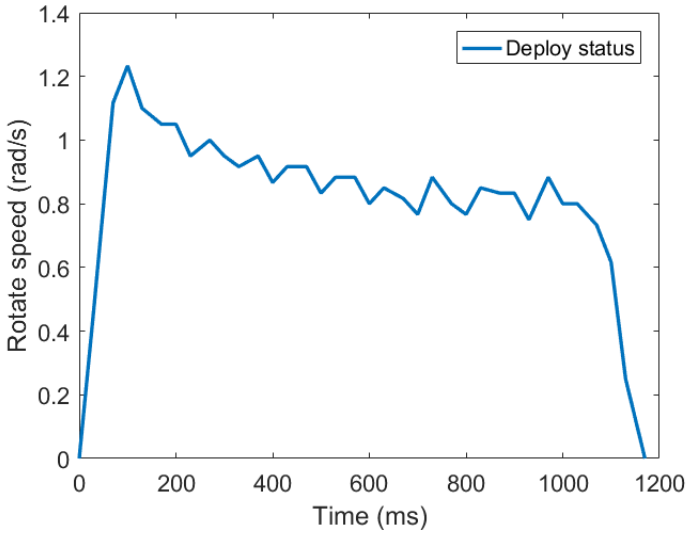

Figure 3-36: Rotation speed changing with the time

3.13 STATIC STABILITY

3.13.1 Longitudinal stability

By importing the data from the wind tunnel experimental test to the Eq. (48), the static margin $K_N = 13.96\%$ is calculated.

$$K_N = -\frac{dC_M}{dC_L} \tag{48}$$

The static margin is in a reasonable range, which is from 5% to 15% [47]. Above the range, the control will be heavy, and the vehicle would be inactive. If the static margin is excessively low, the vehicle will be sensitive about the pilot inputs and hard to control. The acquired static margin is slightly high, but it is adequate for the surveillance flight with less manoeuvre.

Figure 3-37 presents that the negative gradients in the $C_L - C_M$ plots describe stable longitudinal static behaviour of the BUUAS. Figure 3-38 describes the variation of the moment coefficient versus the angle of attack. As the angle of attack increases, the moment coefficient decreases. This trend is throughout the whole curve. The moment coefficients keep a positive value from the angle of attack 0° to 6°. In this region, the vehicle has a nose up pitching moment. Afterwards, the moment coefficients are negative and keep decreasing in a similar slope. The negative pitch moments pitch the nose downward. This behaviour can recover the vehicle during the stall.

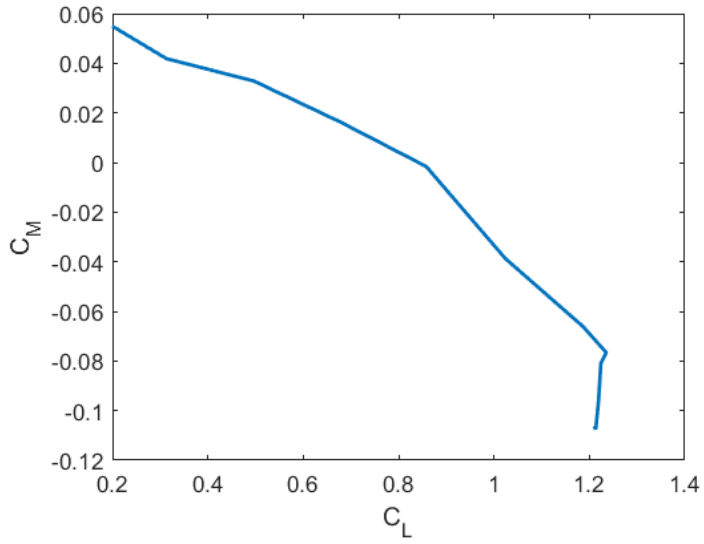

Figure 3-37: Lift coefficient against moment coefficient

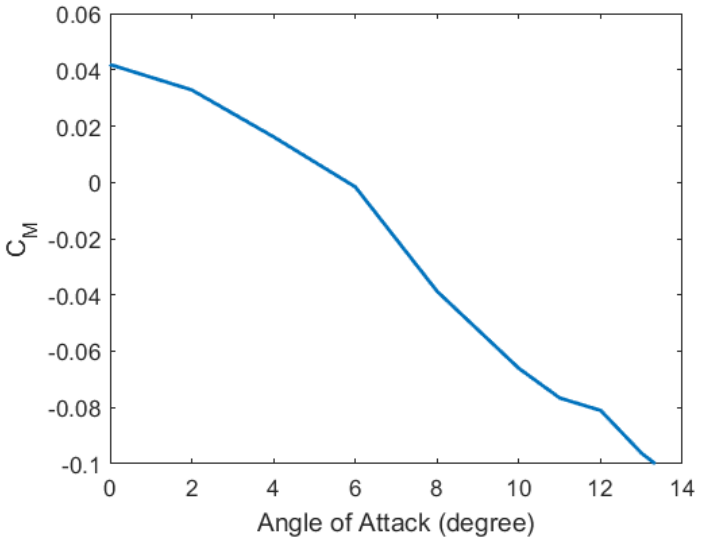

Figure 3-38: Moment coefficient against the angle of attack

3.13.2 Directional stability

The positive $\frac{dC_N}{d\beta}$ in Figure 3-39 indicates the stable behaviour in directional stability. The yaw moment coefficient presents a linear growth from 0º to 12º. After 12º, the negative $\frac{dC_N}{d\beta}$ shows the vehicle no longer possesses directional stability. The reason is that under the high angle of sideslip, the flow separation on the vertical tail decreases the side-force on it, thus the vertical tail does not have the capability to ensure adequate stability. During the flight, this can be solved by the deflection of the vertical stabilator, so a negative side force can be generated with the negative deflection of the vertical stabilator. It can provide a positive yaw moment to rectify the vehicle.

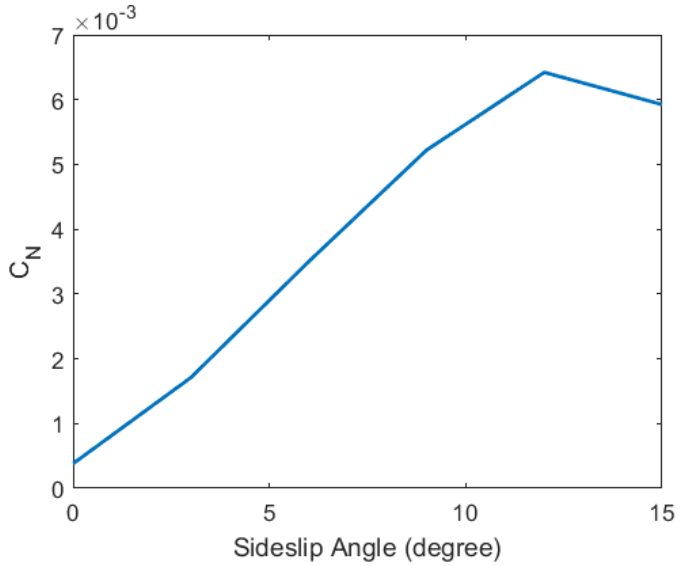

Figure 3-39: Yawing moment against sideslip angle

3.13.3 Lateral stability

As shown in Figure 3-40, the negative value of the slope from 0º to 12º indicates the static stability in the roll. It can recover the aircraft to level flight from the disturbance in the roll. One of the reasons for correcting the displacement of the vehicle in the roll angle is the "dihedral effect". Since the wing is not absolutely rigid, it can be deformed slightly by the load, which is the lift. Therefore, the lift on the wing creates the dihedral angle, further produces the "dihedral effect". Except the main wing, the vertical tail also contributes the lateral stability. The reason for the instability after 12º is similar to the analysis in directional stability. In this case, the flow separations on the main wing and the vertical tail produce the lateral instability. To rectify the vehicle, the roll control can be dominant by the deflection of the aileron.

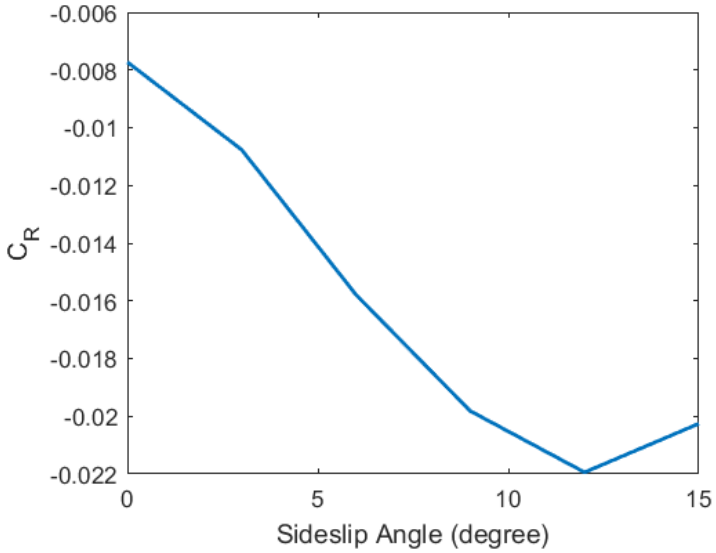

Figure 3-40: Rolling moment against sideslip angle

3.14 DYNAMIC STABILITY

A dynamic stability analysis is conducted to evaluate short period, phugoid, Dutch roll, roll and spiral modes. If not available from the experiment, CATIA® was used to extract necessary properties such as the moments of inertia. Likewise, the lift curve slope of the tail is evaluated from XFLR5®. The method from the well-known book of Etkin [72] is applied to describe the dynamic stability. Besides, the dynamic derivatives and equations below are cited and summarized from the book [47, 72-75].

The dynamic stability analysis mainly focuses on the steady flight motion with small deviations. Therefore, the small-disturbance theory is used for the evaluation. It can provide enough accuracy in this condition for the engineering analysis. The subscript zero indicates the reference flight condition, which is the steady flight and is assumed to be symmetric without angular velocity. u_0 is the reference flight speed.

3.14.1 Longitudinal dynamic stability

Phugoid

The undamped circular frequency and damping ratio for the Phugoid mode can be obtained from the equations below:

$$\omega_n^2 = -\frac{gZ_u}{mu_0} \tag{49}$$

$$\zeta = -\frac{X_u}{2}\sqrt{\frac{u_0}{-mgZ_u}} \tag{50}$$

The derivatives of Z_u and X_u are unknown. They can be yielded by:

$$Z_u = -\rho u_0 S C_{w_0} \cos\theta_0 + \frac{1}{2}\rho u_0 S C_{z_u} \tag{51}$$

$$X_u = \rho u_0 S C_{w_0} \sin\theta_0 + \frac{1}{2}\rho u_0 S C_{x_u} \tag{52}$$

The C_{w_0} is the weight coefficient. It is expressed as,

$$C_{w_0} = \frac{mg}{\frac{1}{2}\rho u_0^2 S} \tag{53}$$

The u derivatives C_{x_u} and C_{z_u} describe the variation of forces changing with the forward speed. They are given by:

$$C_{x_u} = \mathbf{M}_0(\frac{\partial C_T}{\partial \mathbf{M}} - \frac{\partial C_D}{\partial \mathbf{M}})_0 - \rho u_0^2(\frac{\partial C_D}{\partial p_d})_0 + C_{T_u}(1 - \frac{\partial C_D}{\partial C_T})_0 \tag{54}$$

$$C_{z_u} = -\mathbf{M}_0\left(\frac{\partial C_L}{\partial \mathbf{M}}\right)_0 - \rho u_0^2\left(\frac{\partial C_L}{\partial p_d}\right)_0 - C_{T_u}(\frac{\partial C_L}{\partial C_T})_0 \tag{55}$$

The aeroelastic effect and Mach number is tiny for above derivatives in this vehicle. So, the $\frac{\partial C_D}{\partial p_d}$ and M_0 is neglected, and then Eq. (54) and (55) become

$$C_{x_u} = C_{T_u}(1 - \frac{\partial C_D}{\partial C_T})_0 \tag{56}$$

$$C_{z_u} = -C_{T_u}(\frac{\partial C_L}{\partial C_T})_0 \tag{57}$$

For the constant speed propellers in cruising flight, the C_{T_u} can be given by:

$$C_{T_u} = -3C_{T_0} \tag{58}$$

In the steady flight condition, C_{T_0} can be gained by the force equations:

$$X_0 - mg_0\sin\theta_0 = 0 \tag{59}$$

$$Z_0 + mg_0\cos\theta_0 = 0 \tag{60}$$

Thus,

$$C_{T_0} = C_{D_0} + C_{L_0}\tan\theta_0 \tag{61}$$

So that,

$$C_{x_u} = -3C_{D_0} - 3C_{L_0}\tan\theta_0 \tag{62}$$

The C_{z_u} can be expressed as,

$$C_{z_u} = -C_{L_u} \tag{63}$$

where,

$$C_{L_u} = \mathbf{M}\frac{\partial C_L}{\partial \mathbf{M}} \tag{64}$$

Following the Prandtl-Glauert similarity law for subsonic flow, Eq. (64) can be transferred to

$$C_L = \frac{C_L|_{\mathbf{M}=0}}{\sqrt{1 - \mathbf{M}^2}} \tag{65}$$

So,

$$\frac{\partial C_L}{\partial M} = \frac{\mathbf{M}}{1 - \mathbf{M}^2}C_{L_0} \tag{66}$$

Hence,

$$C_{Z_u} = \frac{\mathbf{M}^2}{1-\mathbf{M}^2} C_{L_0} \tag{67}$$

The only unknown C_{L_0} and C_{D_0} are the coefficients in the steady flight condition, and C_{L_0} can be represented as,

$$C_{L_0} = \frac{mg}{\frac{1}{2}\rho u_0^2 S} \tag{68}$$

The C_{D_0} can be acquired by using the curve fitting function in Matlab® based on the data from the wind tunnel experimental test.

Short period

The characteristic equation of a short period is,

$$\lambda^2 + B\lambda + C = 0 \tag{69}$$

where,

$$B = -\frac{1}{t^*}\left[\frac{C_{z_\alpha}}{2\mu} + \frac{1}{\hat{I}_y}(C_{m_q} + C_{m_{\dot{\alpha}}})\right] \tag{70}$$

$$C = -\frac{1}{t^{*2}\hat{I}_y}\left(C_{m_\alpha} - \frac{C_{m_q}C_{z_\alpha}}{2u_0}\right) \tag{71}$$

In the equations above, the unknown derivatives are t^*, C_{z_α}, μ, $C_{m_{\dot{\alpha}}}$, C_{m_α}, C_{m_q} and $\hat{I}_y$. The non-dimensionalized moment of inertia about the Y axes $\hat{I}_y$ can be calculated from the following equation based on the value of the I_y estimated from the 3D model in the CATIA®.

$$\hat{I}_y = \frac{I_y}{\rho S(\frac{1}{2}\bar{c})^3} \tag{72}$$

The pitch moment coefficient of aircraft with the change of angle of attack $C_{m_{\dot{\alpha}}}$ can be obtained by the Eq. (73):

$$C_{m_{\dot{\alpha}}} = -2C_{L_{\alpha_t}}\eta_H V_H \frac{l_t}{\bar{c}}\frac{d\epsilon}{d\alpha} \tag{73}$$

The $\frac{d\epsilon}{d\alpha}$ is the average low-speed downwash gradient at the horizontal tail,

$$\frac{d\epsilon}{d\alpha} = 4.44\left[K_A K_\lambda K_H\left(\cos\Lambda_{c/4}\right)^{1/2}\right]^{1.19} \tag{74}$$

$$K_A = \frac{1}{AR} - \frac{1}{1+AR^{1.7}} \tag{75}$$

$$K_\lambda = \frac{10-3\lambda}{7} \tag{76}$$

$$K_H = \frac{1 - \left|\frac{h_H}{b}\right|}{\sqrt[3]{\frac{2l_H}{b}}} \tag{77}$$

The location of the tail means aerodynamic chord is estimated by the technique presented in Figure 3-41 from the book of Raymer [47].

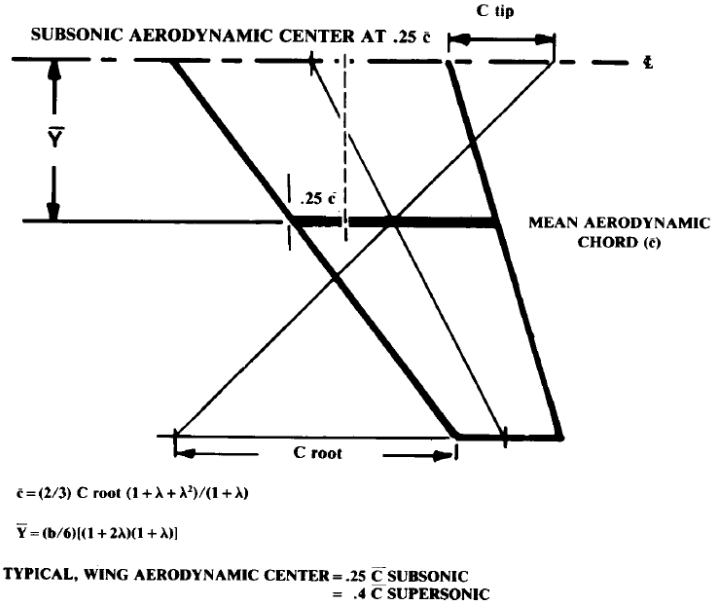

Figure 3-41: Wing aerodynamic centre estimation technique

The pitch moment coefficient with angle of attack C_{m_α} can be evaluated from the Eq. (78):

$$C_{m_\alpha} = C_{L_\alpha}(h - h_n) \tag{78}$$

where the h is the location of the CG, and the h_n is the location of the neutral point, which is estimated by the Eq. (79) from the book of Simon [75].

$$h_n = (h_0 + \eta_s \times V_H \times \frac{C_{L_{\alpha_t}}}{C_{L_\alpha}} \times (1 - \frac{d\epsilon}{d\alpha})) \tag{79}$$

where the h_n is the position of the neutral point as a decimal fraction of the wing standard mean chord, h_0 is the position of the aerodynamic centre of the wing on the standard mean chord. The $C_{L_{\alpha_t}}$ is the tail lift-curve slope $\frac{\partial C_{L_t}}{\partial \alpha_t}$, and $C_{L_{\alpha_t}} = 4.1224$ is estimated on the software XFLR5® based on the geometry of the tail. η_s is the stabilizer efficiency of 0.4.

The pitch moment coefficient with the pitch rate C_{m_q} describes the aerodynamic effects that the vehicle is rotating around the span-wise axis. It can be known from the book of Etkin

[72] that tail contributes most of the C_{m_q}. The 10% increase can be added on C_{m_q} of the tail to represent the allowance of wing and body. The $(C_{m_q})_{tail}$ can be acquired by:

$$(C_{m_q})_{tail} = -2C_{L_{\alpha_t}} V_H \frac{l_t}{\bar{c}} \tag{80}$$

$$l_t = x_{ac_t} - x_{cg} \tag{81}$$

where x_{ac_t} and x_{cg} is the location of the tail aerodynamic centre and centre of gravity

The relative density of the aircraft μ can be obtained by:

$$\mu = \frac{2m}{\rho S \bar{c}} \tag{82}$$

The equation for C_{z_α} is described below,

$$C_{z_\alpha} = -\left(C_{L_\alpha} + C_{D_0}\right) \tag{83}$$

t^* is the characteristic length, which is the MAC divide the velocity,

$$t^* = \frac{\bar{c}}{u_0} \tag{84}$$

3.14.2 Lateral stability

The lateral motion equation in matrix form is presented in Eq. (85):

$$\begin{bmatrix} \dot{v} \\ \dot{p} \\ \dot{r} \\ \dot{\phi} \end{bmatrix} = \begin{bmatrix} \frac{Y_v}{m} & \frac{Y_v}{m} & (\frac{Y_v}{m} - u_0) & \\ (\frac{L_v}{I'_x} + I'_{zx}N_v) & (\frac{L_v}{I'_x} + I'_{zx}N_v) & (\frac{L_v}{I'_x} + I'_{zx}N_v) & g\cos\theta_0 \\ (I'_{zx}L_v + \frac{N_v}{I'_z}) & (I'_{zx}L_p + \frac{N_p}{I'_z}) & (I'_{zx}L_r + \frac{N_r}{I'_z}) & 0 \\ 0 & 1 & \tan\theta_0 & 0 \end{bmatrix} \begin{bmatrix} v \\ p \\ r \\ \phi \end{bmatrix} \tag{85}$$

The moments of inertia for the equations are estimated from the 3D model of the CATIA®. Therefore,

$$I'_x = (I_x I_z - I_{zx}^2)/I_z \tag{86}$$

$$I'_z = (I_x I_z - I_{zx}^2)/I_x \tag{87}$$

$$I'_{zx} = I_{zx}/(I_x I_z - I_{xz}^2) \tag{88}$$

The derivatives for (L, N, Y), roll rate p and yaw rate r can be yielded by the following equations:

The L derivatives

$$L_v = \rho u_0 S \frac{b}{2} C_{l_\beta} \tag{89}$$

$$L_p = \frac{1}{4}\rho u_0 b^2 S C_{l_p} \tag{90}$$

$$L_r = \frac{1}{4}\rho u_0 b^2 S C_{l_r} \tag{91}$$

The N derivatives

The N derivatives is in a manner similar with the L derivatives:

$$N_v = \rho u_0 S \frac{b}{2} C_{n_\beta} \tag{92}$$

$$N_p = \frac{1}{4}\rho u_0 b^2 S C_{n_p} \tag{93}$$

$$N_r = \frac{1}{4}\rho u_0 b^2 S C_{n_r} \tag{94}$$

The Y derivatives

$$Y_v = \rho u_0 S C_{y_\beta} \tag{95}$$

$$Y_p = \frac{1}{4}\rho u_0 b S C_{y_p} \tag{96}$$

$$Y_r = \frac{1}{4}\rho u_0 b S C_{y_r} \tag{97}$$

The value of yawing moment coefficient with angle of sideslip C_{n_β}, rolling moment coefficient with angle of sideslip C_{l_β}, and side force coefficient with angle of sideslip C_{y_β} can be obtained from the curves constructed by the data of the wind tunnel experimental test.

The support centre of the test sting in the wind tunnel is not in the centre of gravity. Therefore, derivatives C_{m_p} and C_{n_p} need to be corrected according to the distance between those two centres,

$$C_{m_p} = \frac{M}{\frac{1}{2}\rho {u_0}^2 S \bar{c}} \tag{98}$$

$$C_m = C_{m_p} + (\frac{(x_{cg} - x_p)}{\bar{c}}) C_L \tag{99}$$

$$C_{n_p} = \frac{N}{\frac{1}{2}\rho {u_0}^2 S b} \tag{100}$$

$$C_n = C_{n_p} + (\frac{(x_{cg} - x_p)}{\bar{c}})C_Y \tag{101}$$

The side force derivative,

$$C_Y = \frac{Y}{\frac{1}{2}\rho V^2 S} \tag{102}$$

The lift coefficient,

$$C_L = \frac{L}{\frac{1}{2}\rho V^2 S} \tag{103}$$

Roll rate p derivatives

$$C_{l_p} = -\frac{C_{L_\alpha}}{12}\frac{1+3\lambda}{1+\lambda} \tag{104}$$

The Eq. (104) is from the book of Nelson [73], where λ is the taper ratio.

$$C_{n_p} = -\frac{C_L}{8} \tag{105}$$

$$C_{y_p} = -C_L \frac{AR + \cos\Lambda}{AR + 4\cos\Lambda}\tan\Lambda \tag{106}$$

where $\Lambda = 0$, so, the $C_{y_p} = 0$.

Yaw rate r derivatives

The main contribution of the C_{y_β} is from the vertical tail. It is assumed that $C_{y_\beta} \approx C_{y_{\beta_{tail}}}$.

Thus,

$$C_{y_r} = -2\left(\frac{l_v}{b}\right)C_{y_{\beta_{tail}}} \tag{107}$$

The l_v is the distance between the CG and the vertical tail aerodynamic centre,

$$l_v = x_{ac_t} - x_{cg} \tag{108}$$

$$C_{n_r} \cong 2C_{y_{\beta_{tail}}}\left(\frac{l_v}{b}\right)^2 \tag{109}$$

$$C_{l_r} = \frac{C_L}{4} - \frac{z_v}{b}C_{y_r} \tag{110}$$

z_v is the distance above the vehicle centre of mass to the vertical tail aerodynamic centre.

3.14.3 Dynamic stability result and discussion

The result in Figure 3-42 and 3-43 demonstrates that the BUUAS has satisfactory stability characteristics in most of modes, but the positive values in the spiral mode indicates the spiral

instability. This spiral instability is usually caused by the vehicle being more directionally stable than laterally. Due to the wing-deployment mechanism design, the wing only has a little dihedral when it is carrying the load. Besides, a large fin is designed due to the short moment arm. Those factors give the vehicle a stronger directional stability than lateral. Accordingly, the disturbance introduced from the sideslip can bank, and turn the vehicle. Then, with the increase of the slip, the turn rate continues to grow accompanying violent height loss. The whole process is spiral divergence, and may turn into high speed spiral dive without the control from the pilot. However, with the velocity increasing from 15 m/s to 25 m/s, which are marked on the side of points, the stability margin of the spiral mode decreases, and the spiral mode is moving closer to the instability boundary. Besides, the time to double the amplitude of the spiral mode is 5.78 s. This indicates the rate of divergence in the spiral motion is gradual, and the pilot has time to correct the vehicle. The stable behaviour and adequate rectifying time substantiate the vehicle can be put in the future flight test.

The uncertainty on the CATIA® measured moment of inertia value and its impact on the frequency and damping of the modes has been quantified. The reason is that the slight difference of this measurement between manufactured parts and the 3D model may exist. In CATIA®, the actual mass for each component has been applied on the 3D model to measure the moment of inertia. However, since the manufacturing technic is not perfect, manufactured parts may not be ideally homogeneous like the 3D model, especially for the long and solid wing. It could be known from equations above that the short period mode is more sensitive about the I_y than phugoid mode. Particularly, with the increase of the I_y, the natural frequencies will decrease, and damping ratio will increase both in short period mode, if the I_y decrease, vice versa. To quantify this uncertainty, trials have been made based on the stability analysis model. The result shows that with 10% variation of I_y, the natural frequency has -4.37% and damping ratio has 0.39% variation. Similarly, the variation of I_x has more impact on natural frequency in roll subsidence mode and damping ratio in Dutch roll mode than other modes. Especially, with 10% variation of I_x, -9.09% variation will appear in the natural frequency of roll subsidence mode, and -1.56% in damping ratio of Dutch roll mode. Regarding to I_z, the 10% variation will produce -4.69% variation of natural frequency and -2.80% variation of damping ratio both in Dutch roll mode.

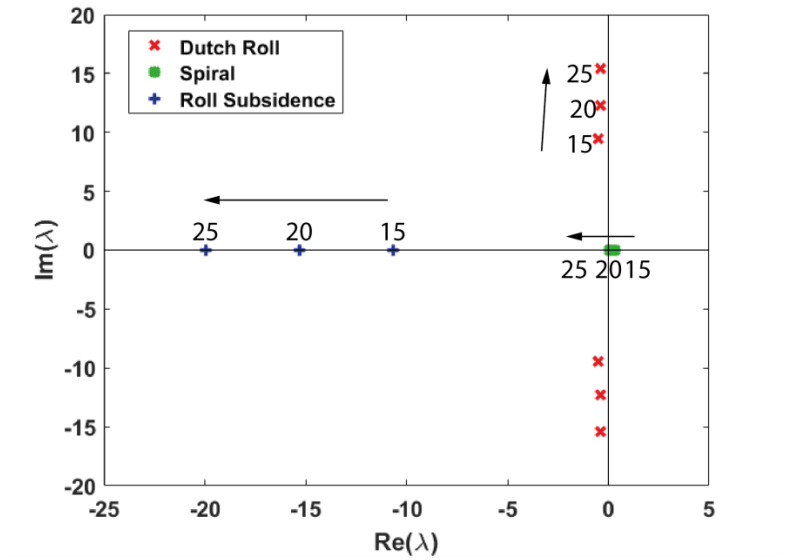

Figure 3-42: Root locus – Dutch Roll, Spiral, Roll Subsidence mode

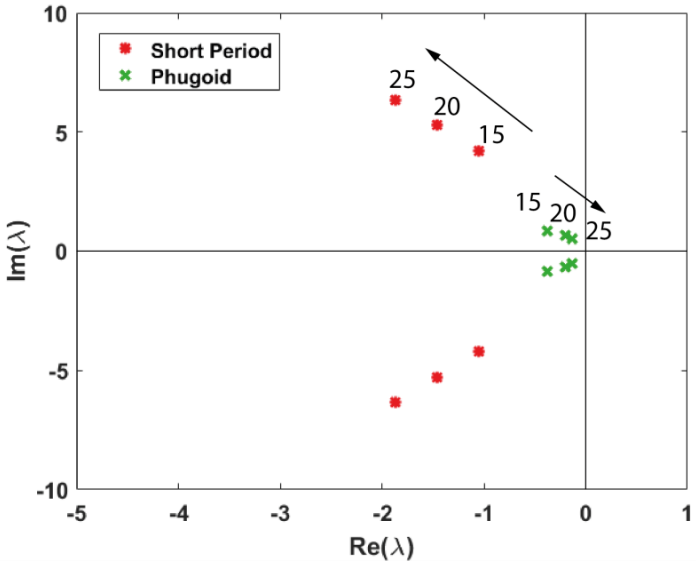

Figure 3-43: Root locus – Short-period and Phugoid mode

Chapter 4: Transition Propulsion System

4.1 DESIGN PRINCIPLE

4.1.1 Bionics study

Flying squid is a particular kind of squid with a mantle up to 50 cm in length and up to 500 g in weight. This squid can propel itself into the air by taking the water into its mantle and by expelling water to generate thrust, a simple way to save energy during migration and to evade predators [76]. High speed water, accelerated by the muscle inside the mantle, is used as a propellant. Then, the high mass flow rate and velocity of the expelled water can produce a significant amount of thrust. In an underwater environment, water is the most accessible resource that can provide a high mass flow rate. By imitating from nature, the high pressurized CO_2 gas stored in a cartridge can be used as an energy source to expel water. A transition propulsion system with high specific impulse, a thruster that mimics the one used by fly squid, is developed as described in Figure 4-1. Particularly, the water is stored in a water chamber and a CO_2 inflator is used to activate the CO_2 cartridge for releasing pressurised CO_2 into the water chamber.

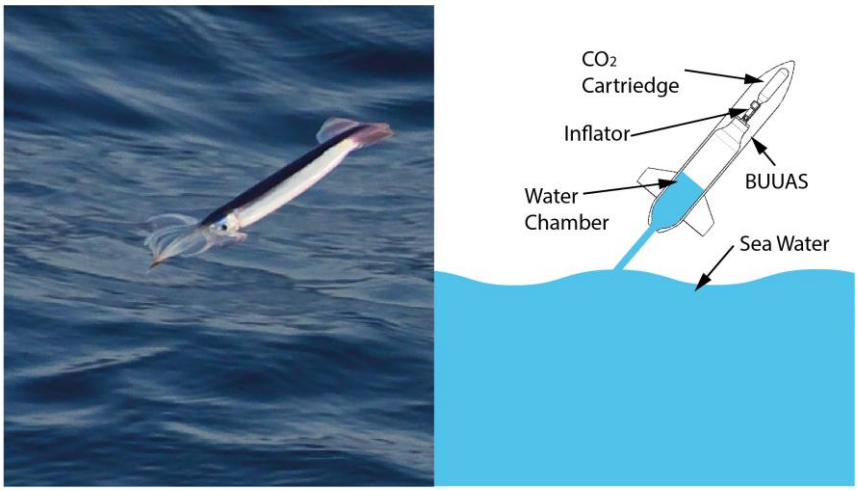

Figure 4-1: Flying squid inspired a transition propulsion system layout

4.1.2 Objective and requirements

The objective of this work is to develop a transition propulsion system that can be fitted into the BUUAS. A scaled unit was designed and manufactured with the primary purpose of testing its functionality at the conceptual stage. After the completion of this phase, the system can be scaled up to the BUUAS size. The scale-up process adopts the strategy of increasing the

size of the water chamber and amount of the pressurized CO_2 stored in the cartridge, which are the relatively light parts of the system, so the upgrade will not produce a huge weight penalty. As a result, it is assumed that the scaled transition propulsion system is 468 grams, which is 10% lighter than the initial estimated in the conceptual design.

A small vehicle is built with the sole purpose of testing the transition propulsion system. It has a rocket shape with a simple round fuselage and tail. The vehicle length is 600 mm, which is predicted from the length of the water chamber and mechanisms inside. Equal to the fuselage's diameter of the assembled BUUAS, the diameter of small vehicle is 79.7 mm. The total weight of the small vehicle including the airframe and avionics is about 1 kg.

The requirement is set based on the launch environment. During a pretty rough sea state, open ocean waves with a height above 7 meters are expected [77]. The vehicle is set to be launched higher than this height to avoid premature mission failure due to sudden attitude changes caused by hitting waves or spray drag. Therefore, the required launch height $h_{require}$ is set at 8.5 meters.

4.1.3 Iterative design process

To optimize the water chamber dimensions, an iterative design process involving an analytical model, numerical simulations and experimental tests was carried out with an analytical model calibration through CFD approach as illustrated in the flow chart shown in Figure 4-2. The volume of the water chamber and the exit area are two critical parameters that affect the generated thrust. Thus, the sizing process identifies the volume firstly, and then the desired exit area is evaluated.

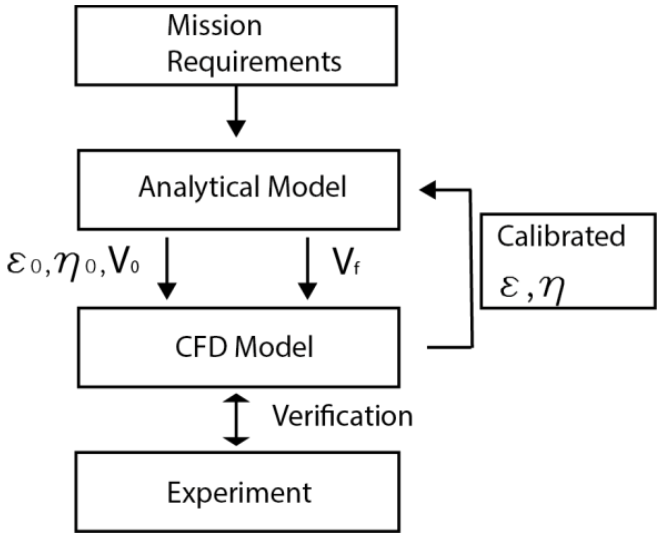

Figure 4-2: Iterative design process flow chart

In particular, the design method initially models the transition propulsion system behaviour using an analytical model implemented in Matlab® describing the physical phenomena with low fidelity as the flow chart in Figure 4-2 presents. Initial volume V_0, initial pressure drop coefficient ε_0 [78], and wall friction and general losses coefficient η_0 along the CO_2 inflator are estimated as a first "guess" to generate enough thrust and to satisfy mission requirements which is the minimum altitude $h_{require}$. In the following sections, the proposed analytical model is refined through high-fidelity and physically based numerical simulation to estimate the actual pressure drop coefficient along the CO_2 inflator ε and actual wall friction and general losses coefficient η. As the correlation of pressure behaviours for the analytical model and numerical model is considered satisfactory, optimized water chamber volume V_f is estimated to satisfy the already cited mission requirements. This water chamber volume value is then used in the numerical simulation to compute the final thrust with selected exit area sizes (A_5). Then, the influence of exit area sizes has on the transition propulsion system performances is estimated. To validate the numerical simulation, an experimental campaign is performed using the water chamber with volume V_f and different exit area sizes A_5.

4.2 ANALYTICAL MODEL

In the analytical model, the whole system is simplified into an equivalent ideal propulsion unit and is divided into several sections depicted in Figure 4-3. Section 1 is the interior of the CO_2 cartridge. A 25 g CO_2 cartridge with 5.5 MPa pressure is used by referring to the similar water escape system [79]. The junction of the cartridge and inflator is section 2 while the junction of the inflator and water chamber is section 3. Section 4 is the interior of the water chamber, and section 5 is the exit of the water chamber. In addition, the exit diameter was originally set as 9 mm. Consequently, the indexes in the following equations are set according to the sections. Since the water chamber needs to be fitted into the fuselage, its diameter is designed based on the diameter of the fuselage while the wall thickness of the fuselage and chamber are also considered. As a result, an internal diameter of 66 mm was chosen after subtracting the thickness above from the fuselage diameter. Accordingly, the volume of the water chamber is changed by varying its length $L_{chamber}$.

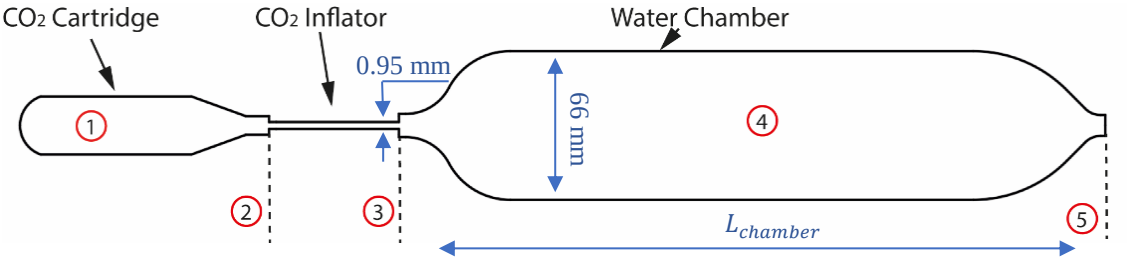

Figure 4-3: Transition propulsion system layout and indexes explanation

In the analytical model, several assumptions are considered:

• The working fluid is homogeneous in composition and obeys the perfect gas law.

• The structure in the CO_2 inflator is complex, and it is almost impossible to calculate the flow inside. Hence, the CO_2 inflator is regarded as a pressure drop tube. The diameter of the tube is the same as the exit of the CO_2 inflator, which is 0.95 mm.

• The gas flow inside the CO_2 cartridge is isentropic [80].

• The cartridge rapid discharge can freeze the liquid CO_2. This behaviour was not considered, since the water jet duration is very short, and it was not noticed during the experimental phase.

• The gas flow inside the water chamber has an adiabatic expansion, since the duration is quick, about one second [81].

• The water-gas interface is stable along the whole chamber until all the water is expelled.

Under these assumptions, the thrust can be calculated by knowing the exiting mass flow rate ($\dot{m}$) and the velocity (v_5) resulting in Eq. (111):

$$T = \dot{m} v_5 \tag{111}$$

The CO_2 cartridge discharge can be modelled in the time domain using Eq. (112) to Eq. (115)[80], by knowing the initial pressure (P_{1_0}), temperature ($\boldsymbol{T}_{1_0}$) inside the vessel, section (A_2) and volume (V_{CO_2}). The subscript zero indicates the initial value.

$$P_1(t) = \frac{P_{1_0}}{\left[1 + \left(\frac{\gamma - 1}{2\gamma}\right)\sqrt{\gamma R \boldsymbol{T}_{1_0}}\,\boldsymbol{\Gamma}\,\frac{A_2}{V_{CO_2}}\right]^{\frac{2\gamma}{(\gamma-1)}}} \tag{112}$$

$$\boldsymbol{T}_1(t) = \boldsymbol{T}_{1_0}\left(\frac{P_1(t)}{P_{1_0}}\right)^{\frac{(\gamma-1)}{\gamma}} \tag{113}$$

$$\dot{m}_1 = \frac{\boldsymbol{\Gamma} A_2 P_1(t)}{\sqrt{\gamma R \boldsymbol{T}_1(t)}} \tag{114}$$

$$\boldsymbol{\Gamma} = \gamma\left(\frac{2}{\gamma+1}\right)^{\frac{\gamma+1}{2(\gamma-1)}} \tag{115}$$

where R is the gas constant of CO_2, $R = 188.9$ and γ is the CO_2 heat capacity ratio, $\gamma = 1.3$. In this way, the CO_2 physical quantities are known in each instant of time during the discharge process.

The pressure ratio, which is used to examine the choked flow at the section 2, between the inner gas and the atmospheric pressure is,

$$\frac{P_{atm}}{P_1} \leq \left(\frac{2}{\gamma+1}\right)^{\frac{\gamma}{\gamma-1}} \tag{116}$$

At the initial thrust phase, the pressure ratio with a high pressure P_1 inside the cartridge is less than or equal to the critical value, which is the right side of the Eq. (116). Then, the flow is choked at section 2. This is a sonic condition with the Mach number at section 2 equalling one. With the pressure inside cartridge P_1 decreasing, the pressure ratio becomes higher than the critical value. In this situation, the Mach number along the CO_2 inflator can be evaluated as,

$$\boldsymbol{M}_2 = \frac{\dot{m}R\boldsymbol{T}_1}{P_1 A_2\sqrt{\gamma R\boldsymbol{T}_1}} \tag{117}$$

Moreover, the gas pressure inside the inflator can be expressed as,

$$P_2 = \frac{P_1}{\left[1 + \left(\frac{\gamma-1}{2}\right)\boldsymbol{M}_2{}^2\right]^{\frac{\gamma}{\gamma-1}}} \tag{118}$$

Based on the flow status from the inflator, the pressure in the water chamber P_{4_0} is,

$$P_{4_0}(t) = \boldsymbol{M}_2\sqrt{\frac{2+(\gamma-1)\boldsymbol{M}_2^2}{\gamma+1}}P_2(t) \tag{119}$$

Since there is a pressure drop when the flow passes through the CO_2 inflator, a coefficient ε is introduced to calibrate the water pressure inside the water chamber (P_4) according to Eq. (120). The initial value of ε_0 is evaluated based on literature and the complicated inner structure of the CO_2 inflator [78],

$$P_4(t) = \varepsilon_0 P_{4_0}(t) \tag{120}$$

By using the calibration method through the numerical simulation, the final pressure coefficient ε is maintaining at 0.069. The details of the numerical model are explained in section 4.4. Particularly, in the numerical model, the water chamber dimension is used the one

same as the analytical model. The variations of P_4 with time for both the calibrated analytical model and the numerical model are shown in Figure 4-4.

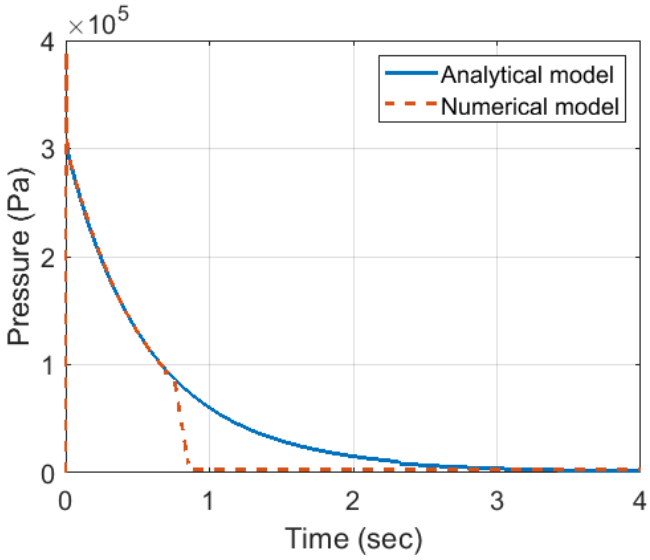

Figure 4-4: Pressure calibration result

The result indicates that the calibrated analytical model correlates accurately with the high-fidelity numerical model up to 0.7 s when all the water is expelled out. After 0.7 s, the water chamber becomes empty and the environment inside the water chamber has changed. In the numerical model, the environment change causes that the pressure rapidly drops. However, in the analytical model, only the important water jet phase is evaluated. Since the environment change is not included in the analytical model, the curve after 0.7 s is inaccurate.

For evaluating the thrust, the exit water flow velocity must be known. The water inside the chamber produces an impulsive flow, with a fast response in a short time window. For this reason, the transient Bernoulli equation is used to evaluate exit velocity (v_5) and as a consequence, the exiting mass flow rate[82],

$$B(H)\frac{dv_5}{dt} + C(H)v_5^2 + D(H)\frac{P_4 - P_5}{\rho_w} + gH = 0 \tag{121}$$

$$B(H) = \int_0^H \frac{A_5}{A(z)}dz \tag{122}$$

$$C(H) = \frac{1}{2}\left[\left(\frac{A_5}{A(H)}\right)^2 - 1\right] \tag{123}$$

$$D(H) = \left(\frac{V_b - V_{w_0}}{V_b - V_w(H)}\right)^{\gamma} \tag{124}$$

where the $B(H)$, $C(H)$, $D(H)$ are the function of the height of water/air interface and the water chamber geometry respectively. In addition, H is the water/air interface height measured

from the chamber outlet. V_w is the amount of water inside the chamber and V_{w_0} is the initial water volume. The volume of the water chamber is V_b. And, z describes the axial distance from the outlet of the water chamber.

Accordingly, the mass flow rate of water, which is a function of the exit velocity and exit diameter, can be obtained,

$$\dot{m}_5 = \rho_w v_5 A_5 \tag{125}$$

After the calibration, wall friction and general losses along the water chamber are considered with η coefficient of 33% and final thrust is obtained with Eq. (126),

$$T_f = \eta T \tag{126}$$

As a result, thrust behaviour in time is evaluated analytically after the refinement process, and is presented in Figure 4-5. Three different volumes were evaluated and compared from 700 mL to 900 mL. Obviously, the volume varies the duration of the thrust, but the trend of the curve and the peak thrust, which is about 34 N, remain the same. Afterwards, the thrust result is used in the vehicle dynamic model to evaluate the vehicle performance in the next trajectory predict section.

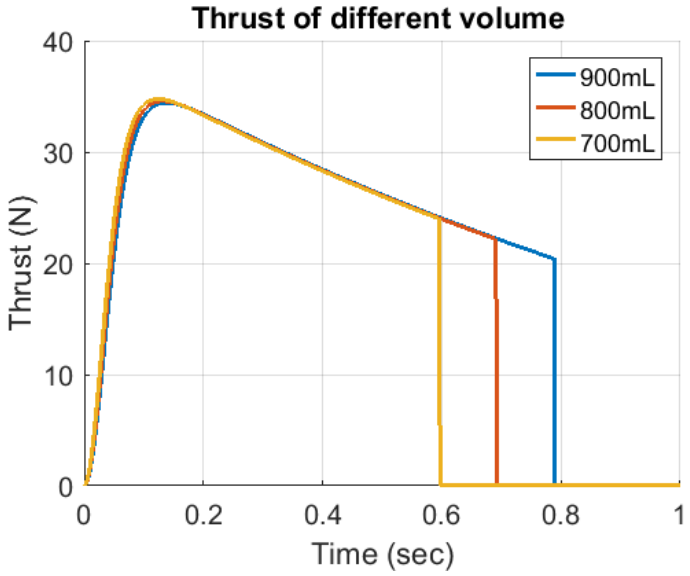

Figure 4-5: Analytical model result - Thrust vs time with different volume of a water chamber

4.3 TRAJECTORY PREDICTION

In order to analyse the transition trajectory for designing a qualified transition propulsion system, the whole process is separated into three phases, namely water phase, water to air phase and air phase as described in Figure 4-6.

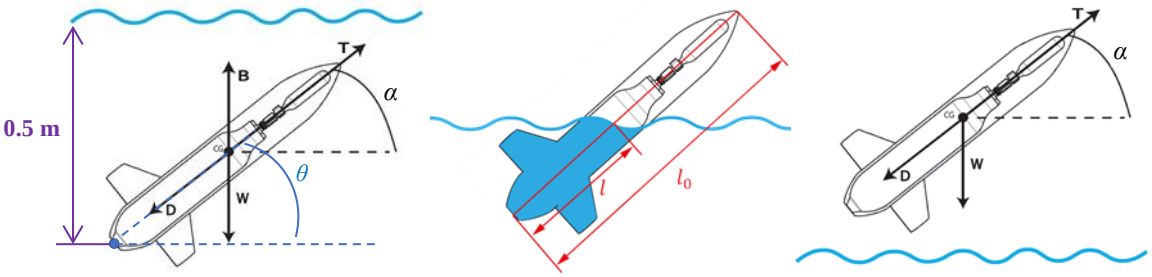

Figure 4-6: The free body diagrams in three phases

A trajectory model is developed from the free body diagrams in Figure 4-6 representing the vehicle motion in different phases. In the water, it is assumed that vehicle is launch at the depth where the bottom centre of the vehicle is located at half meter away from the water surface. Further, the launch angle is changed around the bottom centre. The model evaluates the trajectories of the different launch angle from 45 to 65 degrees with 5 degrees increments to obtain the optimum launch condition. Besides, the mass is reducing along with the launch, since the water is being expelled. Therefore, the vehicle mass changing model is introduced, which is the model used in the thrust analysis.

The vehicle is assumed in the neutral buoyancy constantly, which means that gravity is equal to buoyancy. There are two reasons: one is that the model is only used for verifying the thrust and launch angle, and another is that the travelling distance of underwater phase is very short compared with the air phase, since the vehicle is launched when it is close to the water surfaces. In this model, the used thrust is the result of the previous analytical model. The equations for three phases are demonstrated below:

Water phase

$$T - \frac{1}{2}\rho_w C_{D_w} S V^2 = m\frac{dV}{dt} \tag{127}$$

Transition phase

$$-G\sin\alpha - kD + T + B\sin\alpha = m\frac{dV}{dt} \tag{128}$$

$$k = \frac{l}{l_f} \tag{129}$$

Air phase

$$T\sin\alpha + \frac{1}{2}\rho C_L V_1^2 S\cos\alpha - G - \frac{1}{2}\rho C_D V_1^2 S\sin\alpha = m\frac{dV_1}{dt} \tag{130}$$

$$T\cos\alpha - \frac{1}{2}\rho C_L V_2^2 S\sin\alpha - \frac{1}{2}\rho C_D V_2^2 S\cos\alpha = m\frac{dV_2}{dt} \tag{131}$$

During the transition phase, the primary drag is produced underwater, which should be evaluated precisely. As the vehicle exits the water, the underwater wetted area is decreased. To represent the changing of wetted area, a coefficient k, which is the remained underwater fuselage length l to the whole fuselage length l_f, is introduced. It is assumed that the resistance is a uniform distribution on the prototype. Thus, the underwater drag is changing along with the change of underwater fuselage length. Moreover, the remained underwater fuselage length l is a function of time. Therefore, the changing of the underwater drag can be described.

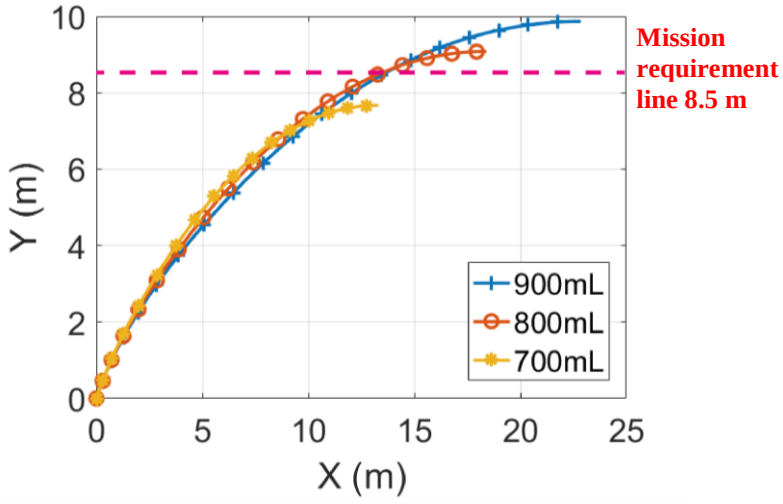

Figure 4-7: Trajectories with different V_f water chamber size at 60 degrees launch angle

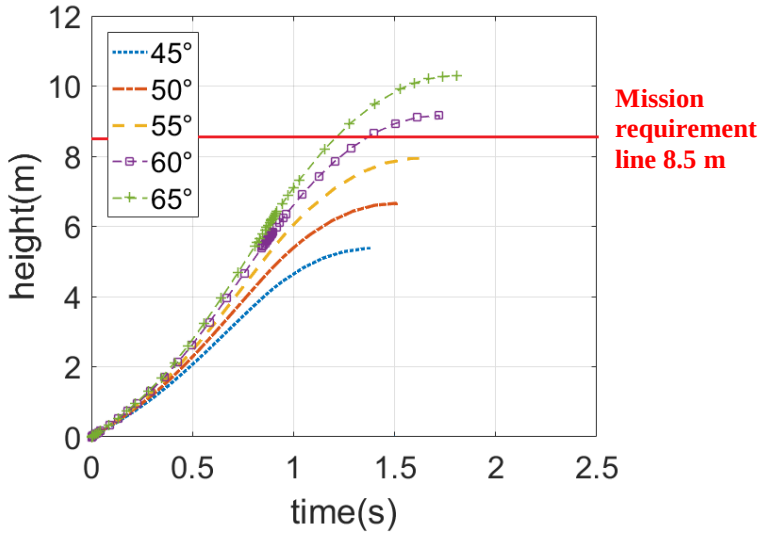

Figure 4-8: Trajectories with different launch angles using 800 mL water chamber size

The results in Figure 4-7 present that the vehicle with the 800 mL volume water chamber at 60 degrees launch angle can be launched out of 8.5 meters. Identical to the expectation, the more volume of water like more volume of fuel can gain a longer launching trajectory. Figure 4-8 presents the trajectories under different launch angles. Evidently, with the same time, the higher launch angle can obtain higher altitude. This is because the vehicle will travel longer

distance underwater and consume part of the thrust to overcome the water drag under the lower launch angle. However, an excessive high launch angle may take the vehicle to stall, which should be avoided. As presented in Figure 4-7 and Figure 4-8, the 800 mL and 900 mL water chamber volume can result in a level flight trajectory with 60 degrees launch angle. Nevertheless, increasing the water chamber volume also increases the system weight. Hence, the water chamber volume is limited to 800 mL.

4.4 NUMERICAL SIMULATIONS

In the analytical simulation on Matlab®, the size of the water chamber is defined. This simplified analytical model is not physics-based, and it has low fidelity. To improve the fidelity of the model, a high-fidelity numerical model was developed, which is used to calibrate the analytical model and verify the effect of the exiting area.

4.4.1 Mesh building

The transition propulsion system is axisymmetric. Hence, the 2D structured mesh shown in Figure 4-9 is created in the commercial software ICEM® based on the axisymmetric cross-section geometry of the transition propulsion system. The mesh can be imported into the Fluent® axisymmetric model to simulation the complete transition propulsion system, which can reduce the meshing and simulation effort. To increase the simulation accuracy, the inside tunnel geometry of the CO_2 inflator is measured and added to the whole system geometry. The final computational domain, which includes the CO_2 cartridge, inflator and the water chamber, is limited by the outside wall, outlet and axis. To separate the fluids initially, the inside wall 1 and wall 2 are introduced as illustrated in Figure 4-9.

4.4.2 Influence of exit area in the thrust system

The size of the outlet, which is the nozzle area indicated in Figure 4-9 has a great effect on the mass flow rate and exit velocity of water, and then the thrust. To investigate how is the thrust behaviour differs with different exit areas and verify the numerical model by comparing with next experimental test, the simulation for different sets of outlets are carried out. With other geometries remain the same, 5 different meshes are built according to five sets of exit diameter size (5 mm, 7 mm, 9 mm, 11 mm, and 13 mm).

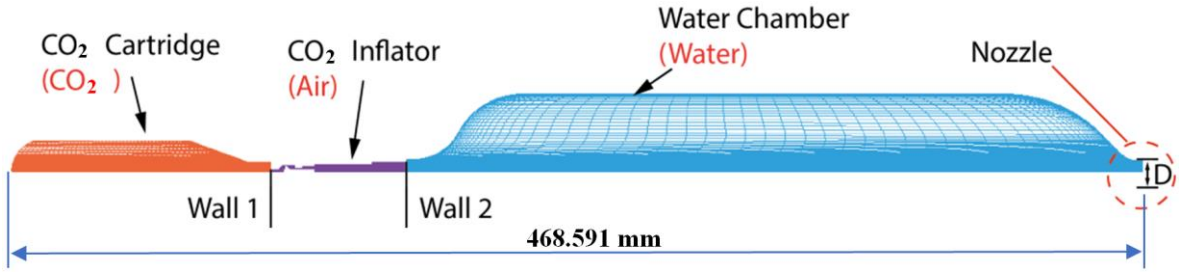

Figure 4-9: Configuration of the computational domain for numerical simulations

4.4.3 Numerical method and boundary conditions

Numerical simulation model

As illustrated in Figure 4-9, initially there are three different media in the system. They are CO_2 in the CO_2 cartridge, air in the CO_2 inflator and water in the water chamber. Accordingly, the flow domain is separated into three small domains for CO_2, air and water, which are represented in different colours. In the jet process, the water is expelled from the chamber by the high-pressure gas. The gas/water interface is regarded as a free surface in this case. Thus, the volume of fluid (VOF) technique is adopted, since it is widely used in the numerical simulation for free surface flows [83]. In addition, an axisymmetric transient-state model, and the $k-\varepsilon$ turbulent equations are applied in this simulation.

Boundary condition

To model three different media, multi-phases are employed to represent the material of the media. Specifically, phases with the materials can be specified in domains of media. For instance, the material of CO_2 is specified into the CO_2 cartridge domain, which is also same for the air and water. Afterwards, the material properties are set into their own phase. Accordingly, a 5.5×10^5 Pa pressure is implemented to the carbon dioxide phase to simulation the actual pressure inside cartridge. Besides, the model simulates a condition in which the water chamber is fully submerged underwater to compare with the experiment performed in the laboratory. Therefore, the outlet boundary condition is modelled as a pressure outlet, and the gauge pressure is 2,829 Pa to simulate the water pressure in the nozzle. The wall 1 and wall 2 are defined as the interior wall. It separates the different domains just in the initial stage. In the last, the outside wall is set as no-slip wall.

4.4.4 Results and discussion

Figure 4-10 presents the variations of the thrust with time for the selected nozzle exit diameters. The curves show that the thrust increases rapidly to the peak from zero, then the thrust decreases with the pressure decreasing of the CO_2 inside the system. This tendency is the

same as the analytical model, but the result from high-fidelity numerical simulation is more realistic and detailed. It provides the results that the thrust is generated to the peak thrust faster than the analytical model. The reason is that the analytical model is not infinitesimal as in numerical simulation and relies on approximations with the simplified geometry of the water chamber. Nevertheless, the analytical model is still important for obtaining the general water chamber dimension and predict the influence about how dimension parameters will change the result.

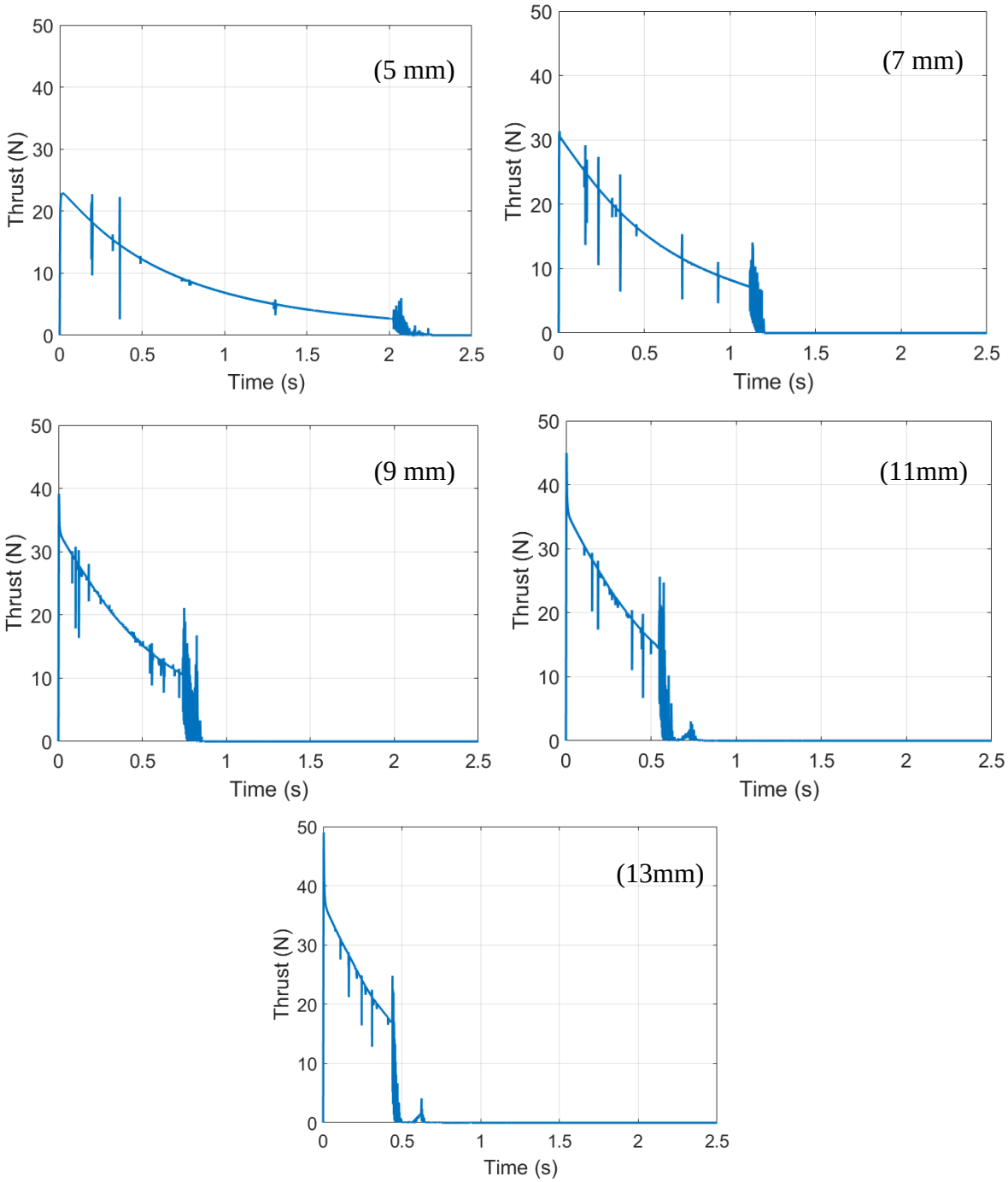

Figure 4-10: Numerical simulation results - Thrust vs time for different exit area dimensions

The summary in Figure 4-11 demonstrates that the peak thrust is increasing with the increasing nozzle diameter while duration and impulse are decreasing. The maximum thrust of 48.96 N is obtained at 13 mm diameter. On the contrary, the maximum impulse of 19.79 Ns is acquired at the 5 mm diameter. Consequently, large exit area can provide high peak trust in a short time, but the small exit area can have large impulse with long duration.

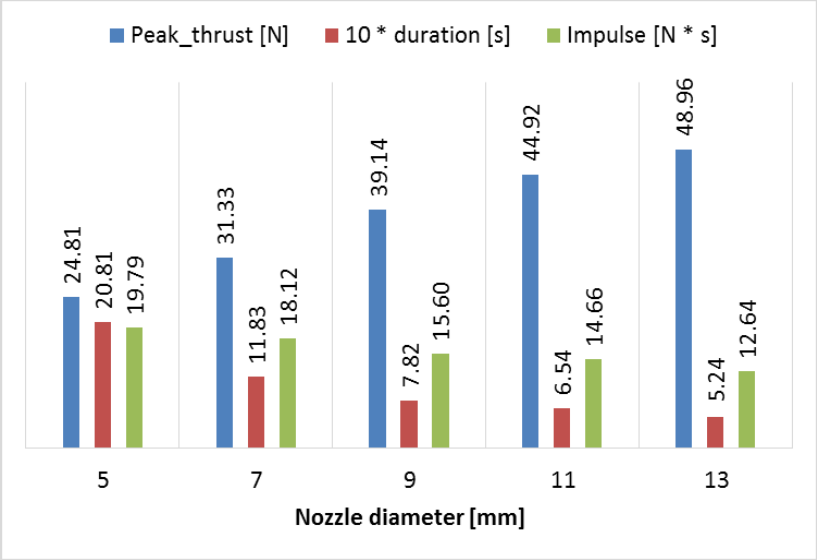

Figure 4-11: Numerical simulation results - Peak thrust, total impulse and duration for different exit area size

The oscillations could be observed during the water jet process and the burnout time. The reason for this slightly unstable thrust behaviour approaching the burnout time is that the water and gas mix together at the last stage of the thrust as illustrated in Figure 4-12. The high velocity gas mixed the water is ejected from the nozzle, and the mass flow rate rapidly changes, thus the thrust shows oscillation. The same reason also explains the oscillation in the middle stage of the thrust. A small group of high-pressure gas go through the water in the chamber and escape from the exit faster than the main group of high-pressure gas, which behaves as oscillation. This phenomenon is observed in the contours shown below during the jet.

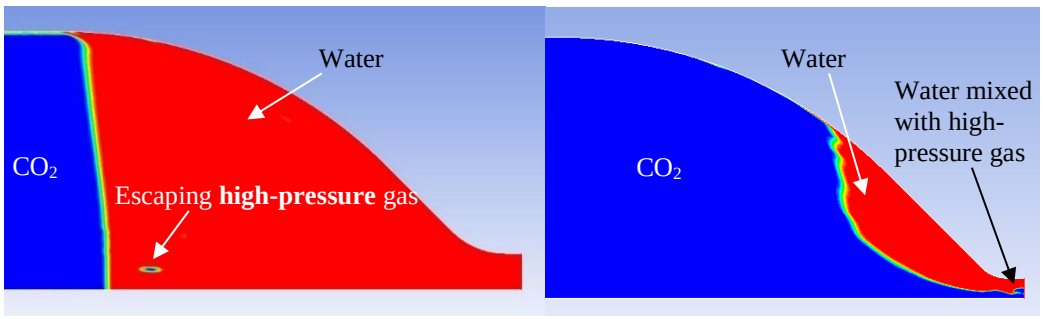

Figure 4-12: Contours of the jet process of 9 mm diameter (left) and 5 mm diameter exit area (right)

It is easy for gas to escape in the presence of the large exit area, which explains why there is the more oscillation in the large exit area from 9 mm to 13 mm. Since outlets with small exit areas such as 5 mm and 7 mm diameter are narrow, the exited water jet width is thin and is difficult to spread into droplets immediately. Therefore, the upstream water-gas interface in water chamber of small exit area is more stable compared with large exit areas. As a result, only a small amount of gas is mixed into the water, then escape out faster than the main group CO_2 gas. It makes the whole jet process more stable than large exit areas. So, the small exit areas produce less oscillation.

4.5 GAS RELEASE MECHANISM DESIGN

According to results from the numerical simulation and analytical model, it can be concluded that building the small vehicle integrated with the transition propulsion system is feasible. The following design stage focuses on the transition propulsion system prototype building for experimental validation. In the design process, many off-the-shelf components, which are easy to acquire and maintain, are used to reduce the period of fabrication.

4.5.1 Transition propulsion system layout

The complete system shown in Figure 4-13 consists of the CO_2 cartridge, gas release mechanism, adapter, and water chamber. Particularly, the gas release mechanism is designed to release the pressurized gas in the cartridge into the water chamber. The components are described in the following sections.

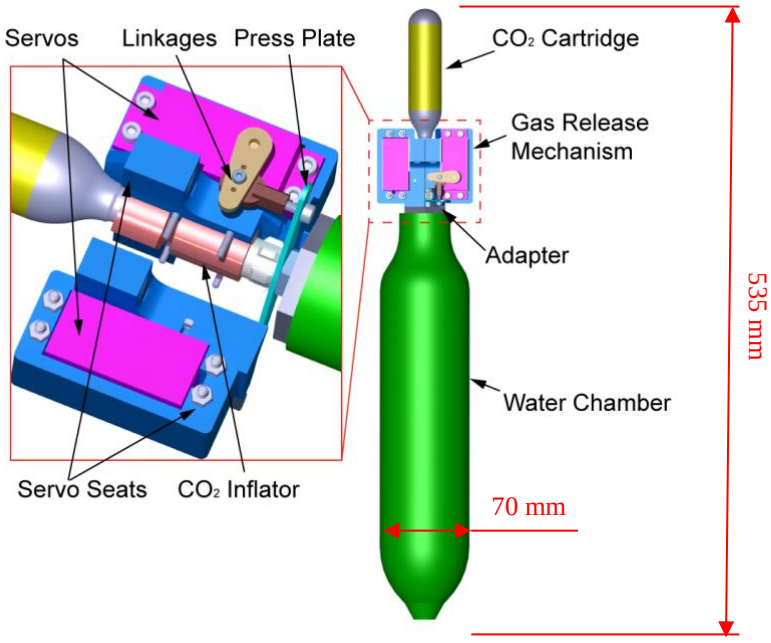

Figure 4-13: Computer-Aided Drafting transition propulsion system layout

4.5.2 CO_2 cartridge

A 25 grams CO_2 cartridge is used for providing the high pressurized CO_2 gas as shown in Figure 4-14. As mentioned before, it contains a high pressure of 5.5 MPa. The cartridge is made of thick steel with a thin welded cap. The cap has to be punctured by the external mechanism to release pressurized carbon dioxide. To do that, a sharp needle was considered for penetrating the CO_2 cartridge, but as a drawback, the solid needle and relative mechanism may block the exiting flow. Additionally, the commercial hydraulic valves that can hold high pressure are generally heavy, so they are not suitable for the vehicle. In order to solve these problems, a CO_2 inflator is introduced to be used as the valve. As shown in Figure 4-14, the threads on the top of the CO_2 cartridge are used to engage with the CO_2 inflator. The total weight of the CO_2 cartridge is 96 g.

Figure 4-14: 25 grams CO_2 cartridge

4.5.3 CO_2 inflator

The CO_2 inflator is used as an external mechanism to release the gas inside CO_2 cartridge. The inflator and cartridge are engaged by the threads in the engagement at the rear of the CO_2 inflator and top of the CO_2 cartridge as shown in Figure 4-15. Inside the inflator engagement, there is a hollow body piercing needle indicated in Figure, which punctures the cartridge cap while the CO_2 cartridge is being threaded in, namely installation of the CO_2 cartridge. Then, the CO_2 is released through the tunnel of the hollow needle. The valve in the inflator can block the gas until the inflation head is pressed back as depicted in Figure 4-15. The CO_2 inflator weight is only 15.5 g and the maximum diameter is 2.2 cm.

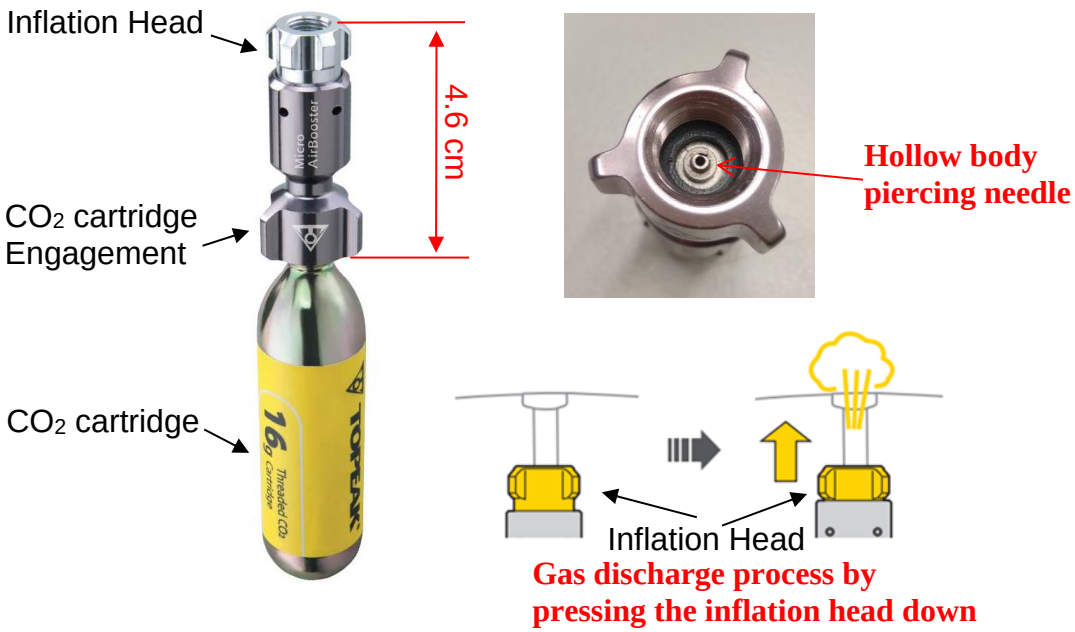

Figure 4-15: CO_2 inflator engaged with the CO_2 cartridge and the gas discharge method [84]

4.5.4 Actuator

The servo is used as an actuator to operate the press plate, which presses the inflation head and releases the pressurized gas, through the linkage as shown in Figure 4-13. The tests were conducted to measure the force for pressing the inflation head, which is 147 N. Therefore, the Savox® SV-1272SG Digital Metal Gear servo displayed in Figure 4-16 is selected as the actuator. The servo weight is 62 g. It can provide the 30 kg·cm torque under 7.4 V voltage power supply. The moment arm for the servo is 1.5 cm. Thus, 196 N force can be provided. Two servos are arranged in axisymmetric distribution around the inflator, which provides a balanced moment and stable actuation force. In addition, the servo has a relatively low profile, which can be contained in the fuselage. Two 3D printed servo seats are used to clamp the inflator in the middle and mount the servos.

Figure 4-16: Savox® SV-1272SG Digital Metal Gear Servo [85]

4.5.5 Telescopic adapter

There is a telescopic adapter needs to be introduced to make sure that the gas can be released into the water chamber without changing the transition propulsion system configuration. During the actuation of the gas release mechanism, the inflation head needs to be pressed down. This moves the water chamber if it is connected directly to the inflation head, which changes the system configuration. As shown in Figure 4-17, a fixed guide tube is used as a guide that a movable tube can be slid inside, and the fixed guide tube is screwed on the top of the water chamber by M18 threads to avoid any leakage. Moreover, the movable tube is screwed on the inflation head by 5/16" × 32 threads. A press plate is clamped by the inflation head and the locating nut, which is screwed on the thread of the movable tube. In this way, when the servos operate the press plate to press down the inflation head, the movable tube moves with the inflation head along the fixed guide tube. Then, the released CO_2 gas can pass through the adapter, and be injected into the water chamber without moving the fixed water chamber and gas release mechanism.

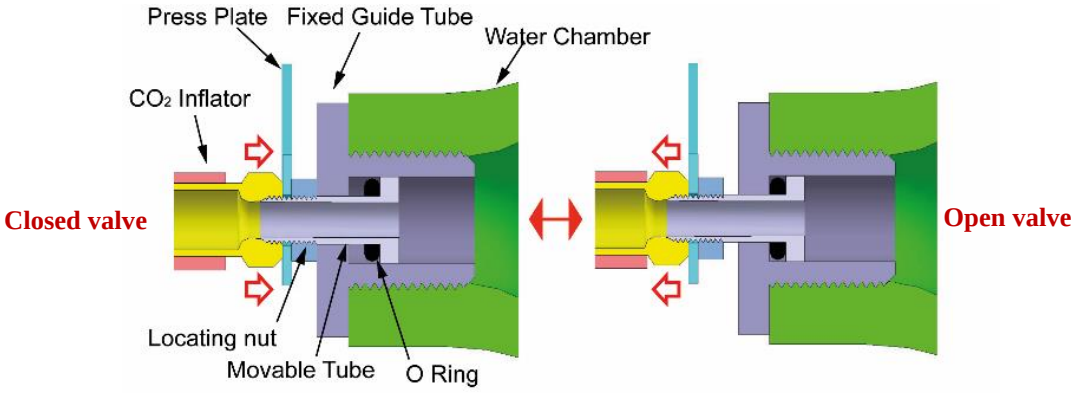

Figure 4-17: Telescopic adapter valve working principle

An O ring is placed over the inner cylinder of the movable tube under the tube shoulder. After the movable tube is pulled down, the O ring fills the gap between the movable tube and fixed guide tube to block the pressurised gas leakage. As a design result, the whole system is lighter if compared to the heavy hydraulic valve. The fabricated movable tube and the fixed guide tube are displayed in Figure 4-18. They are made from aluminium, which is rust resistant and lightweight. Those two parts have a weight of 11.5 g.

Figure 4-18: Fabricated movable tube and fixed guide tube

4.6 THRUST EXPERIMENT

An experimental approach is used to validate data coming from analytical and numerical simulations for the described transition propulsion system. Different experimental tests were performed on the water chamber with five different set of exit areas same as the simulation. The experimental tests also obtain the influence rule of the exit area on thrust and detect the optimal size of this critical element.

4.6.1 Experiment set-up

Water chamber samples

The tested water chamber is 3D printed in high strength and dense vero-white plastic material. The chamber is fabricated into two parts, the main part and the nozzle. One main part is fixed, and the nozzle part is changeable with different exit diameter size (5 mm, 7 mm, 9 mm, 11 mm, and 13 mm). Those two parts are connected by bolts and rubber washer to prevent the leakage as described in Figure 4-19. This two-parts design reduces the fabrication time and is economical.

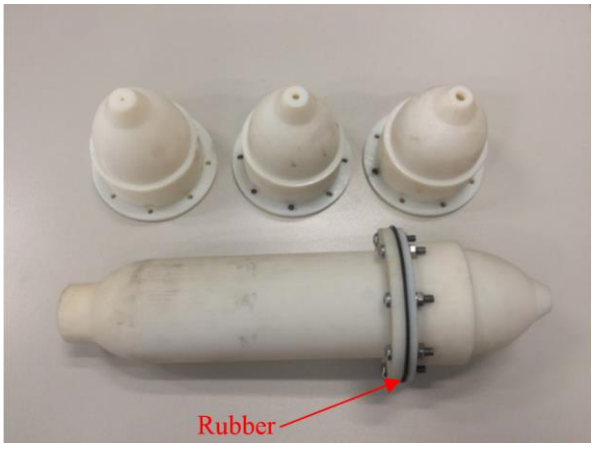

Figure 4-19: Manufactured water chamber with different size nozzle

Control system

The controller is the Futaba 14SG, which is a 14-Channel 2.4 GHz radio system. It sends out a signal that is picked up by the receiver and then sent to the servos. The power supply should pair with the servo working voltage. Then, the selected battery is the Dualsky® 7.4 V 800 mAh Lithium polymer (LiPo) Battery with a weight of 42.5 g. Besides, the battery also connects with the ESC to provide power for the receiver. The selected ESC is the 5.5 g Dualsky® 6 Amps ESC, which can easily handle the power supply for the receiver. The pictures of devices and their connection diagram are displayed in Figure 4-20.

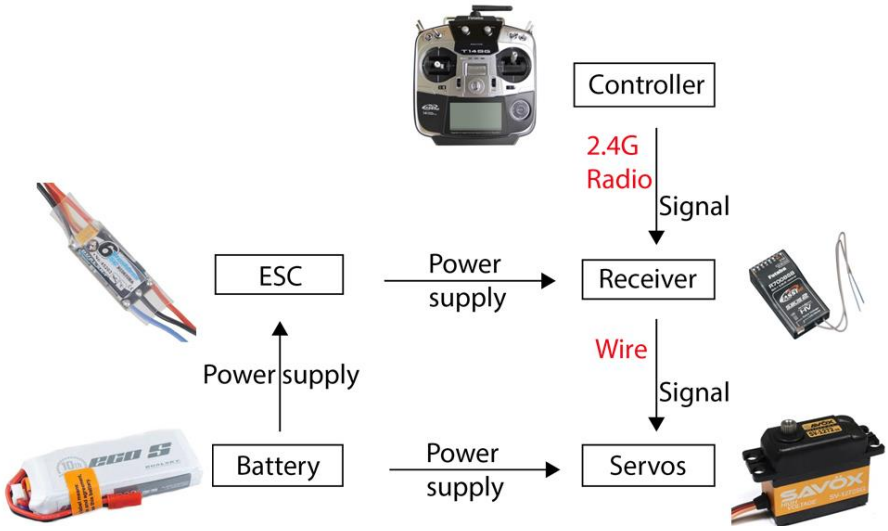

Figure 4-20: Devices connection diagram

Set-up

The devices arrangement on the test rig is illustrated in Figure 4-21. The experiment was conducted in the water tank, which size is 1,650 mm × 760 mm × 870 mm. A test rig was placed on the water tank bottom and pressed by weights. This test rig was designed and built as rigidly as possible to avoid any vibrations and oscillations that may affect the results. The load cell, which was used to measure the thrust, was fixed on the test rig. To connect the transition propulsion system firmly with the load cell, the transition propulsion system was fastened rigidly on a steel holder while the steel holder was securely mounted under the load cell. As a result, the nozzle of the water chamber was 500 mm away from the bottom of the tank to reduce the grounds effects.

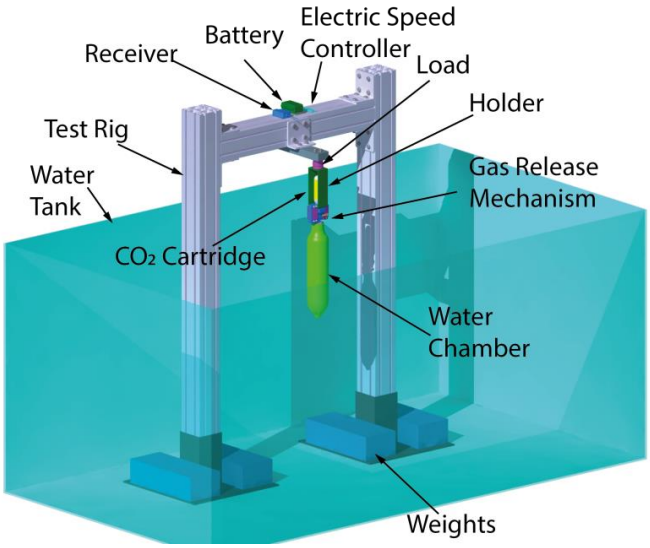

Figure 4-21: Transition propulsion system experiment layout

To detect and record the generated thrust, the load cell was connected to a data acquisition module as shown in Figure 4-22. After the CO_2 cartridge was threaded into the CO_2 inflator engagement and punctured, the gas release mechanism was activated remotely by the controller. Then, the water jet process started. The data was collected by the data acquisition module and recorded on a laptop while the thrust was being generated. Specifically, the HBM® U93 force transducer was used as the thrust load cell. It can measure thrust up to 1kN. The data acquisition module was composed by the laptop and the amplifier, which is the HBM® MX440A universal amplifier. During the experiment, the water chamber was totally submerged, while the mechanism was out of the water surface. Consequently, the pressure from the surround water will keep the water contained in the chamber before the actuation of the gas release mechanism.

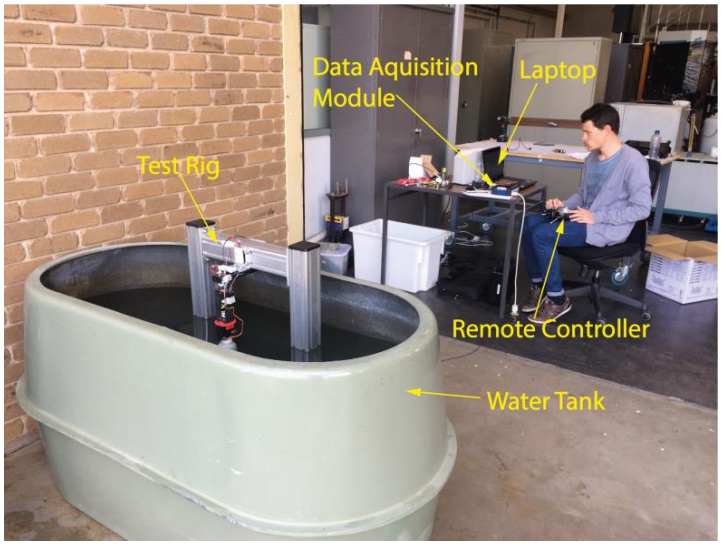

Figure 4-22: Actual experiment layout

4.6.2 Experiment results

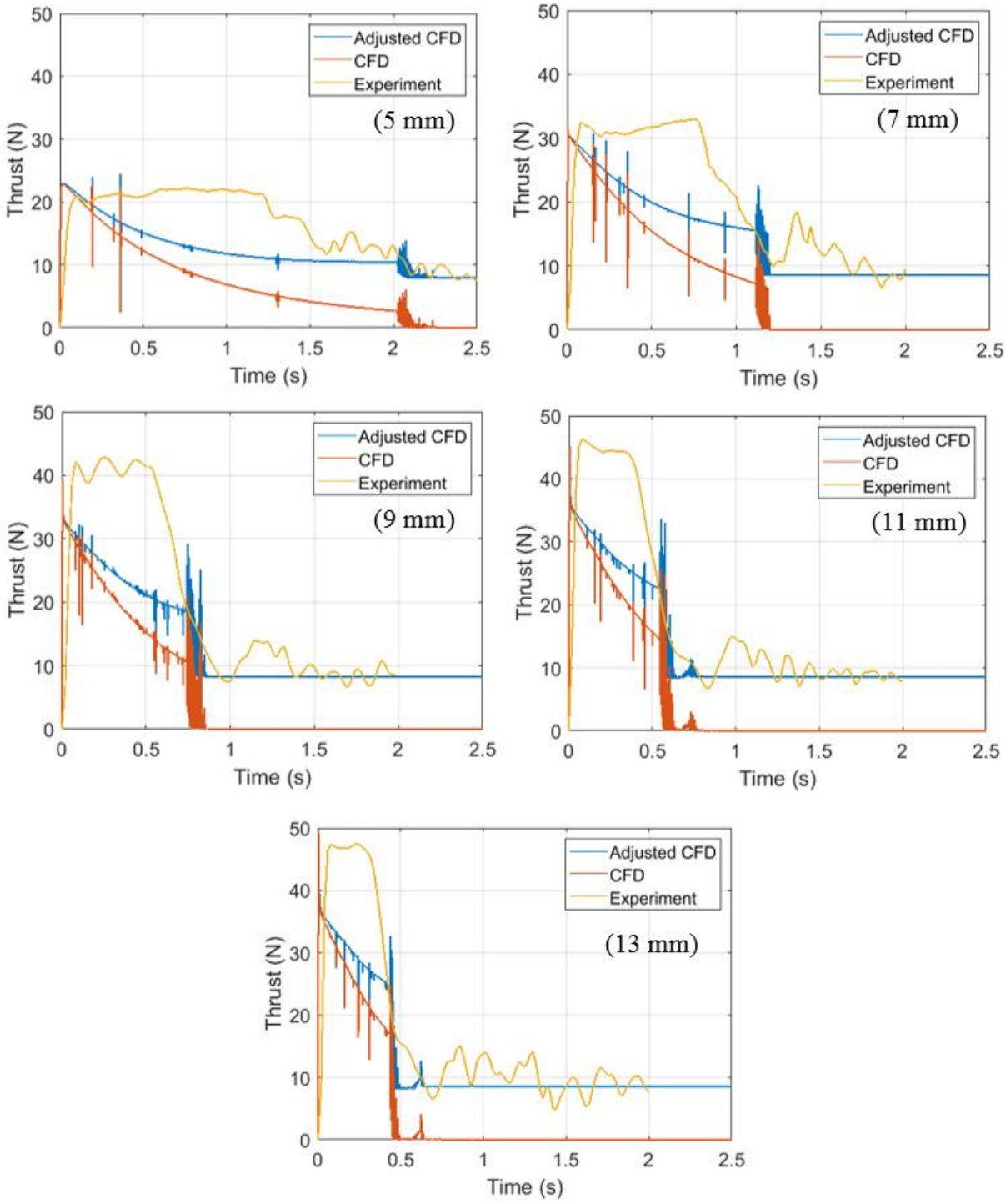

Figure 4-23: Experimental results - Thrust vs time for different exit area dimensions

The result of the experiment provides a similar behaviour with respect to the numerical simulation as shown in Figure 4-23. In addition, the results demonstrate that the consistent between numerical simulation and experiment in the peak thrust and thrust duration. However, in the experimental test, the thrust maintains at around 8.1 N after the water is expelled, rather than returns to zero. The reason is that as the water was being discharged, the lost weight of the

water was measured by the load cell as part of the thrust, with an increasing value up to 8.1 N. This value was the total weight of water in the chamber, which also extended the duration of peak thrust. Besides, this lost weight behaved like buoyancy of the system that was increasing along the jet process. It is important to highlight that the numerical simulation did not consider this aspect and as a matter of fact, the thrust value returned to zero after all the water was expelled. In order to verify the result from the numerical model, the water weight change was added into numerical simulation results according to the mass flow rate varying with time as presented in the adjusted numerical simulation curves.

In spite of the peak thrust only appeared at the beginning of the jet in numerical simulations, the peak thrust of experimental test last longer, and several peaks were detected. The multi-peaks could be explained by the water environment and the wave created by the jet and bubbles. Limited by the size of the water tank, the high-speed water expelled out of chamber stirred the water in the tank and created the wave that lifted the water chamber up. This produced part of the thrust. In addition, after all the water was expelled, the high-pressure gas was being expelled out of the water chamber and created a huge bubble, which was observed by the underwater camera. Then, the bubble produced a huge weave and lifted the chamber in a short time, which also generated a supplementary thrust. In the same time, the bubble might also decrease the thrust slightly since it might reduce the buoyancy force when the bubble was passing through the chamber, but this assumption should be verified by additional experiments. The whole process can be observed in the thrust curve. The peak thrust is prolonged and then the thrust decreases till the buoyancy produced by the chamber.

Moreover, the discrepancy in the appear time of the peak thrust between the simulation and experiment is observed. In the simulation, the valve in the inflator was opened instantly, while in the experiment the valve was actuated by servos. The servo response and actuation time was not as fast as in numerical simulation. This delayed the thrust peak and contributed a small mismatch on the initial thrust curve slope between experimental tests and numerical simulations.

In Figure 4-24, a summary of the transition propulsion system performances is demonstrated. The same trend of duration and peak thrust behaviour between the simulation and experiment changing with nozzle size can be noticed. Comparing the peak thrust between numerical simulation and experimental test, the average deviation is 7.4% while the average deviation for the thrust duration is 19.8%, since the wave and bubble effects increase the duration in the experiment. Regarding impulse values, the external elements such as wave and

bubbles increased the impulse in the experiment. In a practical application, these elements would be far from the vehicle in the transition phase, since the vehicle is moving forward. Despite these mismatches, the numerical simulation model implemented in the design process is a suitable model to predict the behaviour of the transition propulsion system.

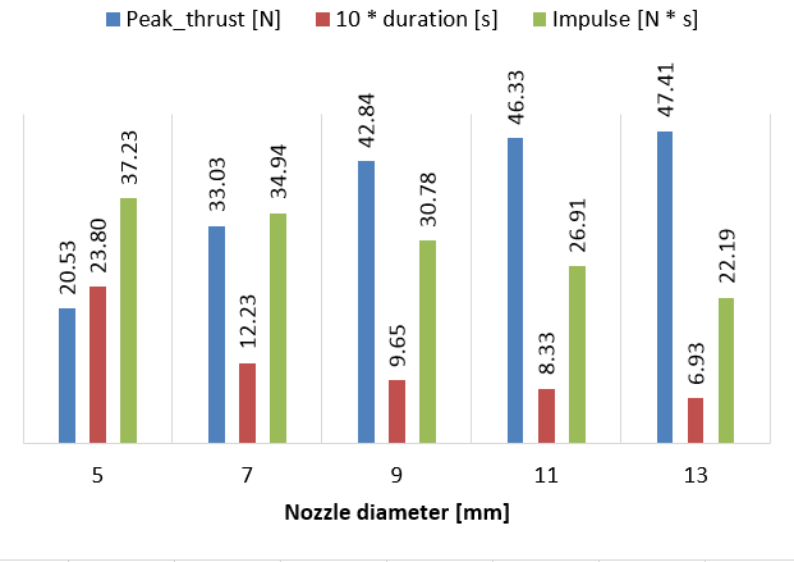

Figure 4-24: Experimental results - Peak thrust, impulse and duration for different exit area size

4.7 DESIGN PROCESS OUTCOME

In the presented study, a transition propulsion system for water/air transition application in the BUUAS is proposed. An iterative design process with analytical sizing, CFD refinement and experimental validation is described. Results of the experimental tests are compared with numerical simulations. It indicates the consistent behaviour especially on the peak thrust and thrust duration, but the wave and bubble effects increase the impulse in the experimental test. On the other hand, the amount of thrust given by the analytical model has a relatively lower peak and a shorter duration compared with the numerical simulation and experimental tests. This is because the assumptions are made to simplify the equations. However, the calibrated result is still satisfactory for the sizing purposes of the model.

The whole system can be upgraded to the BUUAS by using the approach above. The volume of the water chamber can be enlarged by extending the length to fit the thrust requirement. And the CO_2 cartridge can be upgraded to a higher-pressure cartridge with more volume of CO_2 gas. The gas release mechanism is responsible for the majority weight of the transition propulsion system. Therefore, the upgrade will not have a lot of weight penalties.

Some limitations are noticed in the CO_2 inflator, where the rubber seal requires a considerable period to recover its elasticity. This jeopardizes rapid operations. A better quality

seal rubber will be considered to improve the gas release mechanism performance. In conclusion, the results from the simulation and experiment support that the transition propulsion system fulfils the requirement. It is feasible to integrate the transition propulsion system with the proposed small vehicle and conduct the launching experimental test.

4.8 LAUNCH EXPERIMENT

The aspiration of the launching test is proofing the feasibility of the transition propulsion system on the prototype to present a sufficient thrust for the water escape and the validation between trajectory dynamic model and experimental results. As presented in Figure 4-25, the vehicle was launched from underwater using a remote-control trigger. A high-speed camera was used to record the vehicle trajectory, and a post-process software was used to analyse the trajectory to extract the velocity and height as a function of time. Since the launch angle is crucial for the entire trajectory and the vehicle performance, the launch experimental tests were carried at launch angles from 45º to 70º, which covered the range in the previous trajectory dynamic model.

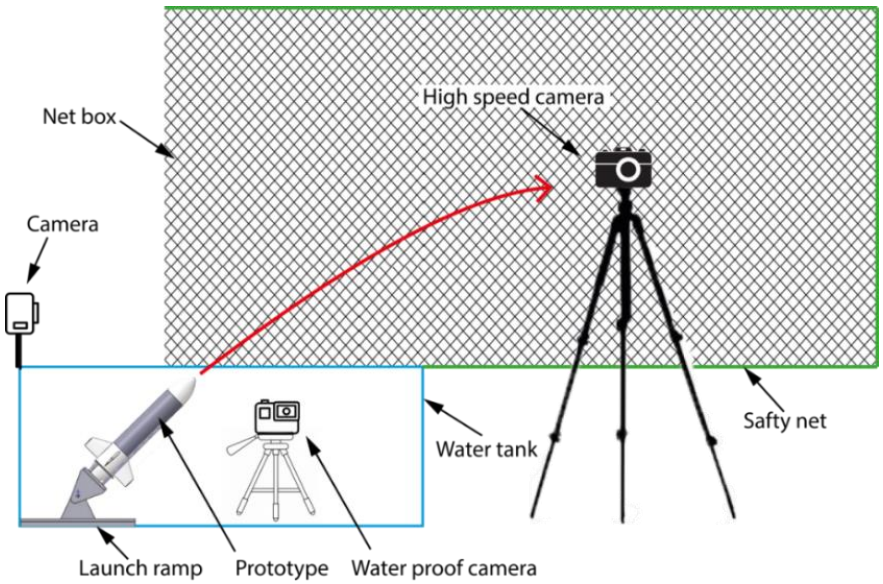

Figure 4-25: Experiment layout

4.8.1 Transition propulsion system integration

After the complete characterization of the transition propulsion system in terms of generated thrust, the system is integrated with a scaled vehicle. The integrated system layout is displayed in Figure 4-26. A new integral water chamber is constructed by 3D printing technology. It is made of ABS plastic, which is sufficiently rigid and water tightness. The diameter of the exit area is 7 mm due to its high impulse and sufficient thrust. The whole system

is 545 mm long and the total weight is 498.9 g, which is 4.1% lighter compared with the original predicted weight.

The proposed small vehicle is built to contain the transition propulsion system. The fuselage of the small vehicle is made by glass fibre tube. Four 3D printed fins are allocated in the rear to stabilize the vehicle. Besides, the support ring inside the fuselage supports the water chamber, and the gas release mechanism is fixed on a circular plate structure, which can perfectly fit into the fuselage tube and support the whole mechanism. Components can be slid into the fuselage by plugging out the nose. Likewise, the nose can be plugged out to access the devices inside for maintenance and replacing the CO_2 cartridge. The interference assembly between the 3D printed nose and fuselage guarantees that the whole vehicle is waterproof. The devices, such as the receiver, the battery, and the ESC, are hosted inside the nose. All the components are arranged as axisymmetric as possible to maintain the CG aligned with the axis of the vehicle. The total weight of the vehicle is 1088.1 g, which satisfies the original setting.

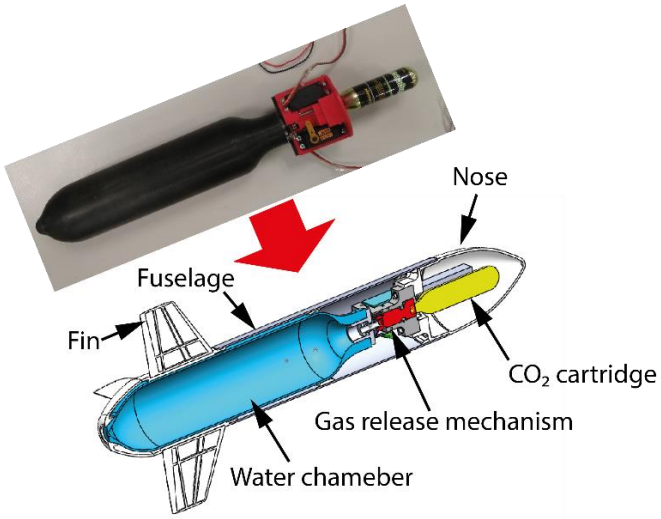

Figure 4-26: Transition propulsion system integration with a scaled vehicle for future transition simulations

4.8.2 Experiment set-up

As shown in Figure 4-27, the experiment set-up consists of a water tank, launch ramp, protection net, one high speed camera, and two waterproof cameras. Limited by the view range of the high-speed camera, only the initial trajectory after the vehicle exits water was recorded to assess the transition process and minimize the adverse effect from wind or other factors from the outside environment.

The arrangement of cameras is illustrated in Figure 4-25, three cameras were used to record the vehicle motion. One underwater camera provided motion tracking from an

underwater side view. One camera was located at the back of the water tank to record the front view after the vehicle exited the water. The primary high-speed camera Sony RX0® was used to record the side view of the whole aerial trajectory. It shot slow motion videos at high frame rates up to 1,000 fps, which was especially sufficient for the post-process.

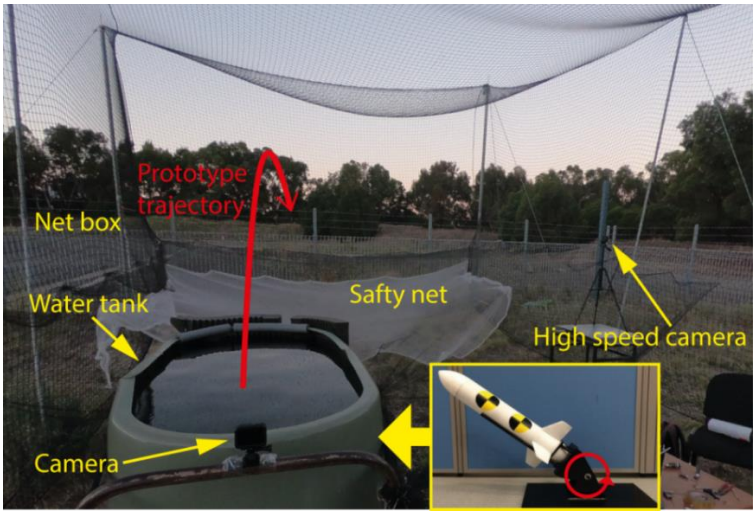

Figure 4-27: Experiment layout

A protection net was installed to ensure the vehicle was collected after launch without damage. The netted area was 3 meters in height, 3.5 meters in width and 4 meters in length. There were also two layers of safety nets constructed on the bottom of the net box to prevent the vehicle from falling to the ground, since the vehicle was expected to take a parabola trajectory or directly crush on the net wall, then fell to the safety net. A launch ramp, which was fixed on the basement of the water tank rigidly, was used to place the vehicle. Because the signal from the controller could not reach to the deep water, the variation of the depth where the vehicle would be launched was not included in this test. Same as the previous dynamic model, the vehicle was placed at the location that its bottom centre is 0.5 meters away from the water surface. The water tank was the same one used in the thrust test for the transition propulsion system. It was big enough to contain the vehicle for launching and instruments inside.

4.8.3 Experiment data process

The videos from the high-speed camera were imported into the post-process software Kinovea® to obtain the variation of the velocity, launch distance and attitude with time. As displayed in Figure 4-28, the yellow and black dummy symbol was tracked in the software with the real-time velocity and angle on the tag. Besides, the distance was examined by setting the calibration length, which was marked on the vehicle. The view range size of the camera at the plane of the vehicle trajectory was around 1.6 meters in high and 2.4 meters in wide, so

trajectories were analysed within this view range. This work was done in collaboration with the University of Bologna [86].

Figure 4-28: Kinovea tracking example [87]

4.8.4 Experiment results

During the test, the vehicle was successfully launched with sufficient thrust. Due to the view range of the camera and limited size for the net, not the whole trajectory was performed. In fact, outside of the camera view range, the vehicle could dash to the net celling easily, which revealed the excellent potential of the transition propulsion system as the power for the water escape. Figure 4-29 presents the vehicle behaviour inside the camera frame under different launch angles from 45° to 70°. In the presented result, the 45, 55, and 70 launch angles had obtained more than 1.5 meters height within the camera view range. The results from other launch angles are slightly smaller but still had 1 to 1.3 meters height gain, which means that the vehicle took a lower parabola trajectory.

The outcome of the experimental tests is similar to the analytical analysis. The result indicates that 1 to 1.5m height is gained in 0.3 seconds. However, the variation of the maximum altitude with increasing angle of attack is not consistent with the results from the analytical model. In the analytical model, with the increasing of the launch angle, the height is increasing. This irregular result can be explained by the following reasons. Firstly, the buoyancy caused the underwater trajectories deviation. Compared with the high launch angle, the vehicle travelled more distance under the low launch angle, so buoyancy could change the vehicle attitude when the vehicle was exiting water. Nevertheless, at the high launch angles, less underwater travel distance minimized the deviation caused by buoyancy. Secondly, the sealing between the CO_2 cartridge and inflator was rubber, and the sealing performance decreased with the wear and tear caused by frequent use. This caused leakage, which changed the vehicle performance. Thirdly, since the path of the vehicle without control surface mainly depends on

the launch angle and centre gravity of the vehicle, the different weight distribution between the analytical model and experiment could also cause the deviation.

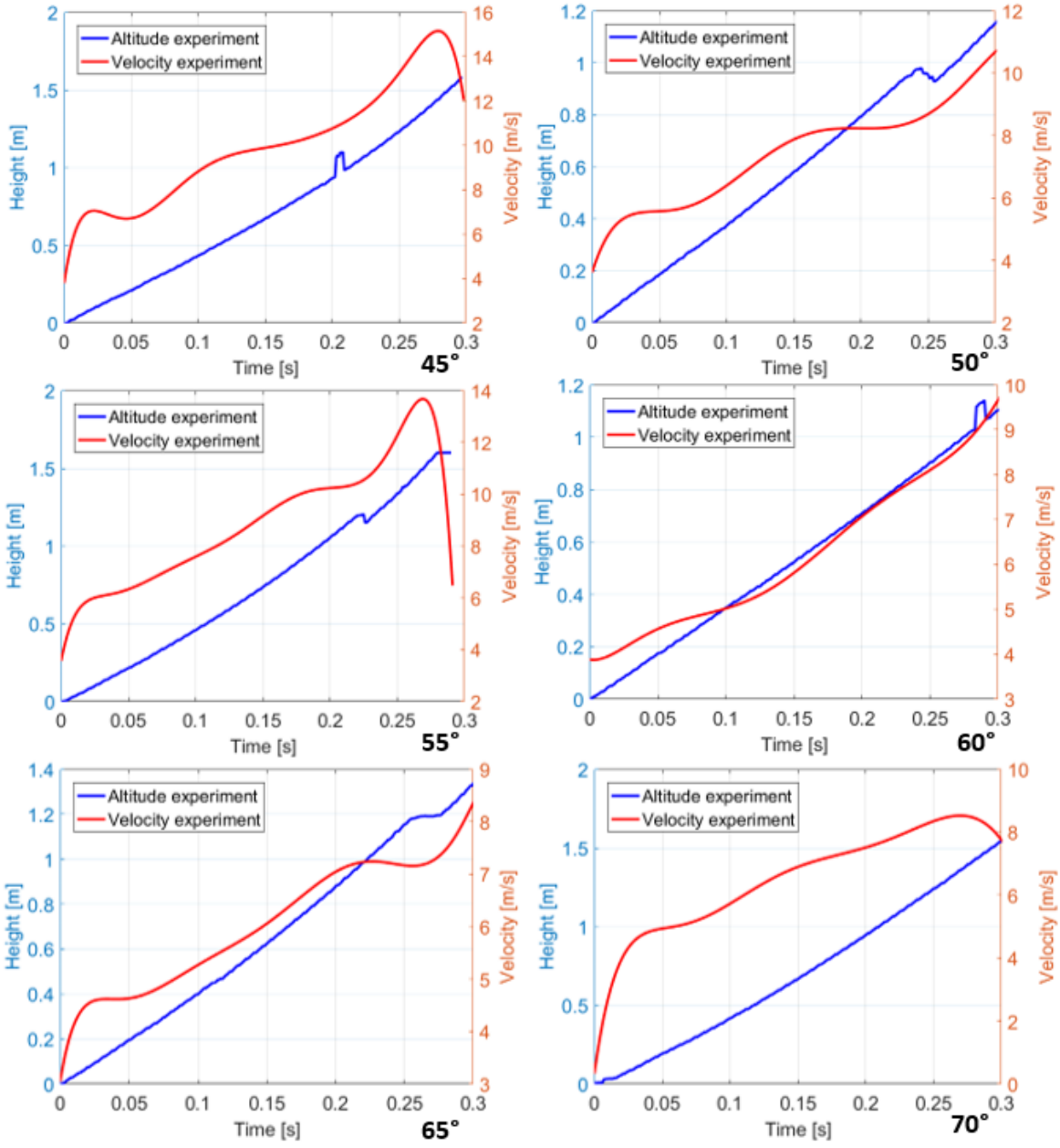

Figure 4-29: Altitude and velocity comparison between analytical model and experimental test

Regarding to the variation of the velocity, the general trend is that the velocity increases with a steep slope at the beginning state of the launch, and then a gentle slope in the middle of the trajectory. The steep slope of the velocity curve means the high thrust acceleration produced by the thrust. It can be explained from results of the previous thrust experiment. At the beginning of the thrust, there is a short time peak, which produces a short time high acceleration in the beginning of the trajectory. Besides, at the end of the trajectory, velocity drops appear at the launch angles at 45° and 55°. Due to the lack of control surfaces and the instability of the

vehicle, the pitch angle of the vehicle kept increasing. Then, the vehicle was stalled with a rapid velocity drop, and did not perform a desired parabolic at 45° and 55° launch angles. In addition, since the quality of the video is not clear enough and vehicle attitude was changing during the flight, the software lost tracking the yellow and black dummy symbol on the vehicle in a short time, which created the discontinuity in the altitude curve. This reduced the accuracy at some part of the curve, but the overall trajectory is still precise enough to analysis the vehicle performance.

To predict the complete launch height, the tested velocity and height in 70° launch angle were imported into the distance equation. The result indicates the vehicle can be launched up to 9.3 meters without the environmental and self stability interference. As a result, the height is satisfactory for a successful water escape. The design of the transition propuslion system fulfils requirements and demanded functions.

Chapter 5: Hybrid Propulsion System Design

5.1 PROPULSION SYSTEM LAYOUT

5.1.1 Hybrid propeller

A hybrid propeller, designed in collaboration with a student from the University of Bologna, is proposed for the BUUAS [87]. As displayed in Figure 5-1, the diameter of the propeller is 310 mm in the open configuration. The propeller includes an outside 4 blades air propeller and an inside 4 blades water propeller. They are connected by the middle hub. The air propeller can be folded back by the pressure of airflow or water flow when the motor stops running. This simple action avoids its damage when the vehicle impacts on the water surface in a dive. The folded air propeller in water also reduces the overall drag during the underwater cruise. Once the motor begins to rotate, the centrifugal force and aerodynamic force will spin fold the propellers outward to function as a normal air propeller. Additionally, the propeller test result indicates that at 6,000 RPM it produces at least 11.8 N thrust, which is adequate for the requirement mentioned in the concept design.

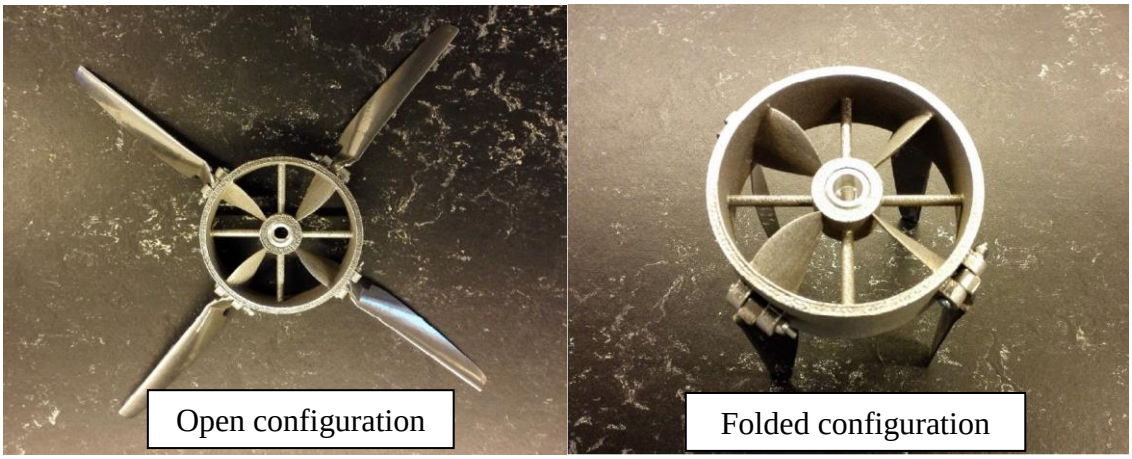

Figure 5-1: Titanium 3D printed hybrid propeller [87]

5.1.2 Propulsion system layout

The cross-section of the propulsion system is described in Figure 5-2. The hybrid propeller and motor are arranged at the aft of the vehicle. Given the axisymmetric design, the water-jet thrust produced by the transition propulsion system should be centred at the fuselage axis to minimize the unfavourable pitch up or pitch down moment which increases the control load during the transition. Since both the transition propulsion system and the hybrid propulsion system are concentric, a hollow shaft with inner diameter of 12 mm is used to allow the water-

jet to be rapidly expelled through a water tube inside. A short and straight tube is used to reduce the energy losses for the exiting water. Given assembly constraints, the water tube is 118.5 mm long with 10 mm inner diameter and 11 mm outer diameter. A 0.5 mm gap is set between the hollow shaft and the water tube to isolate the spinning for the fixed water tube. The water tube is connected to the nozzle of water chamber and mounted on the support plate by the lap joint to align with the vehicle central axis.

In a typical design, a motor would be placed centrally to directly drive the propeller. However, considering the presence of the water tube, a gear transmission system is developed to offset the motor. Accordingly, the transmission gears can transfer the torque to the hollow shaft, which the hybrid propeller is screwed on. Specifically, the hollow shaft is carried by two bearings mounted on the support plate and tail cone. Afterwards, the tail cone is mounted on the aft fuselage by inserting its sleeve into the aft fuselage structure and fastened by screws. Consequently, the components in the aft fuselage can be repaired and replaced by opening the tail cone. Besides, the sleeve of the tail cone with the O ring composes the waterproof structure. The water leakage can also develop around the bearing 1 area, since the shaft extends to the outside. This possible leakage is solved by the interference assembly between the bearing 1 and hollow shaft, and the interference mount between bearing 1 and aft tail cone.

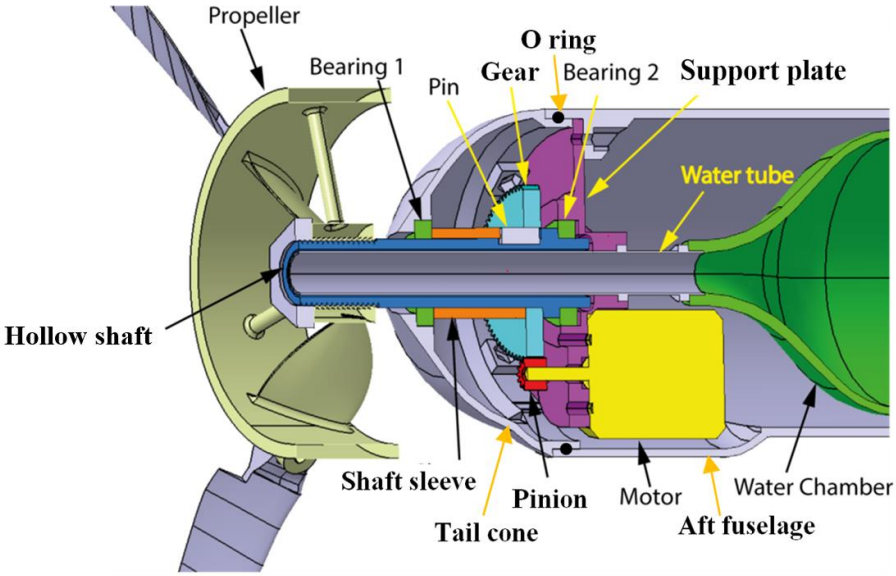

Figure 5-2: Propulsion system

Particularly, the shaft sleeve, hollow shaft, water tube and pin are made from the aluminium to take its advantages of lightweight and corrosion resistance to water. Additionally, the support plate is the 3D printed ABS plastic, which has enough strength to hold components

especially in the circumferential direction. It is fastened on attachments on the aft fuselage, which also provides strength in axis direction.

5.1.3 Gear transmission system design

The layout of the propulsion system produces the design constraint for the transmission system. Accordingly, the gear on the shaft should have large diameter to offset the motor. Thus, the reduction spur gears were used, which are a big gear on the hollow shaft and small gear on the motor shaft. Besides, this reduction gear design requires a high rotation speed motor with a small diameter configuration.

The gear transmission design is limited by the dimension of the fuselage and the diameter of the motor. At the beginning, the distance between the hollow shaft and the motor shaft, which is the centre distance is estimated as $C = 25mm$ based on the general size of the motors. Then, the small gear, which is 14T pinion, on the motor shaft is selected. Its module $\boldsymbol{m}_1$ is 0.5 mm and tooth number z_1 is 14. Therefore, the pitch diameter can be calculated by the Eq. (132)

$$d_1 = \boldsymbol{m}_1 z_1 \tag{132}$$

Eq. (132) yields the pitch diameter $d_1 = 7\ mm$. Accordingly, the pitch diameter of the big gear is given by,

$$d_2 = 2C - d_1 \tag{133}$$

Then, the gear pitch diameter is $d_2 = 18\ mm$. The modules must match to mate those two gears, which means that the gear modules $\boldsymbol{m}_2$ must equal to $\boldsymbol{m}_1$. Hence, the tooth number of the big gear can be obtained by using Eq. (132) with its own module and pitch diameter. This yields the big gear tooth number $z_2 = 86$. However, the supplier can only provide the gear with 84 tooth number, so the dimension is slightly changed to adopt the available gear. After the refinement, all the parameters are determined as presented in Table 5-1. Especially, the material of the pinion is aluminium, and the big gear is the Nylon, which can provide self-lubrication and low noise.

Table 5-1: Specification of the gear transmission

Category	Value
Module of the gears	0.5 mm
Pinion tooth number	14
Big gear tooth number	84
Pinion pitch diameter	7 mm

Big gear pitch diameter	42 mm
Centre diameter	24.5
Transmission ratio	6

5.1.4 Motor selection

After completing the reduction gear system design, the motor is selected based on the required RPM and available space in the aft fuselage. The operation range of the propeller is up to 6,000 RPM. Hence, the maximum RPM of the motor should be no less than 36,000, due to the reduction transmission ratio of 6. As a result, the selected motor is the Scorpion® HK-2520 brushless motor with KV value of 3,500. It is worth to mention that the KV is the specification of the brushless motor, which is the ratio of the RPM to the applied voltage and is usually taken to be the RPM/Volt. Therefore, the RPM of the motor is decided by the supplied voltage. In the previous section, the voltage of the selected battery is 14.8 V, so the maximum RPM that this motor can reach is 51,800, which satisfies the design requirement. As described in Figure 5-2, the motor is fastened on the support plate by M3 screws. The diameter of this motor is 31.5 mm, which can fit with the other components inside fuselage, but it exceeds the diameter of the fuselage after assembly. Thus, the shape of the aft fuselage is modified slightly to contain the motor without huge change on the configuration. The specification and dimension of the motor are presented in Appendix B.

5.1.5 ESC selection

An Electronic Speed Controller (ESC) is selected to pair with the motor. Besides, the ESC also works with the controller and receiver. The controller gives the signal to the receiver. Then, the receiver conveys the command to the ESC, which drives the brushless motor by providing an appropriate level of electrical power. The current rating is one of the critical criteria to choose ESC, since the ESC should be able to handle the current drawn from the spinning motor. Otherwise, the ESC will overheat and fail. According to the specification of the motor, there are two kinds of current ratings. One is the continuous current 55 A, which is the maximum continuous current during the normal flight. Another is the peak current 70 A, and this is the burst current rating when the motor is experiencing its maximum load. Nevertheless, it is just for the short periods of 2 seconds, otherwise the motor will be overheated even damaged. The most suitable ESC is the Dualsky® 60 A ESC. It can supply 60 A maximum continuous current and 80 A max burst current, which can easily handle the motor required current. In addition, the Dualsky® 60 A ESC is compatible with all brushless motor types up to 210,000 RPM and

works well with the 14.8 V LiPo battery. The specification and dimension are presented in Appendix B.

5.1.6 Remote control system

The 14 channels receiver and the controller for the transition propulsion system are used to control the vehicle. 10 channels of the receiver have been used so far. They are 2 channels for the linear actuators, 2 channels for the transition propulsion system servos, 2 channels for the aileron servos, 3 channels for the tail servos, and one channel for the ESC. The rest spare 4 channels can be used for the flight control and payload in future development.

5.2 PROPULSION SYSTEM INTEGRATION

The whole system integration is described in Figure 5-3. The components arrangement follows the initial weight distribution, which has been presented in Figure 2-7. After the assembly of the aft fuselage including the tail and hybrid propulsion system, the sleeve on the aft fuselage is inserted into the main fuselage tube to construct the lap joint and fixed by the 3M® 810 adhesive. This adhesive is compatible with plastic and composite and can deliver great strength of 3,600 psi. It guarantees the connection strength between aft fuselage and main fuselage.

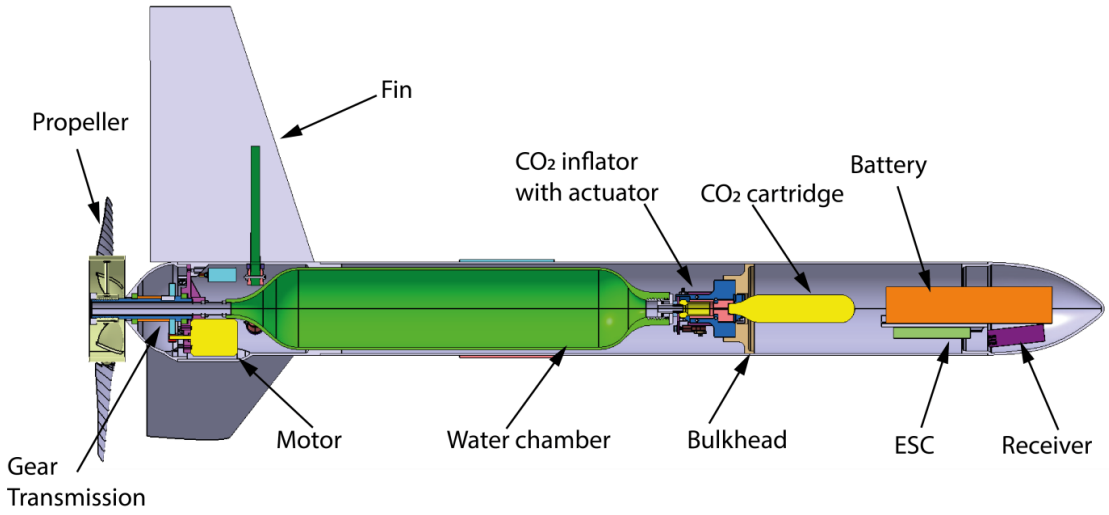

Figure 5-3: Propulsion system integration

The transition propulsion system is installed by plugging out the nose and sliding transition propulsion system into the fuselage tube. It is held by the bulkhead at the front and the aft fuselage sleeve at the rear. Moreover, the bulkhead also fixes the movement of the transition propulsion system along the fuselage axis. The avionics such as the battery, ESC and receiver, are arranged at the front. They can be accessed by taking the nose off. The wires from

the front are passing through the gap between the water chamber and fuselage to supply power and signal for the aft devices. In addition, the connection between the nose and fuselage is the interference lap joint design, which can make it water resistant, and be available to disassemble. As a result, the whole propulsion system is compact, and the space is efficiently used. Furthermore, the designed tolerance between components can guarantee the components running without interference. However, there is a potential problem that the hybrid propulsion may overheat since there is no heat dissipation system and the whole system is completely sealed. Due to the technology demonstrator design, only a short duration high speed flight operation, which can generate a lot of heat, is required. Therefore, the heat dissipation system is not required to be developed at the current stage, but it should be investigated for the fully functioned vehicle. Figure 5-4 shows the integration test in the wind tunnel while the hybrid propulsion system was working with all other components. In the meantime, the tail could function effectively without any interference. As a result, the hybrid propulsions system works properly with other components, which indicates the successful integration and structure design in propulsion systems and airframe structures.

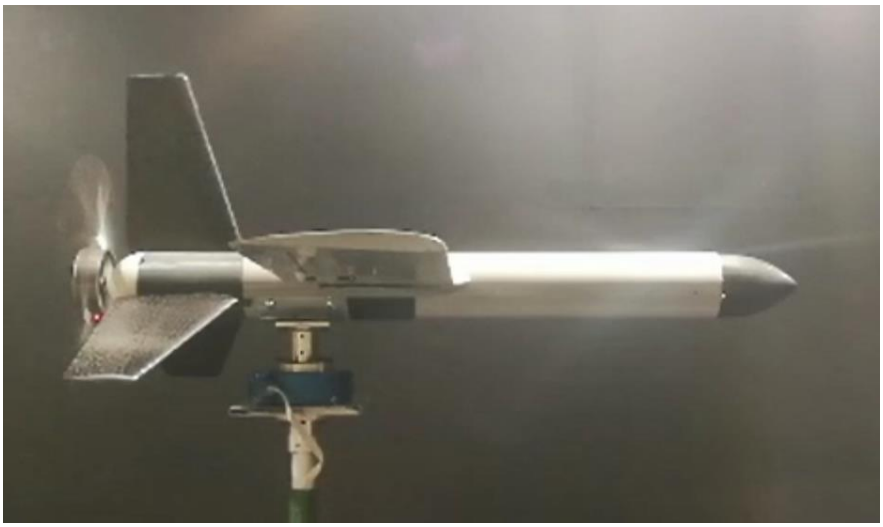

Figure 5-4: Vehicle integration test

5.2.1 Weight comparison

After integration, the actual weights of components are compared with the estimated weights in the conceptual design. The result is demonstrated in Table 5-2. The weight of transition propulsion system is increased 10% based on the constructed prototype due to the upgrade. As a result, the whole vehicle after the integration is 3.65 kg. In addition, after the final assembly, both the front and rear of the vehicle has gained the weight, so the location CG did not change.

Table 5-2: Verification of weight estimation

Components	Estimated Weight(g)	Actual Weight(g)	Precent Error
Hybrid propulsion system	460	530	15.21%
Transition propulsion system	520	548.8	5.53%
Avionics (receiver, ESC)	280	283.2	-1.13%
Battery	200	200.5	-0.25%
Tails with the structure and servos	445	453	1.81%
Fuselage tube	500	504.8	0.96%
Nose	64	52.4	-18.13%
Wing	640	667.4	4.28%
Wing-deployment mechanism	252	263	4.37%
Sleeve beam	150	151.4	0.93%
Total	3511	3654.5	4.09%

The final assembly weight increased by 4.09% compared with the initial estimate. The additional weight is from the manufacturing, support structure of the avionics system and hybrid propulsion system. Out of the expectation, the 3D printed titanium hybrid propeller is 250 grams, which is almost the half weight of the whole hybrid propulsion system. It increases the amount of weight. The alternatives materials such as nylon and carbon fibre can be considered in the future design. Besides, the manufacturing process also increased the weight of the wing due to lack of manufacturing experience. As a result, this increased weight has a small effect on the performance of the vehicle in the future experimental test, but this can be eliminated by optimizing the structure and propulsion system.

5.3 AIR EXPERIMENT SET-UP

The objective of the hybrid propulsion system experimental tests is to verify the performance and integration of the system in both air and water. The air experiment set-up depicted in Figure 5-5 consists of a test rig, load cell, data acquisition system, 14.8 V direct current (DC) power supply, RPM measurement and control system. An 3D printed adapter was introduced to firmly connect the hybrid propulsion system with the load cell. They were fastened together by the bolt connections. The RC benchmark® was used as the RPM measurement and control system. It provided the Pulse Width Modulation (PWM) signal for the ESC to control the RPM of the motor and received the feedback from the motor to calculation the real-time RPM.

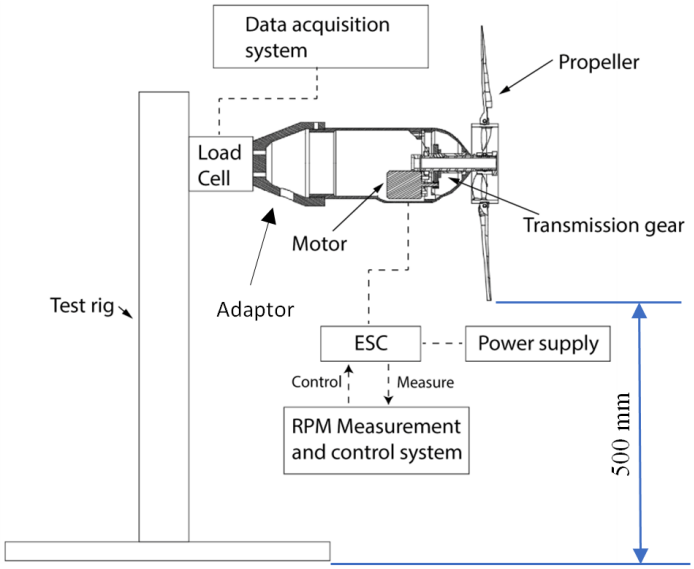

Figure 5-5: Air experiment set-up sketch

HBM® U93 force transducer was used as the thrust load cell. It measured the tensile and compressive force, which was the thrust in this experiment. The nominal force of the transducer is 1kN. Besides, the torque was measured by the torque sensor on the RC benchmark® using the same set-up. Particularly, the signal from the force transducer went through the HBM® MX440A universal amplifier, and was sent to a laptop where the signal was captured by the software. Then, the data was exported in a proper format for analysis. During the experiment, 100 samples were taken for each RPM. Afterwards, the data were processed, and the average values for each RPM were obtained. The actual set-up is displayed in Figure 5-6.

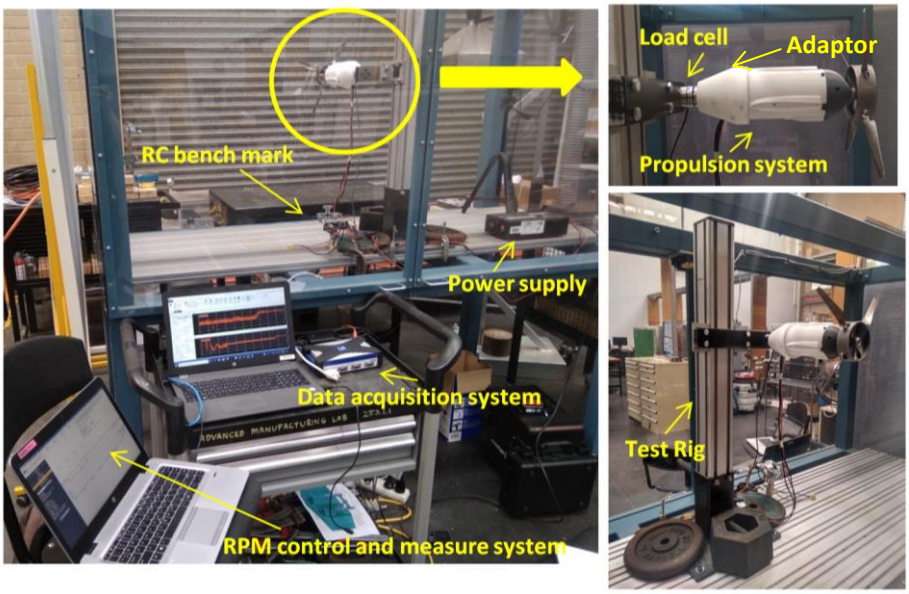

Figure 5-6: Air experiment set-up

As shown in Figure 5-6, the experiment was conducted in the cabinet with transparent plastic walls for the safety reason. The side that the propeller was facing, and the top of the cabinet were opened for the airflow. A 49 mm wide and 25 mm height steel spar, sufficiently rigid to avoid any bending was used to fix the load cell. Then, the spar is securely mounted on the test rig which was fastened on the cabinet bottom and pressed by weights to reduce any possible movement.

5.4 AIR EXPERIMENT RESULTS

The measurement results for the thrust and torque changing with the RPM are presented in Figure 5-7 and Figure 5-8. At 6,000 RPM, the system generates a thrust of 11.57 N, a torque of 0.84 Nm. Further, the tested thrust to weight ratio is 0.311, which satisfies the initial design requirement of 0.301. The result also indicates the consistent outcome with previous propeller test performed without the propulsion system reported in Figure 5-9 from [87]. In the propeller test, the thrust at 6,000 RPM is 11.8 N, which shows a minimal 1.95 % loss after the integration with the gear transmission system. Comparing to the 0.66 Nm maximum torque of the propeller test, the torque of the whole propulsion system increases to 0.84 Nm with an increase of 27.3%. The reason for this is that more torque is needed to counter the resistance between the gears. In conclusion, the air experiment shows the successful integration and sufficient thrust of the hybrid propulsion system for the BUUAS.

The thrust at 20 m/s flight speed is measured in the wind tunnel as shown in Figure 5-10. Limited by equipment in wind tunnel, only 2,500 to 4,500 RPM were performed. The result shows that the efficiency is increasing with the increase of RPM, which is also the decrease of propeller advance ratio under a constant fluid velocity. Particularly, around 4,200 RPM the efficiency of the propeller exceeds the result from the static thrust experiment. To acquire the maximum efficiency and the thrust change with different fluid velocity, more experiment can be performed in the future development.

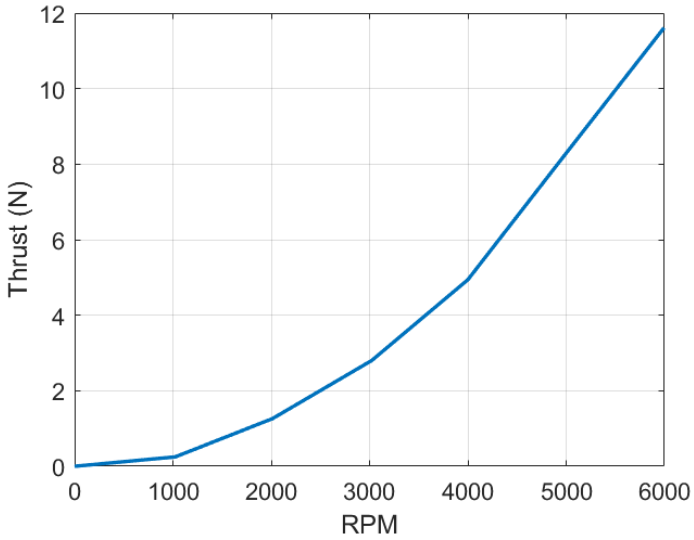

Figure 5-7: Thrust versus RPM

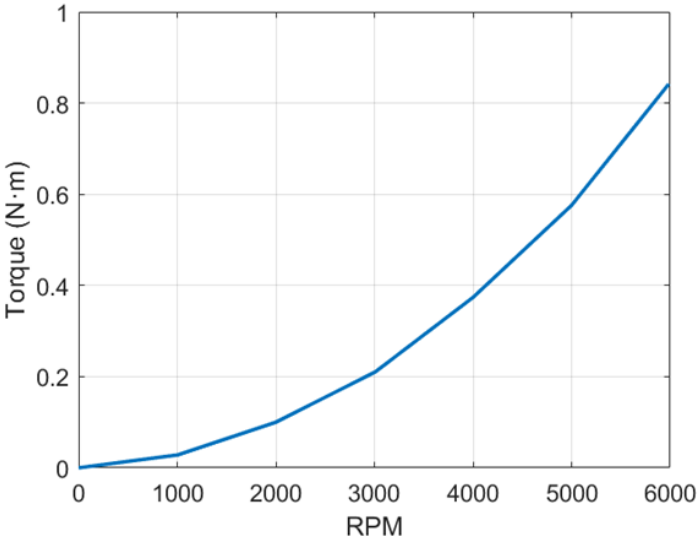

Figure 5-8: Torque versus RPM

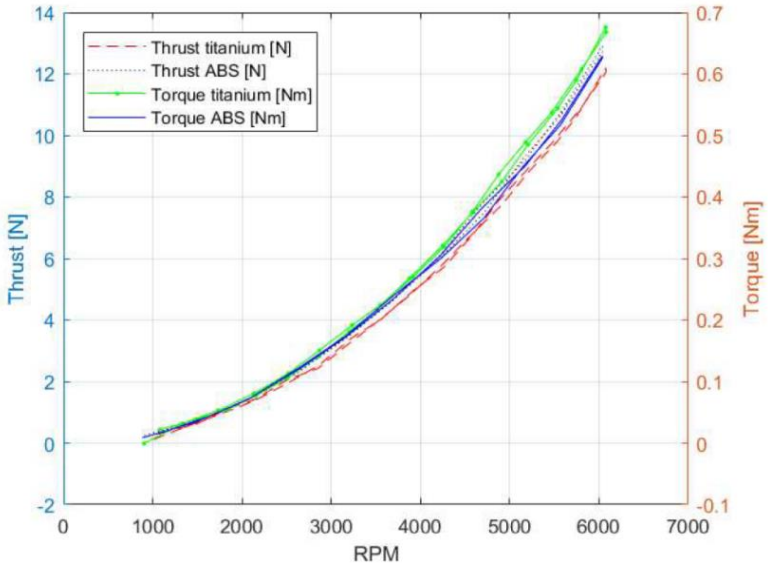

Figure 5-9: Test result of the hybrid propeller [87]

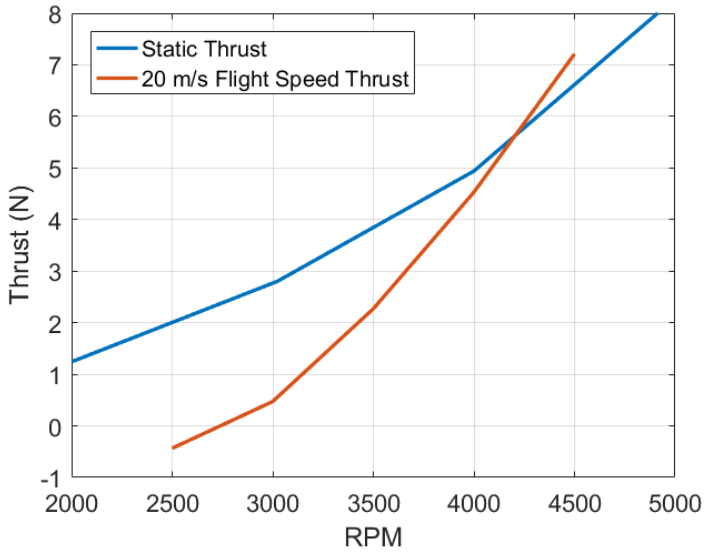

Figure 5-10: Thrust versus RPM at 20m/s fligth speed

5.5 WATER EXPERIMENT SET-UP

The set-up layout for the underwater test is depicted in Figure 5-11. The devices of the underwater experimental test were the same as the air experimental test, but the configuration of the test rig was changed. In the underwater experimental test, the spar holding the load cell faced downward. Therefore, the propulsion system could be submerged into the water to enable underwater testing after the propulsion system was mounted on the load cell. The test rig was placed in the water tank, which was the one used in the transition propulsion system thrust test and the launch test. Same as the air test, the base of the test rig was pressed by the weights underwater.

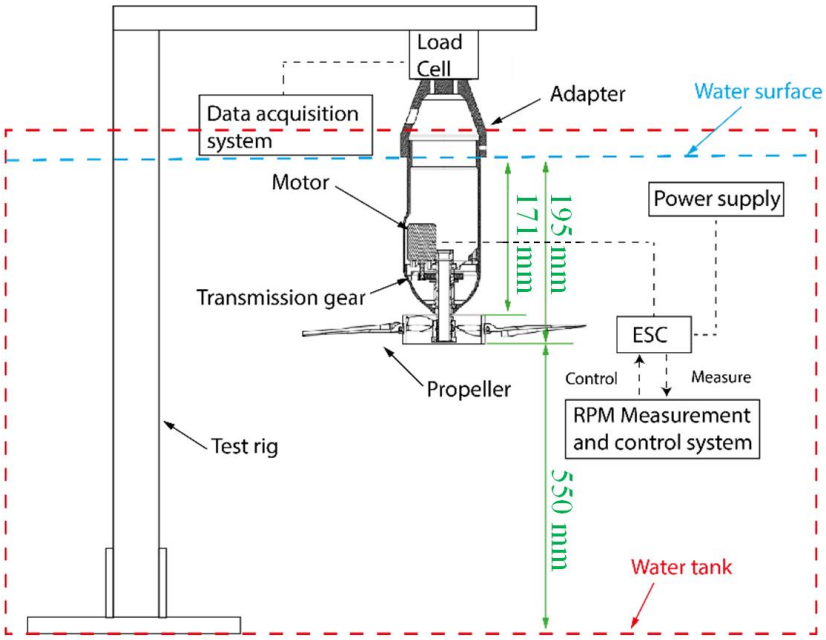

Figure 5-11: Water experiment set-up sketch

Since the connection between the propulsion system and the adaptor was not totally sealed, and the load cell was not waterproof, the submerged length of the propulsion system was 195 mm. The set-up photo in Figure 5-12 displays the actual experiment set-up, when the propulsion system was not fully submerged into the water yet. Limited by the lack of splash waterproof torque measurement equipment, only the thrust was measured in the underwater experiment test.

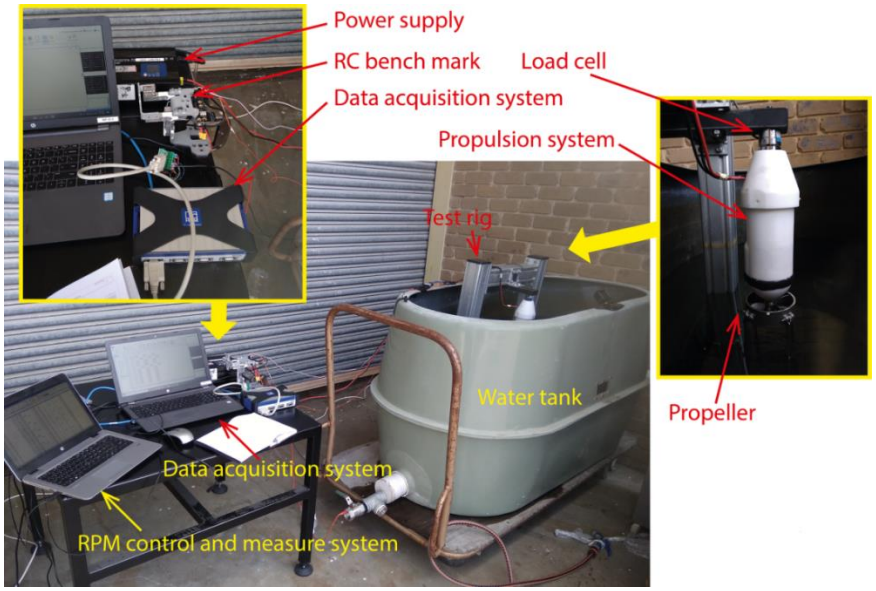

Figure 5-12: Water experiment set-up

5.6 WATER EXPERIMENT RESULTS

Figure 5-13: Screen capture of the underwater propulsion system testing

A camera was placed on the bottom of the water tank to record the status of the spinning propeller as shown in Figure 5-13. The air propeller was folded out in the underwater water operation. However, during the actual underwater cruise situation, the vehicle moves forward, so the drag may fold the propeller back, which is in the opposite direction that the vehicle

travels. In the experiment, the opened air propeller introduced an amount of the resistance and torque acted on the whole propeller. The selected motor can run at high RPM with low torque, but at the low RPM and high torque scenario, the motor does not function appropriately. At about 400 RPM, the motor stop working properly. It was noted that an increase in RPM produces an increase in torque, but the motor could not provide enough torque to drive the propeller.

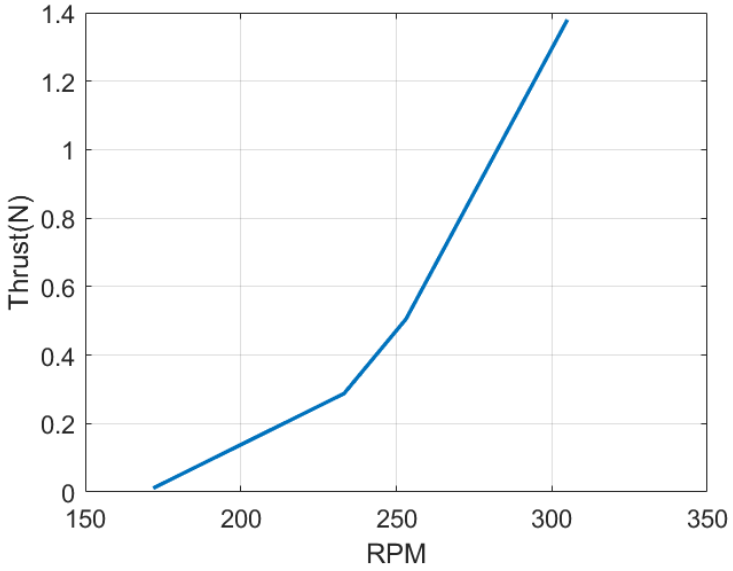

Figure 5-14: Thrust versus RPM

Due to the limited operational range of the motor, only data at the RPM below 400 could be acquired as presented in Figure 5-14. At the 300 RPM, the thrust can reach to 1.380 N. The trend of the thrust curve shows the potential of the underwater propulsion, even though the thrust did not reach the required level. Consequently, the motor should be carefully selected or modified to fulfil both air and water requirement. In addition, there were small eddies on the water surface when the propeller was spinning underwater. It indicates that the propulsion system might not be submerged in an enough depth condition, which can have influence on the test result. To increase the test depth, the adapter and load cell on the test rig can be designed to be waterproof in the future, so the water surface effect can be removed.

Chapter 6: Conclusions and Future Work

This thesis provides details on the development of the BUUAS, a novel bi-modal unmanned underwater/air system. It focuses on three main design aspects: A variable-sweep wing configuration design, the water-to-air transition propulsion system, and the hybrid propulsion system.

The deployed and folded configurations, which are used for the air and water operation, are designed following the aircraft design process with the compromise for underwater movement. Especially, the proposed solution includes a variable-sweep wing with an inverted Y-tail configuration. Furthermore, the numerical simulation for the aerodynamic and the hydrodynamic configurations predicts the capability of the vehicle to operate in air/water. To achieve the change of the configuration, the wing is deployed with the linear actuator in a rapid response time of 1.17 seconds, so that the vehicle obtains lift quickly during the water-to-air transition. Moreover, the result of the numerical analysis indicates importance of optimising the fairing area, which produces a large part of drag due to its bluff shape. Regarding the manufacturing, the foam core with carbon fibre sandwich structure used in the wing produces a lightweight structure with sufficient strength, which is proved during the wind tunnel test.

The performed wind tunnel experimental test verifies the results from design and numerical simulation. Moreover, the test results indicate that the folded wing configuration leads to a 10.43% drag coefficient reduction, which benefits the underwater cruise and the beginning stage of the transition, since the transition load can be reduced for the transition propulsion system. In addition, the lift coefficient increases by 52% when the vehicle transfers from folded to the deployed configuration. This demonstrates the importance of the transformation between the water and air configurations. Besides, the flaps produce an increase of 8% of the lift, which indicates that the rigid deploying wing equipped with a control surface is beneficial for the manoeuvrability and smooth water-to-air transition. Further, the stability analysis model presents the static and dynamic stable behaviour in most modes. However, a slightly unstable behaviour in spiral mode is detected, which can be rectified by an autopilot. By far, the underwater behaviour of the vehicle is still unknown. Unlike the flight condition, it is crucial to analysis buoyancy for the underwater locomotion. Additional numerical simulation and water tunnel testing are still required to assess the underwater performance and can be conducted in future work.

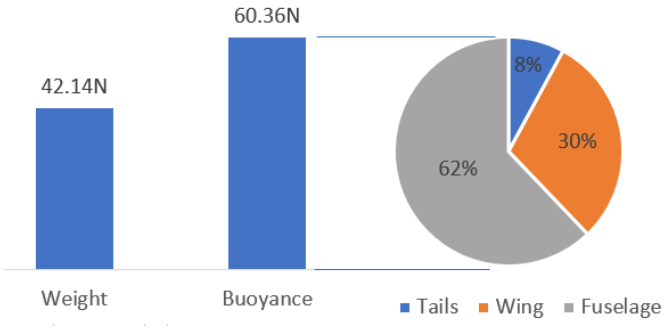

Figure 6-1: Buoyancy and weight comparison and components contribution

After the whole design process, the buoyancy of the vehicle has been measured according to its volume. As a result, the comparison between vehicle buoyancy and weight included water in the chamber has been shown in the Figure 6-1. It can be seen the buoyancy is larger than the weight 30%, which may produce amount of difficulty for the underwater control. Particularly, the wing contributes 30% buoyancy. If the wing can be eliminated or modified to reduce the effect of redundant buoyancy, the vehicle can achieve neutral buoyancy which is beneficial for the underwater travelling. In addition, the wing has less avionics and components inside as presented before, so it is an ideal part to be modified or adopted. Therefore, a hollowing wing structure has been proposed for a future consideration. As shown in Figure 6-2, the wing root and tip are open, so the water can pass through the inside of hollow wing. Therefore, the volume of the wing is tremendous reduced. On the other hand, when vehicle is launched from water to air, the water inside the wing can be easily emptied by gravity and its inertia. Regarding to the manufacture and structure difficulty for this new wing design, the utilization of composite material can overcome the fabrication challenge by reinforcing the strength of the skin instead of the beam and spar.

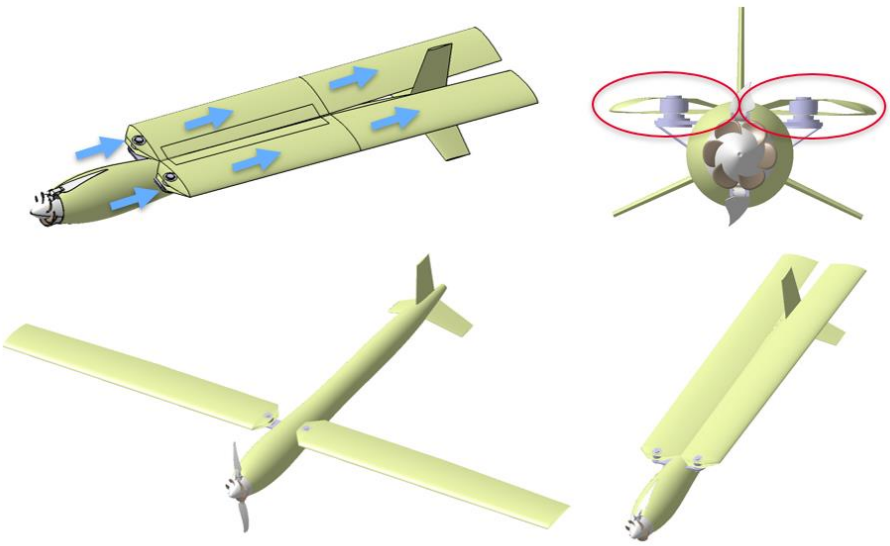

Figure 6-2: Hollow wing design and future configuration

The transition propulsion system is properly sized using analytical models calibrated by high-fidelity numerical simulation approach in combination with a trajectory prediction model. The calibration approach takes the advantages of the fast calculation time under less resources of the analytical model and the high fidelity of the numerical model. It is identified that the water volume inside the chamber domain the duration of the thrust. Subsequently, the proper water volume is optimized by the evaluation from the trajectory prediction model. According to the analytical model, the numerical model and experimental test are carried out based on the different size of the exit area. The variations of peak thrust, impulse, and duration with the size of the exit area were proposed and the trend of the variations between simulation and experiment is consistent. However, the difference of the peak thrust duration between those two methods indicates adverse effects in the experiment. Those unfavourable effects are waves and bubbles created during the water jet process. Further work should be done to eliminate those adverse conditions. In addition, the water-to-air launch experiment was conducted after the transition propulsion system was applied on the scaled small size prototype vehicle. The launch trajectories present promising result in terms of altitude reached. On the other hand, results also reveal the vehicle random behaviour, which was caused by limited control and buoyancy effect. As a result, the whole transition propulsion system can be upgraded for the full scaled model by using the strategy above.

This thesis mainly focusses on how the vehicle exits from the water. The landing and submerging process should be studied in future work. Additionally, the water collection system should be conceived to fill the empty water chamber as well as add the volume of the propellant, which can also help the vehicle submerge into the water by introducing the weight. A design concept has been conceived for the transition from air to water by using minimum extra mechanisms. As shown in Figure 6-3 below, two channels are introduced to conduct water from outside to the water chamber. When the vehicle is diving into the water, the pressure and impact from water which is passing through channels, can open the doors on the chamber. After that, the water chamber will be filled with water, while the air inside chamber will escape from the exit nozzle on the chamber. In between, with the vehicle weight increasing with added water, the vehicle can achieve neutral or negative buoyancy. If the vehicle needs to transit from water to air, the high pressure CO_2 from the CO_2 cartridge can close doors by using its pressure after being injected into the water chamber. Due to the corn shape design of doors, the chamber can be sealed. In addition, a simple mechanism, which can assist the door open and close movement can be introduced if it is necessary.

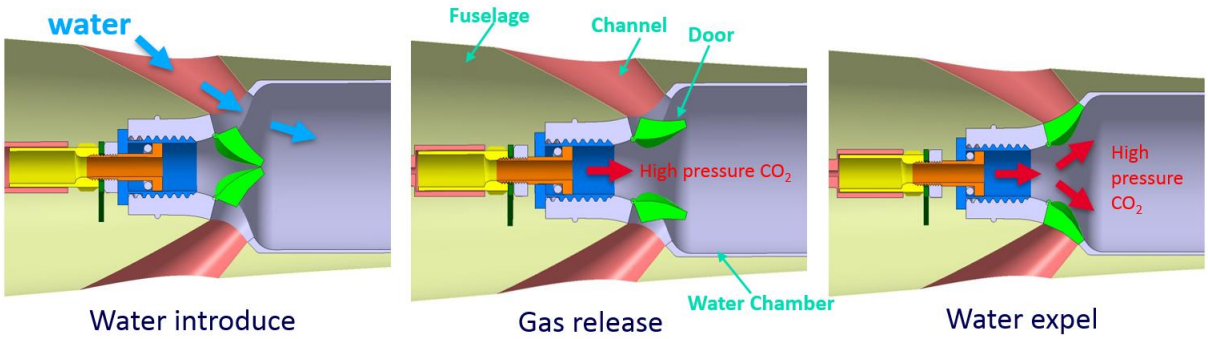

Figure 6-3: Water to air transition strategy

The air experiments for the hybrid propulsion system indicate a satisfactory propeller and transmission system performance, and the sufficient thrust to weight ratio. Comparing to the propeller design, there is almost no energy loses, which demonstrates the high efficiency of the gear reduction system. Limited by the torque of the motor, the RPM for the underwater test did not exceed 400 RPM. Nevertheless, the results show the potential to reach the required thrust, which is a valuable experience for the selection of a new motor capable of operating at low RPM with high torque.

Comparing to the multi-motor propulsion, the hybrid propulsion system shows significant advantages given the compactness, lightweight, and suitable integration with the transition propulsion system and the tail structure. After the integration, the weight of the whole system is 3.65 kg. Notably, the 3D printed titanium hybrid propeller is heavier than expected. Its 250 grams weight occupies almost half of the whole propulsion system total weight. It is recommended using other material, such as nylon or carbon fibre, for future propellers. Consequently, the light propulsion system can improve the weight distribution, so the wing can be placed forward, which can increase the distance between wing and tail. This can increase the sweep back angle and reduce the front area, which assists the underwater cruise and water to air transition. In addition, the size of the tail can be reduced further due to the longer moment arm, and vehicle weight can also be reduced with potential positive benefit in terms of performance and stability of the vehicle.

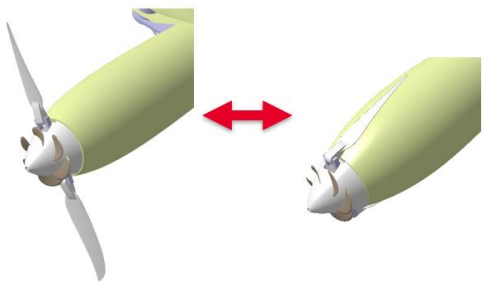

Figure 6-4: Front propulsion strategy

Figure 6-4 shows another possible design which can be considered in the future development. The propulsion is allocated at the front of the vehicle, and the air propeller is a foldable propeller design. Besides, the water propeller sits on the cone in the front of air propeller. The transformation between water and air mode can be realized by a clutch mechanism. In this way, the centre of gravity can be moved forward, the ideal sweep back angle and small tail size can be achieved as mentioned above.

References

1. Siddall, R. and M. Kovač, *Launching the AquaMAV: bioinspired design for aerial–aquatic robotic platforms.* Bioinspiration & biomimetics, 2014. **9**(3): p. 031001.
2. Yang, X., et al., *Survey on the novel hybrid aquatic–aerial amphibious aircraft: Aquatic unmanned aerial vehicle (AquaUAV).* Progress in Aerospace Sciences, 2015. **74**: p. 131-151.
3. Malhotra, C., *Conceptual Design for A Single Stage Dual Mode Unmanned Underwater Aerial Vehicle*. 2016, RMIT University: Melbourne. p. 44.
4. Low, K.H., et al., *Perspectives on biologically inspired hybrid and multi-modal locomotion.* Bioinspir Biomim, 2015. **10**(2): p. 020301.
5. Yang, X., et al. *Submersible unmanned aerial vehicle concept design study*. in *2013 Aviation Technology, Integration, and Operations Conference*. 2013. Los Angeles, USA.
6. G.Petrov. *Flyingsubmarine*. 1995; Available from: http://www.airforce.ru/aircraft/miscellaneous/flying_submarine/index.htm.
7. Reid, B.D., *The Flying Submarine: The Story of the Invention of the Reid Flying Submarine*. 2004, Berwyn Heights: Heritage Books Inc.
8. Austin, R., *Unmanned Aircraft Systems: UAVS Design, Development and Deployment*. 2010, Hoboken: Hoboken : Wiley.
9. Siddall, R. and M. Kovac, *Launching the AquaMAV: bioinspired design for aerial-aquatic robotic platforms.* Bioinspir Biomim, 2014. **9**(3): p. 031001.
10. Renilson, M., *Submarine hydrodynamics*. 2015: Springer.
11. Nicholson, J. and A. Healey, *The present state of autonomous underwater vehicle (AUV) applications and technologies.* Marine Technology Society Journal, 2008. **42**(1): p. 44-51.
12. Davis, R.E., C.C. Eriksen, and C.P. Jones, *Autonomous buoyancy-driven underwater gliders*. 2002, Taylor and Francis, London. p. 37-58.
13. Blidberg, D.R., *The development of autonomous underwater vehicles (AUV); a brief summary*, in *Ieee Icra*. 2001. p. 1.
14. Schofield, O., et al., *Slocum gliders: Robust and ready.* Journal of Field Robotics, 2007. **24**(6): p. 473-485.
15. Loh, B. and J. Jacob, *Hybrid Rigid/Inflatable Wings for Low Volume Wing Storage*. 2008, SAE Technical Paper.
16. Fabian, A., et al., *Hybrid aerial underwater vehicle.* SCOPE Projects Olin College of Engineering, 2012.
17. Gao, A. and A.H. Techet, *Design considerations for a robotic flying fish*, in *OCEANS 2011*. 2011, IEEE. p. 1-8.
18. Siddall, R. and M. Kovac, *Fast aquatic escape with a jet thruster.* IEEE/ASME Transactions on Mechatronics, 2017. **22**(1): p. 217-226.
19. Siddall, R., A. Ortega Ancel, and M. Kovac, *Wind and water tunnel testing of a morphing aquatic micro air vehicle.* Interface Focus, 2017. **7**(1): p. 20160085.
20. Dalamagkidis, K., *Aviation history and UAS.* Intelligent Systems, Control and Automation: Science and Engineering, 2009. **36**: p. 9-28.
21. Porter, B. *Diving Gannet Sequence*. [Picture] 2016; Available from: http://benporterphotography.blogspot.com/2016/04/diving-gannet-sequence.html.

22. Drews Jr, P.L., A.A. Neto, and M.F. Campos, *A Survey on Aerial Submersible Vehicles*, in *IEEE/OES Oceans International Conference*. 2009: Bremen, Germany. p. 4244-2523.
23. Wadoo, S. and P. Kachroo, *Autonomous underwater vehicles: modeling, control design and simulation*. 2016: CRC Press.
24. Yao, G., et al., *Submersible unmanned flying boat: Design and experiment*, in *Robotics and Biomimetics (ROBIO), 2014 IEEE International Conference on*. 2014, IEEE. p. 1308-1313.
25. Siddall, R., G. Kennedy, and M. Kovac, *High-power propulsion strategies for aquatic take-off in robotics*, in *Robotics Research*. 2018, Springer. p. 5-20.
26. Adm, R., *INTRODUCTION TO TORPEDO TECHNOLOGY*. 1993, Delhi: Defence Scientific Infonnation & Documentation Centre (DESIDOC),. 93.
27. Lock, R.J., et al., *Development of a biologically inspired multi-modal wing model for aerial-aquatic robotic vehicles through empirical and numerical modelling of the common guillemot, Uria aalge.* Bioinspiration & biomimetics, 2010. **5**(4): p. 046001.
28. Tan, Y.H., R. Siddall, and M. Kovac, *Efficient Aerial–Aquatic Locomotion With a Single Propulsion System.* IEEE Robotics and Automation Letters, 2017. **2**(3): p. 1304-1311.
29. Watson, S.A. and P.N. Green, *Propulsion systems for micro-autonomous underwater vehicles (μauvs)*, in *Robotics Automation and Mechatronics (RAM), 2010 IEEE Conference on*. 2010, IEEE. p. 435-440.
30. Brandt, S.A., *Small uav design development and sizing*, in *Handbook of Unmanned Aerial Vehicles*, K. Valavanis, Vachtsevanos, George J., Editor. 2018, Springer, Cham: Intelligent Technologies and Robotics. p. 1-18.
31. Kontogiannis, S.G. and J.A. Ekaterinaris, *Design, performance evaluation and optimization of a UAV.* Aerospace Science and Technology, 2013. **29**(1): p. 339-350.
32. Parada, L.M.A., *Conceptual and Preliminary Design of a Long Endurance Electric UAV*. 2016, Master's thesis, Instituto Superior Técnico.
33. Rajendran, P. and H. Smith, *Development of Design Methodology for a Small Solar-Powered Unmanned Aerial Vehicle.* International Journal of Aerospace Engineering, 2018. **2018**: p. 10.
34. Roskam, J., *Airplane Design VII: Determination of Stability, Control and Performance Characteristics: FAR and Military Requirements*. 1985: DARcorporation.
35. Gupta, S.G., M.M. Ghonge, and P. Jawandhiya, *Review of unmanned aircraft system (UAS).* International journal of advanced research in computer engineering & technology (IJARCET), 2013. **2**(4): p. 1646-1658.
36. Jacob, J. and S. Smith, *Design limitations of deployable wings for small low altitude UAVs*, in *47th AIAA Aerospace Sciences Meeting Including The New Horizons Forum and Aerospace Exposition*. 2009. p. 745.
37. Zaugg, E., D. Hudson, and D. Long, *The BYU SAR: A small, student-built SAR for UAV operation*, in *2006 IEEE International Symposium on Geoscience and Remote Sensing*. 2006, IEEE. p. 411-414.
38. Rajendran, P. and H. Smith, *Implications of longitude and latitude on the size of solar-powered UAV.* Energy conversion and management, 2015. **98**: p. 107-114.
39. Logan, M., et al., *Technology challenges in small UAV development*, in *Infotech@ Aerospace*. 2005. p. 7089.
40. IV, G.P.J., L.G. Pearlstine, and H.F. Percival, *An assessment of small unmanned aerial vehicles for wildlife research.* Wildlife Society Bulletin, 2006. **34**(3): p. 750-758.
41. Marta, A.C. and P. Gamboa, *Long endurance electric UAV for civilian surveillance missions*, in *St. Petersburg: International Council of Aeronautical Science*. 2014. p. 19.

42. Landolfo, G. and A. Altman, *Aerodynamic and structural design of a small nonplanar wing UAV*, in *47th AIAA Aerospace Sciences Meeting including The New Horizons Forum and Aerospace Exposition*. 2009. p. 1068.
43. Harmon, F.G., A.A. Frank, and J.-J. Chattot, *Conceptual design and simulation of a small hybrid-electric unmanned aerial vehicle.* Journal of Aircraft, 2006. **43**(5): p. 1490-1498.
44. Secanell, M., A. Suleman, and P. Gamboa, *Design of a morphing airfoil using aerodynamic shape optimization.* AIAA journal, 2006. **44**(7): p. 1550-1562.
45. Goraj, Z., *UAV platforms designed in WUT for border surveillance*, in *AIAA Infotech@ Aerospace 2007 Conference and Exhibit*. 2007. p. 2965.
46. Mueller, T.J. and J.D. DeLaurier, *Aerodynamics of small vehicles.* Annual review of fluid mechanics, 2003. **35**(1): p. 89-111.
47. Raymer, D., *Aircraft Design: A Conceptual Approach 5e and RDSWin STUDENT*. 2012: American Institute of Aeronautics and Astronautics, Inc.
48. Gertler, M., *Resistance experiments on a systematic series of streamlined bodies of revolution-for application to the design of high-speed submarines*. 1950, DAVID TAYLOR MODEL BASIN WASHINGTON DC.
49. Moonesun, M., et al., *Optimum L/D for submarine shape.* Indian Journal of Geo-Marine Sciences (IJMS), 2016. **45** (01): p. 38-43.
50. Jones, D.A., et al., *The calculation of hydrodynamic coefficients for underwater vehicles*. 2002, DSTO Platforms Sciences Laboratory: Victoria Australia. p. 31.
51. Traub, L.W., *Range and endurance estimates for battery-powered aircraft.* Journal of Aircraft, 2011. **48**(2): p. 703-707.
52. Gabriel, D.L., J. Meyer, and F. Du Plessis, *Brushless DC motor characterisation and selection for a fixed wing UAV*, in *IEEE Africon'11*. 2011, IEEE. p. 1-6.
53. Brandt, J. and M. Selig, *Propeller performance data at low reynolds numbers*, in *49th AIAA Aerospace Sciences Meeting including the New Horizons Forum and Aerospace Exposition*. 2011. p. 1255.
54. D'Epagnier, K., *AUV propellers: Optimal design and improving existing propellers for greater efficiency*, in *OCEANS 2006*. 2006, IEEE. p. 1-7.
55. Hwang, S.-J., et al., *Aerodynamic Design of the Solar-Powered High Altitude Long Endurance (HALE) Unmanned Aerial Vehicle (UAV).* International Journal of Aeronautical and Space Sciences, 2016. **17**(1): p. 132-138.
56. Akay, M. and R. Hanna, *A comparison of honeycomb-core and foam-core carbon-fibre/epoxy sandwich panels.* Composites, 1990. **21**(4): p. 325-331.
57. IRROBOT. *Dimension 27mm Stroke Version*. [Picture] 2019; Available from: http://www.irrobot.com/en/product-01-1/#lineup.
58. Ariff, M., S.M. Salim, and S.C. Cheah, *Wall y+ approach for dealing with turbulent flow over a surface mounted cube: Part 1—Low Reynolds number*, in *Seventh International Conference on CFD in the Minerals and Process Industries*. 2009. p. 1-6.
59. Lian, Y. and W. Shyy, *Laminar-turbulent transition of a low Reynolds number rigid or flexible airfoil.* AIAA journal, 2007. **45**(7): p. 1501-1513.
60. Johansen, J., J.N. S-oacute, and rensen, *Prediction of laminar/turbulent transition in airfoil flows.* Journal of aircraft, 1999. **36**(4): p. 731-734.
61. Jonker, A., et al., *Flow over a glider canopy.* The Aeronautical Journal, 2014. **118**(1204): p. 669-682.
62. Husaini, M., Z. Samad, and M.R. Arshad, *CFD simulation of cooperative AUV motion.* CSIR, 2009. **38**(3): p. 346-351.

63. de Barros, E.A., et al., *Investigation of normal force and moment coefficients for an AUV at nonlinear angle of attack and sideslip range.* IEEE Journal of Oceanic Engineering, 2008. **33**(4): p. 538-549.
64. Dantas, J.L.D. and E. De Barros, *Numerical analysis of control surface effects on AUV manoeuvrability.* Applied Ocean Research, 2013. **42**: p. 168-181.
65. Simpson, M. and D. Guo, *Design, Development and Integration of a Wing-Morphing, Bimodal Unmanned Vehicle*, in *SAE Technical Paper*. 2018.
66. Simpson, M. *Investigating the Effects of Wing Folding on the Performance of a Multi-Modal Unmanned Aerial Vehicle*. Department of Aeronautics [Master Thesis] 2018 29/05/2018 [cited Master degree; 54].
67. Polhamus, E.C., *A concept of the vortex lift of sharp-edge delta wings based on a leading-edge-suction analogy*. 1966: p. 15.
68. Borchardt, J.K., *Unmanned aerial vehicles spur composites use.* Reinforced plastics, 2004. **48**(4): p. 28-31.
69. Kopeliovich, D. *Carbon Fiber Reinforced Polymer Composites*. 14 May 2012 [cited 2019 30/01/2019]; Available from: https://web.archive.org/web/20120514092827/http://www.substech.com/dokuwiki/doku.php?id=carbon_fiber_reinforced_polymer_composites.
70. Yang, X., et al., *Modeling and Analysis of Variable Buoyancy Device Imitating Waterfowl Plumage Structure*, in *The Twenty-first International Offshore and Polar Engineering Conference*. 2011, International Society of Offshore and Polar Engineers.
71. *Material for 3D Printing*. 2017 [cited 2019 07/02/2019]; Available from: http://3dprintingsystems.com/products/filament/#1445554184401-ed7e990e-d95a.
72. Etkin, B. and L.D. Reid, *Dynamics of flight: stability and control*. Vol. 3. 1996: Wiley New York.
73. Nelson, R.C., *Flight stability and automatic control*. Vol. 2. 1998: WCB/McGraw Hill New York.
74. Pamadi, B.N., *Performance, stability, dynamics, and control of airplanes*. 2004: American Institute of aeronautics and astronautics.
75. Simons, M. and M. Simons, *Model aircraft aerodynamics*. 1999: Nexus Special Interests Hemel Hempstead, UK.
76. O'Dor, R., et al., *Squid rocket science: how squid launch into air*. Deep Sea Research Part II: Topical Studies in Oceanography, 2013. **95**: p. 113-118.
77. National Weather Service. *Wind, Swell and Rogue Waves*. [cited 2019 03/04/2019]; Available from: https://www.weather.gov/jetstream/waves.
78. Yunus, A.C. and J.M. Cimbala, *Fluid mechanics fundamentals and applications.* International Edition, McGraw Hill Publication, 2006. **185201**.
79. Ye, J. and P. Marzocca, *Hybrid Propulsion Strategies for a Multi-Modal UAV*, in *2018 AIAA Aerospace Sciences Meeting*. 2018. p. 1011.
80. Jia, L. and L. Wang. *Equations for gas releasing process from pressurized vessels in ODH evaluation*. in *AIP Conference Proceedings*. 2002. AIP.
81. YE, J.-p., Y.-l. DAI, and Y.-n. LI, *The mathematical model of the pneumatic blowing system of the submarine's ballast tanks [J]*. Ship Science and Technology, 2007. **2**: p. 031.
82. Wheeler, D., *Modeling the thrust phase*, in *Technical report*. 2002, Brigham Young University.
83. Roohi, E., A.P. Zahiri, and M. Passandideh-Fard, *Numerical simulation of cavitation around a two-dimensional hydrofoil using VOF method and LES turbulence model.* Applied Mathematical Modelling, 2013. **37**(9): p. 6469-6488.

84. Topeak. *MICRO AIRBOOSTER 16G*. [Picture] 2019 26/03/2019; Available from: https://www.topeak.com/global/en/products/co2-pumps/1072-micro-airbooster-16g.
85. Savox. *Savox - Servo - SV-1272SG - Digital - High Voltage - Coreless Motor - Steel Gear*. [Picture] 2019 26/03/2019; Available from: https://www.savox-servo.com/Servos/Coreless-Motor/Savox-Servo-SV-1272SG-Digital-High-Voltage-Coreless-Motor-Steel-Gear/.
86. Bacciaglia, A., et al., *Bimodal unmanned vehicle: propulsion system integration and water/air interface testing*, in *31st Congress of the international Council of the Aeronautical Sciences*. 2018.
87. Bacciaglia, A., *Design and Development of a Propulsion System for a Water/Air Unmanned Vehicle*. 2017, University of Bologna: Bologna. p. 86.
88. Scorpion Power System Limited. *Scorpion HK-2520-3500KV motor (3.5mm shaft)*. [Picture] 2019; Available from: https://www.scorpionsystem.com/catalog/helicopter/motors_4/hk-25/HK_2520_3500/.
89. Fibre Glast Developments Corporation. *Building a Vacuum System*. [Picture] 04/20/2019]; Available from: https://www.fibreglast.com/product/vacuum-bagging-equipment-and-techniques-for-room-temp-applications/Learning_Center.

Appendices

Appendix A

Mechanical drawings of the main components

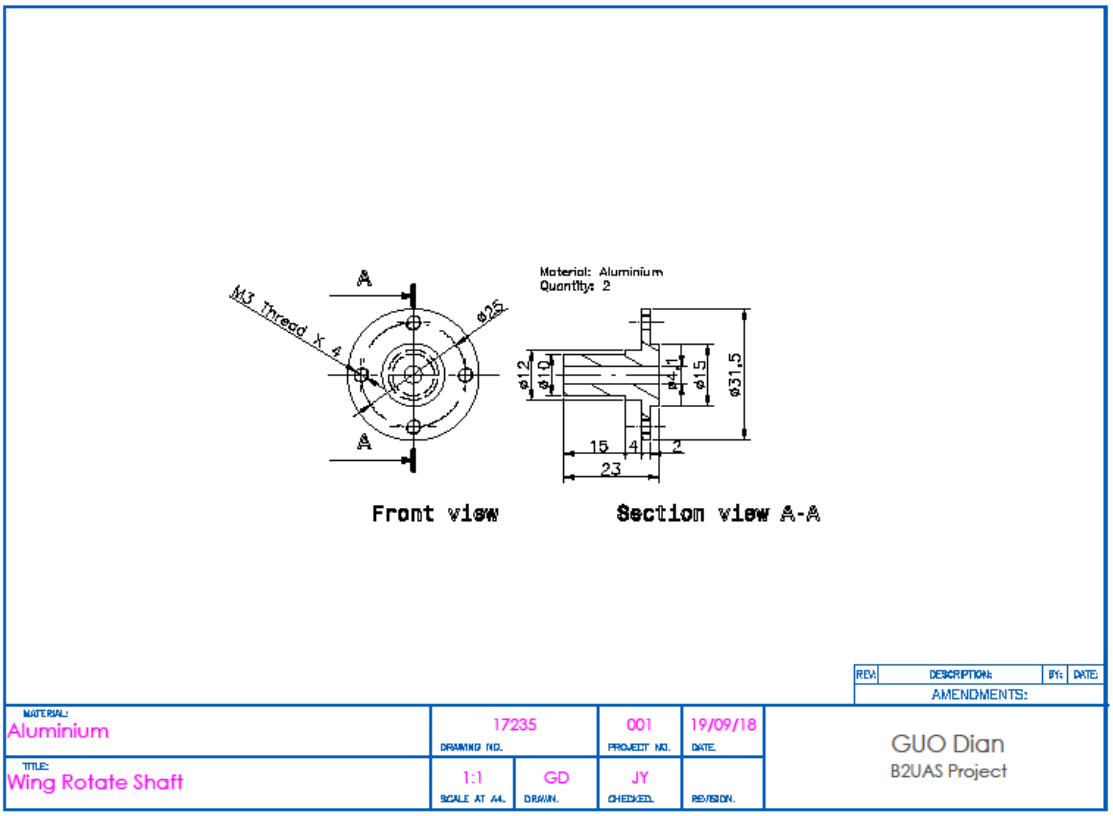

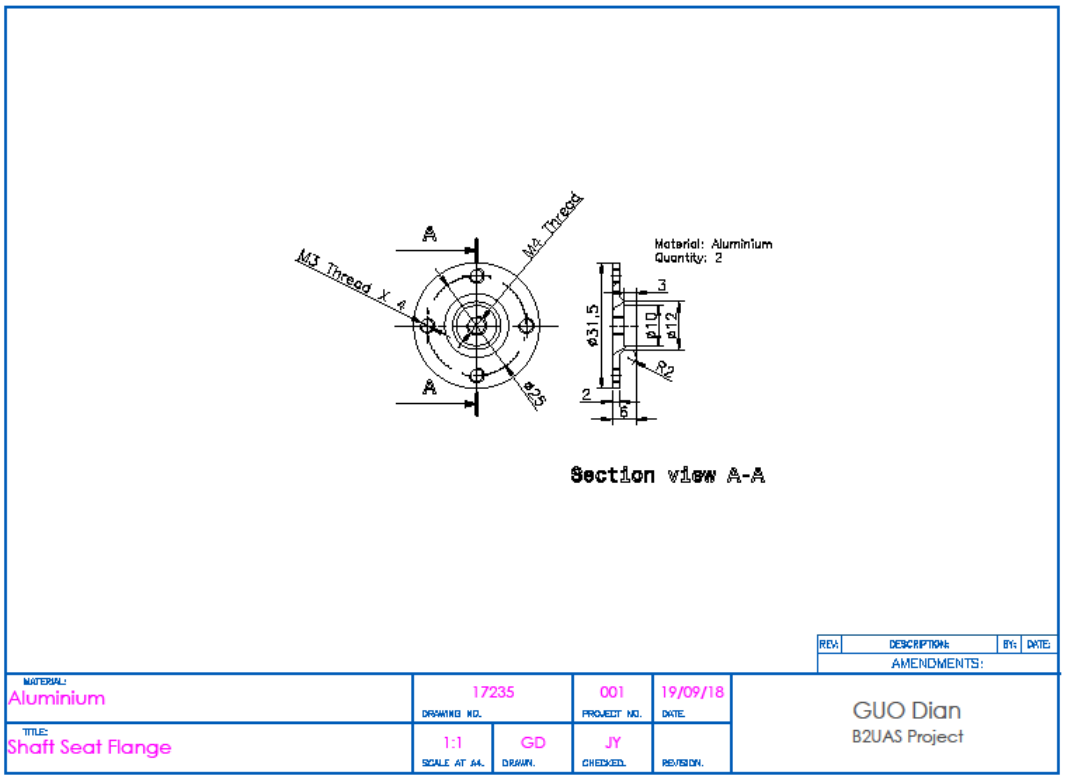
A
M4 Thread
M3 Thread X 4
A
ø25
Material: Aluminium
Quantity: 2
ø31.5
3
ø10
ø12
R2
2
5
Section view A-A
REV.
DESCRIPTION:
BY:
DATE:
AMENDMENTS:
MATERIAL:
Aluminium
17235
DRAWING NO.
001
PROJECT NO.
19/09/18
DATE.
TITLE:
Shaft Seat Flange
1:1
SCALE AT A4.
GD
DRAWN.
JY
CHECKED.
REVISION.
GUO Dian
B2UAS Project

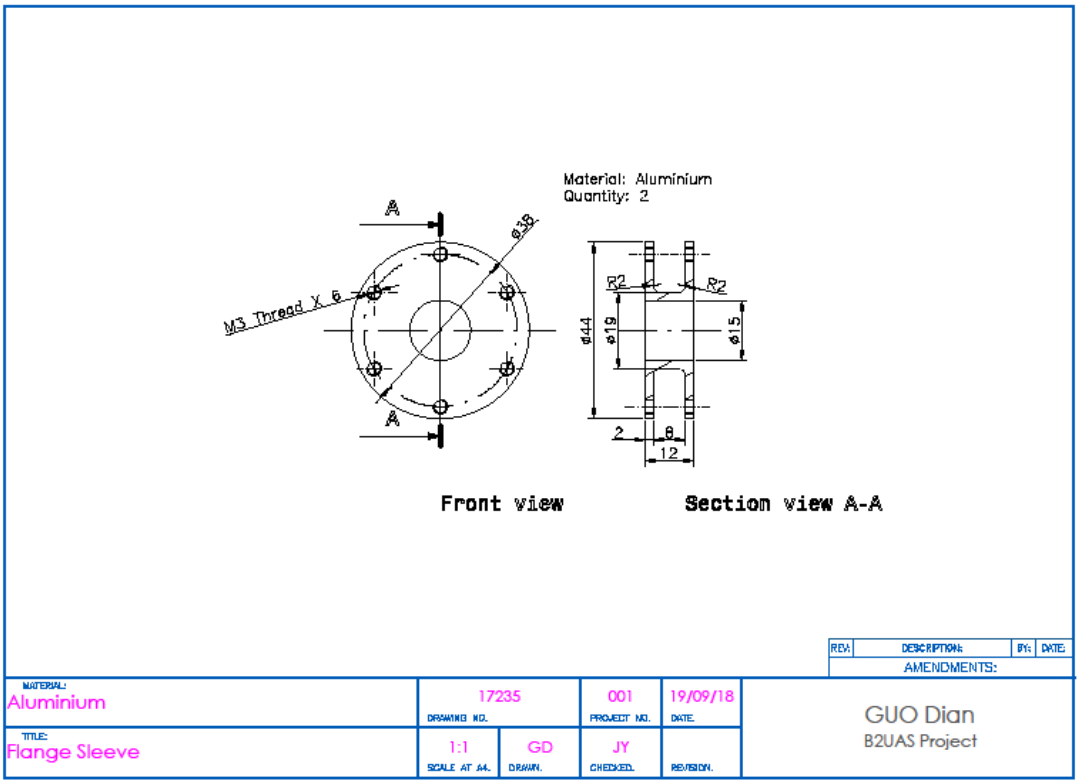
Material: Aluminium
Quantity: 2
A
ø38
M3 Thread X 6
A
R2
R2
ø44
ø19
ø15
2
8
12
Front view
Section view A-A
REV.
DESCRIPTION:
BY:
DATE:
AMENDMENTS:
MATERIAL:
Aluminium
17235
DRAWING NO.
001
PROJECT NO.
19/09/18
DATE.
TITLE:
Flange Sleeve
1:1
SCALE AT A4.
GD
DRAWN.
JY
CHECKED.
REVISION.
GUO Dian
B2UAS Project

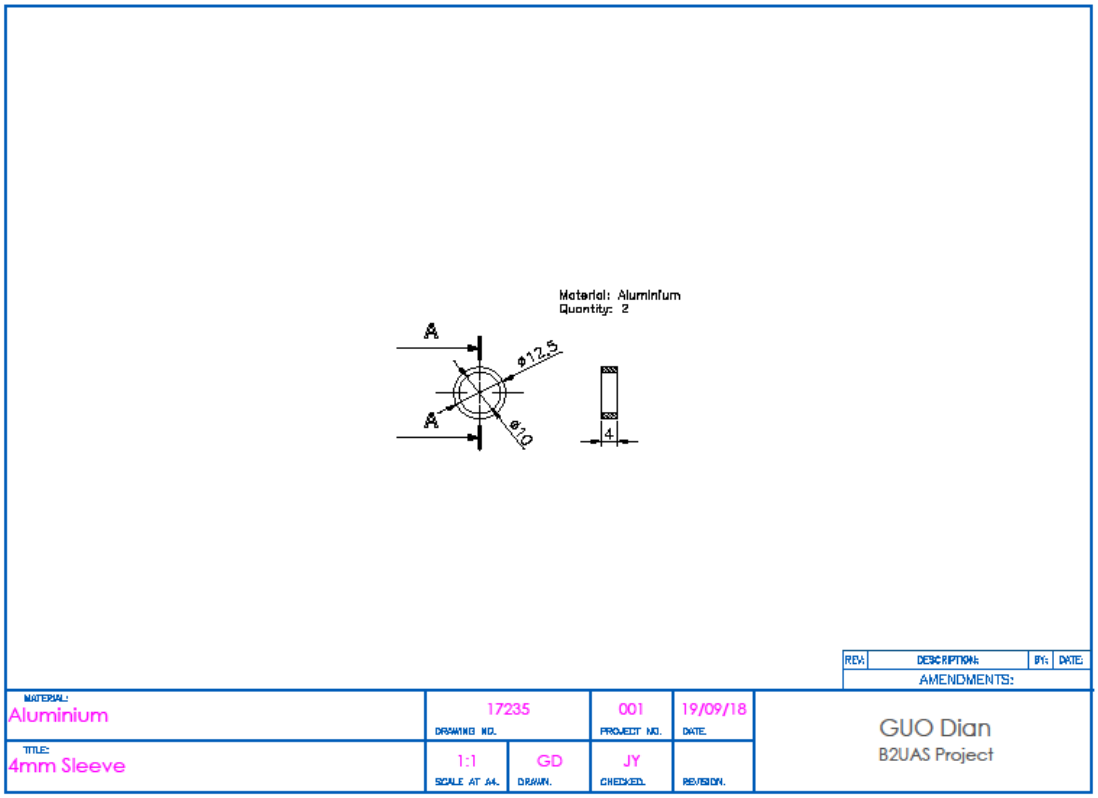

REV.	DESCRIPTION:	BY:	DATE:
	AMENDMENTS:		

MATERIAL: Aluminium	17235 DRAWING NO.		001 PROJECT NO.	19/09/18 DATE.
TITLE: 4mm Sleeve	1:1 SCALE AT A4.	GD DRAWN.	JY CHECKED.	REVISION.

GUO Dian
B2UAS Project

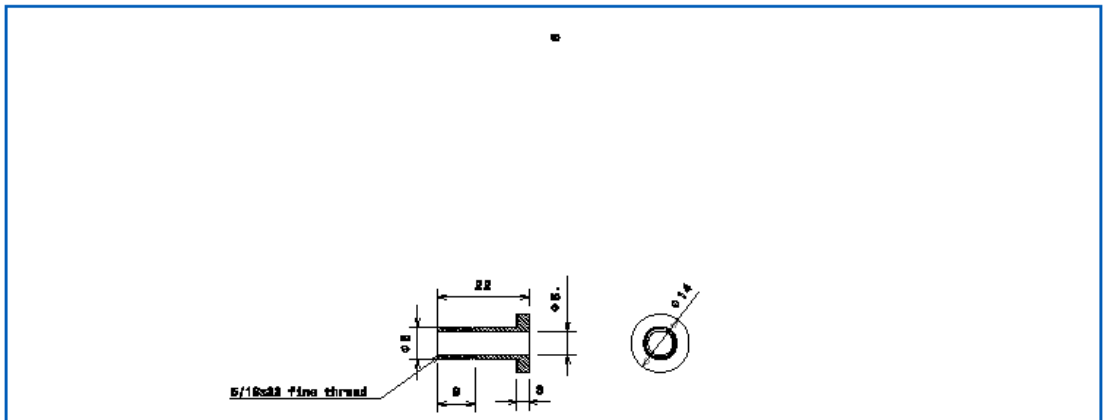

REV.	DESCRIPTION:	BY:	DATE:
	AMENDMENTS:		

MATERIAL: Aluminium	15186 DRAWING NO.		008 PROJECT NO.	12/10/17 DATE.
TITLE: Moveable Tube	1:1 SCALE AT A4.	GD DRAWN.	JY CHECKED.	REVISION.

GUO Dian
B2UAS Project

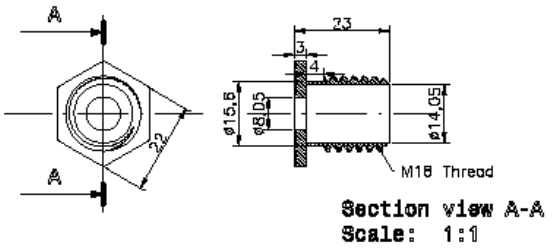

REV:	DESCRIPTION:	BY:	DATE:
	AMENDMENTS:		

MATERIAL: Aluminium	15186 DRAWING NO.		003 PROJECT NO.	17/10/17 DATE.
TITLE: Fixed Guide Tube	1:1 SCALE AT A4.	GD DRAWN.	JY CHECKED.	REVISION.

GUO Dian
B2UAS Project

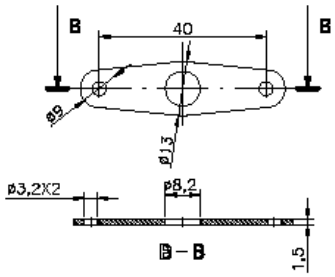

REV:	DESCRIPTION:	BY:	DATE:
	AMENDMENTS:		

SITE: RMIT Work Shop	17235 DRAWING NO.		001 PROJECT NO.	10/01/17 DATE.
TITLE: Press Plate	1:1 SCALE AT A4.	GD DRAWN.	JY CHECKED.	REVISION.

GUO Dian
B2UAS Project

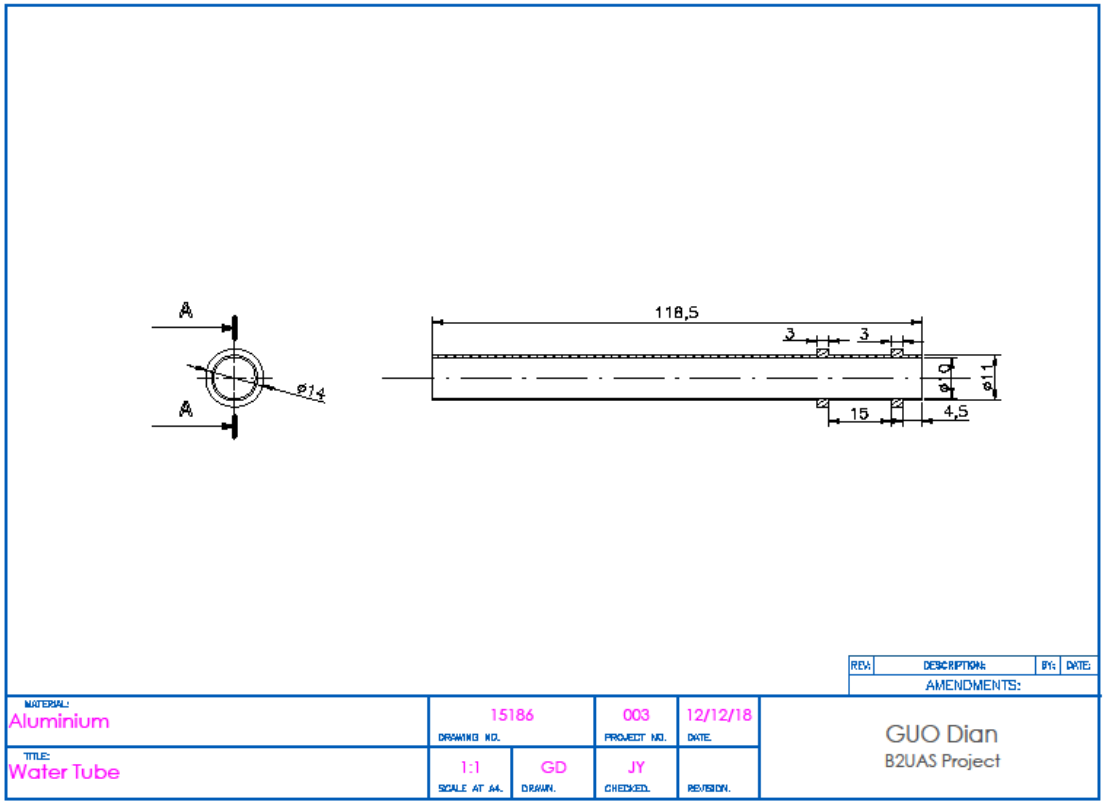
A
A
Ø14
118,5
3
3
Ø9
Ø11
15
4,5
REV:
DESCRIPTION:
BY:
DATE:
AMENDMENTS:
MATERIAL:
Aluminium
15186
DRAWING NO.
003
PROJECT NO.
12/12/18
DATE.
TITLE:
Water Tube
1:1
SCALE AT A4.
GD
DRAWN.
JY
CHECKED.
REVISION.
GUO Dian
B2UAS Project

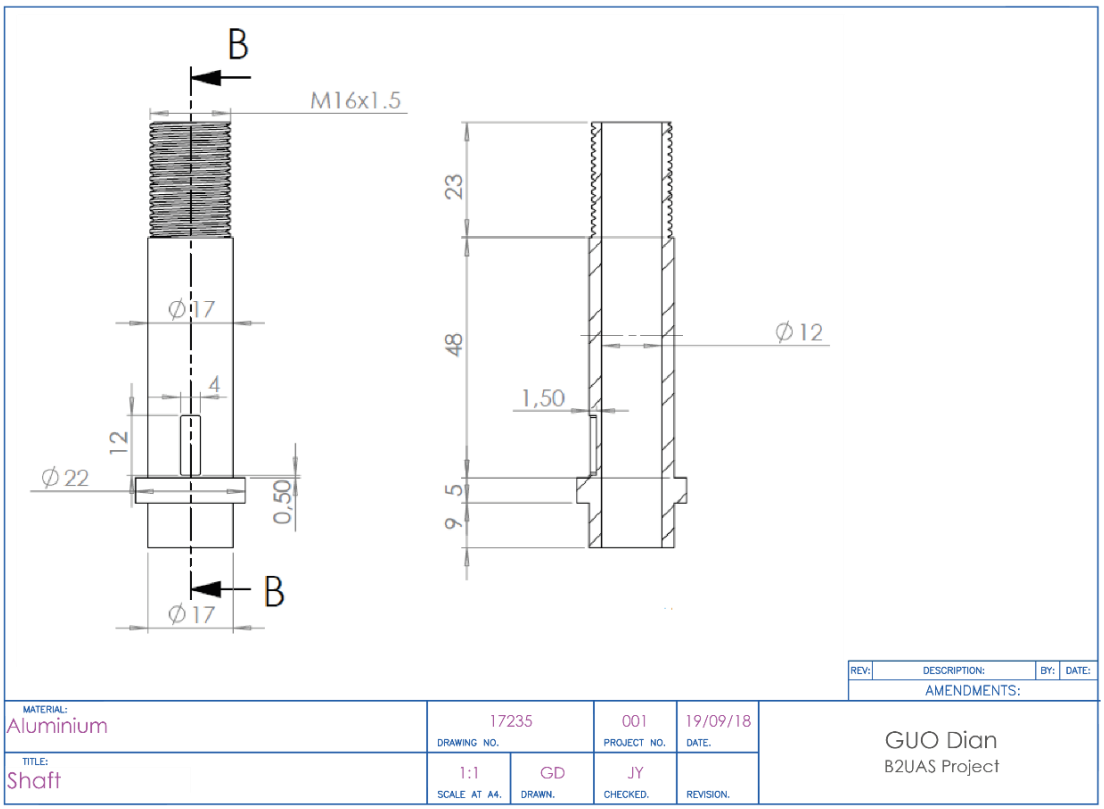
B
M16x1.5
Ø17
4
12
Ø22
0,50
B
Ø17
23
48
9
5
Ø12
1,50
REV:
DESCRIPTION:
BY:
DATE:
AMENDMENTS:
MATERIAL:
Aluminium
17235
DRAWING NO.
001
PROJECT NO.
19/09/18
DATE.
TITLE:
Shaft
1:1
SCALE AT A4.
GD
DRAWN.
JY
CHECKED.
REVISION.
GUO Dian
B2UAS Project

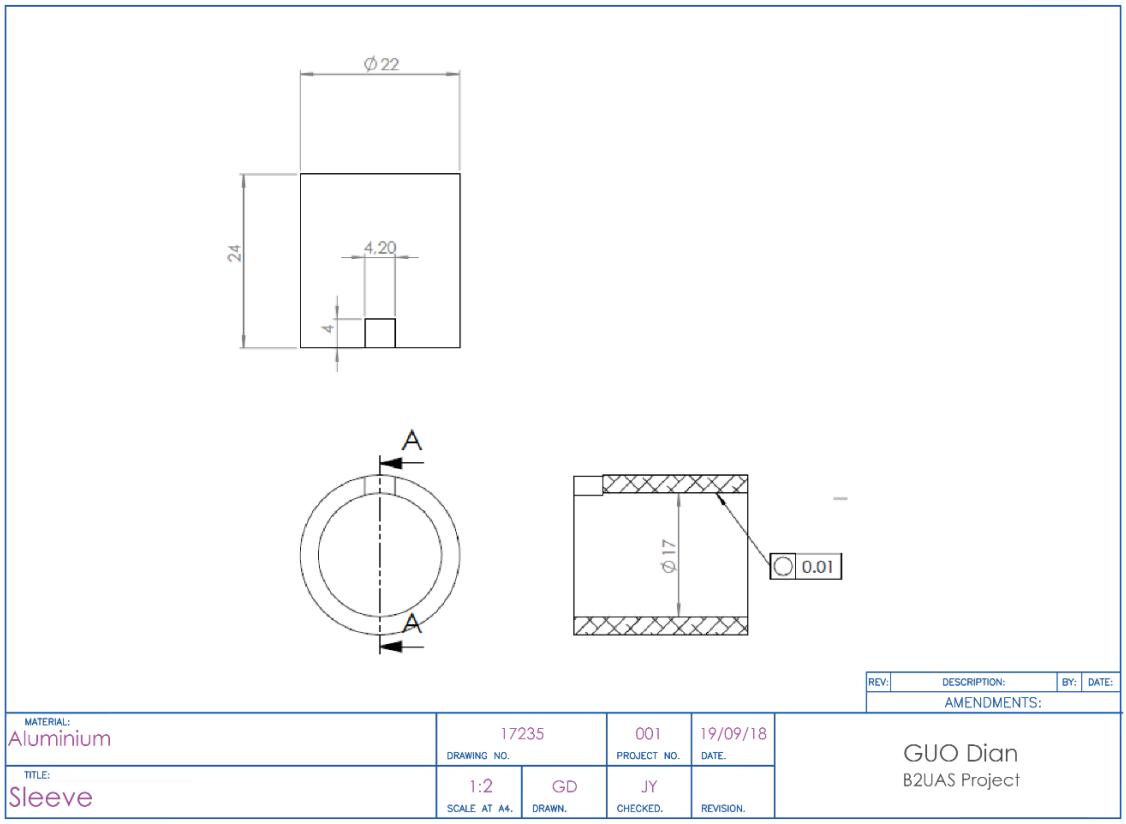
Ø22
24
4,20
4
A
A
Ø17
0.01
REV:
DESCRIPTION:
BY:
DATE:
AMENDMENTS:
MATERIAL:
Aluminium
17235
DRAWING NO.
001
PROJECT NO.
19/09/18
DATE.
TITLE:
Sleeve
1:2
SCALE AT A4.
GD
DRAWN.
JY
CHECKED.
REVISION.
GUO Dian
B2UAS Project

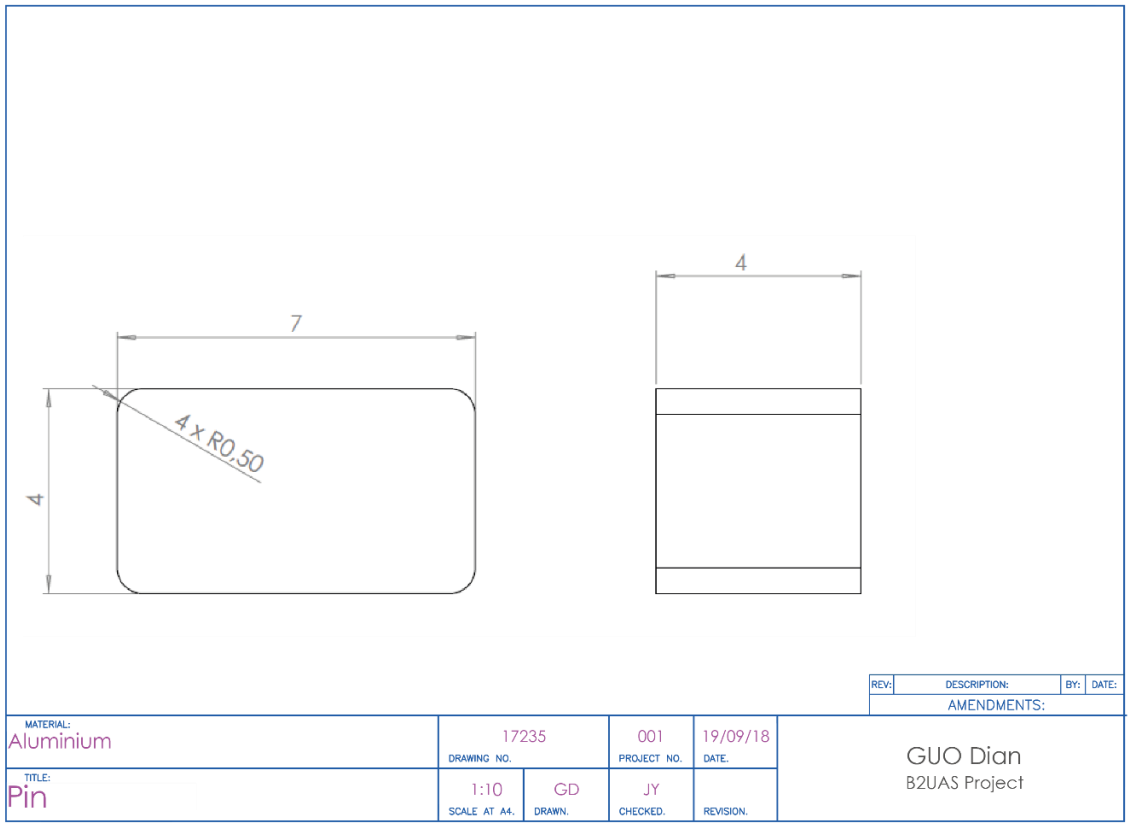
7
4
4 x R0,50
4
REV:
DESCRIPTION:
BY:
DATE:
AMENDMENTS:
MATERIAL:
Aluminium
17235
DRAWING NO.
001
PROJECT NO.
19/09/18
DATE.
TITLE:
Pin
1:10
SCALE AT A4.
GD
DRAWN.
JY
CHECKED.
REVISION.
GUO Dian
B2UAS Project

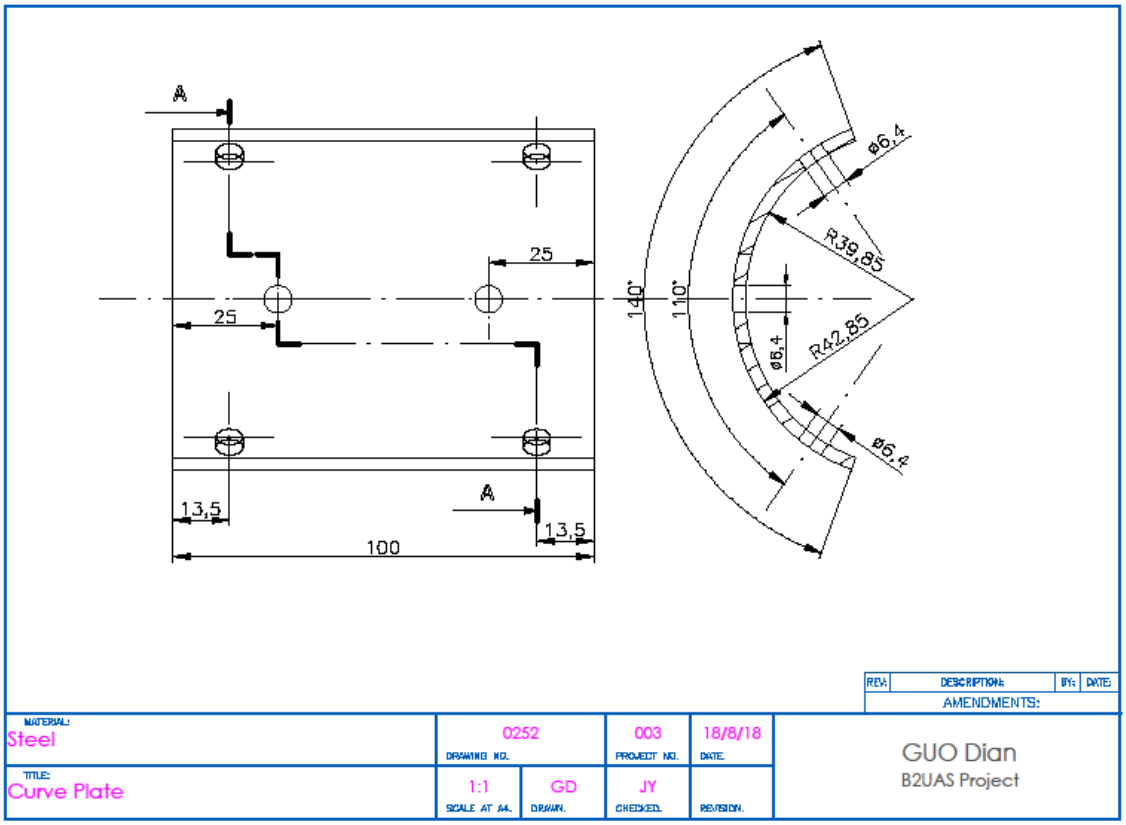

REV:	DESCRIPTION:	BY:	DATE:
	AMENDMENTS:		

MATERIAL:				
Steel	0252 DRAWING NO.		003 PROJECT NO.	18/8/18 DATE.
TITLE: Curve Plate	1:1 SCALE AT A4.	GD DRAWN.	JY CHECKED.	REVISION.

GUO Dian
B2UAS Project

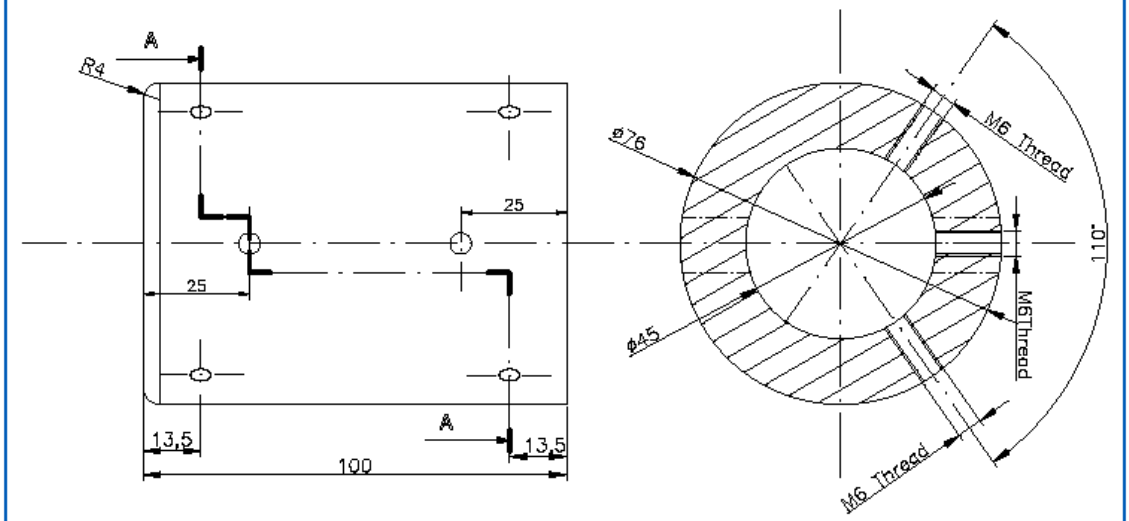

REV:	DESCRIPTION:	BY:	DATE:
	AMENDMENTS:		

MATERIAL:				
Aluminium	0252 DRAWING NO.		003 PROJECT NO.	18/8/18 DATE.
TITLE: Wind Tunnel Cylinder	1:1 SCALE AT A4.	GD DRAWN.	JY CHECKED.	REVISION.

GUO Dian
B2UAS Project

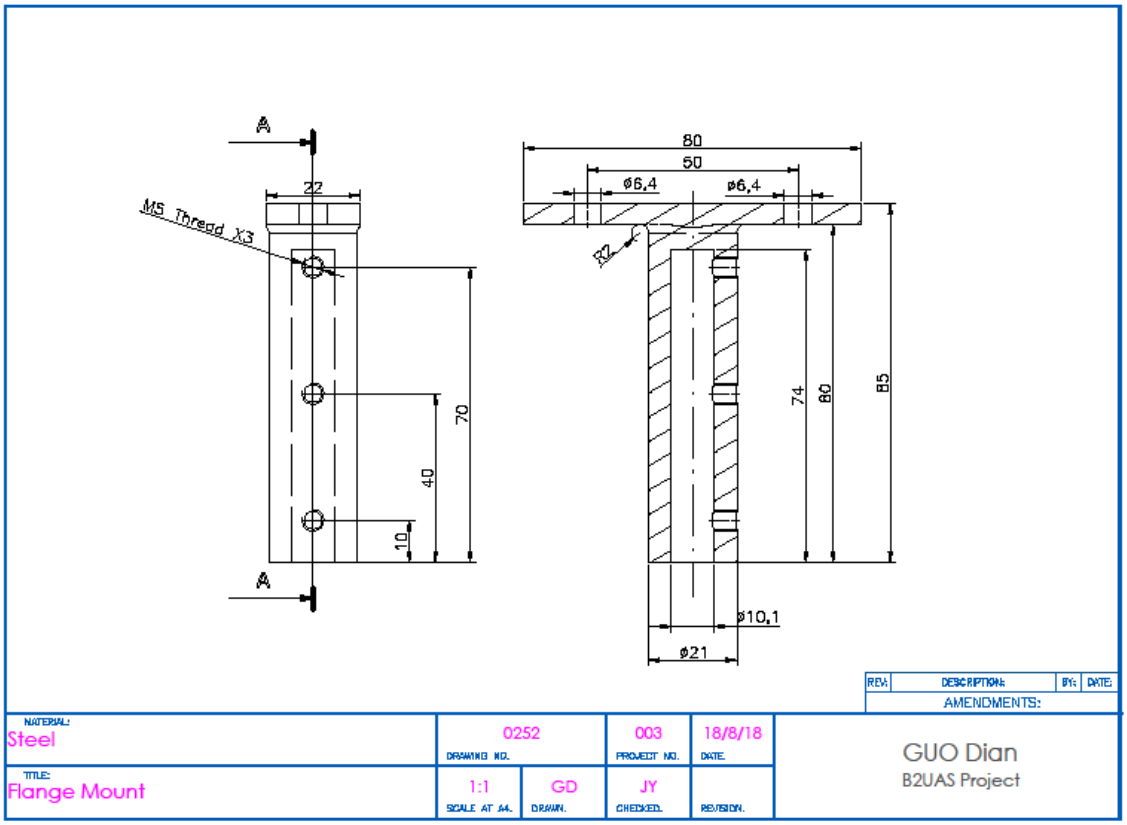
A
22
M5 Thread X3
70
40
10
A
80
50
ø6,4
ø6,4
ø4
74
80
85
ø10,1
ø21
REV:
DESCRIPTION:
BY:
DATE:
AMENDMENTS:
MATERIAL:
Steel
0252
DRAWING NO.
003
PROJECT NO.
18/8/18
DATE
TITLE:
Flange Mount
1:1
SCALE AT A4.
GD
DRAWN.
JY
CHECKED.
REVISION.
GUO Dian
B2UAS Project

Appendix B

Hybrid propulsion system components pictures and specifications

Motor picture

Figure B-1: Scorpion® HK-2520 brushless motor [88]

Motor dimension

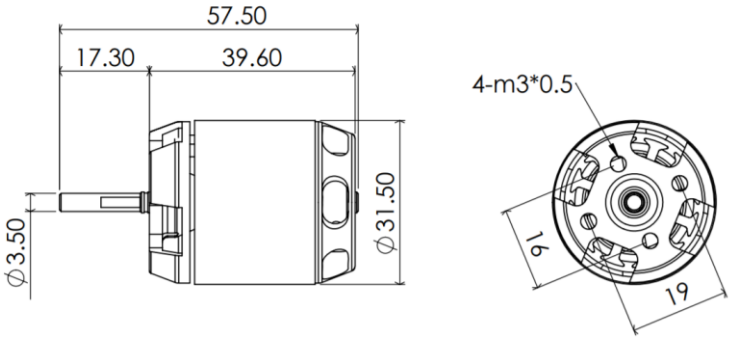

Motor specification

Category	Value
Motor KV	3500 KV RPM/Volt
No-Load Current	5.80 Amps
Max Continuous Current	55 Amps
Max Continuous Power	770 Watts
Weight	104 Grams
Max Peak Current	75A (2 seconds)
Max Peak Power	1050 Watts (2 seconds)

ESC picture

Figure B-2: Dualsky® 60 A ESC

ESC specification

Category	Value
Dimensions (L × W × D)	75 × 30 × 14 mm
Weight	63 Grams
Number of Cells (LiPo)	2-6, 7.4-22.2 Volt
Max Continuous Current	60 Amps
Max Continuous Output	1260 Watts
Max Burst Current	80 Amps
Max Burst Output	1632 Watts

Appendix C

Vacuum system build-up

After the layup is finished, the vacuum is conducted. Since the pot time is only 25 minutes, the vacuum bag was prepared firstly. The rest of the vacuum system was built as the Figure displayed. To begin with, the release film is put on the carbon fibre laminate. It would not adhere with the resin and could retain some resin to make the finished surface smooth. Then a layer of peel was laid down to provide an easy release barrier between the part and breather cloth layer. Next, the breather and bleeder cloth were used to soak up excess resin from the laminate, and provide the path for the vacuum pressure. Finally, the laminate with all the bagging materials were placed in the vacuum bag. The vacuum bag was closed by the sealant tape to isolate the laminate and bagging materials from the atmosphere. After checking of all the connections, the vacuum pump was turned on and the vacuum process began.

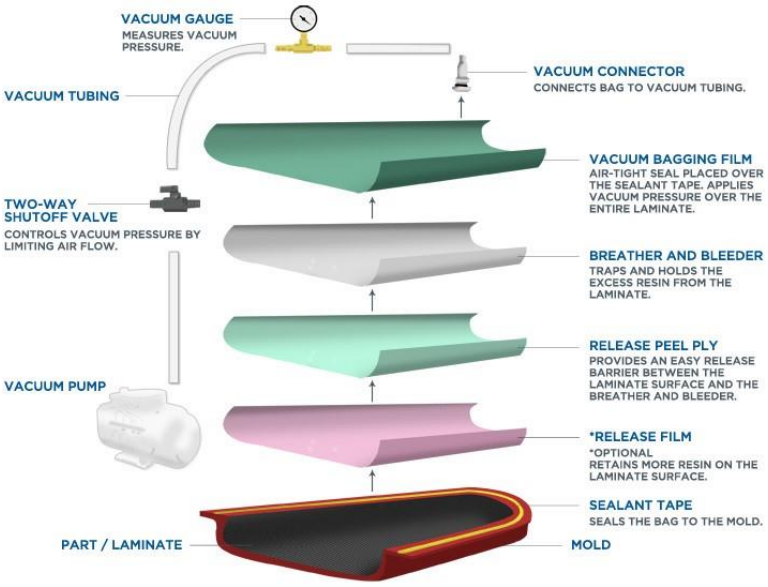

Figure C-1: Vacuum bagging equipment and techniques [89]